



**FLOW MEASUREMENTS USING PARTICLE IMAGE VELOCIMETRY IN  
THE ULTRA COMPACT COMBUSTOR**

**THESIS**

Levi M. Thomas, First Lieutenant, USAF

AFIT/GAE/ENY/09-D04

**DEPARTMENT OF THE AIR FORCE  
AIR UNIVERSITY**

***AIR FORCE INSTITUTE OF TECHNOLOGY***

---

**Wright-Patterson Air Force Base, Ohio**

APPROVED FOR PUBLIC RELEASE; DISTRIBUTION UNLIMITED

The views expressed in this thesis are those of the author and do not reflect the official policy or position of the United States Air Force, Department of Defense, or the United States Government. This material is declared a work of the U.S. Government and is not subject to copyright protection in the United States.

AFIT/GAE/ENY/09-D04

**FLOW MEASUREMENTS USING PARTICLE IMAGE VELOCIMETRY IN  
THE ULTRA COMPACT COMBUSTOR**

THESIS

Presented to the Faculty

Department of Aeronautics and Astronautics

Graduate School of Engineering and Management

Air Force Institute of Technology

Air University

Air Education and Training Command

In Partial Fulfillment of the Requirements for the  
Degree of Master of Science in Aeronautical Engineering

Levi M. Thomas

First Lieutenant, USAF

December 2009

APPROVED FOR PUBLIC RELEASE; DISTRIBUTION UNLIMITED.

**FLOW MEASUREMENTS USING PARTICLE IMAGE VELOCIMETRY IN  
THE ULTRA COMPACT COMBUSTOR**

Levi M. Thomas

First Lieutenant, USAF

December 2009

Approved:

\_\_\_\_\_  
LtCol Richard D. Branam, USAF (Chairman)

\_\_\_\_\_  
date

\_\_\_\_\_  
Paul King, PhD (Member)

\_\_\_\_\_  
date

\_\_\_\_\_  
Mark Reeder, PhD (Member)

\_\_\_\_\_  
date

## Abstract

Velocity measurements were performed using the Particle Image Velocimetry (PIV) technique on the Ultra Compact Combustor (UCC) test rig at the Air Force Institute of Technology (AFIT). Velocity patterns and time-averaged turbulence statistics were calculated for data taken with the UCC burning hydrogen fuel in the straight cavity vane and curved cavity vane configurations. The equivalence ratio was varied from 0.7 to 1.5, while the ratio of cavity air to main air was varied from 5% to 20% in testing performed on the straight vane configuration. Spanwise velocity was observed to decrease linearly with distance from the cavity vane over the width of the main channel, but spanwise turbulence intensity penetrated into less than 50% of the main channel for all conditions except the most fuel rich ( $\phi=1.5$ ) suggesting more rich conditions may prove better for both mixing and operability. A velocity effect study was performed in the curved and straight cavity vane configuration by increasing the flow rates, but holding the equivalence ratio and ratio of cavity to main air flow rates constant. Relative turbulence intensities were found to be independent of overall flow velocity in the straight configuration, while a negative correlation was observed in the curved configuration. Overall turbulence intensity levels were measured at 15% and 21% of the main channel velocity for the straight and curved configurations respectively. The highest average turbulence intensities were observed near the cross-flow of the cavity vane, and peak turbulence was observed just over the Radial Vane Cavity (RVC). The RVC was observed to generate flow rotation. Peak vorticity was observed farthest from the cavity vane suggesting the angle of the RVC is effective in generating increasing flow rotation with streamwise velocity.

## **Acknowledgements**

I would like to start by thanking my wife Erika for being so understanding and supportive during the three years it took to complete the program. I didn't mind all the nerd-jokes that kept the mood light. Thanks to my father for sparking my interest in engineering, and to my mother for tutoring me through the hard stuff – like long division.

I would like to sincerely thank my advisor, LtCol Branam for all the time he spent guiding me, tutoring me, and trusting me enough to play with fire, but not getting too upset when I broke things or “verbed” his last name. Thanks to Dr. Reeder for all the technical guidance. Thanks to John Hixenbaugh for helping me learn the ropes of a technical laboratory. Thanks to the interns Mike Miller and Mike Boehler for staying late and coming in on weekends, and for the pranks like the fake parking ticket on Hixenbaugh's car.

Thanks to my old boss at NASIC, Dave Turich, and my new boss at AFRL, Dr. Hancock, for allowing me to work on this thesis during duty time. Getting that extra hour was like saving structural weight on an aircraft – that one pound of “added lightness” enabled me to carry five pounds worth of academics.

Thanks to the Dayton Area Graduate Studies Institute for the fellowship that paid for most of the tuition. Thanks to Lt Col Branam, yet again, for securing the funding to keep me at AFIT long enough to finish this thesis.

Levi Thomas

# Table of Contents

	Page
Abstract .....	viii
Acknowledgements .....	ix
Table of Contents .....	x
List of Figures .....	xiii
List of Tables .....	xvii
List of Symbols .....	xviii
List of Abbreviations .....	xx
I. Introduction.....	1
I.1 Research and Design Perspective .....	1
I.2 The Ultra-Compact Combustor Concept .....	3
I.3 Research Objectives.....	7
I.4 Methods.....	9
II. Theory and Background.....	14
II.1 The Gas-Turbine Engine.....	14
II.2 Desired Combustor Properties .....	15
II.3 Combustion .....	19
II.3.1 Stoichiometry & the Equivalence Ratio .....	19
II.3.2 Flame Speed & Turbulence .....	22
II.4 Literature Review of Select UCC Research.....	25
II.4.1 Propulsion Directorate/AFRL Research .....	25
II.4.2 AFIT COAL Lab & CFD Research .....	26
II.5 Anatomy of the Ultra Compact Combustor (UCC) .....	28
II.6 Particle Image Velocimetry .....	30
II.6.1 Seed / Tracer Particles .....	31
II.6.2 Laser Type .....	34
II.6.3 Camera Type.....	37
II.6.4 The Cross-Correlation Technique.....	40
II.6.5 Measureable Velocity .....	42
II.7 Error Factors in PIV .....	42
II.7.1 Loss of Pairs.....	43
II.7.2 Parallax Effects .....	45
II.7.3 Zero-Velocity Biasing.....	46

II.7.4	The FFT Error .....	46
III.	Test Setup and Apparatus .....	48
III.1	Methods.....	48
III.2	Experimentation.....	48
III.3	Test Matrix.....	50
III.3.1	Cavity-to-Main Vane Mass Flow & Equivalence Ratio Study.....	50
III.3.2	Velocity Increase Study .....	52
III.4	Lab Setup .....	53
III.4.1	Computer Controls.....	53
III.4.2	Gases .....	56
III.4.3	Infrastructure (80/20) .....	62
III.4.4	Translation of the Experimental Plane.....	64
III.5	Ultra-Compact Combustor Sectional Test Rig Setup .....	67
III.5.1	Placement of the UCC, Exhaust System.....	68
III.5.2	Pressure Taps & Thermocouples .....	71
III.5.3	Sealing the Cracks.....	72
III.5.4	Ethylene Igniter.....	73
III.5.5	Seeder Port .....	76
III.6	Particle Image Velocimetry Equipment Setup.....	78
III.6.1	Seeder Setup.....	78
III.6.2	PIV Camera Setup.....	80
III.6.3	Laser Equipment Setup .....	84
III.6.4	OEM Optics .....	86
III.6.5	Custom Optics.....	89
III.6.6	Pulse Delay Study .....	91
III.7	Data Processing.....	96
III.7.1	Interrogation Regions and Overlap.....	96
III.7.2	Filters & Window Functions.....	98
III.7.3	Validation Techniques .....	101
III.8	Uncertainty Analysis.....	103
III.8.1	Mass Flow Rate Variability Study.....	104
III.8.2	Statistical Accuracy .....	108
III.8.3	Measurement Repeatability .....	113
IV.	Discussion and Results .....	118
IV.1	Data Processing.....	118



IV.1.1 Statistical Analysis.....	118
IV.1.2 Turbulence Intensity: Dynamic Studio Method.....	121
IV.1.3 Turbulence Intensity: New Method .....	123
IV.1.4 Validation of Data Export and Processing.....	126
IV.1.5 Limits Used for Data Filtering.....	129
IV.1.6 Vorticity .....	130
IV.2 Observed Trends .....	131
IV.2.1 Mean Measured Velocity .....	131
IV.2.2 Vector Plots and Flow Direction.....	136
IV.2.3 Vorticity over the Radial Vane Cavity.....	140
IV.2.4 Turbulence Intensity Levels.....	144
IV.2.5 Boundary Layer Induced Turbulence .....	146
IV.2.6 Location of Turbulence Peaks within an Experimental Plane .....	147
IV.2.7 Mean Turbulence Intensity Dependence on Mass Flow Rate .....	153
IV.2.8 Possible Error in PIV Measurement .....	156
IV.3 Summary of Observed Trends .....	161
V. Conclusions and Recommendations .....	163
V.1 Satisfaction of the Research Objectives.....	163
V.2 Physical Interpretation of Observed Trends .....	164
V.2.1 Variance in Velocity .....	164
V.2.2 Variance in Turbulence Intensity.....	165
V.2.3 Variance in Vorticity.....	165
V.3 PIV in the UCC.....	166
V.4 Future work.....	167
Appendix A.....	169
Appendix B.....	175
Appendix C .....	181
Bibliography (In Order of Appearance).....	187
VI. Vita.....	191

## List of Figures

	Page
Figure 1. Transport of combustion gases in the TVC concept (adapted from Greenwood, et al.) <sup>7</sup> .....	5
Figure 2. Comparison of full model UCC concept: on left; to AFIT sector model, straight cavity configuration: on right (adapted from Anisko, et al.) <sup>11</sup> .....	10
Figure 3. Main vane cutaway showing radial vane cavity .....	11
Figure 4. Cavity vane cutaways showing main combustion chambers .....	12
Figure 5. Left: Cross-section of annular burner (adapted from Mattingly) <sup>4</sup> ; right: UCC concept cutaway (adapted from Greenwood) <sup>6</sup> .....	29
Figure 6. Pictorial of the PIV process (used with permission) <sup>23</sup> .....	30
Figure 7. Synchronization diagram (used with permission) <sup>27</sup> .....	37
Figure 8. Flowsense 4M camera showing filter, lens, and CCD .....	38
Figure 9. Interrogation regions and their corresponding vector output from cross-correlation showing loss of pairs from in plane & out of plane velocity .....	44
Figure 10. Coal lab main control center.....	54
Figure 11. Test stand with gas lines.....	57
Figure 12. Air supply and control lines .....	58
Figure 13. Main and cavity air lines connected to the UCC test rig .....	59
Figure 14. Cross-sections of “80/20” aluminum structure <sup>34</sup> .....	63
Figure 15. Seeder table & test stand .....	64
Figure 16. Approximate positions of the four experimental planes (top); laser illumination of experimental plane #4 during testing (bottom) .....	65
Figure 17. Camera mounted on electronic translation device.....	66
Figure 18. Newport ESP300 motion control driver .....	66
Figure 19. Newport ESP300 with faulty amplifier card .....	67
Figure 20. UCC testing orientation used in previous research <sup>22</sup> .....	68
Figure 21. Temporary UCC orientation.....	69
Figure 22. Final lab configuration for the UCC test rig.....	71
Figure 23. Differential pressure transducers used to measure pressure drop .....	72
Figure 24. Fiberfrax® ceramic fiber paper <sup>34</sup> .....	73
Figure 25. Close-up of ethylene igniter .....	74
Figure 26. Steady operation of ethylene/ air igniter .....	75
Figure 27. Seeder manifold installed onto the UCC main vane .....	77

Figure 28. Diagram of PS-10 power seeder (used with permission) <sup>35</sup> .....	78
Figure 29. Seeding drums and related equipment.....	79
Figure 30. Approximate camera field of view on the UCC (left); calibration image showing region of image used for PIV processing (right) .....	81
Figure 31. Screen capture from Dynamic Studio's measure scale factor function.....	83
Figure 32. Diagram of equipment used in COAL Lab for PIV and PLIF experiments .....	84
Figure 33. Diagram of PIV experimental setup .....	86
Figure 34. Plot of laser average power at max repetition rate of 20 Hz .....	87
Figure 35. PIV laser with original optics .....	88
Figure 36. Mirror mounted on linear translator with laser path in green.....	89
Figure 37. Side-view of a half-cylindrical lens.....	90
Figure 38. Top-view of a plano-convex lens .....	91
Figure 39. Pulse delay study .....	93
Figure 40. PIV raw data used in pulse delay study.....	94
Figure 41. Enlarged view of a single interrogation region for an image pair .....	95
Fig. 42. Graphical Representation of the Gaussian Window Weighting Function.....	99
Figure 43. Results from air mass flow variability study .....	105
Figure 44. Variability in air mass flow rates.....	107
Figure 45. Velocity vectors superimposed on a color-map of the % statistical error for a 95% CI: straight cavity, 1.5 kg/min airflow, EqR. = 1.0.....	110
Figure 46. Radial vane cavity <sup>44</sup> .....	111
Figure 47. Velocity vectors superimposed on a color-map of the number of valid samples at each interrogation region: curved cavity, 1.2 kg/min airflow, EqR. = 1.0, position 1 (Near Cavity), mean velocity over experimental plane = 40.92 m/s .....	112
Figure 48. Mean velocity vectors superimposed over statistical error at 95% CI: straight cavity, equiv ratio: 1.5, ratio of mass flows: 0.15, case one .....	114
Figure 49. Mean velocity vectors superimposed over statistical error at 95% CI: straight cavity, equiv ratio: 1.5, ratio of mass flows: 0.15, case two .....	115
Figure 50. Sample mean velocity vector map at position closest to cavity vane.....	119
Figure 51. Spanwise turbulence intensity calculated by Dynamic Studio® PIV software .....	122
Figure 52. Mean velocity vector map at position three – away from cavity vane .....	124
Figure 53. Mean velocity profile away from cavity vane .....	125

Figure 54. Mean velocity profile near cavity vane .....	125
Figure 55. Spanwise turbulence intensity scalar map: Dynamic Studio®.....	127
Figure 56. spanwise turbulence intensity scalar map: Matlab® .....	127
Figure 57. V, U, & RMS turbulence intensity scalar plots of data taken in the UCC flowing 1.5 & 0.15 kg/min in the main and cavity vanes at equivalence ratio = 1.0 .....	128
Figure 58. Mean velocity in the main vane for experimental plane three .....	132
Figure 59. Mean streamwise (U) velocity at each experimental plane for the straight cavity configuration, error bars at 95% CI.....	134
Figure 60. Mean streamwise (U) velocity at each experimental plane for the curved cavity configuration, error bars at 95% CI.....	134
Figure 61. Mean spanwise (V) velocity at each experimental plane for the straight cavity configuration, error bars at 95% CI.....	135
Figure 62. Mean spanwise (V) velocity at each experimental plane for the straight cavity configuration, error bars at 95% CI.....	136
Figure 63. Vector map superimposed on color map of % statistical error at a 95% CI: curved config., main & cav. flows: 1.5 & 0.15kg/min, equivalence ratio: 1.0, position 1 .....	137
Figure 64. Vector map over color map of velocity for straight vane (left) & curved vane (right): main & cav. mass flows: 1.5 & 0.15kg/min, equiv ratio: 1.0, position 1 .....	138
Figure 65. Spanwise turbulence intensity, straight vane config., main & cav. mass flows: 1.5 & 0.15kg/min, equiv ratio: 1.0, position 1 .....	139
Figure 66. Vorticity progression through within the main channel: straight cavity vane, equivalence ratio : 1.0, main & cavity mass flows: 0.9, 0.09 kg/min .....	140
Figure 67. Histograms of vorticity, straight cavity, equivalence ratio: 1.0, main & cavity mass flows: 1.5 & 0.15 kg/min.....	142
Figure 68. Increase in region of high vorticity shown away from cavity vane: vorticity colormaps & histograms for experimental plane positions 2 & 4.....	143
Figure 69. Spanwise turbulence intensity, mass flows of 1.2 & 0.12, eq. ratio 1.0.....	144
Figure 70. Streamwise turbulence intensity, mass flows of 1.2 & 0.12, equiv. ratio 1.0.....	145
Figure 71. RMS average turbulence intensity over the depth of the main channel .....	146
Figure 72. Streamwise turbulence intensity, equiv ratio = 1.0, straight cavity vane config, main & cavity airflows: 0.9 & 0.09 kg/min .....	148

Figure 73. Spanwise turbulence intensity, equiv ratio = 1.0, straight cavity vane config, main & cavity airflows: 0.9 & 0.09 kg/min .....	149
Figure 74. Spanwise turbulence intensity throughout main channel depth: cavity to main mass flow ratio: 0.2, equivalence ratios of 0.7, 1.0, 1.3, & 1.5 .....	150
Figure 75. Spanwise turbulence intensity progression with distance from cavity, main & cavity mass flows: 1.5 & 0.15 kg/min, straight cavity channel .....	151
Figure 76. Spanwise turbulence intensity throughout main channel depth: straight cavity vane, equiv. ratio: 1.5, main mass flow: 0.6 kg/min (left) & 0.8 kg/min (right) .....	152
Figure 77. Mean turbulence intensity dependence on mass flow rate with 95% CI.....	155
Figure 78. Surface & contour plots of v-dir. turb. intensity: straight cavity vane config., 0.6 & 0.06 kg/min main and cavity mass flow rates, equiv. ratio = 1.0 .....	157
Figure 79. Surface & contour plots of v-dir. turb. intensity: straight cavity vane config., 1.5 & 0.15 kg/min main and cavity mass flow rates, equiv. ratio = 1.0 .....	157
Figure 80. Surface & contour plots of v-dir. turb. intensity: curved cavity vane config., 0.6 & 0.06 kg/min main and cavity mass flow rates, equiv. ratio = 1.0 .....	158
Figure 81. Surface & contour plots of spanwise turbulence intensity: curved cavity vane config., 1.5 & 0.15 kg/min main and cavity mass flow rates, equiv. ratio = 1.0.....	159
Figure 82. Histograms of turbulence intensity: streamwise ti on left, spanwise ti on right, ratio of mass flow rates = 0.1, equivalence ratio = 1.0.....	160
Figure 83. Histograms of turbulence intensity: streamwise ti on left, spanwise ti on right, ratio of mass flow rates = 0.1, equivalence ratio = 1.0.....	160

## List of Tables

	Page
Table 1. Seed particle specifications (used with permission) <sup>24</sup> .....	33
Table 2. Test matrix for flow rate ratio & equivalence ratio study.....	51
Table 3. Test matrix for velocity study .....	53
Table 4. Standard liters of air, ethylene, & hydrogen .....	60
Table 5. Flow rates for hydrogen and cavity air at set equivalence ratios .....	61
Table 6. Observed variability in equivalence ratio .....	106
Table 7. Statistical accuracy for straight configuration at equivalence ratio = 1.0.....	109
Table 8. Mean values from a repeated testing condition .....	116
Table 9. Mean values from the mass flow increase study, straight config. ....	153
Table 10. Mean values from the mass flow increase study, curved config. ....	154

## List of Symbols

Symbol	
$\bar{A}$	Effective flame area (m <sup>2</sup> )
CO	Carbon Monoxide
CO <sub>2</sub>	Carbon Dioxide
C <sub>2</sub> H <sub>4</sub>	Ethylene
C <sub>12</sub> H <sub>26</sub>	n-dodecane
C <sub>x</sub> H <sub>y</sub>	hydrocarbon
F <sub>b</sub>	Body force (N)
g	Acceleration divided by gravitational acceleration (-)
H <sub>2</sub>	Hydrogen
H <sub>2</sub> O	Water
Hz	Hertz
M	Molecular mass (kg/kmol)
$\dot{m}$	Mass flow rate (kg/s or kg/min)
(m,n)	pixel position (camera)
N	Number of valid samples
N <sub>2</sub>	Nitrogen
NO	Nitric Oxide
NO <sub>x</sub>	Oxides of Nitrogen
NO <sub>2</sub>	Nitrogen Dioxide
OH	Hydroxyl Radical
O <sub>2</sub>	Oxygen
r	Radius (m)
S <sub>L</sub>	Laminar flame speed (m/s)
S <sub>T</sub>	Turbulent flame speed (m/s)
TI <sub>u,v,rms</sub>	Streamwise, spanwise, or total turbulence intensity
U	Streamwise velocity (m/s)
V	Spanwise velocity (m/s)
$v'_{rms}$	Turbulent velocity fluctuation
V <sub>x</sub>	Streamwise velocity component (m/s)

$V_y$	Spanwise velocity component (m/s)
$\phi$	Equivalence Ratio
$\mu$	mean value
$\rho$	Density (kg/m <sup>3</sup> )
$\sigma$	standard deviation
x	number of carbon atoms
y	number of hydrogen atoms



## **List of Abbreviations**

### Abbreviation

AFIT	Air Force Institute of Technology
AFRL	Air Force Research Laboratory
CCD	Charge Couple Device
CFD	Computational Fluid Dynamics
CI	Confidence Interval
COAL	Combustion Optimization and Laser
CT	Constant Temperature
Da	Damköhler Number
DOD	Department of Defense
DOE	Department of Energy
f	focal length
f/#	f-stop (camera lens-aperture ratio)
HPT	High Pressure Turbine
IGV	Inlet guide vanes
ITB	Inter-stage turbine burner
$l_k$	Kolmogorov microscale
$l_0$	integral scale
LDV	Laser Doppler Velocimetry
LIF	Laser-Induced Fluorescence
LII	Laser-Induced Incandescence
LPT	Low Pressure Turbine
P.#	Position of experimental plane (in fourths of main channel width away from cavity vane)
RMS	Root-Mean Square
RVC	Radial Vane Cavity
SLPM	Standard Liter Per Minute
ST	Specific thrust
T	Temperature (K)
TSFC	Thrust specific fuel consumption

TVC	Trapped Vortex Combustion
UCC	Ultra Compact Combustor
UHC	Unburned Hydrocarbons
W	Power (Watts)
2-D	Two dimensional
3-D	Three dimensional

# **FLOW MEASUREMENTS USING PARTICLE IMAGE VELOCIMETRY IN THE ULTRA COMPACT COMBUSTOR**

## **I. Introduction**

### **I.1 Research and Design Perspective**

Since its birth just over 100 years ago, heavier-than-air flight has blossomed into an integral part of commerce as well as defense. Whether it is a letter in the mail, humanitarian aid, or the projection of military power, if something needs to get from point A to point B quickly, aircraft are used. Designing aircraft that fly farther, more efficiently, and have the capability of holding increased loads has created an entire division of engineering. A century after rudimentary piston engines powered aircraft made of stretched canvas and wood, gas-turbine engines with efficient combustors power supersonic aircraft made of alloys and composites.

Today's society and economy demand aircraft of increased efficiency and with better fuel economy without compromising the environment. While air pollution and global warming are widely debated, rapid transportation is considered vital to the American way of life and to the United States Air Force (USAF) operations. The thrust, and therefore the fuel, required to overcome aerodynamic drag is directly proportional to the square of velocity. Therefore, going faster to get something there more quickly is typically at odds with environmental conservation and fuel economy.

The U.S. consumed 20.68 million barrels of oil but produced only 5.06 million barrels per day in 2007 according to the Energy Information Administration.<sup>1</sup> 5.98 million of those imported barrels came from the Organization of Petroleum Exporting

Countries (OPEC), a historically unstable region of the globe. In 2007, 70% of U.S. oil was consumed for transportation.<sup>1</sup> Engineers continue to pursue more efficient methods of combustion in order to get the most from the oil used. Although efforts such as reducing aerodynamic drag can have the same beneficial end-effect, this thesis will focus on the system that converts the fuel's energy into thrust – the engine.

The section of a gas-turbine engine that includes the compressor, combustor, and turbine is often referred to as the core or the heart since these components are common among turbojets, turbofans, turboprops, and the other derivatives of the gas-turbine engine. The combustor has historically been the least well understood of these three components. Some in the gas-turbine engine industry consider the combustor design to be a black art.<sup>2</sup> Perhaps this is why combustors have benefited from fewer developments compared to compressors and turbines. However, considering the combustor is the component responsible for liberating the fuel's energy, its optimization is essential to an efficient engine. Furthermore, a poorly designed combustor will not only fail to extract as much energy from the fuel, it can also produce more pollution.

Due to the extensive development of the gas-turbine engine, significant advances in efficiency beyond current industry standards will require a considerable amount of engineering-labor. One promising area for design improvement is the combustor. In a gas turbine engine, the combustor extracts as much energy from the fuel as possible while minimizing total pressure loss. The combustor accomplishes this under extreme temperatures and in as little space as possible. The Air Force Institute of Technology (AFIT) and the Propulsion Directorate of the Air Force Research Labs (AFRL), both at Wright Patterson Air Force Base (WPAFB), are currently testing designs for the Ultra

Compact Combustor (UCC). This combustor is designed to burn fuel more efficiently and requires less space than combustors currently used in gas-turbine engines.

## **I.2 The Ultra-Compact Combustor Concept**

The Ultra Compact Combustor (UCC) is an evolving concept for a new type of combustor requiring significantly less axial length within the engine, while maintaining high combustion efficiency, low pressure loss, and low pollution emissions. The two concepts that make the UCC operate in such a revolutionary way are (1) the remixing of bifurcated flow at an angle to introduce circumferential swirl, and (2) the use of trapped vortex combustion (TVC). The idea for a shorter combustor came from research done at the University of California, Irvine.<sup>3</sup> The research concluded that significant increases in specific thrust are attainable using inter-stage turbine burners. If combustors can be made small enough to fit between the stages of the turbine, more energy can be added to approximate a constant temperature process. Although the benefits of a constant temperature process are evident, designing such a small combustor does not seem practical with conventional designs. A more compact combustor could prove beneficial in improving the overall efficiency by reducing the weight of the engine.

Whether used as an inter-stage turbine burner or a conventional burner with shorter axial length, minimizing the length is important for engine weight savings. The spool(s) connecting the compressor and the turbine must run the length of the combustor. This section of the spool(s) is subjected to the highest loads in tension and torque and must, therefore, be structurally reinforced which increases weight. Consequently,

minimizing the combustor length aids in overall weight reduction. However, the flame length for the range of the combustor's operating conditions competes with the push to minimize combustor length. Conventional combustors in use today typically use swirl-stabilized domes to produce an area of high turbulence and flow shear to promote fuel-air mixing.<sup>4</sup> Increased mixing allows the fuel to burn faster and therefore requires less combustor length to contain the flame. The UCC aims to decrease the required length of the combustor section by introducing circumferential flow. Consider this analogy of a length of string to the flow path inside the UCC. When straight, the string is long, but when wound, it takes up less distance in the original direction, just as the UCC will take up less length in the engine.

In a modern combustor, the airflow is divided so that a portion of the air enters the primary combustion zone and is swirled to maintain a region of steady combustion. The remaining air is then mixed in downstream to complete the combustion of any remaining fuel. The UCC also separates a portion of the air flow; rather than remixing in the axial direction, the flow is channeled along the outer annulus of the engine with respect to the engine's centerline. After the fuel is injected and burned in this outer annulus, the circumferential flow channel is remixed in with the main air channel in the axial flow path. The circumferential flow is injected into the main flow at a 45 degree angle, resulting in high centripetal acceleration. Lakusta found this angled injection results in tangential velocities of 3-14 meters per second; this velocity equates to between 300 and 4000 g's on the airflow in the small scale test rig.<sup>5</sup>

In the UCC, the circumferential airflow channel contains cavities where the fuel is injected. These cavities create quasi-stable vortices that stabilize the flame. This

stabilization is known as trapped vortex combustion (TVC), and is the second revolutionary concept within the UCC. The fuel injected into cavities around the perimeter of the annulus burns rich. The flow loaded under centripetal acceleration creates vortices inside the cavities that increase mixing with the fuel which in turn speeds up the combustion process. The swirling flow inside each of these cavities along with the vortices created by the radial vane cavities (RVC) create strong radial density gradients between the heavier un-reacted fuel and the lighter combusted fuel and air.<sup>6</sup> This density gradient promotes mass-transfer of the reacted fuel and air while keeping the un-reacted fuel in the cavity. This mass-transfer prevents unburned fuel from escaping into the main flow channel.

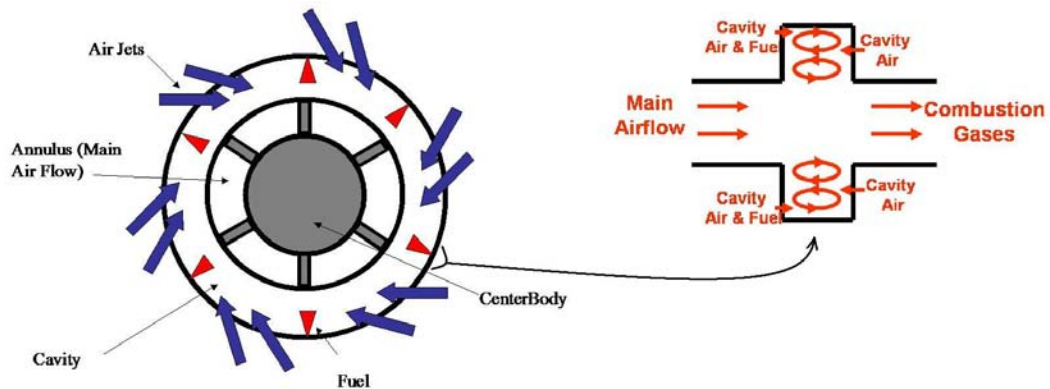


Figure 1. Transport of combustion gases in the TVC concept (adapted from Greenwood, et al.)<sup>7</sup>

The most obvious benefit of the UCC is shorter combustor length. This benefit will allow the length of the spool under the greatest torque to be shortened. In turn, the entire engine will be shortened and lightened. Lakusta found using the UCC as the main

combustor could shorten this section by 66% while maintaining 99% combustion efficiency. He concluded this decrease in weight could increase an engine's thrust-to-weight ratio by up to 25%.<sup>5</sup>

Another advantage the UCC holds over typical combustors is its small size could enable its use as an inter-stage turbine burner (ITB) between the high pressure and low pressure turbine to boost specific thrust. Heat addition in today's gas-turbine engines occurs in the main burner and afterburner. One fundamental way to increase an engine's specific thrust is to raise the turbine inlet temperature.<sup>8</sup> However, the main combustors in modern gas-turbine engines are already temperature-limited by the amount of cooling available for the high pressure turbine. Thrust augmentation already exists in many gas-turbine engines used in fighter aircraft in the form of an afterburner. A simplified explanation of an afterburner is fuel is injected into the flow downstream of the turbine and ignited; the heat addition effectively increases the flow velocity resulting in increased thrust. The afterburning cycle is much less efficient than the Brayton cycle used by the non-afterburning gas-turbine engine. Modern afterburners consume more than twice as much fuel for every unit of thrust they produce.<sup>9</sup> The measure of how much fuel an engine uses to produce one unit of thrust is known as thrust-specific fuel consumption (TSFC). Sirignano found a constant temperature process can raise specific thrust with little or no penalty in TSFC.<sup>3</sup> Due to material constraints, it is impractical for combustion to take place in the turbine. However, if a UCC could be used as an ITB, it could attain some of the advantages of a pure constant-temperature cycle. With these benefits, the UCC design is capable of low pressure drop and increased burner efficiency.



### I.3 Research Objectives

The overarching goal of the research underway at AFIT is to obtain physical understanding of combustion reaction with body force effects so the Ultra Compact Combustor is developed as a practical combustor. Three specific research objectives are identified in order to achieve this goal, two of which will be the focus of this thesis.

The first objective is to investigate the effect of body forces independent of the velocity effect. This thesis will address this research objective by measuring the effect of increasing velocity while holding the other factors constant. A fluid with a density gradient will experience a body force proportional to that gradient as well as to the overall centripetal loading. Centripetal loading is proportional to the square of circumferential velocity and inversely proportional to the radius of curvature.

$$F_b \propto \frac{V^2}{r} \quad (1)$$

These two factors, and the effect they have on the performance of the UCC, must be characterized independently. Real world combustors are not all the same size (different radius of curvature) and are throttled back and forth (changing velocity). Characterizing the body forces' effects on performance will allow the results of small-scale laboratory experiments to be scaled up to the size of full-scale engines. The body force effect on combustion will be examined by comparing results from circumferential flow channels of different curvatures. This thesis will concentrate on comparing results from the straight cavity vane section with those from the one-sixth scale curved cavity vane section. Data from the UCC in the curved cavity vane configuration is expected to show increased mixing in the main vane compared to data from the straight

configuration. Further velocity increase in the curved configuration will result in a corresponding squared increase in centripetal loading. The effect of this velocity increase will be studied.

The second objective is to investigate whether trapped vortex combustion can be sustained effectively in the UCC. Previous research performed at AFIT by Hankins and Lakusta<sup>5</sup> demonstrated a stable double-vortex is sustained at the exit of the primary combustion chamber when using the straight cavity vane. However, minimal mixing of the combustion products into the straight section was observed. The curved cavity vane section has yet to be tested, but is expected to show increased mixing of the two flows. This mixing between the two flows is critical to the UCC concept. This thesis will determine flow velocities over different two-dimensional planes inside the UCC where the cavity vane and main vane flow paths cross to determine how the flow interaction changes inside the full depth of the main channel. These velocity maps will elucidate the flow patterns inside the combustion chamber.

This thesis will use particle image velocimetry (PIV) to measure two-dimensional velocities over the radial vane cavity inside the UCC. These measurements will generate two dimensional velocity maps and turbulence statistics useful in understanding the flow patterns inside the UCC. Experimentation for this thesis will be conducted in the Combustion Optimization and Analysis Laser (COAL) lab at AFIT. This thesis will result in the characterization of flow patterns inside the small-scale UCC at different operating conditions when configured with the straight cavity vane section and then with the curved cavity vane section.

The third objective of the AFIT research is to investigate the interaction between the main cavity, the vane cavity, and the main flow. An optimization study focusing on the performance tradeoff between pressure loss, and mass transport from the cavity to the main flow channel will be performed in this thesis on two different radial vane cavity (RVC) geometries – one straight and one curved. Optimization of the radial vane cavity will not be addressed in this thesis as it would require different geometries. This third objective is primarily supported with computational fluid dynamics (CFD).

#### **I.4 Methods**

A small-scale model of the Ultra Compact Combustor was built by Anderson in order to test and characterize the flow interaction between the cavity and main vanes in the current design. The sector test model rig at AFIT has several optical access panels made from quartz. This enables viewing and access for laser diagnostic techniques. The AFIT rig models one-sixth of the circumferential flow path. Since the UCC is axisymmetric with six radial vane cavities, the flow dynamics will be similar in this small-scale rig. The full concept is shown on left with the AFIT test rig on right in the figure below.

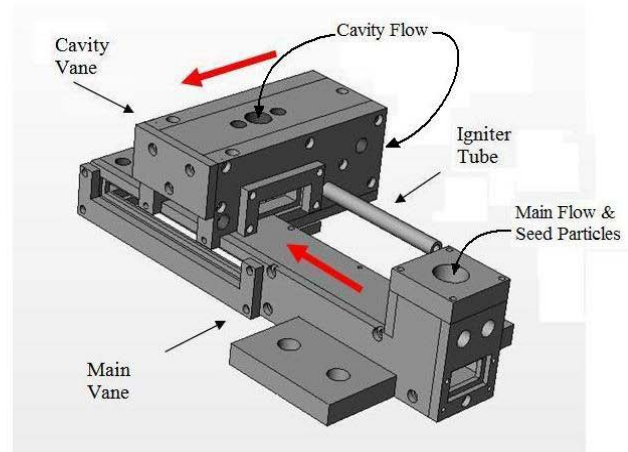
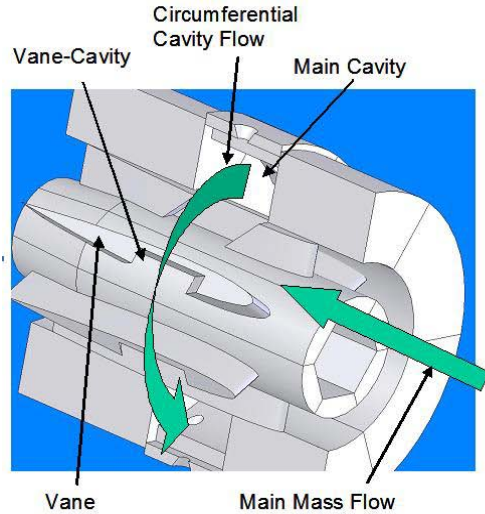


Figure 2. Comparison of full model UCC concept: on left; to AFIT sector model, straight cavity configuration: on right (adapted from Anisko, et al.)<sup>10</sup>

In the figure above, both models are in roughly the same orientation. The main flow path in both is from bottom right to top left with the circumferential cavity flow moving perpendicular originating from the top right and coming out of the page.

The radial vane cavities are positioned directly under (radially) each of the six cavities. The RVCs are vanes designed to create vorticity to stimulate mixing of the main flow with the combustion products coming from the cavity flow. While the complete UCC design has six vanes along the main annulus, the AFIT test rig has one RVC and one main flow channel. A model of the main flow channel from the small-scale UCC is shown below in Fig. 3.

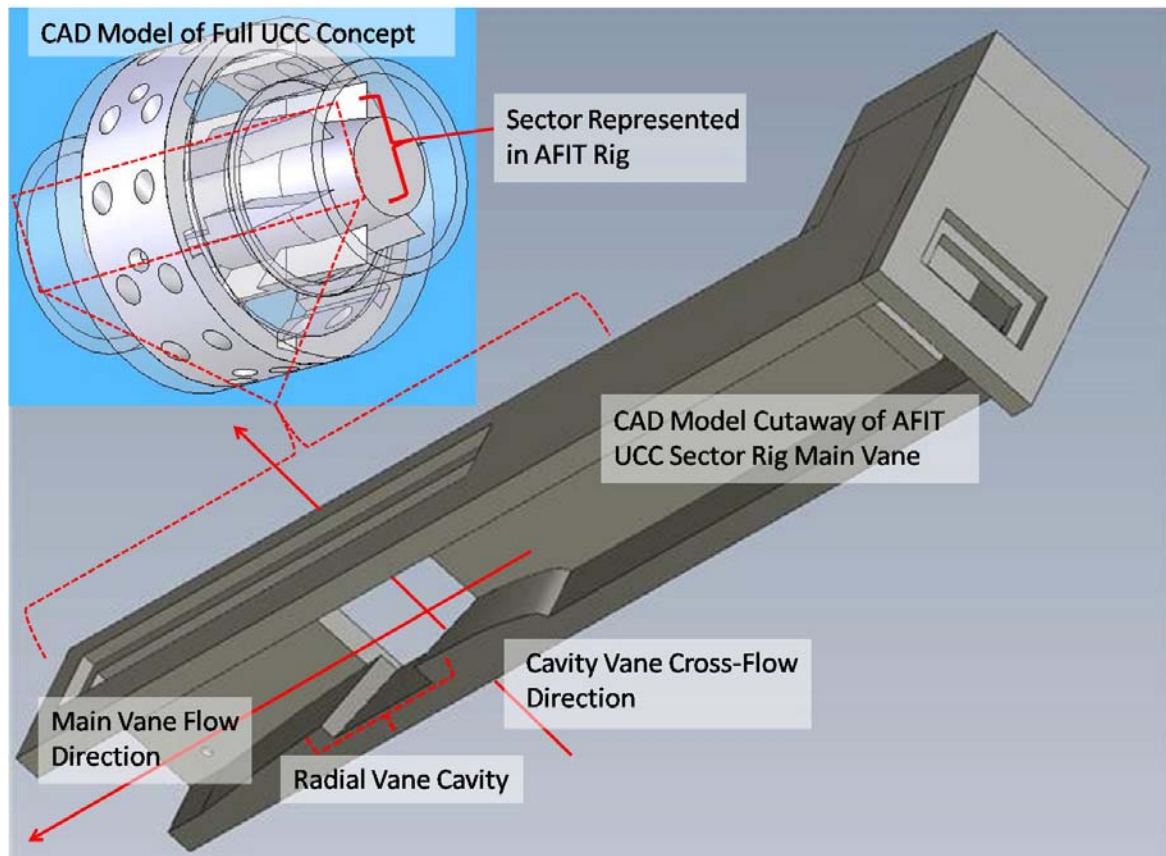


Figure 3. Main vane cutaway showing radial vane cavity

The AFIT UCC rig has two different circumferential cavity vane assemblies bolting onto the main vane directly over the RVC. These two cavity vane sections carry the circumferential airflow. The curved cavity vane represents the one-sixth scale curvature and the straight cavity vane represents a curvature of infinite radius. Cutaways of these cavity vanes are shown below in roughly the same orientation. In these vanes, the fuel is injected into the trapped vortex combustor cavities where the primary combustion occurs. Cutaway

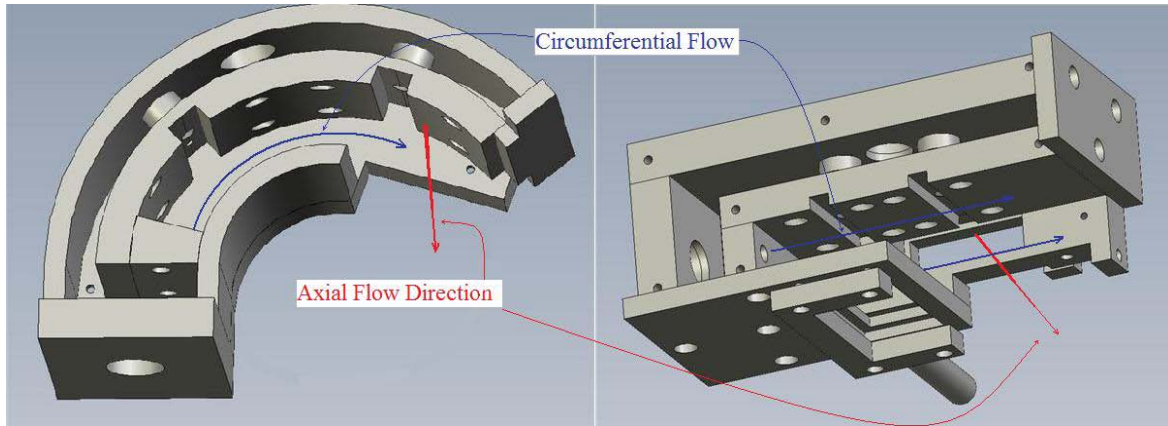


Figure 4. Cavity vane cutaways showing main combustion chambers

In both the straight and curved cavity vanes, the circumferential path goes past the main combustion cavity, where TVC occurs, then moves into the main flow section over the RVC. In both curved and straight cavity vane assemblies, there are two combustion cavities for the TVC. Pairs of air jets are angled 45 degrees into the cavity flow path in between each of the combustion cavities and along the circumference. This design draws exhaust in from the cavity creating an intermediate combustion zone, which provides chemical residence time for any unburned fuel.

Optical viewing windows were built into each of the three main sections of the small-scale UCC: the main flow assembly and the two circumferential assemblies. These windows are critical to laser-diagnostic measurements as direct line-of-sight is required for these techniques. Further, particle image velocimetry (PIV) requires the camera to have nearly 90 degrees of angular separation from the illuminating laser. The windows are made from quartz to withstand high temperatures inherent in combustion environments.

Particle image velocimetry (PIV) is a technique measuring the velocity of particles in a flow of interest. Seed particles are introduced into the flow upstream of the area of interest and quickly approach the velocity of the flow in which they are entrained. A laser, formed into a sheet, is pulsed into the flow at the area of interest at a set rate. A high-speed digital camera is coupled to the laser and records the reflections of laser pulses off the particles. Using computational techniques, the reflections over pairs of laser pulses are correlated to determine the average difference in position over a known time for small regions of particles. Two dimensional velocities of the seed particles are thus determined and assumed to be approximately the same as the flow velocity. The seeds will be mixed into the flow and then enter the small-scale UCC through the main flow port.

Lakusta<sup>6</sup> identified an optimal case of airflows such that the main flow was roughly 20 times the cavity flow and at an overall equivalence ratio of 0.048. Hankins' testing identified the optimal airflow ratio as having the main flow only between 10 and 15 times higher than the cavity vane flow. The test matrix will build around these cases.

## II. Theory and Background

### II.1 The Gas-Turbine Engine

The two main sources of aircraft propulsion today are the piston engine and the gas-turbine engine. Piston engines are generally used when low cost is the design goal, whereas gas-turbine engines are used when a higher thrust-to-weight ratio is needed. Gas-turbine engines are currently used in all aircraft in the USAF inventory except for the MQ-1 Predator UAV. One of the primary reasons gas-turbine engines are more powerful than piston engines are that they have higher compression ratios and higher flow rates. Common compression ratios today are around 10:1 for gasoline piston engines, 20:1 for diesel piston engines, and upwards of 30:1 for gas-turbine engines. Overall, more technologically advanced engines use higher compression ratios to gain efficiency and power.

The benefits of higher compression come with tradeoffs. Some of the engineering challenges include the requirement for closer machining tolerances, lower blade tip clearances, and higher material strength. Higher compression also creates thermal management issues. Even with isentropic compression, a 30:1 pressure increase will cause approximately a 37% higher increase in air temperature compared to a 10:1 compression ratio according to the isentropic relationship:

$$\frac{P_2}{P_1} = \left( \frac{T_2}{T_1} \right)^{\frac{\gamma}{\gamma-1}} \quad (2)$$



With increasing compression, a more advanced combustor is critical in advancing the overall efficiency of the gas-turbine engine. Advances in compressor and turbine design must be accompanied with advances in combustor design. Considering the combustor is responsible for releasing the energy driving the entire engine, it must be as efficient as possible while taking up a minimal amount of space. A new combustor design is required that is spatially compact, has high efficiency and performance, and produces low emissions is required.

## **II.2 Desired Combustor Properties**

Any major component in a system as complex as a gas-turbine engine will have several requirements. The combustor is no exception. It must introduce liquid fuel into a region of high pressure, high temperature, turbulent flow; atomize and ignite the fuel; complete the combustion reactions; and deliver the combustion products to the turbine in a steady manner. Mattingly<sup>2</sup> identifies the following eight desired properties for a combustor in a gas-turbine engine:

- 1) Complete combustion
- 2) Moderate total pressure loss
- 3) Stability of combustion
- 4) In-flight relight ability
- 5) Proper temperature distribution at exit with no “hot spots”
- 6) Short length & small cross section
- 7) Wide operating range of mass flow rates, pressures, and temperatures

## 8) Satisfaction of established environmental limits for air pollutants

As Mattingly<sup>2</sup> points out, each of these desirable characteristics conflicts with at least one of the others. The following paragraphs will further describe these eight desired properties. The UCC concept aims to make gains over conventional combustors in combustion efficiency, shortness in length, and lower emissions (properties 1, 6, & 8 listed above). Preliminary research suggests with the proper design optimization, the UCC could make gains in these areas without making sacrifices in the other categories.

Complete combustion (desired property #1) refers to the stoichiometry of the chemical change from fuel and air into combustion products. In an ideal combustor, all available fuel would combine with oxygen in the flow resulting in only carbon dioxide, water vapor and nitrogen, in addition to liberating heat. Although the combustion efficiency in modern combustors is above 95% percent,<sup>4</sup> there is always some incomplete combustion in which some of the fuel does not react with oxygen. The resulting unburned hydrocarbons are a major form of pollution. The production of this pollutant can be mitigated by the proper mixing of the air and fuel in addition to adequate combustor length. The turbulence and trapped vortex combustion in the UCC is designed to increase mixing and decrease unburned hydrocarbons.

Moderate total pressure loss (desired property #2) refers to the decrease in total pressure in the main burner resulting from friction and heat addition. Total pressure loss for modern combustors is around 5% whereas it can be as high as 10% in less advanced designs.<sup>4</sup> Some moderate pressure loss is needed to drive the bleed air cooling the turbine blades, but it also represents a loss in useable energy.

Stability of combustion (desired property #3) refers to the main burner's ability to continue combustion in off-design conditions. Combustion stability is of utmost importance; for instance, a flameout can turn a fighter aircraft into a glider. The UCC relies on a concept called Trapped Vortex Combustion (TVC) to maintain combustion stability. Ideally, a vortex will remain trapped in a small combustion cavity creating the primary combustion zone. The size and shape of this cavity as well as the cavity in the main vane will be optimized to allow for combustion stability during off-design operation. Stability of combustion must be maintained over a wide range of mass flow rates (desired property #7). Since the cavity geometry will be fixed, the UCC will need to be tested at a wide range of mass flow rates as increases in streamwise velocity have adverse effects on flame stability.<sup>11</sup> On the lower limit of the range of mass flow rates, the burner will have to be designed to relight in the event of a flameout (desired property #4). This situation pushes the engine outside operability limits is a stressing off-design condition.

A proper temperature distribution at the combustor exit with no hot spots (desired property #5) will avoid unnecessary thermal loading on the turbine blades. Turbine designers must go to great lengths to avoid failure due to the severe conditions in which turbine blades operate. In the high-performance, low-bypass turbofans used in modern fighters, the flow temperature exiting the burner often exceeds the melting point of the turbine blade materials requiring active cooling. Considering the thermal stresses are compounded with the substantial mechanical loading at full throttle, regions of considerably higher temperature, hot spots, can cause catastrophic failure. The mixing of the circumferential and main flow paths in the UCC design should distribute the hot

combustion products with the relatively cool unburned air. The use of a circumferential channel in the UCC design should allow for a fairly uniform temperature distribution over a relatively short axial distance.

A combustor of short length and small cross section, desired property #6, makes for a smaller, lighter engine. Because much of the combustion occurs in the circumferential and radial directions, the axial length of the UCC is significantly less than a conventional combustor. Shortening an engine decreases weight in general, but shortness of combustor length is of principal importance due to its location. The greatest torsion loads on the shafts (spools) exist between the last stage of the compressor and the first stage of the turbine – exactly where the burner must be situated. Making the combustor as short as possible will lead to a significant decrease in engine weight.

Desired property #8, satisfaction of established environmental limits for air pollutants, is a current concern. In addition to the desired thermal energy, carbon dioxide, and water vapor, combustion also produces unburned and partially burned hydrocarbons, nitrogen oxides (NO and NO<sub>2</sub>), carbon monoxide, sulfur oxides, (SO<sub>2</sub> and SO<sub>3</sub>), and several types of particulate matter. At the high temperatures and pressures existing in modern combustors, some of these pollutants such as nitrogen oxides are unavoidable. Fuel-lean combustion prevents some NO<sub>x</sub> formation, but this pollutant still remains a major concern.<sup>12</sup> In the UCC design, the primary combustion cavities are located around the circumference of the burner. The trapped vortex combined with the circumferential swirl will create a strong density gradient through centripetal loading. This density gradient, combined with the increased mixing, is beneficial to decreasing unburned hydrocarbons. These unburned hydrocarbons become trapped in the

combustion cavity, as they are naturally heavier than the combustion products. Not only are the pollutants toxic to the environment, but they also represent inefficiency. Usually a combustor that produces less pollutants also uses less fuel to produce the same amount of thrust. Designing more efficient engines producing fewer pollutants is a continuing engineering goal

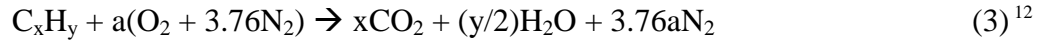
## **II.3 Combustion**

Turns<sup>13</sup> defines combustion as “rapid oxidation generating heat, or both light and heat.” This is a chemical change where bonds in molecules are broken and new molecules of different species are formed. The energy stored in the bonds of the product molecule species is less than the amount of energy stored in the reactants’ original bonds. The energy liberated in the exothermic reaction is the difference between these amounts of energy from reactants to products. This mechanism of energy release has powered human endeavors from the first caveman’s fire to modern jet fighter aircraft.

### *II.3.1 Stoichiometry & the Equivalence Ratio*

Aircraft with turbine engines do not need to carry onboard oxidizer as rockets do because they make use of the oxygen in the atmosphere. The earth’s atmosphere is composed of approximately 78% nitrogen, 21% oxygen, with the remaining 1% comprised mainly of Argon. One of the more common combustion types is hydrocarbon fuel with air. In this reaction, the hydrogen and carbon in the fuel recombine with the oxygen in the air to form primarily water and carbon dioxide. As an exothermic reaction, the energy stored in the product’s bonds is less than the energy stored in the reactant’s

bonds. The remaining energy is released primarily as heat. A chemical equation for the complete combustion of a simple hydrocarbon fuel with air is shown below.



where:  $a = x + y/4$

This assumes the air is 79% N<sub>2</sub> and 21% O<sub>2</sub> by volume, and that the fuel and air are in stoichiometric proportion. When the oxygen and fuel (reactants) are in proportion such that they completely react into products, the chemical equation is balanced and it is referred to as stoichiometric. When there is excess fuel, the condition is referred to as fuel rich, or just rich. Likewise, when there is not enough fuel, and therefore excess oxygen, the combustion is considered lean.

Equivalence ratio,  $\phi$ , is a quantitative measure of the reactants' stoichiometry. It is commonly defined as the ratio of the actual mass of fuel and air used in the process to the amount of fuel and air present for stoichiometric conditions:

$$\phi = (F/A) / (F/A)_{\text{stoic}} \quad - \text{or} - \quad \phi = (A/F)_{\text{stoic}} / (A/F) \quad (4)^{12}$$

Air-to-fuel ratio is a useful and descriptive parameter in combustor design. With knowledge of the fuel and oxidizer's molecular weight and a chosen equivalence ratio, the air-to-fuel ratio is determined. At stoichiometric conditions, the air-to-fuel ratio is the mass of the air divided by the mass of the fuel. Again assuming the oxidizer is air, this ratio can be written:

$$(A/F)_{\text{stoic}} = (m_{\text{air}}/m_{\text{fuel}})_{\text{stoic}} = 4.76aMW_{\text{air}}/MW_{\text{fuel}} \quad (5)^{12}$$

Therefore, if the desired air mass flow rate is known, a fuel-flow rate can be calculated allowing combustion at a desired overall equivalence ratio. The equivalence ratio is one of the primary independent factors in this thesis. Chapter III will include a discussion on the required air and fuel flow rates that equate to the desired equivalence ratios under investigation.

Many combustion applications operate outside stoichiometric conditions. For example, the combustion design point may be fuel lean to suppress unburned hydrocarbons and carbon monoxide. In contrast, operating rich will generally suppress oxides of nitrogen ( $\text{NO}_x$ ). Operating slightly rich generally produces the highest flame temperatures and therefore allows for the maximum heat release. However, the adiabatic flame temperature for hydrocarbons in air that has already been heated to above 1,000 °F from compression is typically higher than the melting point of the materials in gas-turbine engines. The temperature limit set by the turbine stator and blade materials and their cooling is what limit the overall equivalence ratio in the main combustor to the fuel-lean regime. The equivalence ratio must be low enough not to melt the engine, but high enough to propagate stable combustion. There are limits beyond which the flame front cannot propagate and combustion will cease in terms of equivalence ratio ( $\phi$ ). For example, the lower (lean) and upper (rich) limit for n-Decane ( $\text{C}_{10}\text{H}_{12}$ ), one of the primary constituents in jet fuel, are  $\phi=0.36$  and  $\phi=3.92$  respectively.<sup>12</sup> These limits are critical to a combustor design. If the equivalence ratio falls outside this range at any point, combustion is likely to cease causing flame extinction. This is particularly relevant to the UCC because the main combustion cavities are designed to burn rich with a

relatively small proportion of the overall air, then mix with the main flow for an overall lean equivalence.

### *II.3.2 Flame Speed & Turbulence*

Turns<sup>13</sup> defines a flame as a “self-sustaining propagation of a localized combustion zone at subsonic velocities.” As discussed in section II.2, combustion stability is a desired property for the combustor of a gas-turbine engine. The flame must remain at a relatively steady location in the combustor as the air and fuel flow in and the combustion products exit. This requires matching the velocity of the reactants to the local flame speed. If the reactants are flowing too quickly, the flame is likely to blowout. Knowledge of the flame speed is essential to determine the minimum combustor length. High flame speed is preferable as it allows for shortened combustor length. The quicker the chemical reaction takes place, the shorter the combustion chamber can be for a given internal flow velocity.

Calculating the flame speed can be done empirically by measuring the velocity of the combustion reactants. Analytically estimating flame speeds in conditions not already tested and documented is an arduous task. With knowledge of the temperature, pressure, and equivalence ratio, laminar flame speeds can be reliably estimated from empirically based formulas and data. Unlike laminar flames, the air-fuel mixture in a turbulent flame does not flow along smooth streamlines and significant momentum exchange occurs. Although the combustion in the UCC is turbulent by design, the laminar flame speed of a given fuel and oxidizer combination at standard conditions is an essential reference point.



Similar trends can be seen between laminar and turbulent flame speeds in different conditions. For example, increasing the inlet gas temperature will increase both turbulent flame speed as well as laminar flame speed. For a given temperature and pressure, flame speed is dependent on the local equivalence ratio and typically peaks at the same slightly rich equivalence ratio yielding the maximum flame temperature. Temperature, pressure, and flame type are the main factors affecting flame speed for a given fuel composition. Increasing temperature increases laminar flame speed, whereas increasing pressure decreases flame speed, although with a much weaker affect.

Turbulence can significantly increase flame speed through mixing the air and fuel while it is reacting.<sup>13</sup> Turns states, “Turbulent flow results when instabilities in a flow are not sufficiently damped by viscous action and the fluid velocity at each point in the flow exhibits random fluctuations.” In reference to combustion, turbulence creates eddies of different scales acting to mix the reacting fluid. For both laminar diffusion and laminar premixed flames, there exists a well-defined flame front that physically separates the reactants from the products. Laminar flame speeds are based on the thermal and chemical properties of the mixture. Turbulent flame speeds depend upon these flow characteristics as well as the mixture properties.<sup>12</sup> Because of the difficulty in directly measuring unburned gas velocities near a turbulent flame, flame velocities are empirically measured based on reactant flow rates:

$$S_t = \frac{\dot{m}}{\bar{A}\rho_u}. \quad (6)^{12}$$

In this equation,  $\dot{m}$  is the reactant flow rate,  $\rho_u$  is the unburned gas density and  $\bar{A}$  is the effective flame area. Thus for a given unburned gas density and fuel, the reactant flow-rate can be increased by increasing the area of the flame-front.

The ratio of the characteristic flow time to the characteristic chemical time is a non-dimensional parameter allowing for the characterization of combustion regime; referred to as the Damköhler number, Da. For example, when the Da is much greater than unity, a fast chemistry regime is defined. Damköhler developed a model to estimate the turbulent flame velocity based on the laminar flame velocity and the turbulence intensity.

$$S_t/S_L = 1 + v'_{rms}/S_L \quad (7)^{12}$$

With knowledge of the laminar flame speed, turbulent flame speed then becomes a function of the velocity fluctuation,  $v'_{rms}$ , which will be measured in this thesis. This theory is based on the concept of wrinkled laminar flamelets, where the turbulent flame behaves similarly to a laminar flame. The difference is instead of the flame-front defined by a steady plane, the flame front is wrinkled. The flame speed increases proportionally with the wrinkles caused by turbulence. Since a wrinkled surface has a greater surface area compared to a smooth surface, the flame front is increased, allowing for more combustion. When the turbulence has caused enough mixing, there is no longer a defined flame front and combustion takes place throughout the mixture. Laminar flame is measured by the propagation of the flame-front which is limited by the chemical kinetics in and around the flame zone. With the introduction of turbulence, the effective flame speed increases as a function of turbulent transport. This turbulent transport increases

turbulent flame speed and decreases the required flow residence time required for burning. Therefore, more turbulence will allow for a shorter combustor.

## **II.4 Literature Review of Select UCC Research**

Research into the Ultra-Compact Combustor has been ongoing for roughly ten years. Much progress has been made in understanding the mechanics of circumferentially enhanced combustion. Efficient use of resources is made by understanding what previous research in the area has accomplished. The following sections include a brief discussion of research performed in development of the UCC at AFRL and AFIT.

### *II.4.1 Propulsion Directorate/AFRL Research*

In an effort to develop UCC technology for use in gas-turbine engines, the Air Force Office of Scientific Research (AFOSR) has been providing much of the funding for the research performed at the Propulsion Directorate of the Air Force Research Labs (AFRL) since 2001. Tests have been conducted at high pressures simulating engine conditions in addition to atmospheric pressure tests. In 2002 Quaale<sup>13</sup> performed Laser Doppler Velocimetry (LDV) on the small-scale atmospheric UCC test rig at AFRL in both the radial and circumferential directions. Among all research performed at AFRL and at AFIT for the development of the UCC concept, Quaale's work is the most similar to the experiments performed in this thesis. LDV is a velocity measurement in which a particle in the flow is illuminated by only the regions of constructive interference in the fringe pattern created by two coherent and collimated lasers. As the spacing of the light

and dark regions in the fringe pattern is known, the frequency of the reflected light signal is directly proportional to the seed particle's velocity. In this way, velocity is measured over the region of the flow illuminated by the fringe pattern caused by interference of the two lasers.

The radial and circumferential components of velocity were measured with the LDV technique over the same area for a discrete amount of time in the AFRL UCC test rig. Vector statistics were then calculated for each set of data yielding component mean values and standard deviations. Quaale<sup>14</sup> used these parameters to then calculate component turbulence intensities. A similar process, to be discussed in Chapter III, was performed in this thesis. Anthenien and Zelina<sup>14</sup> continued on this work analysis of Quaale's LDV data in 2005. They were able to characterize the turbulent combustion regime by using the two components of fluctuating velocity as the turbulent kinetic energy, the integration of the auto-correlation function to find the turbulent integral length, a temperature correction to find the laminar flame speed of JP-8 fuel, and an assumption that the scaled thermal diffusivity of air is equal to that of the fuel to find the reaction thickness. The Damköhler number was found to be between one and ten for the bulk of the data, and the Kolmogorov scale was found to be less than the reaction thickness. These findings led them to the conclusion the UCC was operating in the distributed reaction (Perturbed flamelets) regime.<sup>14</sup>

#### *II.4.2 AFIT COAL Lab & CFD Research*

Research on a sectional model of the UCC concept for testing up at AFIT started with computational studies. It has become standard practice in industry and academia

alike to perform the initial analysis of any completely new design using computational techniques. Specifically, Computational Fluid Dynamics (CFD) is a broad term used to describe the computer-based analysis performed to make predictions of fluid flow. Broken down into its most basic steps, CFD consists of building a model to define the geometrically of the physical object under investigation with Computer Aided Design (CAD), defining a grid of locations where flow parameters will be calculated, creating or modifying a numerical algorithm that actually calculates the flow parameters, setting the boundary and initial conditions, and finally validating and interpreting the results. In 2005 Anisko<sup>15</sup> and Greenwood<sup>6</sup> used CFD to perform design optimization studies for a sectional model. Greenwood concentrated on validating the CFD model with experimental results from the UCC test rigs at AFRL/ Propulsion Directorate. Anisko focused on different geometries for the sectional test rig to be built for testing at AFIT. His research helped optimize several variables, such as the cavity length and the angle of air injection. Moenter<sup>17</sup> continued on the work of Anisko and Greenwood in 2006 improving the CFD model to enhance turbulent flow characterization. He used this CFD model to help finalize the basic design of a sectional model to be later built. At the time of this writing, Moenter was the last to perform CFD analysis on the AFIT sectional UCC rig.

A parallel effort began in 2005 by Dittman<sup>18</sup> to set up a state-of-the-art laboratory facility capable of combustion experiments with optical diagnostics. Anderson continued on his work in 2006 completing initial design of the small-scale combustion facility known as the Combustion Optimization and Analysis Laser (COAL) Laboratory. Anderson<sup>19</sup> took the geometry of the sectional UCC model from Greenwood's thesis and

modified it so it could be fabricated with appropriate access for instrumentation. Koether<sup>16</sup> was the first to test the newly constructed UCC sectional model in 2007. He took temperature and pressure measurements at different airflow conditions and laid the basic groundwork for future Laser-Induced Fluorescence (LIF) with tests on the Hencken burner. Hankins<sup>21</sup> continued Koether's work with LIF using the Hencken burner. He then used the technique to measure hydroxyl (OH) concentrations in the UCC. He used these species concentrations to compare to Moenter's CFD results<sup>17</sup> and found agreement. Lakusta<sup>5</sup> performed further hydroxyl species concentrations in the sectional UCC rig using Planar Laser-Induced Fluorescence (PLIF) in 2008. He also characterized the operation of the ethylene ( $C_2H_4$ ) igniter allowing the UCC to be consistently lit from a remote location. At the time of this writing, the latest PLIF measurements taken to date were performed by Drenth who performed simultaneous two-color PLIF and characterized the UCC operation with synthetic fuel. His experiments were ongoing in 2009 coincident with those described in this thesis.

## **II.5 Anatomy of the Ultra Compact Combustor (UCC)**

As mentioned in the introduction, combustors for gas turbine engines have evolved from the can-type, to the cannular-type, to the annular-type. Since the annular-type is the most advanced of the three, it will be used for comparison with the Ultra-Compact Combustor (UCC). Fig. 5 below shows a diagram of an annular-type burner next to one of a UCC. Both combustors take in air at the aft end of the high-pressure compressor, then mix and burn the fuel, and lastly feed thermally energized airflow to the

front end of the high-pressure turbine. The front portion of a conventional annular burner is a smooth-wall or dump-type diffuser that slows the flow. The two reasons for this are (1) to prepare some of the airflow to enter the primary combustion zone and, (2) to mitigate total pressure loss, which is dependent on velocity. Instead of a traditional diffuser, the UCC has a bifurcated duct splitting a portion of the flow off into the circumferential channel. Along this channel, formed around the circumference of the burner, is the primary combustion cavity trapping a vortex and sustaining the TVC.

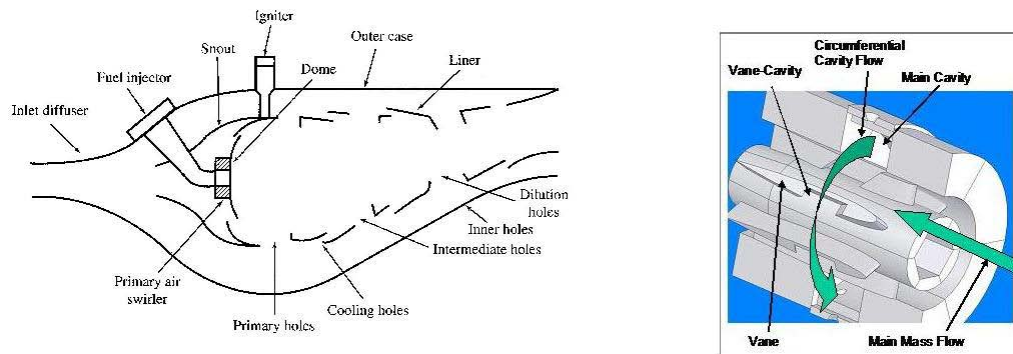


Figure 5. Left: Cross-section of annular burner (adapted from Mattingly)<sup>4</sup>; right: UCC concept cutaway (adapted from Greenwood)<sup>6</sup>

In the annular combustor, a liner with holes allows air into the combustion zone. The successive sets of holes let more air in as the flow approaches the front of the turbine section. Aside from the swirling stabilizing the flame, the flow moves primarily in the axial direction. Unlike conventional combustors, the combustion and dilution process in the UCC takes place in the radial, circumferential, and axial direction and therefore needs less overall axial length. In the UCC, combustion products move radially inward from

the vortex inside the combustion cavity and mix into the main flow around the RVC. At this point, the flow enters the turbine as it would exit from an annular combustor.

## II.6 Particle Image Velocimetry

As outlined in Chapter I, particle image velocimetry (PIV) is a non-intrusive technique measuring the velocity of particles entrained in a flow of interest. The following diagram, from Dantec's website provides a pictographic representation of the process:

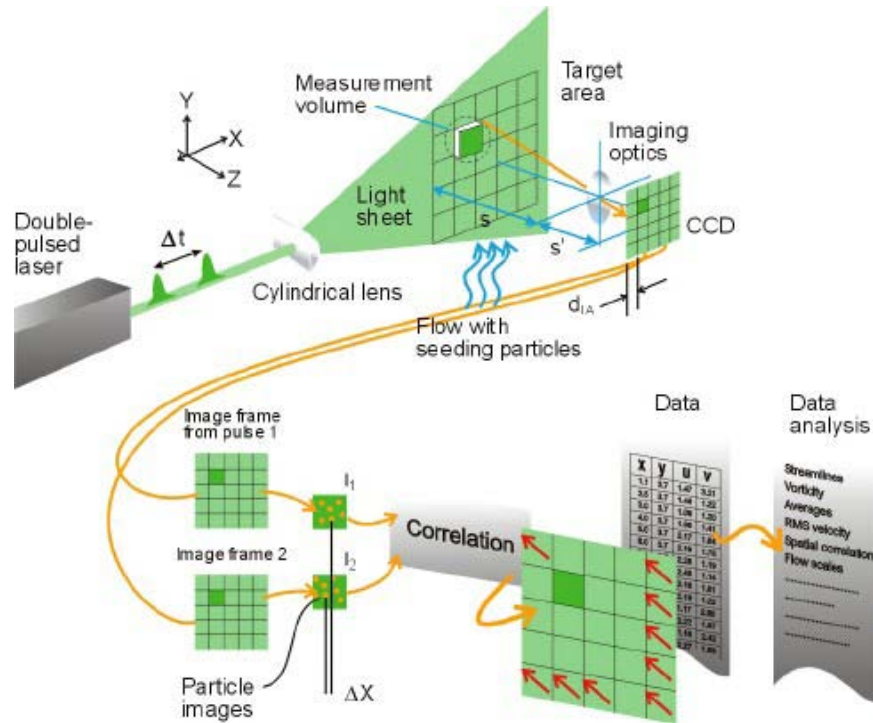


Figure 6. Pictorial of the PIV process (used with permission)<sup>22</sup>

Upstream of the area of interest, micron-sized particles are injected and become entrained in the flow. The flow is then illuminated with a sheet of monochromatic light from a



pulsed laser. The light reflects off the particles and is recorded by a digital camera timed coincident with the laser pulses. Software is then used to correlate reflections from different frames estimating particle-paths. The differential of each particle's displacement is then taken in order to estimate velocity based on the time between laser pulses. This process is performed across the illuminated area of the flow creating a 2-D map of particle velocity. The resulting velocity measurements are not direct measurements of flow velocity, but of the velocity of the particles entrained in the flow. PIV is particularly useful in measuring non-steady and turbulent flows since it is a direct and instantaneous whole-field measurement technique.

Particle image velocimetry can provide non-intrusive, whole-field, 2-D velocity measurements. However, like any technique, it has limitations. In planning an experiment with PIV, these capabilities and limits of PIV must be taken into account. The following paragraphs will discuss some of the more substantial PIV capabilities and limits:

- Seed Particles/ Tracer Particles
- Laser Type
- Camera Type
- Correlation Technique
- Measureable Velocity

#### *II.6.1 Seed / Tracer Particles*

The choice of seed particle is important, as the measured velocity is not a direct measurement of the flow velocity, but of the particles entrained in that flow. Therefore,

the accuracy of the measurements is directly limited by how closely the entrained particles follow the flow. The ideal seed particles are inert, neutrally buoyant, and small enough to accurately follow the flow of interest. Smaller particles are preferred for PIV applications because their relatively low inertia allows them to more accurately follow the flow. Consider two particles of the same substance and shape but of different size entrained in the same flow. The smaller particle will experience higher viscous and pressure forces, with respect to its own inertia, compared to a larger particle. The primary reason is as overall size decreases, the ratio of surface area to internal volume, and therefore mass, will increase. A simple example can be illustrated by taking the ratio of surface area to volume for a sphere:

$$\frac{\text{Surface Area}}{\text{Volume}} = \frac{4\pi r^2}{\frac{4}{3}\pi r^3} \Rightarrow \frac{3}{r} \approx \frac{\text{Surface Area}}{\text{Mass}} \quad (8)$$

Assuming constant density, volume can be replaced by mass in the denominator. This example illustrates how the ratio becomes a comparison of the area over which sheer forces act for a given amount of inertia. This explains why smaller particles will follow a turbulent or quickly changing flow more closely than larger particles. Although larger particles have the ability to scatter more light, smaller particles are still preferred for their ability to more closely follow turbulent flow.

In addition, it is beneficial to match the density of the PIV seed particles to that of the flow in which they are to be entrained. When the particle density is not matched to the flow, the particle will experience a body force due to gravity, as well as different loading in a turbulent or turning flow. The density of conventional PIV tracer particles is greater than the density of air, and much greater than the density of combustion products. This

difference in density between the tracer particles and the flow in which they are entrained results in an error proportional to the density differential and the amount of flow turning. Three tracer particle types generally used in combustion PIV are aluminum oxide ( $\text{Al}_2\text{O}_3$ ), Titanium Dioxide ( $\text{TiO}_2$ ), and Silicon Carbide ( $\text{SiC}$ ). The following table lists several common particle types used for PIV.

Table 1. Seed particle specifications (used with permission)<sup>23</sup>

Seed Particle Specifications						
TSI Model	Particle Type	Nominal Mean Dia. ( $\mu\text{m}$ )	Size Range ( $\mu\text{m}$ )	Density (g/cc)	Refractive Index (real + imag.)	Quantity
900805	Dye-impregnated PSL	1.0	Std. dev. <0.05	1.05	-	10 ml*
10081	Silicon carbide	1.5	Std. dev. = 1.4	3.2	2.65	100 cc
10084	Nylon	4	Std. dev. = 1.5	1.14	1.53	400 cc
10085A	PSL	0.54	Std. dev. = 1.05	1.05	1.55 to 1.6	15 ml**
10086A	Titanium dioxide	3 to 5	-	4.2	2.6	0.45kg (1 lb)
10087	Metallic coated	9	4 to 12	2.6	0.21 + 2.62i	30 cc
10089	Hollow-glass spheres	8 to 12	10%<3 to 5 90%<14 to 17	1.05 to 1.15	1.5	1000 cc
10089-SLVR	Metallic-coated hollow-glass spheres	14	10%<7 90%<21	1.65	0.21 + 2.62i	100 cc
* Aqueous suspension, 1% solids by weight    ** Aqueous suspension, 10% solids by weight Particles highlighted in blue are spherical, particles in gold are irregularly shaped.						

Particle types initially under consideration for this experiment were hollow glass spheres, titanium dioxide, and silicon carbide. Considering the expected centripetal loading inside the UCC, hollow glass spheres with their low specific gravity appear to be a good choice. However, with a melting temperature of less than 1,000K the hollow glass spheres could easily melt inside the combustion chamber and fuse to the walls and the quartz viewing windows. For this reason, the hollow glass spheres received no further consideration. Of the seed particles cleared for combustion environments, silicon carbide ( $\text{SiC}$ ) seemed to be the best choice. Silicon carbide particles were chosen

because they have a small nominal diameter, a lower density, and present none of the environmental hazards that must be considered with the titanium dioxide particles.

Silicon carbide (SiC) is used as an industrial abrasive due to its low reactivity, hardness, and its ability to withstand high temperatures. It is a crystalline solid with a rating of 9.25 on Mohs' scale of relative hardness, a refractive index of 2.65, and is stable above 2,400K.<sup>24</sup>

### *II.6.2 Laser Type*

In PIV, the requirements for the illumination source are the pulses must be able to provide sufficient energy, be close together in time, and short enough in duration that the particle reflections are discrete and not blurred together.<sup>25</sup> Although these requirements do not exclude other light sources, lasers are almost exclusively used for digital particle image velocimetry. Of these, Nd:YAG is the most commonly used laser because of its high output, short pulse duration, and emission which can be frequency doubled to within the visible spectrum: 532 nm wavelength.<sup>25</sup>

The neodymium-doped yttrium aluminum garnet (Nd:YAG) is a triply ionized crystal used as the lasing medium in this particular type of solid-state laser. The chemical structure of this crystal is  $\text{Nd}^{3+}:\text{Y}_3\text{Al}_5\text{O}_{12}$  and its most common emission wavelength is 1064 nm – in the infrared region of the electromagnetic spectrum.<sup>27</sup> The radiation is then passed through a potassium dihydrogen phosphate (KDP) crystal doubling the frequency to 532nm. This phenomenon, known as second harmonic generation, is a non-linear process effectively combining two photons of the same frequency into one photon of twice the frequency (half the wavelength). This frequency doubling is useful for three

reasons: (1) 532nm electro-magnetic radiation is visible as green light making laser alignment relatively simple, (2) digital CCD cameras are available with high quantum efficiency at 532 nm, and (3) the scattering cross section of particles is proportional to  $\lambda^4$ , so shorter wavelength will increase scattering efficiency.<sup>25</sup>

Electromagnetic energy is emitted from most lasers in the form of a low-divergence beam in wavelengths ranging from infrared down to ultraviolet. Laser energy is coherent and is generally monochromatic; that is, it is comprised of a single wavelength or a narrow band of wavelengths. In the case of the Nd:YAG laser used in the COAL Lab, the laser energy is passed through a dichroic mirror allowing the 532nm light to transmit while reflecting any 1064 nm light remaining from the frequency doubling crystal. It then exits the laser housing and is passed through sheet-forming optics. These usually consist of mirrors to orient the beam, a half-cylindrical lens to make the beam diverge at a constant angle, and a spherical lens to focus the beam so that the sheet is thin when it illuminates the test area. There is a tradeoff with sheet thickness. A thin sheet provides the maximum power density and only illuminates particles in both frames that have relatively two-dimensional velocity. This characteristic is beneficial because higher power density increases the signal to noise ratio. Also, less out of plane motion will be recorded minimizing the error due to the parallax effect. However, if the sheet is too thin, it will illuminate too few of the same tracer particles in both frames, leading to a loss of pairs.

The laser timing and camera timing are controlled through a synchronization unit that is linked to the computer and controlled by the software. In order to effectively “freeze” the micron-sized particles in an image, the laser burst must be short in duration.

Releasing the laser energy in short pulses also increases the peak power without requiring more energy. The energy is released over a shorter amount of time, thus increasing the peak power. The laser cavity is Q-Switched emitting laser energy in 6-10 ns bursts.<sup>26</sup> Q-Switch refers to the quality of the reflector, which is quickly changed to control laser emission. Energy pumped into the gain medium can be stored, but is not amplified when the quality of the reflector at the end of the lasing medium is low. During this phase, light leaving the gain medium is not reflected and lasing does not occur. However, the energy being pumped into the gain medium causes a population inversion to develop and stores energy up until the saturation point. Then, the quality of the optical resonator is switched to a high value and the stored energy is stimulated into emission.<sup>27</sup> This emission results in concentrated pulses of laser energy released at controlled intervals.

The PIV laser setup in the COAL Lab uses a dual cavity laser with a Q-Switch on each cavity. The two lasers can fire with a much shorter delay between pulses than would be possible with only one laser cavity. The PIV laser in the COAL Lab can deliver two pulses with as little as 300ns separation between pulses. The delay between pulses must be matched to the expected velocity of the flow. The reflections from the two pulses are close enough together in the acquired image pairs to be successfully correlated. The diagram below illustrates how the synchronization unit commands each Nd:YAG cavity to charge and then fire creating a pair of pulses.

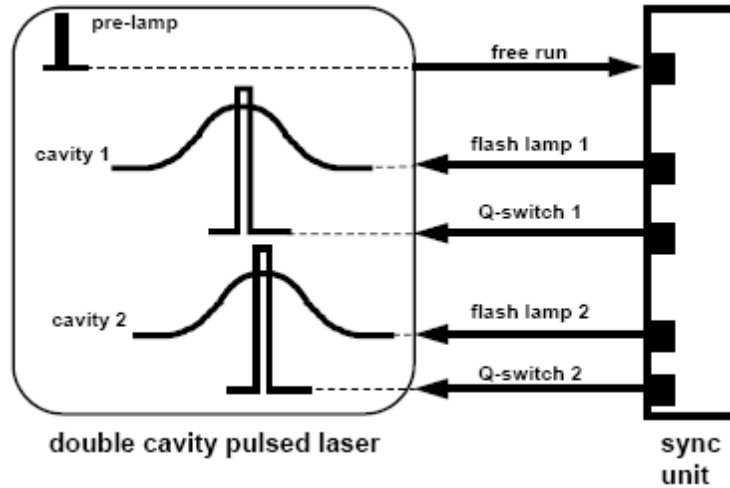


Figure 7. Synchronization diagram (used with permission)<sup>26</sup>

### II.6.3 Camera Type

The image acquisition hardware that came with the Dantec PIV system used in this thesis included two FlowSense 4M cameras paired with Nikon 60mm lenses. These cameras use a charge-coupled device (CCD) which is comprised of a 2048 x 2048 matrix of metal-oxide semiconductor (MOS) elements. The incoming light is focused through the camera's lens onto the CCD. The light hits these MOS elements, or pixels, and is converted into a voltage. The camera has 8-bit data resolution,<sup>28</sup> meaning the voltage magnitude from each pixel can be stored as one of 256 ( $2^8$ ) possible values. The camera's quantum efficiency, which is a measure of how effectively the incident photons are converted into electrons, is approximately 55% at 532nm.<sup>28</sup>



Figure 8. Flowsense 4M camera showing filter, lens, and CCD

Fig. 8 above shows the Flowsense 4M digital camera in its testing configuration. At the top right is a close-up picture of the camera's charge-coupled device (CCD) comprised of the 2048 x 2048 pixels. An optical filter is attached to the end of the Nikon 60 mm lens. This band-pass filter has a 75% transmission band from 530 nm to 540 nm. Although it does block some of the signal at 532 nm, it blocks out 99.99999%<sup>29</sup> of all light below 490 nm and above 570 nm. The underlying idea is the majority of the 532nm light passing through the filter will be light reflected from PIV seeder particles



(the desired signal). The filter will block the majority of the background noise, which will be comprised of wavelengths of light outside the transmission window. Using this method, the 532nm band-pass filter effectively lowers the noise floor.

Historically, PIV data acquisition has relied on photographic film double-exposed to create a picture with pairs of signals. This process of developing film and manually matching particle images from exposure pairs was time consuming. Further, this method retained an inherent directional ambiguity because each image pair was recorded on a single frame. The distance between the signals corresponded to particle displacement, but the signal order was unknown. Examining the double-exposed images, there would be no way to determine which signal was the first or second. This method resulted in maps of velocity vectors, each of which could be positive or negative.

The technological advance of digital photography quickly made photographic film based PIV obsolete. Correlation processing became much quicker, since digital images are readily processed by computers. However, due to the limitations in how quickly images could be taken, the CCD still had to be double-exposed. An autocorrelation algorithm would then determine which signals were likely pairs; average displacements were then calculated for partitioned regions. This process was quicker than developing photographic film and correlating image pairs by hand, but the directional ambiguity remained.

Modern PIV cameras today address this problem by quickly taking pairs of images. The FlowSense 4M cameras have an image buffer of interlaced pixels allowing it to take a second picture before the camera has stored, transferred and processed the first image. The shutter exposes the CCD to the first image in the same manner as with any

digital camera. Then, the image is quickly transferred to a storage buffer, allowing the CCD to be exposed to the second image. After the second exposure, the image stored on the buffer (image 1) and the image currently on the CCD (image 2) are both processed and sent to the computer. To illustrate the advantage in timing, consider the FlowSense 4M camera has a maximum frame rate of 15 Hz. That is, it can take 15 images per second continuously. However with the use of the image buffer, it can take 7.4 image pairs per second where the image pairs are spaced as little as 0.5  $\mu$ s apart. Overall, the camera is still limited to capturing and processing no more than 15 images per second, but pairs of images can be taken with much shorter delays between them. This advance in camera technology has made cross-correlation of image pairs the PIV technique of choice.

#### *II.6.4 The Cross-Correlation Technique*

Cross-correlation is a computational technique used to determine how similar two signal samples are for a given spatial shift. Over a small time scale, the signals within an interrogation region of the image map will shift in proportion to its velocity, but remain relatively unchanged. Therefore, if the first image is offset in proportion to the true flow velocity, the interrogation regions within the two image maps should line up and correlate with one another. That shift, combined with the knowledge of the elapsed time between signals, corresponds to velocity. In digital PIV, the two image maps are the signals and the shift must be determined in the two dimensions that the camera is observing. The shift determines the average displacement vector between samples of two image pairs.

The cross-correlation function for two discretely sampled images of the same size  $f(i,j)$  and  $g(i,j)$  is defined as:

$$\Phi_{fg}(m,n) = \sum_i \sum_j f(i,j) \times g(i+m, j+n) \quad (9)^{30}$$

The cross-correlation function is a measure of how closely the two image maps, or regions within the two image maps, correlate with one another when offset by a number of pixels  $(m,n)$ . The highest value for  $\Phi(m,n)$  is taken as the true correlation, where ‘m’ and ‘n’ are the number of pixels defining the vector by which the image was shifted. This vector is the output of the cross-correlation function; it is then multiplied by a scale factor in order to calculate an average displacement. The scale factor is the ratio of distance in the image plane to distance on the CCD, also known as pixel pitch. It is a function of the distance from the experimental plane to the CCD as well as the magnification of the camera’s lens.

In direct cross-correlation, the image maps are shifted by every possible value to determine the highest cross-correlation value. This makes direct cross-correlation computationally intensive. For a given interrogation region of area  $N$ , the number of operations which must be computed is on the order of  $N^4$ . By introducing the Fast Fourier Transform (FFT) into the cross-correlation algorithm, the computational effort is on the order of  $N^2 \ln(N)$ ,<sup>30</sup> a considerable decrease compared to  $N^4$ . In this technique, the Fourier Transform is taken of each image map. Then, instead of performing a sum over all the elements in the sampled interrogation region, the complex conjugates of each corresponding pair of Fourier coefficients from the transform of each image map are

multiplied. The products are then inversely transformed, resulting in the cross-correlation function in Cartesian coordinates.

#### *II.6.5 Measureable Velocity*

In theory, the maximum measurable velocity is a function of the size of the camera's plane of focus and the pulse delay. For example, velocities of up to 2,000 m/s could be resolved in a 1mm region of interest with image pairs taken 0.5  $\mu$ s apart. However, there are competing interests between dynamic range, spatial, and temporal resolution. In order to measure the maximum velocity, the delay between pulses should be as short as possible. Conversely, the pulse delay must be long enough to accurately determine an image displacement. The optimal pulse delay is short enough that the majorities of the signals remain in the same interrogation region from one image to the next, but long enough in time that there is a measurable shift. With these considerations and the Nyquist sampling criterion associated to the discrete Fourier transforms of the image maps, the Dantec Flow Manager Software Manual recommends a maximum displacement of one quarter of the window size.

### **II.7 Error Factors in PIV**

The first step in minimizing sources of error in an experiment is recognizing and understanding them. Many sources of error can be minimized. Those that cannot be minimized can be characterized and accounted for resulting in a quantifiable uncertainty. The main sources of error are discussed in the following sections of Chapter

II. Uncertainty will be addressed at the end of Chapter III as it is dependent on several test factors.

### *II.7.1 Loss of Pairs*

Loss of pairs occurs when the signal from a particle is recorded in only one of the two frames. Loss of pairs is primarily caused by two factors: (1) the finite nature of interrogation regions, and (2) out of plane velocity. Because an interrogation region is bounded, there will be particles that cross the region's boundary from frame one to frame two (the pulse delay). This crossing is most pronounced near the borders and is exacerbated by longer pulse delays. With an estimate of the bulk velocity, this error can be mitigated by setting the pulse delay to a value corresponding to a small expected displacement. Dantec, the company which assembled the PIV system, recommends average displacements corresponding to less than one fourth of the interrogation region size. There are also filters and other processing techniques that help reduce this error. The specific techniques used in this thesis will be discussed in Chapter III. The three main techniques are: (1) using overlapping interrogation regions, (2) interrogation region center-biasing, and (3) data validation.

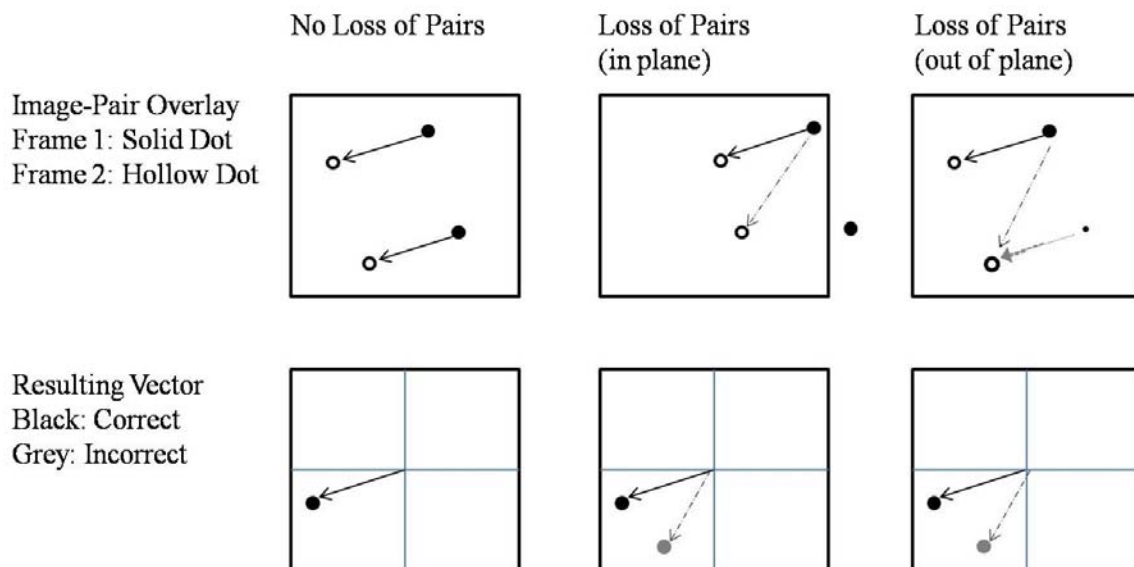


Figure 9. Interrogation regions and their corresponding vector output from cross-correlation showing loss of pairs from in plane & out of plane velocity

In Fig. 9 above, the top row shows three examples of interrogation regions with their image pairs overlapped. The solid dots represent signals from image one and the hollow dots represent signals from image two. The solid arrows show true displacements and the dashed arrows show false displacements over the pulse delay. The bottom row shows the displacement vectors calculated from the cross-correlation. Similarly, the solid arrows are the correct displacements and the dashed arrows are false. In the leftmost column there is no loss of pairs; the control group. In the middle column, loss of pairs occurs with one of the particles as its initial position is outside the interrogation region. This results in a 1:1 ambiguity, in that the particles in image two are both equally likely to be the final position corresponding to the particle in image one. In this case, the cross-correlation would result in two equal peaks and the true displacement would be unknown.

The second main cause of loss of pairs is out of plane velocity, shown above in the rightmost column of Fig. 9. This loss occurs when the particle velocity is not parallel to the focal plane. The particle at the top of the interrogation region shows in-plane motion. That is, it is traveling in the experimental plane over which the camera is focused. The bottom particle in the figure is traveling with the same top right to bottom left motion, but also has an “out-of-the-page” component in its velocity vector. Because of this out-of-plane component, the particle is behind the experimental plane in image one but moves into the experimental plane in image two. The image map from frame one shows only one particle, but the second shows two particles. This loss of pairs results in the same error as in the first example – an ambiguity the cross-correlation cannot resolve.

### *II.7.2 Parallax Effects*

Any out of plane velocity, small enough relative to the experimental plane’s thickness such that both images are still captured, will introduce an error due to parallax effect. The parallax effect results from the projection of 3-D motion onto a 2-D image. This is different from the inability for a 2-D measurement to capture 3-D effects. Error from the parallax effect is a function of the image scale factor, in that two images at different depths within the experimental plane are multiplied by the same scale factor even though they are at different distances from the camera’s CCD. The maximum error caused by the parallax effect is directly proportional to the thickness of the experimental plane and inversely proportional to the camera’s scale factor. Therefore, a thinner laser sheet and camera placed farther away from the experimental plane will allow for less error due to the parallax effect.

### *II.7.3 Zero-Velocity Biasing*

PIV measurements have a natural bias towards zero particle displacement. In the experimental setup, the pulse delay setting the camera and laser timing is chosen so that the average particle displacement between frames will be less than one quarter of the interrogation region size. In a steady one- or two-dimensional flow parallel to the illumination area, this experimental design should provide accurate flow measurements. The problem is the flow-field is not already known and it is rarely a steady 2-D flow. The experimental setup and timing of equipment is based on estimates. Even in a fairly steady and well developed flow, there will be irregularities. The seed particles moving at the bulk velocity or lower will be measured with a high degree of accuracy. However, seed particles entrained by quickly moving eddies or other turbulent flows are far more likely to have their initial or final position outside the interrogation area, and are therefore less likely to be accurately recorded. This propensity toward measuring the slower velocities with more accuracy is known as “zero velocity biasing.” Quick pulse delays, sufficient particle seeding, and certain post processing techniques mitigate this problem.

### *II.7.4 The FFT Error*

As mentioned in the discussion of cross-correlation, the Fast Fourier Transform (FFT) method is used in place of direct cross-correlation. Although this greatly decreases the required computational time, it also introduce potential errors. In using FFTs, an infinite and periodic sample space is assumed.<sup>30</sup> This assumption limits the interrogation regions to square sizes of pixels at multiples of two, for example 32 x 32 or 64 x 64. One consequence of applying the infinite assumption onto the finite domain of an



interrogation region is an artificial increase in the background noise along the interrogation region borders.<sup>26</sup>

### **III. Test Setup and Apparatus**

#### **III.1 Methods**

The following experimental steps were taken to meet the objectives of this thesis in support of the UCC research being done at AFIT.

1. Laboratory Setup: The Combustion Optimization and Analysis Laser (COAL)

Laboratory was partially redesigned to make room for another laser table in addition to another dye-laser.

2. UCC setup: The small-scale UCC had been previously designed and built and required few modifications. Major joints in the test rig were sealed with gasket-like material. The test rig was mounted in a different configuration for optimal experimental setup as well as for safety concerns. The igniter was redesigned and built.

3. PIV setup: The stand-alone PIV system proved to be versatile and user-friendly. However, the mirrored swivel-arm and sheet-forming optics proved to be sub-standard in producing a thin laser sheet of near constant energy density.

4. Experimental runs with straight and curved cavity vane sections.

5. Data Processing with Dynamic Studio® software.

#### **III.2 Experimentation**

From the goals and objectives identified, the process for the experiment is designed. The objectives of this thesis are to record 2-D velocity measurements of the flow inside the UCC test rig. These “velocity maps” allow for flow visualization as well

as quantification of the flow turbulence. An ideal experiment would collect continuous velocity data at every point in order to fully understand the flow field dynamics. This would be the equivalent of PIV measurements at an infinite frequency and at perfect accuracy. The higher sample frequency would allow accurate measurement of the different turbulence scales, such as the Kolmogorov microscale ( $l_K$ ) and the integral scale ( $l_0$ ), which measure the smallest and largest eddies. As the PIV equipment in the COAL Lab is limited to a measurement frequency, in terms of the number of image pairs acquired per second, of 7.4 Hz, direct measurement of these flow structures is not possible. However, by comparing the flow variance over time at each location relative to the average velocity, the average flow turbulence was measured in terms of turbulence intensity.

Isolating the experiment's many extraneous variables allows for more meaningful results.<sup>31</sup> Ideally, this control would permit a cause and effect relationship to be established between the independent and dependent variables. The independent variables are either varied one at a time or in conjunction with one another. Assuming only these factors are varying, the responses are studied to determine effect. The factors, or independent variables, varied in this experiment in order to study the system response are:

1. Main vane air mass flow
2. Cavity vane air mass flow
3. Equivalence ratio: as measured in terms of fuel mass flow and cavity mass flow
4. Cavity Vane type: (Straight or Curved)
5. Position of experimental plane within the main vane

Other factors either beyond the control of the experimenter or whose dynamic influence on the response will not be studied must also be accounted for. These factors are recorded and corrected for so data taken from different experiments may be compared. In this experiment, these factors are the temperature and pressure of the airflows.

### **III.3 Test Matrix**

Previous research had identified two optimal flow rate ratios in the UCC test rig for vortex trapping in terms of mass flowing through the main channel to mass flowing in the cavity channel. Hankins found this ratio to be between 10:1 and 5:1, whereas Lakusta's work on laser induced fluorescence to quantify flame location identified this ratio as 20:1. In order to focus on the physics of the problem, the test matrix for this thesis was centered on these previously identified flow cases.

#### *III.3.1 Cavity-to-Main Vane Mass Flow & Equivalence Ratio Study*

Four ratios of main to cavity mass flow rates were chosen as: 20:1, 10:1, 7.5:1, and 5:1. These correspond to cavity mass flow rates that are 5%, 10%, 15%, and 20% of the main channel mass flow respectively.

The mass flow rates for the main channel and the cavity channel were varied. Therefore, stratifying the test conditions based on the overall equivalence ratio would have been slightly ambiguous. In keeping with previous AFIT research, test conditions were stratified based on the cavity equivalence ratio. The ratio of mass flow rates was then varied holding the cavity equivalence ratio constant.

Four cavity equivalence ratios were chosen to investigate the dynamics between stoichiometry and the flow field interaction at the intersection of the cavity and main flow channels (over the RVC). In keeping with previous research, the four equivalence ratios chosen were: one lean ( $\phi=0.7$ ), stoichiometric ( $\phi=1.0$ ), and two rich ( $\phi=1.3$  and  $\phi=1.5$ ). In building the experimental test matrix, the four variables were: the main air mass flow rate, the cavity air mass flow rate, the cavity equivalence ratio, and the depth at which the 2-D experimental plane would be set. By picking overall flow rates similar to those in previous research, the four variables actually condensed to three variables by only varying the ratio of cavity to main air mass flow rates.

The experimental test matrix is shown in Table 2 below for one configuration of the UCC test rig.

Table 2. Test matrix for flow rate ratio & equivalence ratio study

<b>Test Matrix: Ratio of Flow Rates</b>				
<b>Cavity Equivalence (-)</b>	<b>0.7</b>	<b>1</b>	<b>1.3</b>	<b>1.5</b>
<b>Hydrogen Flow (SLPM)</b>	<b>30</b>	<b>30</b>	<b>30</b>	<b>30</b>
<b>Cavity Airflow (kg/min) →</b>	<b>0.13</b>	<b>0.09</b>	<b>0.07</b>	<b>0.06</b>
<b>Ratio of Cavity to Main Airflow</b>	<b>Main Airflow (kg/min)</b>			
0.2	0.66	0.46	0.35	0.31
0.15	0.88	0.61	0.47	0.41
0.1	1.31	0.92	0.71	0.61
0.05	2.63	1.84	1.41	1.23

In the test matrix shown above, there are four groups of runs arranged into columns. For each of these four groups of runs, the cavity air mass flow rate and the cavity equivalence ratio are held constant. The main air mass flow rate is set by the four ratios of flow rates shown in the leftmost column. For each of these settings that define the conditions for a single run, the fuel flow, the cavity air mass flow, and the main air mass flow are held constant. At each test condition, the camera and laser sheet are translated in concert, as previously described, to one of four experimental planes within the UCC main vane. Fifty image pairs are captured for each test condition. These image pairs constitute the raw PIV data. In short, the testing investigates four equivalence ratios, four air mass flow ratios, and four 2-D experimental planes. This corresponds to fifty image pairs for each set of PIV data, four sets of PIV data for each air mass flow ratio, four air mass flow ratios for each equivalence ratio, and four equivalence ratios. Overall, the result is 64 sets of data or 3,200 image pairs. However due to test equipment issues, all conditions in the test matrix above were run with the straight cavity vane section, only.

### *III.3.2 Velocity Increase Study*

The second set of experimental runs focused on increasing mass flow while keeping the equivalence ratio constant at 1.0 and the ratio of mass flows constant at 0.1 (10% cavity flow relative to the main flow). The test matrix for this set of experimental runs is shown below in Table 3.

Table 3. Test matrix for velocity study

<b>Test Matrix: Mass Flow Increase</b>		
<b>Cavity Equivalence Ratio: 1.0</b>		
<b>Ratio of Cavity to Main Air: 0.1</b>		
<b>Main Airflow (kg/min)</b>	<b>Cavity Airflow (kg/min)</b>	<b>Hydrogen Flow (SLPM)</b>
0.61	0.06	20
0.92	0.09	30
1.23	0.12	40
1.53	0.15	50

Each flow condition in this test matrix was run with the UCC configured with both the straight and the curved cavity vane sections. Unlike the flow ratio study, all test conditions in this matrix were run successfully for both UCC configurations.

### III.4 Lab Setup

#### III.4.1 Computer Controls

The COAL Lab's main control station was used to perform the following tasks:

- Turn on/off and set the flow rates for the main and secondary airflow lines
- Turn on/off and set the flow rates for all fuel mass flow controllers connected to the test stand

- Record temperatures for all thermocouples
- Record pressures for all pressure transducers
- Turn on/off the fuel and air lines for the igniter
- Turn on/off the spark plug for the igniter
- Turn on/off the exhaust system

Once all the manual safety valves are open, it is possible to operate all equipment required for the UCC test rig from behind this control station shown in Fig. 10 below.



Figure 10. Coal lab main control center

The laser diagnostic equipment, including the PIV system, is not controlled through this station. Therefore, it is beneficial to have several people to help operate the equipment. For a typical test run, one person would be behind this computer while the other was in



the back of the lab operating the PIV equipment. A brief list of the steps required to perform one experimental run after all the manual and safety valves are open is listed below.

The person operating the main control station would take the following steps

1. Close the air recapture duct to prevent exhaust from entering AFIT's HVAC system
2. Turn on the laser warning light
3. Turn on the exhaust fan
4. Set the igniter fuel and air flow rates
5. Turn on the cavity airflow
6. Turn on the igniter fuel and air
7. Turn on the igniter's spark plug for approximately one second
8. Turn off the spark plug (person at back of lab verifies igniter is lit)
9. Turn on the cavity vane fuel to a low initial setting
10. Turn off the igniter (person at back of lab verifies UCC is burning)
11. Increase the cavity fuel and cavity airflow to set-point values
12. Turn on main vane airflow
13. Report to person at back of lab when flow rates have steadied

The person at the back of the lab operating the PIV equipment would then do the following:

1. Command the electronic translation devices to position the experimental plane

2. Set the camera and laser pulse delay based on the calculated velocity within the main vane in the PIV software
3. Turn on the pressurized gas for the particle seeder
4. Turn on the particle seeder motor
5. Initiate image acquisition in the PIV software
6. Turn off the seeder motor
7. Turn off the pressurized gas
8. Save the images

At this point, one complete set of PIV data has been taken. The person at the back of the lab would command the motion controllers to translate the camera and laser plane to the next experimental plane for PIV data acquisition. Once that section of the PIV data acquisition is complete, the person at the main control station would perform the following steps:

1. Turn off the fuel flow
2. Turn down the main air flow to a minimal value for cooling
3. Leave the cavity airflow on for one to two minutes for cooling
4. Turn off both airflows once UCC has cooled
5. Turn off exhaust fan

#### *III.4.2 Gases*

The three gasses used in this thesis were air, hydrogen, ethylene, and zero air (air filtered to reduce residual hydrocarbon content). Air and hydrogen were the primary gasses used to investigate the flow through the UCC test rig. The zero air and the

ethylene were used to initiate the combustion of the hydrogen and air, and then turned off prior to data acquisition. The gasses are stored in bottles outside the lab in the “tank farm.” Tubing carries the gasses from their storage containers into the COAL Lab. Except for the main and cavity air, the gases are plumbed to the test stand through the white tubing shown in the figure below. Once at the test stand, the gasses pass through electronic solenoid valves that turn the flow on and off. These solenoid valves are controlled by the main control station through the program written in Labview®. After passing through the solenoids, the gas goes through a filter and onto the mass flow controllers. As with the solenoids, the mass flow controllers are controlled by the main control station. Once through the mass flow controllers, the gasses are sent to the UCC test rig through braided metal hoses.

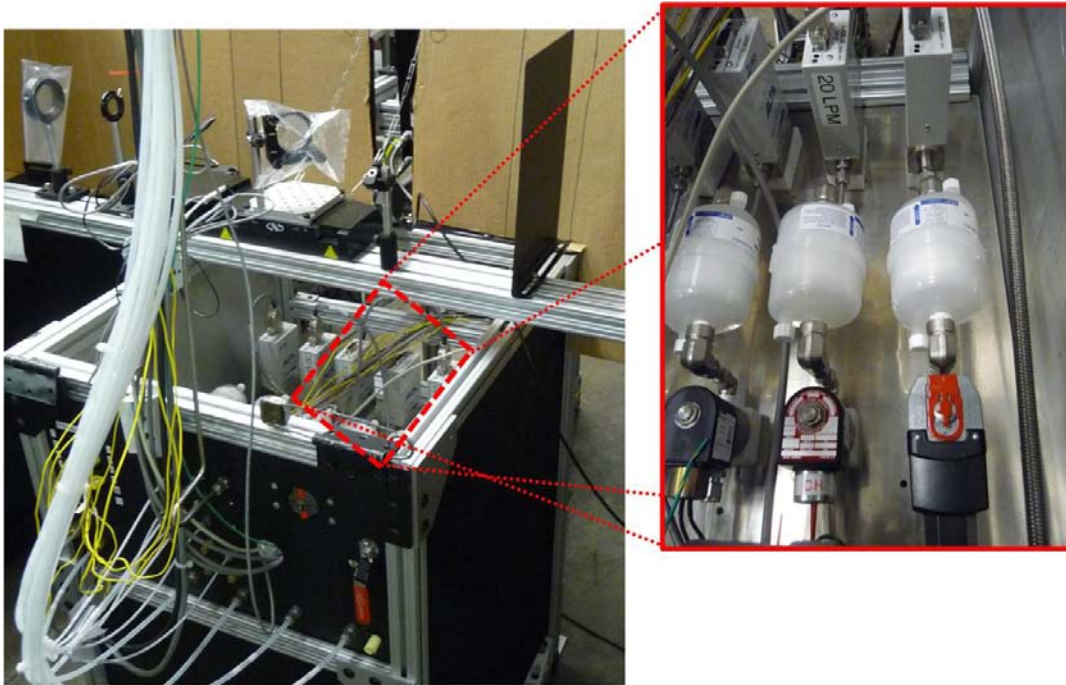


Figure 11. Test stand with gas lines

The primary air supply comes from compressor tanks and enters the COAL Lab in copper tubing, as shown in the figure below. It passes through the manual isolation valve then splits into two paths. The upper path supplies the cavity vane with air while the lower supplies the main vane with air. The air passes through manual ball valves and then through the pneumatic-driven valves. These valves, with the blue actuators, shown in the figure below are commanded to open and close by the main control station. The air passes through pressure regulators and then through the red mass flow controllers, which are also set by the main control station. Lastly, the air is plumbed up through the electric heaters and over to the UCC test rig.



Figure 12. Air supply and control lines

The electric heaters are essential when running liquid fuel to promote droplet evaporation and stable combustion. Hydrogen was the only fuel used in this thesis, and the electric air heaters were not used. Orange rubber corrugated hoses connect the main and cavity air supply lines to the UCC test rig as shown below. The seed supply connects to the

main air inlet at an angle of 90 degrees to the main air supply. This hose is darker orange with a smaller diameter shown in the figure below. The cavity air flow is bifurcated with one part entering the aft of the cavity vane and the other entering the long flat section. This portion of the air then enters a small manifold inside the cavity vane where it is injected at a 45 degree angle.

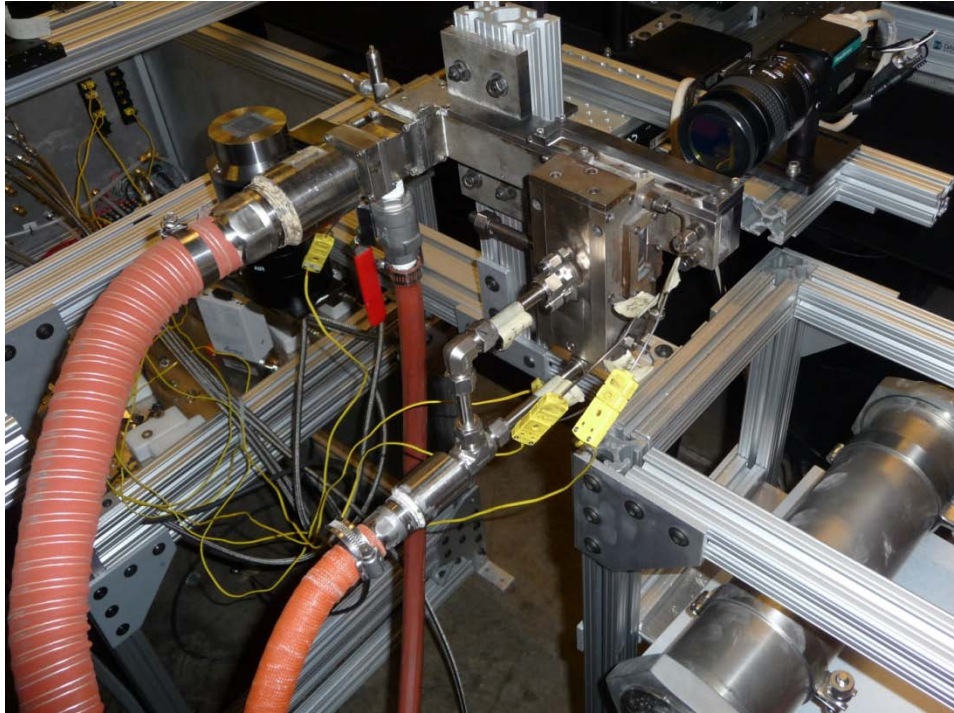


Figure 13. Main and cavity air lines connected to the UCC test rig

The Alta Mass flow controllers used in the COAL Lab meter gas in standard liters per minute (SLPM). A standard liter is a measure of the mass of a species of perfect gas at 0 degrees Celsius and 101,325 Pa pressure (1 atmosphere). Since a standard liter is a measure of mass, SLPM is a measure of mass flow. The only basic fluid property left unconstrained in the definition of a standard liter is density. However, the standard liter definition implies a perfect gas which has a defined density at a given temperature and

pressure. Therefore, it is the molecular weight of the species differentiating between standard liters of different substances. Two of the gasses used in this experiment are standard air and ethylene ( $C_2H_4$ ). Since these two gasses have similar average molecular weights, 28.85 and 28.05 respectively, the mass contained in a standard liter of each differs by less than 3% ( $1.287E-3$  kg and  $1.252E-3$  kg). However, a standard liter of a gas with a lower molecular weight, such as hydrogen, will contain significantly less mass. Therefore, hydrogen requires a much higher flow rate in terms of SLPM compared with air and ethylene. Table 4 below lists these properties.

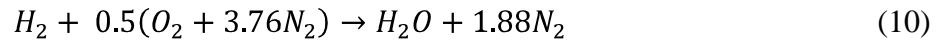
Table 4. Standard liters of air, ethylene, & hydrogen

<b>Mass in one Standard Liter</b>			
Assumes perfect gas at 273.15K temperature & 101,325 Pa pressure			
Property	Standard Air	Ethylene ( $C_2H_4$ )	Hydrogen ( $H_2$ )
Molecular Weight (kg/k-mol)	28.85	28.05	2.02
Specific Gas Constant (J/kg-K)	296.38	288.19	4124.41
Density (kg/cu.m)	1.25	1.29	0.09
<b>Mass per Standard Liter (kg)</b>	<b>1.25E-03</b>	<b>1.29E-03</b>	<b>9.00E-05</b>

The mass flow controller used for the hydrogen fuel has a maximum flow rate of 50 SLPM. In terms of flow rates for the main air line, cavity air line, and fuel line, this maximum fuel flow was the limiting factor. As was discussed in the test matrix section of this chapter, the parameters under investigation in this thesis are mainly ratios. The



highest equivalence ratio for the highest cavity to main airflow ratio required the highest fuel flow rate. This value was set to 50 SLPM of hydrogen fuel. The other fuel set-points were calculated based on equivalence ratios. As discussed in the previous chapter, the equivalence ratio compares an actual fuel to air ratio to that same ratio at stoichiometric conditions. The fuel to air ratio for a hydrogen air mixture is 0.029, or 34.06 in terms of air to fuel. This value is found by comparing the mass of fuel to the mass of air at stoichiometric conditions.



As seen in the balanced chemical equation for the combustion of hydrogen in air, shown above, the reactants are made up of one mole of hydrogen (2.016g) and one half of a mole of air (68.66g). Therefore, the ratio of fuel to air is:  $2.016/68.66 = 0.029$ .

Table 5. Flow rates for hydrogen and cavity air at set equivalence ratios

<b>Hydrogen &amp; Cavity Flow Rates</b>							
Stoichiometric fuel:air ratio			0.0293583				
SLPM	% of Max	kg/min	Cavity Airflow (kg/min)				
			Eq. Ratio =	0.7	1	1.3	1.5
20	40	1.80E-03		0.09	0.06	0.05	0.04
25	50	2.25E-03		0.11	0.08	0.06	0.05
<b>30</b>	<b>60</b>	<b>2.70E-03</b>		<b>0.13</b>	<b>0.09</b>	<b>0.07</b>	<b>0.06</b>
35	70	3.15E-03		0.15	0.11	0.08	0.07
40	80	3.60E-03		0.18	0.12	0.09	0.08
45	90	4.05E-03		0.20	0.14	0.11	0.09
<b>50</b>	<b>100</b>	<b>4.50E-03</b>		<b>0.22</b>	<b>0.15</b>	<b>0.12</b>	<b>0.10</b>

Table 5 above illustrates how flow rates were set. Several of the initial runs were conducted with a lower capacity mass flow controller. This controller had a maximum of 30 SLPM mass flow, but was upgraded to a controller with a 50 SLPM maximum mass flow capacity. The two **bolded** conditions in the table above correspond to maximum hydrogen flow rates for the 30 SLPM and a 50 SLPM mass flow controller.

#### *III.4.3 Infrastructure (80/20)*

Other experiments in the COAL Lab, in addition to the PIV, were being conducted concurrently on the small-scale UCC rig including laser-induced fluorescence and laser-induced incandescence. In order to coordinate equipment use and eliminate recurring build-up / tear-down time and effort, care was taken in the placement and design of the lab layout to make the parallel experiments compatible. The two tables and a support structure making up the test stand were built from extruded 6105-T5<sup>33</sup> aluminum called “80/20.” The three primary sizes of “80/20” used in the COAL Lab setup were 1.5” x 1.5”, 1.5” x 3”, and 3” x 3” in cross-section. This framing material has T-slots running along the middle of each side in which lab-equipment can be anchored.



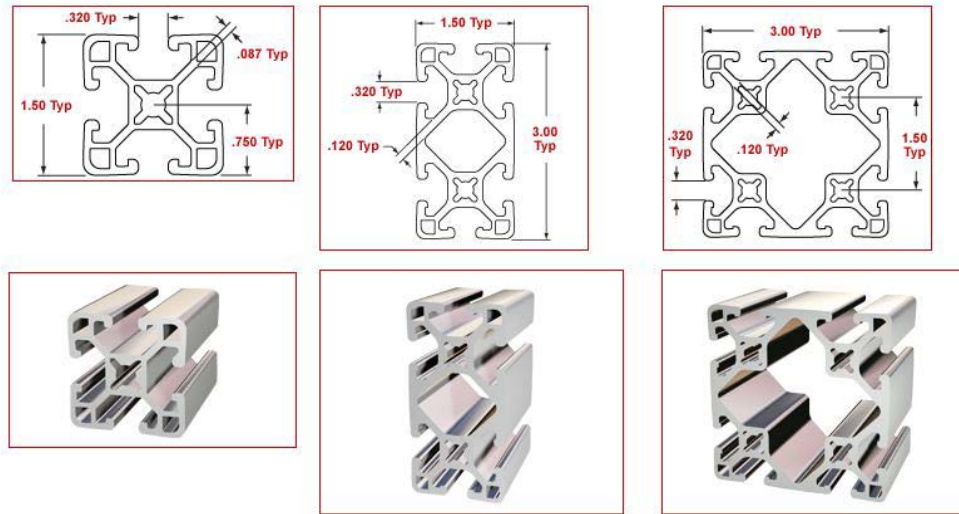


Figure 14. Cross-sections of “80/20” aluminum structure<sup>33</sup>

The first table holds the solenoids, filters, and mass-flow controllers for each gaseous line running to the test area. It also holds the thermocouple mounts, the pressure tap mounts, and a fire-valve for the liquid fuel supply. This stand is shown in Fig. 11 above on page 57 from the front, and Fig. 15 below from the back. The Hencken burner and the UCC test rig are mounted to this table on a cross-brace of double-thick 80/20 anchored to the second table. The second table was built primarily to hold the PIV seeder equipment and to provide another structure by which to anchor the mounting for the UCC test rig.

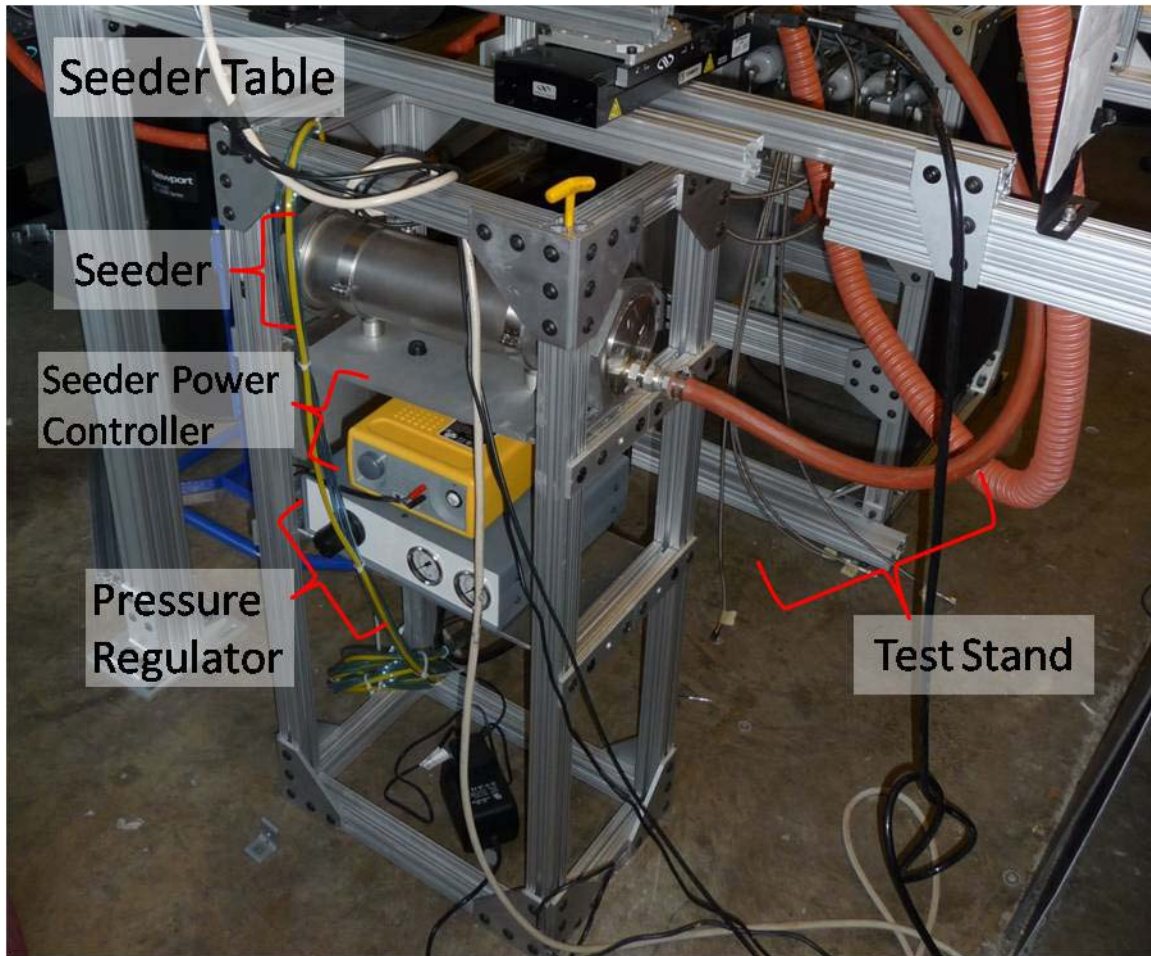


Figure 15. Seeder table & test stand

This seeder table holds the power control unit, the pressure regulator for the seeder, and the seeder itself.

### III.4.4 Translation of the Experimental Plane

The UCC test rig main vane is 30.5 mm in height and 14 mm in width at the exit plane. With the laser on high power, the sheet is approximately 3.0 mm thick at the experimental plane. The main channel volume and laser sheet thickness allowed for four distinct experimental planes. The camera and final mirror in the optics train were each mounted to a Newport ESP300 linear translation device. By translating the final mirror

in the optics train, the laser sheet was swept through the main vane of the UCC. Each of the four experimental planes was approximately 3 mm in thickness, and positioned directly behind each other in terms of depth away from the cross flow of the cavity channel. A pictorial of the four experimental planes with their locations relative to the back wall (also relative to the interface between the cavity and main channel) is shown below in Fig. 16.

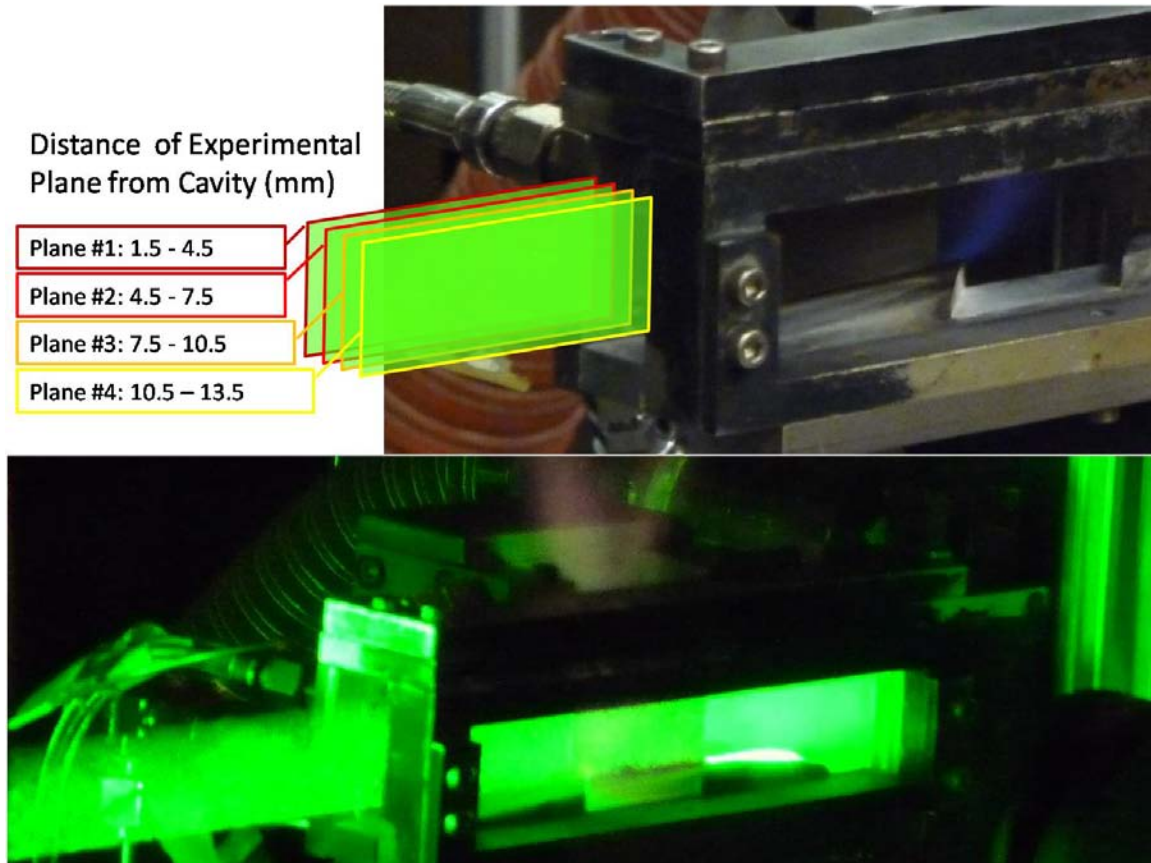


Figure 16. Approximate positions of the four experimental planes (top); laser illumination of experimental plane #4 during testing (bottom)

The translation devices allowed for quick and exact movement of the experimental plane. The Newport ESP300 Motion Controller was used to command the two linear translation

devices to move in unison. A picture of the FlowSense 4M camera mounted on the other translation unit is shown below.

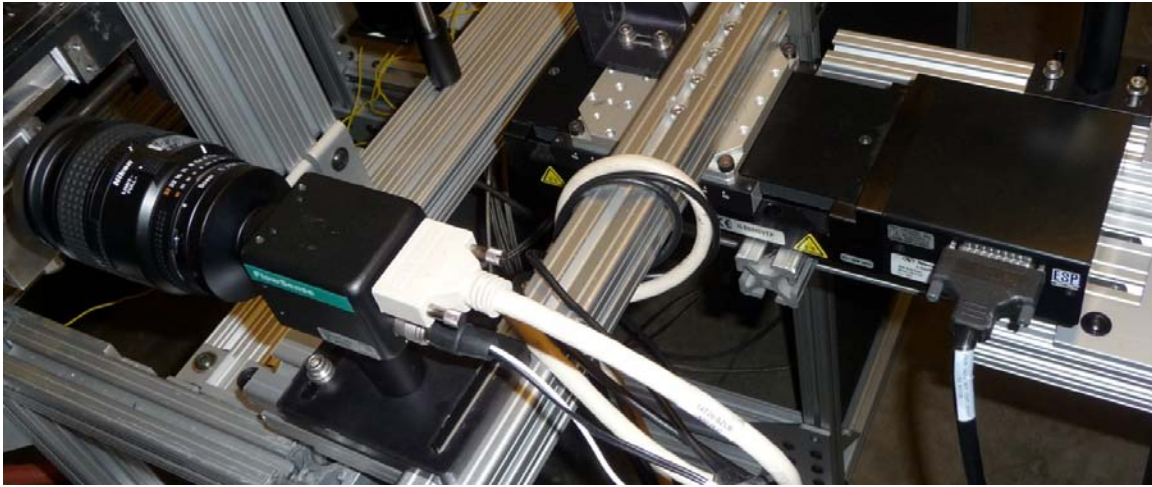


Figure 17. Camera mounted on electronic translation device

These translation devices are controlled electronically through the Newport Universal Motion Controller. This unit, shown in the figure below, can control up to three translation devices independently through direct user input or through computer control.



Figure 18. Newport ESP300 motion control driver

In order to ensure consistent repeatability of the tests, the absolute positions for each translation device were stored in four command-line programs. In these programs, the user would store a set of commands under a program name. For example, when setting



up an experimental run where the test plane was adjacent to the cavity vane, the user would input the command “1ex,” and the translation devices would move to their programmed positions. Similarly, commanding “4ex” would execute the program that translates the laser sheet and the camera’s focal plane to the position near the quartz window.<sup>32</sup>

The Newport Motion Controller can control up to three translation devices – one on each “axis.” However, the controller in the COAL Lab had only two amplifier cards. Each of these axes requires an amplifier card stepping up the current to command a movement. An amplifier card can be seen sitting on top of the ESP300, above where it would regularly be installed, in Fig. 19 below.

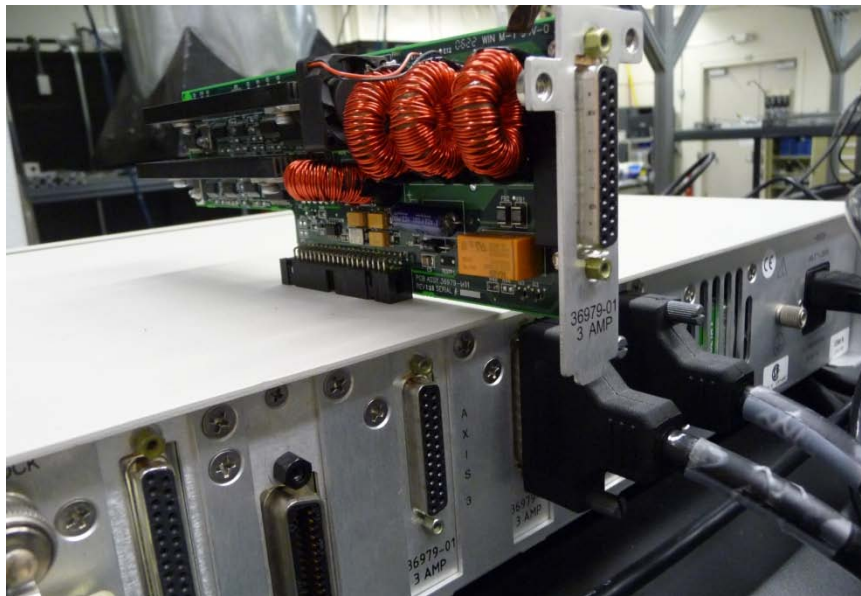


Figure 19. Newport ESP300 with faulty amplifier card

### III.5 Ultra-Compact Combustor Sectional Test Rig Setup

The following sections describe the construction and layout of the experimental setup.

### *III.5.1 Placement of the UCC, Exhaust System*

The UCC test rig was originally set up with the main flow toward the back of the lab and the cavity flow moving from right to left if the observer was looking at it from the front of the lab. This setup is shown in Fig. 20 below.

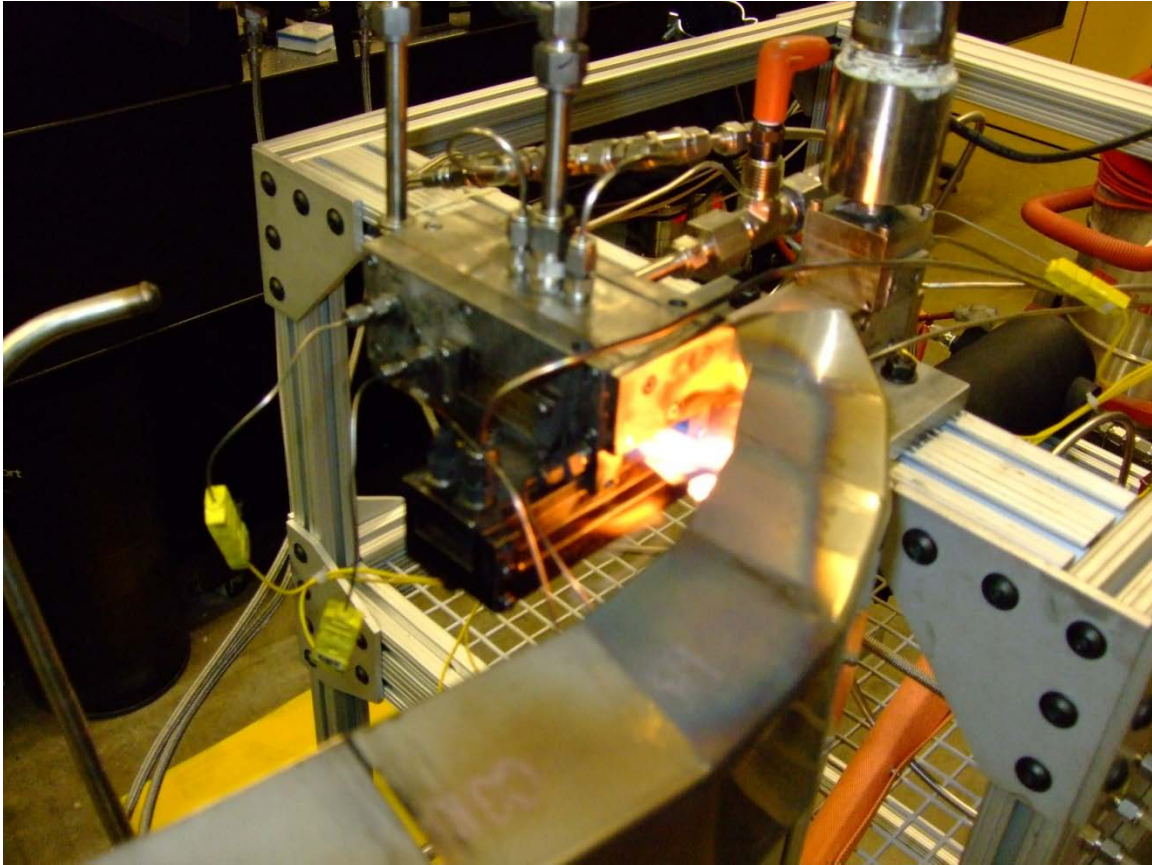


Figure 20. UCC testing orientation used in previous research<sup>21</sup>

In this setup, the high temperature exhaust gasses from the cavity flow came in contact with a metal channel that turned the flow ninety degrees to duct it into the exhaust system. When setting up the equipment for this experimentation, the UCC test rig was repositioned to satisfy two concerns. First, the main flow channel needed to flow directly

into an exhaust duct so the seed particles would not contaminate the laboratory equipment in the vicinity. Second, the cavity flow, which contains most of the hot combustion products and flame, needed to flow directly into exhaust ducting without requiring turning.

The first option was to rotate the UCC test rig ninety degrees about the main flow path direction and ninety degrees about the cavity vane path direction. In this orientation, the high temperature combustion products from the cavity vane would be flowing up and directly into the exhaust ducting and the main flow path would be moving from left to right, as viewed from the front of the lab. This required an auxiliary exhaust duct for the main flow, which was setup to duct the main flow out the back door. This setup is shown below in Fig. 21.

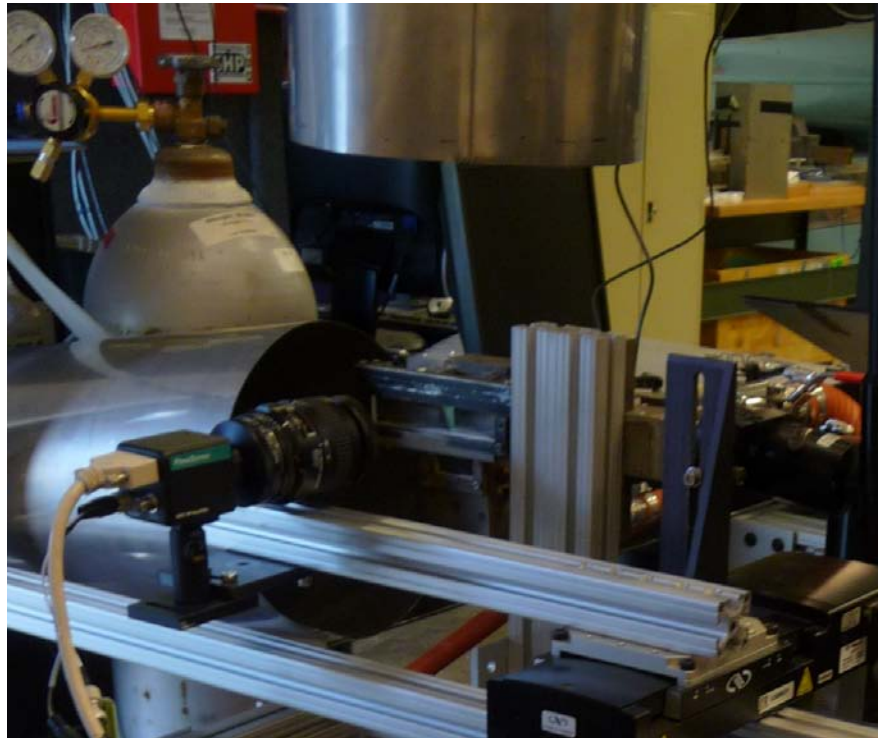


Figure 21. Temporary UCC orientation

The primary reason a separate exhaust duct was to direct the PIV tracer particles out of the lab. Installing a filter capable of removing micron-sized particles from high-temperature flow would have required major modifications to the exhaust system in the COAL Lab. The separate exhaust duct was an attempt to avoid this issue. After review, the current exhaust system proved to adequately handle the particles from the experiment with only minor modification.

To minimize impact to the experiment and ensure personnel safety, a third configuration was required. In the first configuration, the high temperature flow was impinging on the exhaust flow diverter and smoke could be seen coming off the test equipment. The second configuration did not require either flow path to be turned until it was diluted far downstream of the test rig, but required a separate exhaust duct out of the lab. The final configuration was somewhat of a mix of the previous two. It has the main flow path directed toward the back of the lab, requiring a ninety degree elbow in the exhaust ducting, and the cavity flow channel pointing directly up into the main exhaust as seen below in Fig. 22.



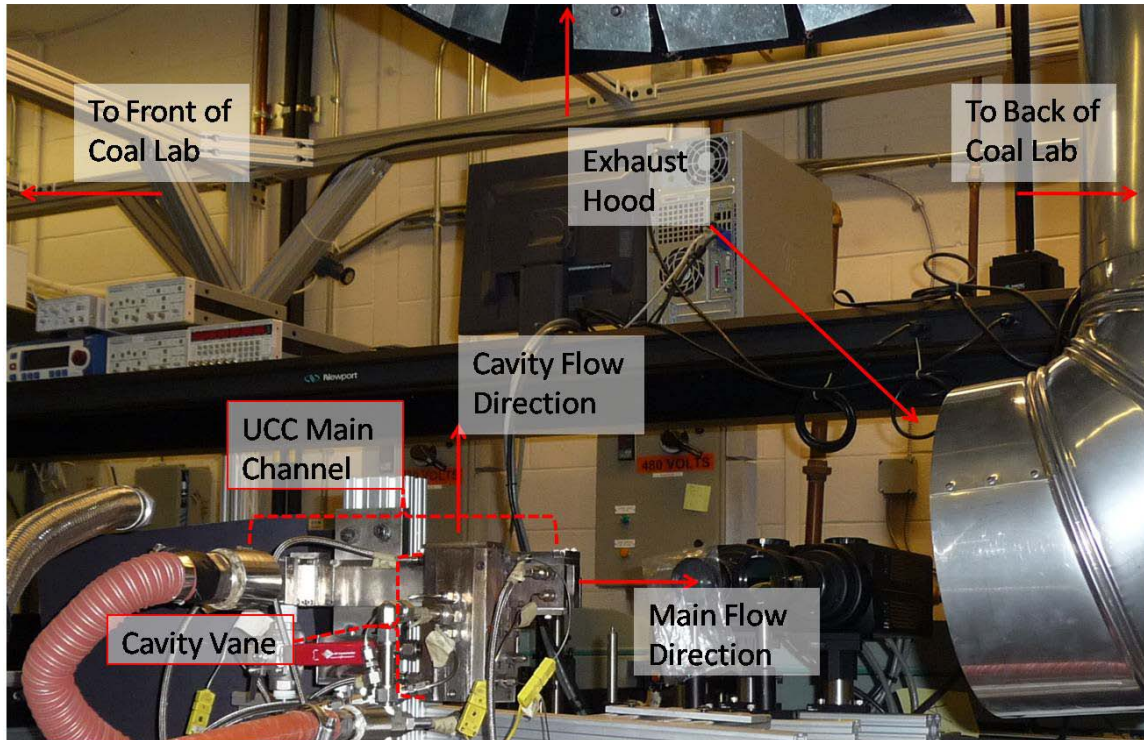


Figure 22. Final lab configuration for the UCC test rig

This configuration allows optical access from the aft and side of the UCC test rig with angular separation from the high temperature flow paths.

### III.5.2 Pressure Taps & Thermocouples

The two pressure taps shown in the figure below measure differential pressure. Each has two lines connected on either side. These devices measure the pressure differential between the gas in the two lines and transmit the signal back to the main control computer through the black interface on the top of the housing.

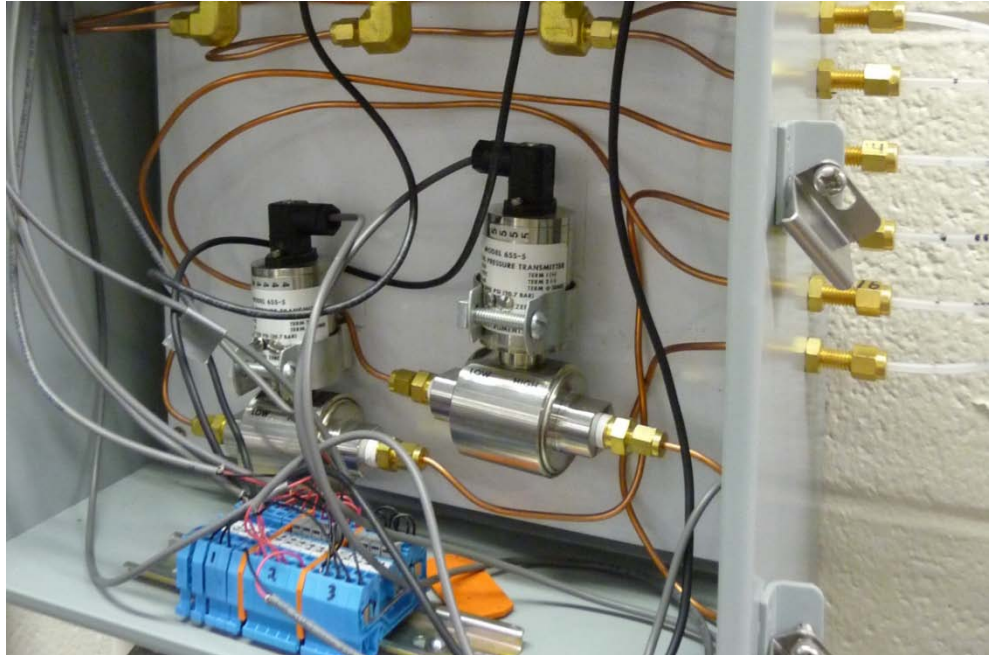


Figure 23. Differential pressure transducers used to measure pressure drop

The pressure transducer on the bottom right measures the pressure difference from the inlet of the cavity vane to the exit. The unit on the bottom left measures the pressure difference from the inlet of the main vane to the exit. In previous thesis work,<sup>21</sup> this pressure drop across the main vane was not measured due to what was thought to be a faulty pressure transducer. The electrical harness was not wired correctly and the problem has since been fixed.

### *III.5.3 Sealing the Cracks*

The UCC test rig also had several joints with gaps which needed sealing. When operating with gaseous fuel, the main concern is keeping the seeded airflow from spilling out into the lab. With a heavy kerosene-based fuel, the concern is pooling or dripping fuel leaking out and catching the lab on fire. Because the seed particles are an abrasive

material that could damage the laboratory optics, care was taken to ensure they were properly vented out of the lab environment. In order to seal several of these joints, Fiberfrax® ceramic fiber paper was cut and fit to fill the gaps as a gasket material. This material was chosen for its compressibility and its tolerance for high temperature which is up to 2,000 °F.<sup>33</sup>

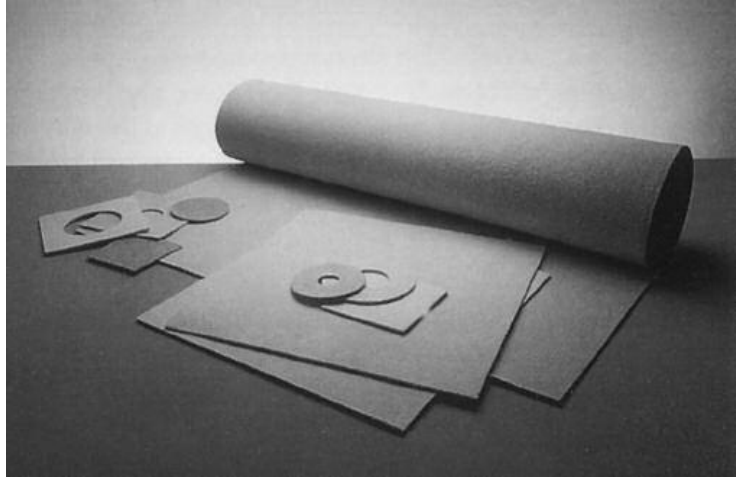


Figure 24. Fiberfrax® ceramic fiber paper<sup>33</sup>

#### *III.5.4 Ethylene Igniter*

In a previous thesis effort, Lakusta characterized and developed operating procedures for the UCC's ethylene ( $C_2H_4$ ) igniter. This igniter is a basic rectangular box manifold with two input ports for ethylene and air, a spark plug to ignite the mixture, and an exit port for the burning mixture to flow into the cavity vane of the UCC.

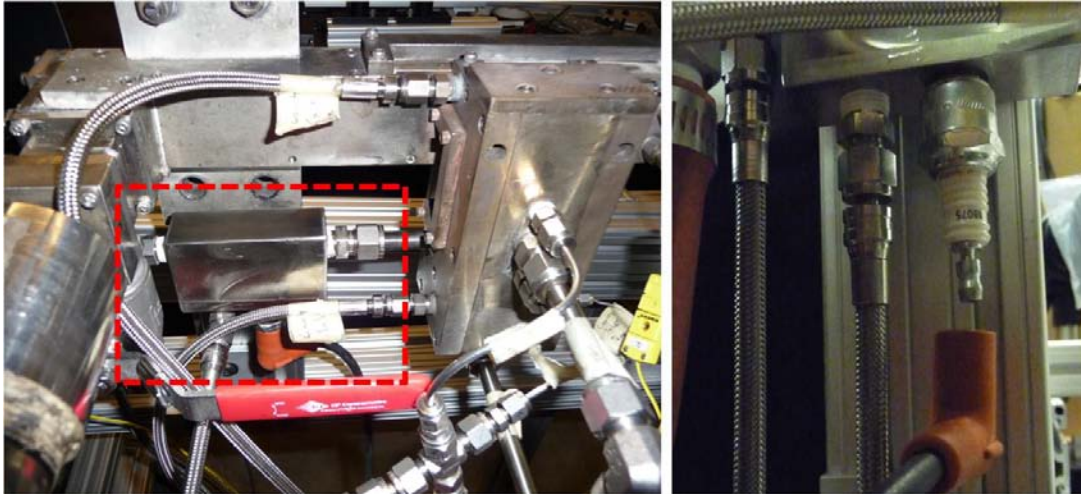


Figure 25. Close-up of ethylene igniter

Lakusta found the ethylene igniter operated with stable combustion at rich conditions at equivalence ratios of 1.8 to 2.2. He concluded the optimal equivalence ratio was 2.1.<sup>5</sup> This optimal equivalence ratio was chosen as the starting point for the new igniter, as it is similar in concept to the original.

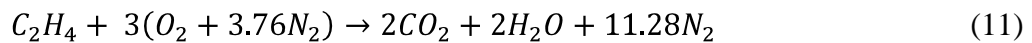
A full characterization was not performed on the new igniter. The air and fuel flow rates were adjusted and observed until a stable condition was found that consistently ignited and remained lit when initiated with a spark. The best method for operating the igniter was to start with the main airflow turned off, the cavity airflow at 0.1kg/min. Once the cavity airflow became steady, the airflow into the igniter was set to 5 SLPM (10% of its 50 SLPM mass flow controller), the ethylene was set to 2.6 SLPM (13% of its 20SLPM mass flow controller), and lastly the spark plug was commanded to spark for approximately one second and then turned off. At this point, the ethylene igniter would consistently stay lit in the cavity with a visible flame illuminating the cavity vane as shown in Fig. 26 below.





Figure 26. Steady operation of ethylene/ air igniter

The most striking difference between these startup procedures and those recommended by Lakusta was the flow rates that resulted in the most stable flame were extremely rich. The stoichiometric fuel to air ratio for the combustion of ethylene in air is 0.07.



With flow rates of 2.6 SLPM of ethylene and 5.0 SLPM of air, the fuel to air ratio is 0.51.

This corresponds to an average equivalence ratio of  $0.51/0.07 = 7.22$ . A mixture with an equivalence ratio this high is usually outside the flammability limits of most fuels.

However, the rich extinction limit for ethylene and air is above 6.1.<sup>12</sup> If the reactants inside the igniter behaved as steady, plug flow, one would expect the igniter to sustain stable combustion at a less rich condition. The explanation as to why this extremely rich mixture created the most stable igniter flame remains an unexplained phenomenon, as a full characterization of the igniter was not performed. However, one possible explanation

is the mixture was not as rich as was calculated based on the mass flow controllers. The mass flow controllers have a specified uncertainty of  $\pm 1\%$  at operating conditions from 20% up to 100%. Since the mass controllers for both ethylene and zero air were below this value, the actual fuel and air flow rates could be significantly different. It is possible the actual equivalence ratio was much lower than 7.2. One interesting finding was the spark plug had to be replaced or cleaned relatively frequently due to being covered in soot. This soot suggests the mix was quite rich in the igniter manifold.

#### *III.5.5 Seeder Port*

Prior to this thesis, the UCC test rig had not been setup to accept seeded airflow. An extra port was needed in the main air supply line in order to get the seed particles into the airflow. Rather than modify the main air supply line to accept seeded airflow, a manifold was created to act as a “T-junction” for the airflow, as shown in Fig. 27 below

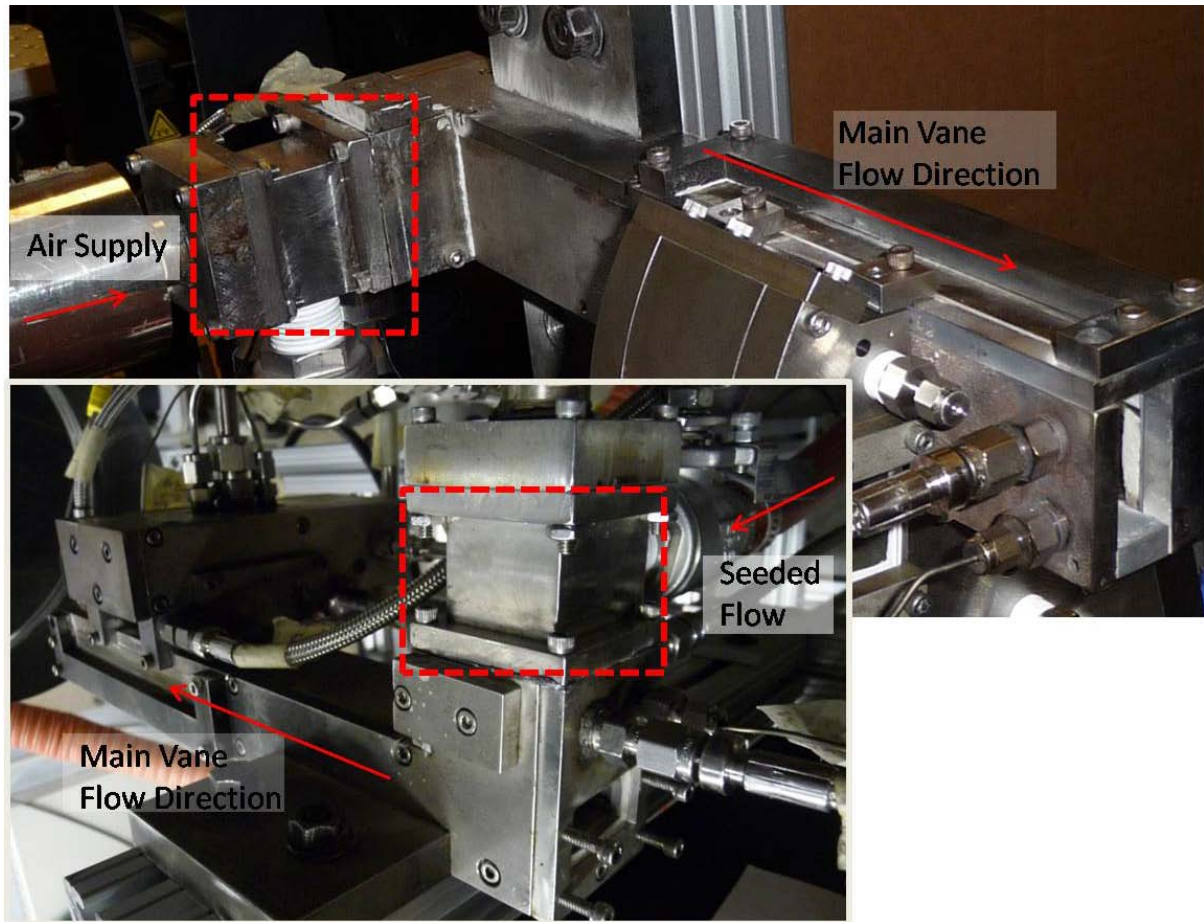


Figure 27. Seeder manifold installed onto the UCC main vane

The connecting hole-pattern was repeated onto this manifold so it could be inserted in-series in between the main air supply and the UCC main vane without modifying the connecting hardware. There is a port on the side of this manifold where the seeded flow enters and mixes with the main airflow at a 90 degree angle. This setup was chosen so the UCC test rig would be able to accept seeded flow into the main air line, or be returned to its original configuration by inserting or removing a ported manifold between the main air hook-up and the UCC main vane.

### III.6 Particle Image Velocimetry Equipment Setup

The PIV equipment is part of a complete kit from Dantec Dynamics. The setup includes the laser with dual Nd:YAG rods, the laser power supply and controller, a flexible optical arm with sheet-forming optics, two cameras, a synchronization unit, the power seeder and its control units, and a computer and monitor.

#### III.6.1 Seeder Setup

The Scitek PS-10 Power Seeder was used to seed the airflow with silicon carbide tracer (SiC) particles. A gas pressurized at 1.5 to 2 times the pressure of the main flow is required to drive the seeder and entrain the seed particles. The high pressure gas enters the chamber, mixes with the seeds and exits through the outlet port. A diagram of this seeder taken from the Scitek User Manual is shown below

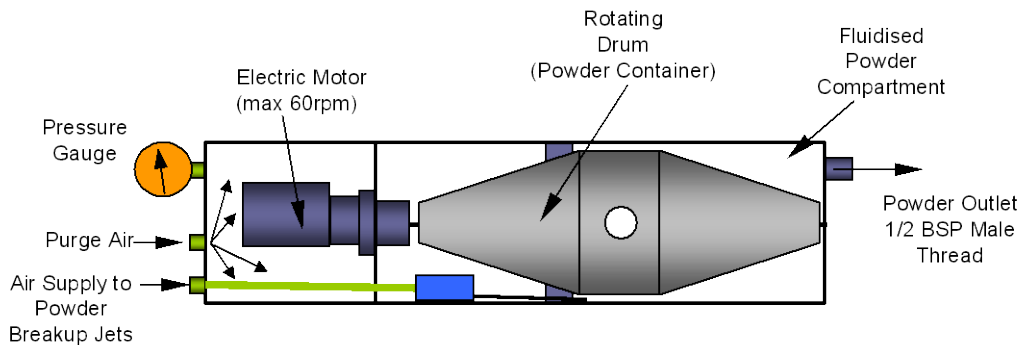


Figure 28. Diagram of PS-10 power seeder (used with permission)<sup>34</sup>

A 2,200 psi nitrogen tank was used to supply the pressurized gas. This seeder operates by spinning a drum filled with seeds to mix the particles. As the drum spins and the single hole approaches the bottom of the cycle, the seeds fall out into the space between the drum and the vessel where the pressurized gas flows by. The operator can increase



the seeding rate by increasing the drum's rotational speed. As the hole in the drum is nearly one centimeter in diameter, the seeder flooded the airflow through the UCC. The seed density was so high that individual particles were indistinguishable. This problem was partially mitigated by turning the drum's rotational speed to its lowest setting. However, this resulted in periodic swells of seeds followed by times of very low seed density. This problem was solved by inserting a plastic cap into the hole. This plastic cap had its center drilled out to effectively restrict the amount of seed particles falling out of the drum on each rotation. With this restricted area, the drum rotational speed was increased, and the particle seeding became steadier. The seeding drums and these restricting plugs are shown in Fig. 29 below.

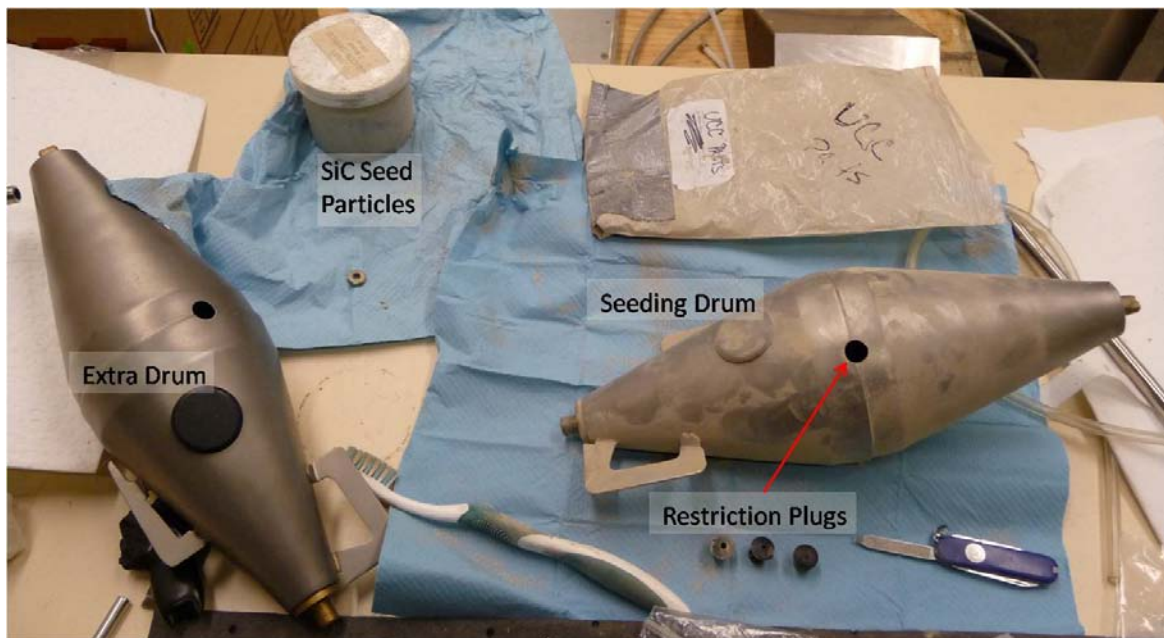


Figure 29. Seeding drums and related equipment

### *III.6.2 PIV Camera Setup*

The Flowsense 4M camera was used for all data acquisition. As discussed in Chapter II, this camera has 2048 x 2048 pixels, which equates to just over four megapixels. It has 8-bit data resolution and a quantum efficiency of 55% at 532nm.<sup>28</sup> It was outfitted with an optical band-pass filter with a center wavelength of 532nm. The camera uses a Nikon 60mm lens to focus incoming light onto its CCD. This lens has no zoom, so the camera must be moved closer to the UCC to enhance the detail of the images. The aperture on this lens, which is similar to an iris, is controlled by changing the f-stop setting. The f-stop is not a direct measurement, but a ratio of the focal length of the lens to that of the aperture. Therefore, lower f-stop values allow more light to pass than higher f-stop. One disadvantage of using a lower f-stop is a more narrow depth of focus. A higher f-stop allows less incoming light, but has a deeper depth of focus. This means “closing down” the f-stop (increasing the f-stop number) reduces the overall light captured. However, the depth of focus (the range of distances in sharp focus) will increase. For the PIV application, lower f-stop settings are advantageous because the signal energy captured on the CCD will be higher. However, the higher signal energy is predicated on the assumption the dual laser sheets are coplanar and the illuminated experimental plane and the camera are translated in unison.

As data was acquired over several weeks, the camera was setup and taken down in between runs. In each setup, the camera was no more than 30 cm away from the UCC. Each time the camera was setup, it had to be aligned and focused. This involved setting the camera on “free run” mode and manually shifting the focus with the f-stop on the lens fully opened. The Nikon lens has f-stops from f/2.8 to f/32.<sup>35</sup> An f-stop of 2.8, the most

open setting, was initially used for focusing the camera on the experimental plane. However, the aperture had to be closed down two settings to an f-stop value of 5.6 for data acquisition. At this higher f-stop setting, the camera was more easily focused as it was translated. The camera and laser sheet were then translated through the four experimental planes to verify the camera was focused on both laser pulses. This alignment and focusing was perhaps the most time consuming part of the PIV setup procedure. The figure below shows a red dashed box around the approximate field of view for the camera. This field was the location where all PIV data was taken. The results presented in Chapter IV were taken in the region traced in the dashed red line.

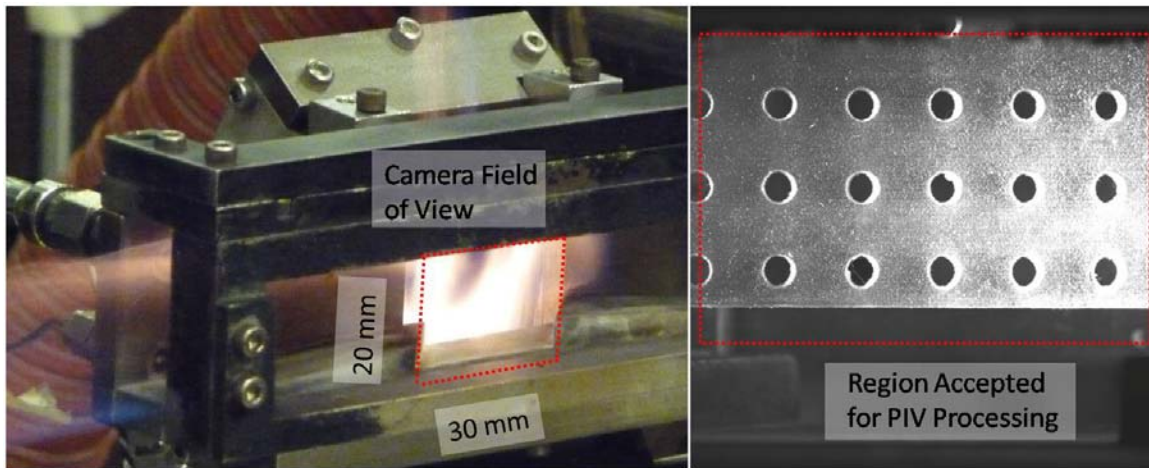


Figure 30. Approximate camera field of view on the UCC (left); calibration image showing region of image used for PIV processing (right)

Even after switching to the COAL Lab's custom optics, the two laser pulses were not entirely collinear. The PIV laser is effectively two lasers in one package. There are two Nd:YAG rods producing laser light that is then sent through the same optical path. Ideally, these two lasers appear to be a single double-pulsed laser. The small

misalignment between the pulses was verified by firing each laser independently and observing the difference in their locations. Particles would appear to be in focus in one image but out of focus in the second image. Although the camera lens allows less light onto the CCD, the f-stop was closed down to 5.6 for the majority of the runs. The laser power had to be increased to compensate for the higher f-stop setting. With a more meticulous and exact experimental setup, a lower f-stop could have been used even with the more narrow depth of focus and the slight non-coplanar nature of the laser sheet. However, the camera's focus was more forgiving at the higher f-stop setting. Consequently, more corresponding particle pairs were found in the cross-correlation resulting in data of higher quality.

Once the camera was properly focused, a calibration picture had to be taken to set the scale factor in the PIV software. The PIV software has no knowledge of the distance between the camera and the experimental plane. It has pictures of particle reflections in the form of 2048 x 2048 pixel light intensity maps. It processes these and outputs the average particle displacement for each interrogation region in terms of camera pixels. The scale factor allows the velocity vectors to be converted from pixels per second to meters per second. Fig. 31 below shows the scale factor being set in Dynamic Studio for one set of runs.

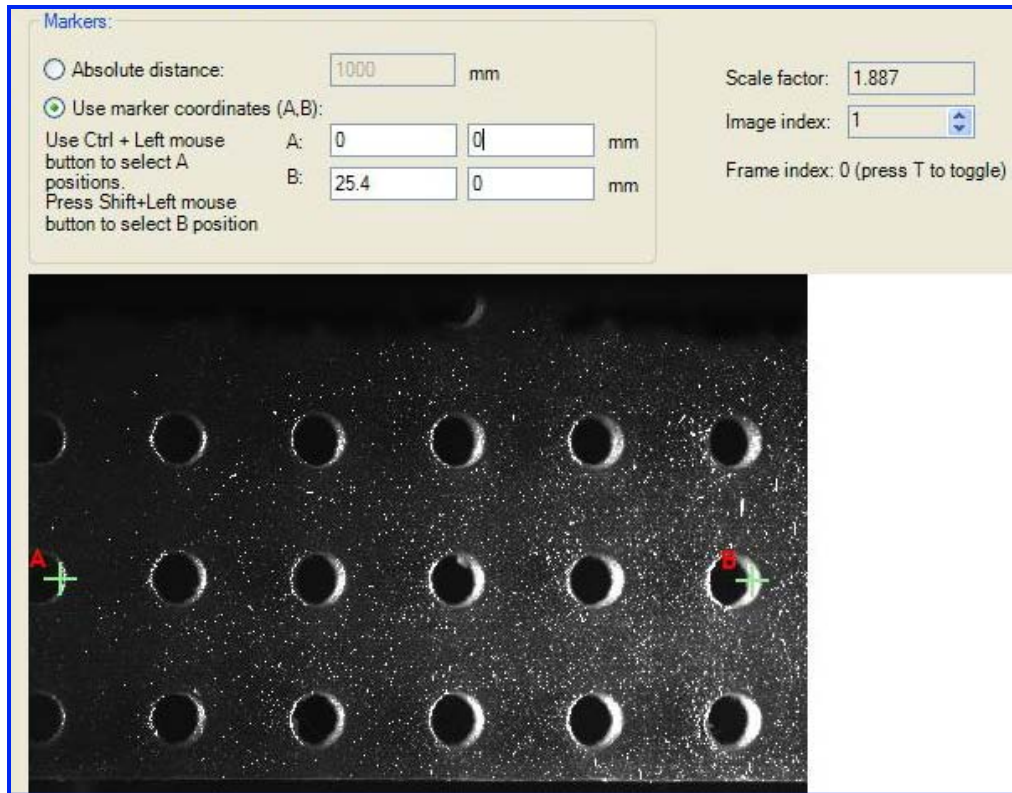


Figure 31. Screen capture from Dynamic Studio's measure scale factor function

The process used to set the scale factor is relatively straight forward. A picture was taken of an object of known dimension and stored as a calibration image. Then, two points are plotted on the image through Dynamic Studio's "Measure Scale Factor" function. The software then takes the coordinates of the input points and determines the scale factor by dividing this input distance by the pixel pitch multiplied by the number of pixels by which the two points were separated. This scale factor is then used to map the coordinate system in the CCD pixel plane to the coordinate system in the experimental plane.

### III.6.3 Laser Equipment Setup

During this thesis, two concurrent experimentations were ongoing. This thesis experiment used particle image velocimetry (PIV) to measure flow velocity; and another student used two-color planar laser-induced fluorescence (PLIF) to measure species concentrations within the UCC. These two experiments were setup in a coordinated manner so they would overlap and require minimal time and effort to switch from running one experiment to running the other. The laboratory setup was continually changing to accommodate the simultaneous experiments, but the basic layout is shown in Fig. 32 below:

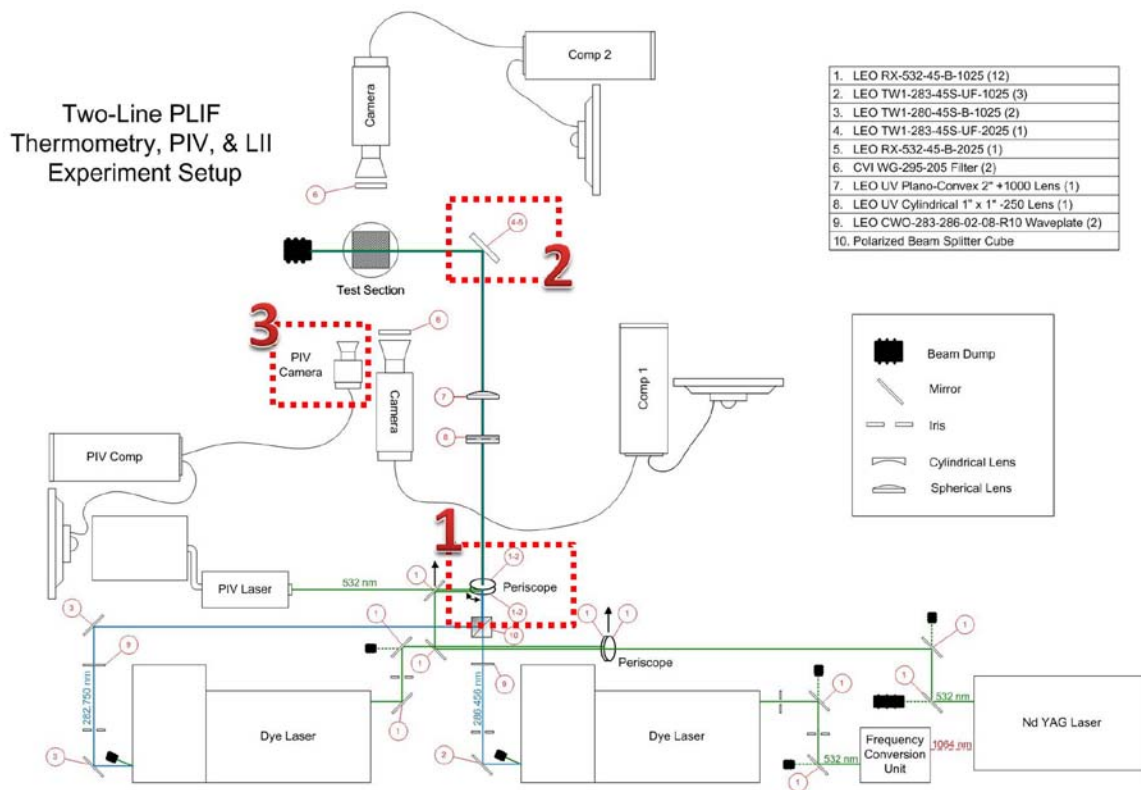


Figure 32. Diagram of equipment used in COAL Lab for PIV and PLIF experiments

As PIV and PLIF are both laser diagnostic methods, some of the equipment is compatible. For example, the optics used to shape the beam into a diverging sheet was shared for both experiments. Three steps, which correspond to the numbered boxes in the figure above, were required to switch the setup from PLIF to PIV:

1. Insert mirror in top of periscope: a periscope of mirrors is used to raise the beam height. The mirrors are designed to reflect at least 99% of 532nm light at a 45 degree incidence angle. When the lab is setup for PLIF, this mirror is taken out of its mount leaving a space through which the laser used for PLIF passes. When setting up the lab for PIV, the mirror at the top of the periscope is inserted into the mirror mount and aligned to direct the laser through the sheet forming optics.
2. Switch the final mirror: shown above in Fig. 32, the red dashed box number 2 is drawn around the final mirror that directs the laser sheet into the UCC test rig. The PLIF experiment is using 280nm laser energy, which is in the ultraviolet region of the light spectrum. Mirrors designed to be highly reflective in the ultraviolet spectrum are not as reflective in the visible spectrum around 532nm. For this reason, different mirrors are required for the different lab setups. The mirror must then be adjusted to direct the light sheet parallel to and into the UCC main vane.
3. Position the PIV Camera: the Flowsense 4M camera is then put into its mount and its lens is focused on the experimental plane. Both the final mirror (box#2) and the camera (box#3) are positioned on translation tables and moved in concert so the experimental plane is swept along the UCC main vane. The camera must be focused on the laser sheet in more than one position to ensure accurate focusing.

With these three steps accomplished, the lab is setup to run PIV measurements in the UCC test rig as shown below in Fig. 33.

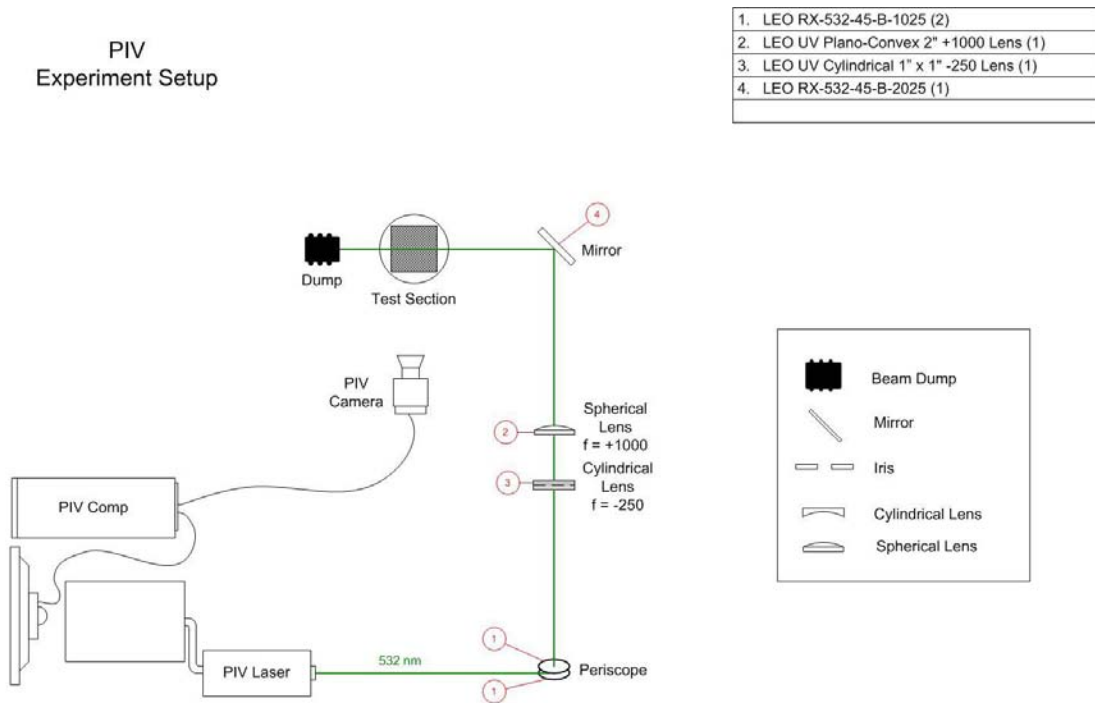


Figure 33. Diagram of PIV experimental setup

#### III.6.4 OEM Optics

The laser unit's internal optics are designed to overlap the pulses from each Nd:YAG rod so they are collinear, with approximately a 6mm diameter.<sup>26</sup> The laser energy is then reflected up into a swiveling 3-joint arm that allows the beam to be positioned without moving the laser unit. The light is then diffracted through a semi-cylindrical lens and diverges at an angle of 28°.<sup>36</sup> Much time and effort was spent aligning the laser. This alignment improved the laser's performance, most notably at the low power setting. A photodiode was used to quantify the average power output of the



laser at its maximum repetition rate of 15Hz. At maximum power the Solo 200XT Nd:YAG laser emits 200 mJ of 532 nm electromagnetic radiation per pulse.<sup>37</sup> At a 4 ns pulse width, 200 mJ corresponds to 50 MW of peak power, but only over those 4 ns. At the maximum pulse repetition rate of 15 Hz, the 200 mJ equates to an average power of three Watts. The results from the laser power study, presented in Fig. 34 below, show a maximum average power of 2.99 W. This supports that the laser was operating to its specification.

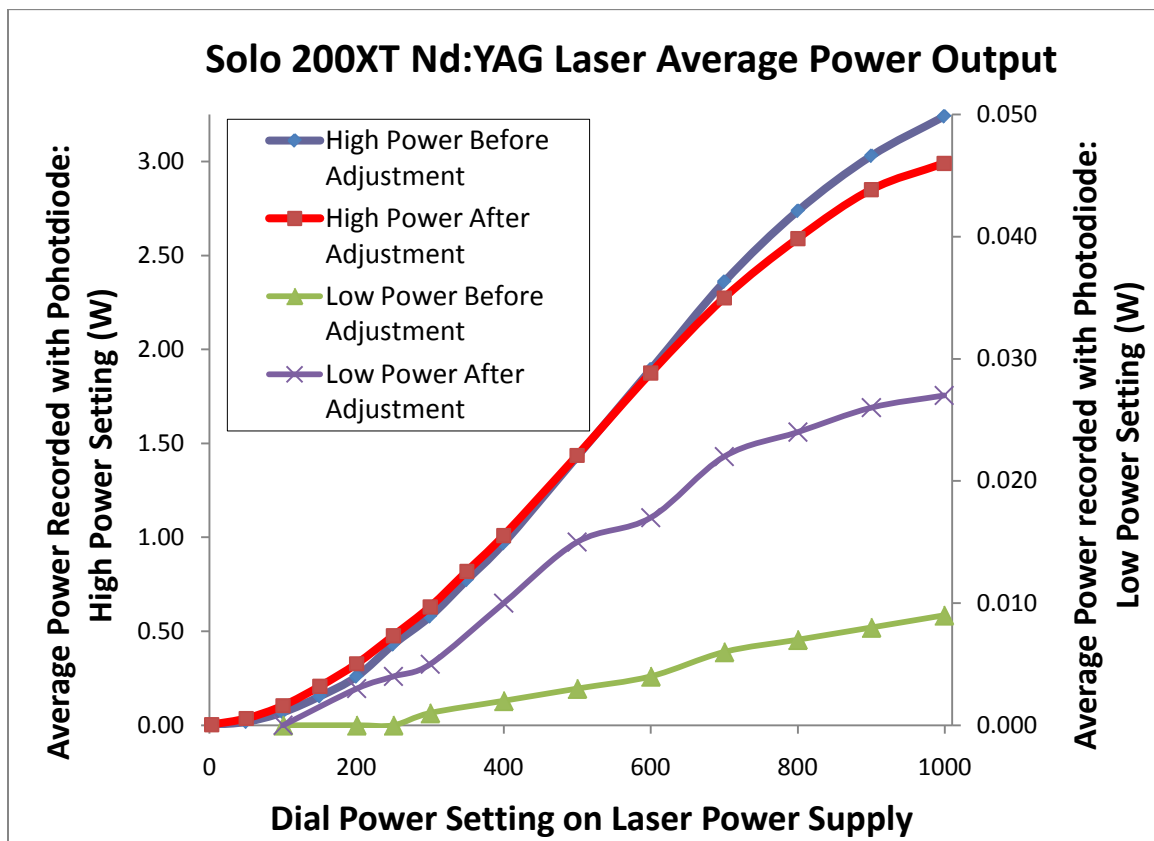


Figure 34. Plot of laser average power at max repetition rate of 20 Hz

In Fig. 34 above, the vertical axis on the left corresponds to the average power recorded at the “high” power setting. The vertical axis on the right has been scaled so that the

“low” power setting results can be shown on the same plot. The improved alignment appeared to enhance the beam quality of the laser. When directed back into the swiveling arm, the sheet was thinner with a more constant thickness. However when the swiveling arm moved, the quality of the laser sheet varied dramatically. The specified laser sheet thickness of 6 mm was observed after alignment, but this thickness increased to approximately 10 mm when the linear translator caused the reflective arm to move. As the problem seemed to present when the arm was moved, the most likely cause of this problem was poor alignment of the mirrors mounted at each swiveling joint. The arm was partially disassembled to try to better align these mirrors as shown in Fig. 35 below.

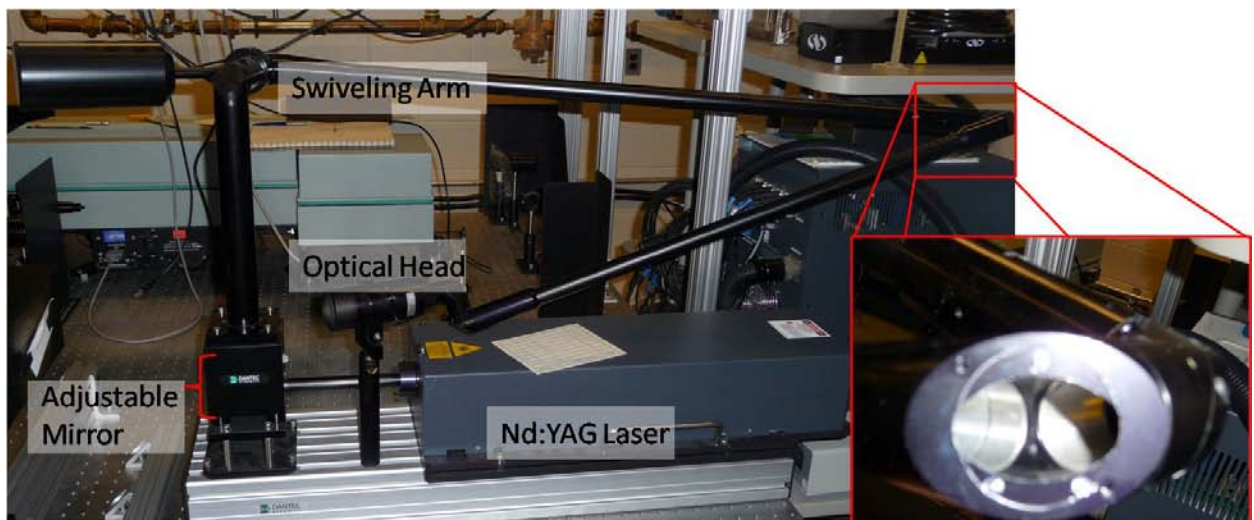


Figure 35. PIV laser with original optics

These mirrors cannot be adjusted because they are mounted with glue. After discovering this issue, the decision was made to abandon the swiveling arm and accompanying optics in favor of custom optics.

### III.6.5 Custom Optics

The laser energy produced by the Nd:YAG comes out as a beam. The beam is then passed through the center of an iris that blocks the highly divergent light. It then hits the base mirror on the periscope reflecting it 90 degrees upward. The top mirror on the periscope reflects it another 90 degrees directing it into the sheet forming optics. Fig. 36 below is a picture of the optics train with a green line superimposed to represent the laser path.

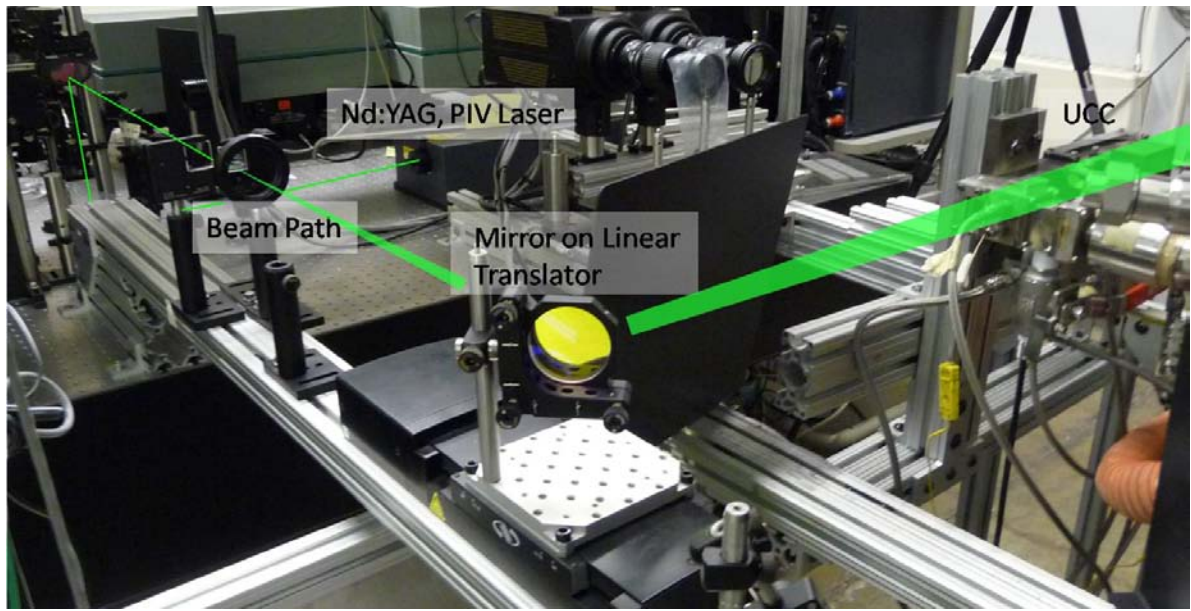


Figure 36. Mirror mounted on linear translator with laser path in green

A half-cylindrical lens and a spherical lens are used to shape the laser beam into a sheet. The half-cylindrical lens is planar on the back side and is convex in the shape of a half-cylinder on the front side. It has a focal length of -250 mm, meaning that the focal point is 250 mm behind the lens. This lens causes the beam to diverge in the plane perpendicular to the lens and parallel to the incoming beam. It takes in a beam of circular

cross-section and outputs a beam of elliptical cross-section expanding in its semi-major axis as the beam propagates.

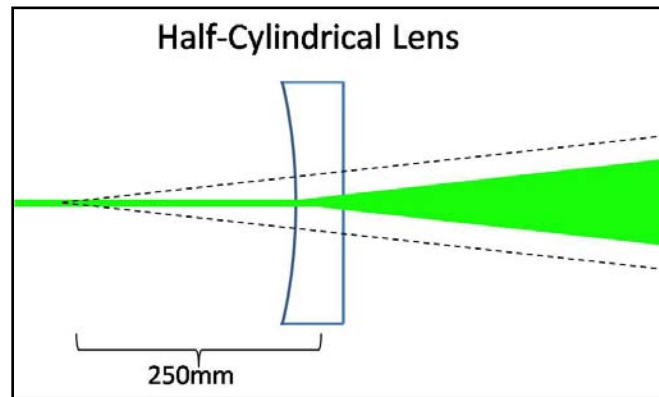


Figure 37. Side-view of a half-cylindrical lens

After passing through the half-cylindrical lens, the beam is diverging from the side view, but is approximately the same width from the top view. This width is the thickness of the laser sheet and must now be focused to form a thin sheet at the experimental plane. The figure above shows a side-view of a half-cylindrical lens that creates divergence in a beam. The figure below shows a top-view of how a half-spherical, or “plano-convex” lens will focus a beam of elliptical cross-section into a thin sheet. Prior to going through this lens, the beam has an elliptical cross-section with an expanding semi-major axis. After passing through this lens, the beam’s cross-section is still an ellipse with an expanding semi-major axis, but now the semi-minor axis begins to decrease as the beam propagates. This causes the laser sheet to thin until it reaches the focal length of 1000mm. After reaching the focal length, the beam will again begin to diverge. For this reason, this lens is located one meter from the UCC test rig as measured by the laser path-length.

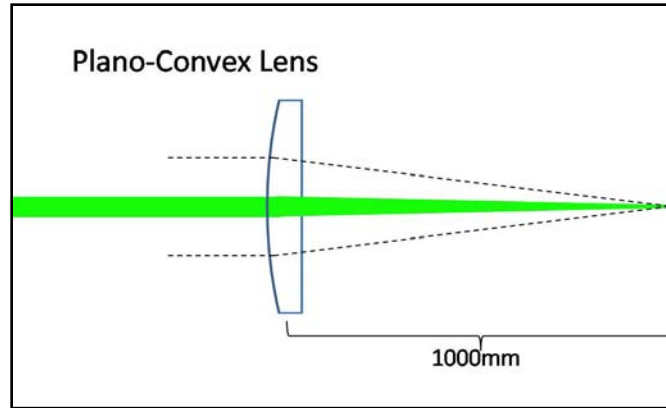


Figure 38. Top-view of a plano-convex lens

After passing through the plano-convex lens, the beam hits the final mirror and is redirected toward the UCC test rig. This last mirror is located on a translation table that moves back and forth to translate the laser sheet along the inside of the UCC test rig. In summary, the beam emanates from the laser with a circular cross-section, is redirected with mirrors, passes through two lenses that shape the cross section into an ellipse with an increasing aspect ratio of height to width, and is sent into the UCC test rig where it illuminates the experimental plane. In using the custom optics train, the laser sheet appeared more even in power distribution. The sheet thickness was measured at 3 mm and did not vary with translation of the experimental plane. This was a significant improvement from the 6 – 10 mm sheet thickness produced by the original laser reflecting arm. As the UCC main vane is 14 mm in width, the new 3 mm laser sheet thickness was more conducive to taking measurements at discrete planes.

### *III.6.6 Pulse Delay Study*

The final step in setting up the PIV equipment was to perform a pulse delay study. This step must be performed last because it involves taking actual PIV data in the test

configuration. At this point the UCC is setup and plumbed with the airflow and seed particle lines, the laser is aligned, the camera is focused and the scale factor in the PIV software has been set. The last remaining variable for conducting PIV is the pulse delay. As described in Chapter II, the pulse delay is the time between the two laser pulses and their corresponding camera frames. This value must be matched to the flow velocity so the seed particles are close enough over the two frames to be correlated. Although the purpose of PIV is to measure flow velocity, the operator must have some knowledge of the flow velocity beforehand to set this pulse delay. An estimate of the bulk velocity in the main vane is determined by using the equation defining steady mass flow rate and the equation of state for a perfect gas.

$$\dot{m} = \rho AV \quad (12)$$

$$P = \rho RT \quad (13)$$

The temperature and pressure are measured with pressure transducers and thermocouples. These two values are used to find density. The mass flow rate for the main air supply is set by the flow controllers. At the exit plane, the UCC main vane is 30.5 mm in height and 14 mm in width.

The bulk flow velocity is then found by dividing the mass flow rate by the density and the flow area. This velocity determines the estimated pulse delay for a given interrogation region size and a field of view for the camera. The width of the camera's field of view (38 mm) is divided by the number of interrogation regions (32) making up the field of view. This distance, 1.19 mm is the width of one interrogation region. It is then divided by four, since the flow should not move more than one quarter of the width of the interrogation region over an image pair. This distance divided by the bulk velocity

results in the time it will take for a particle moving at the calculated bulk velocity of the flow to move one quarter of the width of an interrogation region. This value is divided by the square root of two, the root mean square value. This result is approximately 70.7% of the time it would take for a particle to travel the equivalent distance of one quarter of an interrogation region (16 pixels) if it were traveling at the bulk flow velocity measured by the mass flow meter, pressure transducer, and thermocouple. The results for these calculations are shown in purple for the hot runs and red for the cold runs in Fig. 39 below:

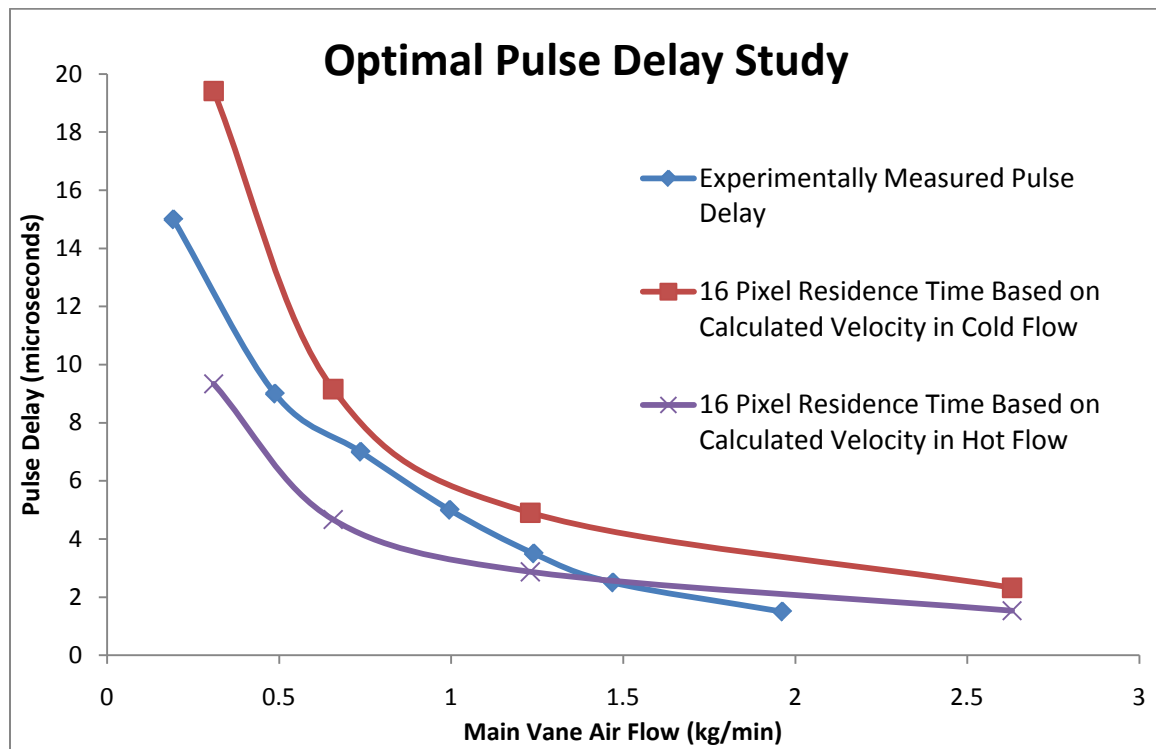


Figure 39. Pulse delay study

The calculation of velocity, described in the previous paragraph, makes a critical assumption that the mass flow rate at the exit of the main vane is the same as the mass

flow rate going into the main vane. This assumption oversimplifies the situation because there are two airflows moving through the UCC. The amount of main airflow which spills out into the cavity flow relative to the amount that remains in the main channel is unknown. This same parameter is also unknown for the cavity flow. For this reason a more experimental pulse delay study was also performed. The results of this study are shown in blue with 'x' symbols marking the data points in the figure above. In this study, several sets of PIV data were taken with varying pulse delays for each mass flow rate in the main vane. The raw data was then observed to determine which pulse delay resulted in the appropriate particle displacement. Fig. 40 below shows a single frame from the raw data used in the pulse delay study.



Figure 40. PIV raw data used in pulse delay study



The rectangular body in the lower left corner of Fig. 40 above is the cavity in the main vane, which is also called the radial vane cavity. The bright vertical line near the left edge of the picture is the corner reflections of the cavity vane. The rest of the small dots are reflections of the Nd:YAG laser energy off the SiC seeder particles. These reflections are the intended raw data. Fig. 41 below shows a side-by-side, zoomed-in view of a single interrogation region for an image pair.

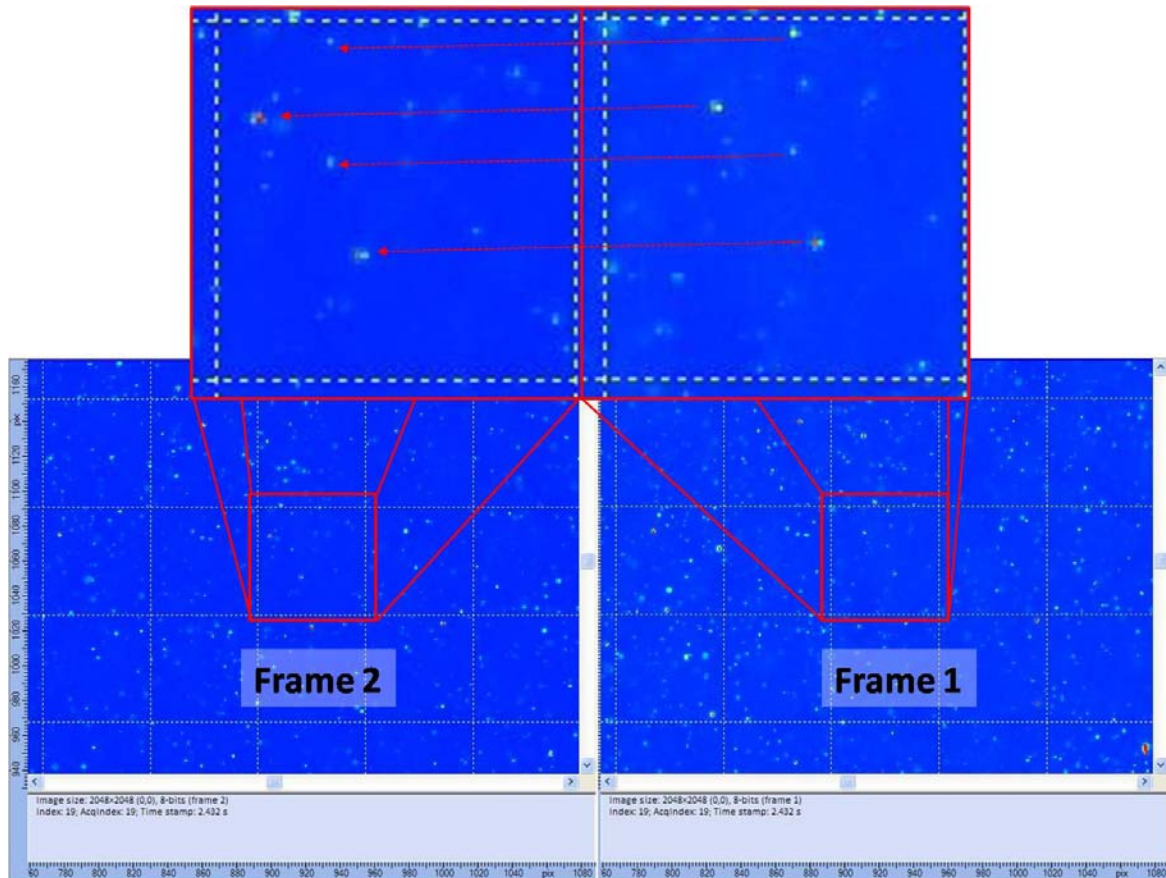


Figure 41. Enlarged view of a single interrogation region for an image pair

By simple observation, particle displacement can be seen at less than one quarter of the width of the interrogation region. This observation is an example of a properly set

pulse delay. If the pulse delay were set too short, the images would appear identical or with very small particle displacement. If the pulse delay were set too long, there would be no recognizable pattern, as the particles from the first image would be displaced beyond the boundaries of the interrogation region by the time the second image was captured. The results from this study were used in setting the pulse delay for each experimental run.

### **III.7 Data Processing**

As described in Chapter II, Dynamic Studio® does not perform direct cross-correlation for each interrogation region, but rather uses the Fast-Fourier Transform (FFT) to find correlation peaks. This process decreases computational time, but introduces potential errors mainly around the boundaries of the interrogation regions. The boundaries of these regions are inherently more susceptible to other forms of error such as loss of pairs. For these reasons, the data quality is sensitive to the method by which the cross-correlation algorithm is implemented. The four parameters used to maximize the efficacy of the cross-correlation were: (1) interrogation region size, (2) amount of overlap, (3) window weighting function, and (4) filtering function.

#### *III.7.1 Interrogation Regions and Overlap*

Due to the underlying assumptions made in the implementation of the FFT algorithm, the size of the interrogation regions is constrained to square dimensions. The Dynamic Studio® software offered regions of the following sizes as measured in camera pixels: (1) 16 x 16, (2) 32 x 32, (3) 64 x 64, or (4) 128 x 128. The factors which must be

considered when setting the interrogation region size are seed density, the smallest flow structures under investigation, how dynamic the flow velocity is, and processing time. Smaller interrogation region sizes allow for higher resolution of flow structures, as only one velocity vector is determined for each region. Using smaller interrogation regions in the cross-correlation analysis is analogous to taking more measurements of the flow. The limiting factor for interrogation region size in this thesis was particle seeding density. In order to maintain at least five particles per region, interrogation regions needed to be approximately 1 mm in width corresponding to 64 pixels. This relatively large interrogation region size allowed for more consistent seed density. It also allowed for more dynamic velocity measurements and quicker processing time. However, this window size appeared to be too large to adequately capture the dynamic flow structures near the cavity in the main vane. Even with smaller interrogation regions, the maximum frame rate of 7.4 Hz appeared to be inadequate to capture the highly unsteady flow in this region.

The overlap of interrogation regions is meant to mitigate the loss of data around the boundaries of these regions. The data near the boundaries is often lost and is also intentionally ignored with weighting and filtering functions. In order to capture the data otherwise lost in the regions near the boundaries, the interrogation regions are set to overlap by a user-specified amount. Based on recommendations made by the Dantec User Manual<sup>26</sup> and the specific weighting function, which will be described in the next paragraph, the overlap was chosen to be 50%. Cross correlation is performed on a 64 x 64 pixel region with the next region starting on the 33<sup>rd</sup> pixel instead of the 65<sup>th</sup> pixel. In this way, 50% of the data in the previous region is analyzed in the next cross-correlation.

### III.7.2 Filters & Window Functions

Several filters can be applied after the cross-correlation implementation. These techniques are limited in that they can only eliminate data deemed to be invalid by user input after the cross-correlation has generated the velocity maps for each image pair. However, there are two algorithms applied during the cross-correlation that improve the method's efficacy – a window weighting function and a data filter. As previously discussed in the camera section, each pixel in the camera's charge-coupled device (CCD) registers the intensity of light it absorbed as an 8-bit value. When analyzing an interrogation region from an image pair, the computer is comparing two 64 x 64 matrices of these 8-bit values for similarity. The degree by which these matrices are similar is known as the “correlation coefficient.” The cross-correlation technique measures the similarity of each value in the matrices with no bias. A window function applies a bias based on the location with respect to the boundaries of the interrogation region. This technique is useful because image correlation is known to be more accurate in the center of an interrogation region compared with its boundaries, as the “loss of pairs” phenomenon is less likely to occur there.

The Gaussian window function weights each value in the matrix by a number between zero and one based on the distance from the center of the interrogation region, where the pixel position  $(m,n) = 0$  is the center of the region. The variables  $M$  and  $N$  are the size of the interrogation region (64 x 64). The equation for the Gaussian window function is:

$$W(m,n) = \exp \left[ - \left[ \frac{1}{k} \right]^2 \left( \left( \frac{2m}{M} \right)^2 + \left( \frac{2n}{N} \right)^2 \right) \right] \quad (14)^{26}$$

The value 'k' is set by the user and specifies the strength of the window function. The maximum k-value of 1.19 was used for the processing of all data in this thesis. This value allows for the greatest window width, largest maximum particle displacement, and least aggressive filtering near the boundaries of the interrogation region. In implementing this window function, the influence of the value of the camera pixel closest to the center of the interrogation region remains nearly constant, while that of the value of the pixel farthest from the center will be reduced to 25.4% of its original influence. For reference, the most aggressive k-value of 0.71 would have reduced the influence of the value of the outermost pixel to 2.14% of its original strength.

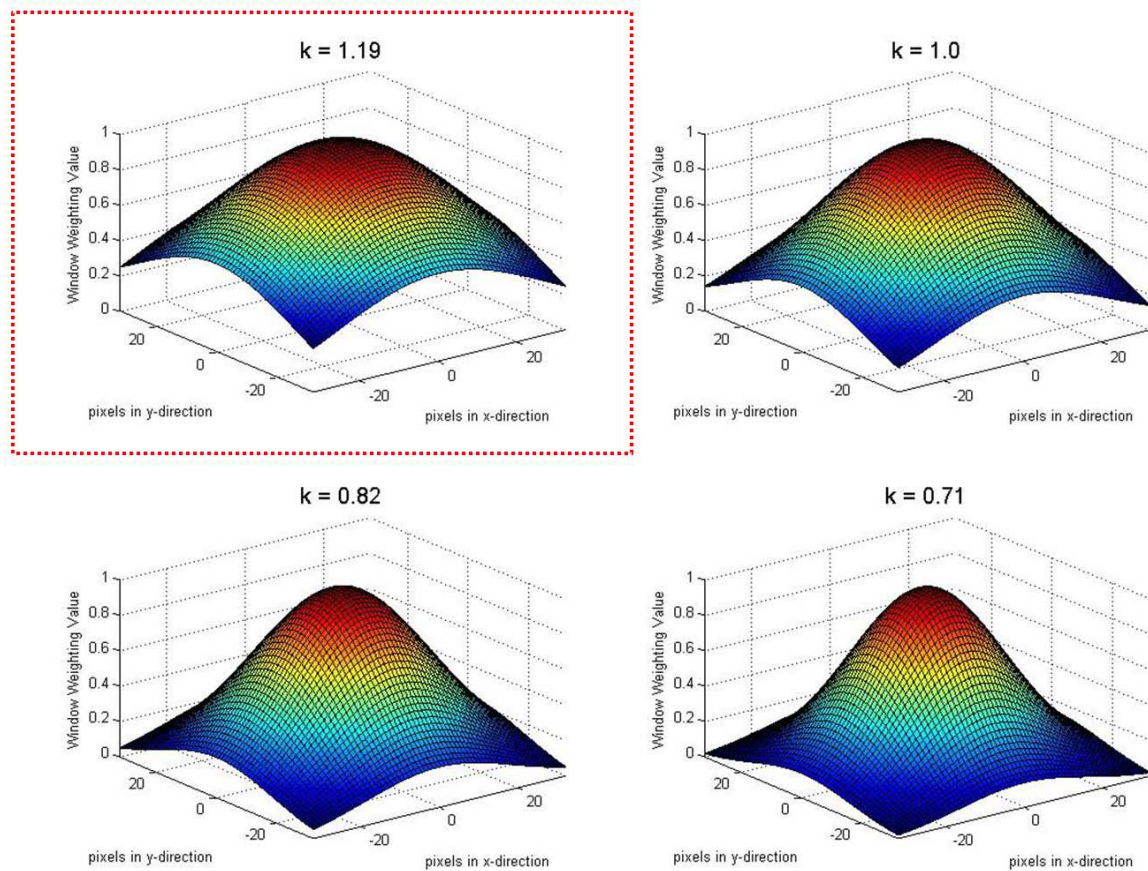


Fig. 42. Graphical Representation of the Gaussian Window Weighting Function

Fig. 42 above is a surface representation of the Gaussian window-weighting function coefficients over a 64 x 64 pixel interrogation region. There is a red dashed box around the top left subplot as it was the one used in processing. It shows the influence coefficients by which the values are multiplied at each point in the interrogation region. These coefficients effectively bias the cross-correlation measurement toward the center where error caused by loss-of-pairs is known to present less frequently.

The “No-DC” filter function is less complex than the Gaussian window function. It reduces the “noise-floor” by eliminating the signals corresponding to zero velocity. It eliminates these signals by multiplying the corresponding Fourier coefficient by zero.<sup>26</sup> Much of the background noise as well as the thermal noise in the camera is time-invariant. This function sets the pixel’s registered value to zero if it is the same in both image pairs.

$$W(u,v) = \begin{cases} 0 & \text{for } (u,v) = (0,0) \\ 1 & \text{otherwise} \end{cases} \quad (15)^{26}$$

The UCC test rig is made of 316-stainless steel, which is fairly good at scattering the 532 nm laser energy. Since the laser sheet is expanding as it propagates through the UCC, there is a significant amount of the sheet reflecting off and is scattered by the UCC walls. If the laser sheets from the two pulses are perfectly aligned, much of this reflected light will appear to be identical in both frames and will be eliminated with the “No-DC” filter.

### *III.7.3 Validation Techniques*

After processing the raw data with the cross-correlation algorithm, the resulting velocity vector maps were processed with two validation techniques. These validation techniques are designed to filter inconsistent data. They require the user to estimate what values to accept and which to reject. This involves an iterative approach where the user applies the validation technique to a set of vector maps and observes the results. The technique is then adjusted to be less or more aggressive to ensure obvious inconsistent data is filtered. Because a high degree of user input can shape the data, the specified same set of filters and validation techniques were applied for all data.

The first technique applied was range validation. This is a basic filter rejecting any vectors outside the user-specified limits. The limits applied in this filtering in m/s, were: (1)  $0 \rightarrow 125$  for the overall vector length, (2)  $-100 \rightarrow 10$  for the streamwise component, and (3)  $-25 \rightarrow 25$  for the spanwise component. Any velocity vectors outside this region were rejected. The primary flow direction was in the negative streamwise direction relative to the PIV coordinate frame.

The second technique applied was peak-to-peak validation. This filter rejects any vectors formed by correlation peaks less than a specified amount larger than the next highest peak. Cross-correlation will always result in an output of the highest peak correlation, even when there is poor correlation. On average, cross-correlation will result in several random peaks of similar magnitude when measuring noise. The underlying idea of this validation technique is that when the correlation peak is not significantly higher than the next largest peak, it is more likely to have resulted from correlating noise instead of valid signal pairs. All vector maps were filtered with this validation technique

to reject any velocity vectors generated from correlation peaks that were not at least 20% higher than the next highest peak.

Summarizing the data processing up to this point:

- The camera records pairs of images and the computer stores 8-bit intensity values from each of the 2,048 x 2,048 pixels.
- These light intensity values are partitioned into overlapping sets of 64 x 64 matrices
- Values in each matrix are then weighted based on their relative position with respect to the center of the interrogation region. The value for this Gaussian window function was  $k=1.19$ .
- Any values identical in both images are then deleted with the “No-DC filter.”
- An image shift corresponding to average particle displacement is generated with a cross-correlation algorithm based on Fast-Fourier Transforms of the image intensity maps.
- This average particle displacement for each interrogation region is divided by the pulse delay to create the velocity vectors.
- The maps of velocity vectors are then filtered based on their component’s magnitudes and the relative size of the correlation peak used to create them.

At this point, there were up to 74 velocity maps for each test case. These velocity maps show only snapshots of the velocity field over relatively discrete regions of time.

However, when viewing them sequentially at the sample rate, 7.4 Hz, one can see how the flow moved and changed.



The Dynamic Studio® software was used to analyze the velocity maps using the “Vector Statistics” function. This function compares the respective velocity vectors from each map to determine the average velocity vector, standard deviation, and the number of valid vectors at each point. These statistics are then used to find turbulence intensity, vorticity, and statistical error.

### **III.8 Uncertainty Analysis**

An uncertainty analysis is designed to estimate the “degree of goodness” of measured data, as well as results and conclusions drawn from that data. It is defined by Coleman<sup>38</sup> in Experimentation and Uncertainty Analysis for Engineers as, “the analysis of the uncertainties in the experimental measurements and results.” Due to the imperfect nature of experimentation, real instruments are not able to measure the true value of a parameter without some level of error. The true value of a measured parameter is typically unknown; the engineer has only the measured value. Quantification of uncertainty in an experiment allows for the results and conclusions to be prefaced with their level of accuracy. If an identified trend shows an effect outside the bounds of the uncertainty level, it is likely to have resulted from some actual phenomenon, whereas any trend measured within the bounds of uncertainty could have resulted from the underlying system noise and measurement error.

Uncertainty can be divided into its contributing components, systematic and random, and assessed separately. The systematic error, also known as measurement bias, can usually be reduced by instrument calibration. Random error, also known as precision error, is limited by the quality of the instrument and cannot be “calibrated out.”<sup>38</sup> The

only way to reduce this error is by taking several measurements. An infinite number of readings would result in a random error average equal to zero. The uncertainty due to precision error is inversely proportional to the square root of the sample size.<sup>38</sup> Both the bias error ( $B_j$ ) and precision error ( $P_j$ ) for each instrument are quantified in the same way:

$$\text{Bias Error:} \quad B_j = \left[ \sum_{k=1}^M (B_j)_k^2 \right]^{1/2} \quad (16)^{38}$$

$$\text{Precision Error:} \quad P_j = \left[ \sum_{k=1}^M (P_j)_k^2 \right]^{1/2} \quad (17)^{38}$$

These quantities are multiplied by their influence coefficients and their root-mean-square (RMS) is calculated. This results in the total bias and precision errors. Then, the RMS of the total component errors is then calculated to determine the total uncertainty in the experiment.

An uncertainty analysis was performed but due to the nature of the experimental setup proved to be difficult leaving some uncertainty not quantified. Specifically, there was no direct method of measuring these errors against a standard for two of the main factors in this thesis – the main and cavity mass flow rates. Instead of a calculated uncertainty for each flow condition, the overall level of instrument fluctuation was measured to approximate the bounds on some of the experimental factors.

### *III.8.1 Mass Flow Rate Variability Study*

The primary factors under investigation were the air mass flow rates and the cavity equivalence ratio. According to their product data sheet, the Alta Mass flow controllers are accurate to  $\pm 1\%$  of the set point from 20 to 100%.<sup>39</sup> Each flow channel is regulated by an active mass flow controller, which reduces the effective area of the flow

path through a valve. This is known as a throttling process in thermodynamics. When a mass flow rate was set, it would then take approximately 20 seconds before a semi-steady value was reached. Further, an error would remain between the set value and the actual mass flow rate even after the flow became semi-steady. With the complexities of this system in mind, a more straightforward variability study was performed in lieu of the traditional uncertainty analysis.

This airflow variability study was performed by setting the cavity and main airflow rates to each value in the experimental test matrix. The flow was then allowed to equilibrate, which typically took from 20 to 30 seconds. Afterwards, the flow rates' maximum and minimum values were recorded.

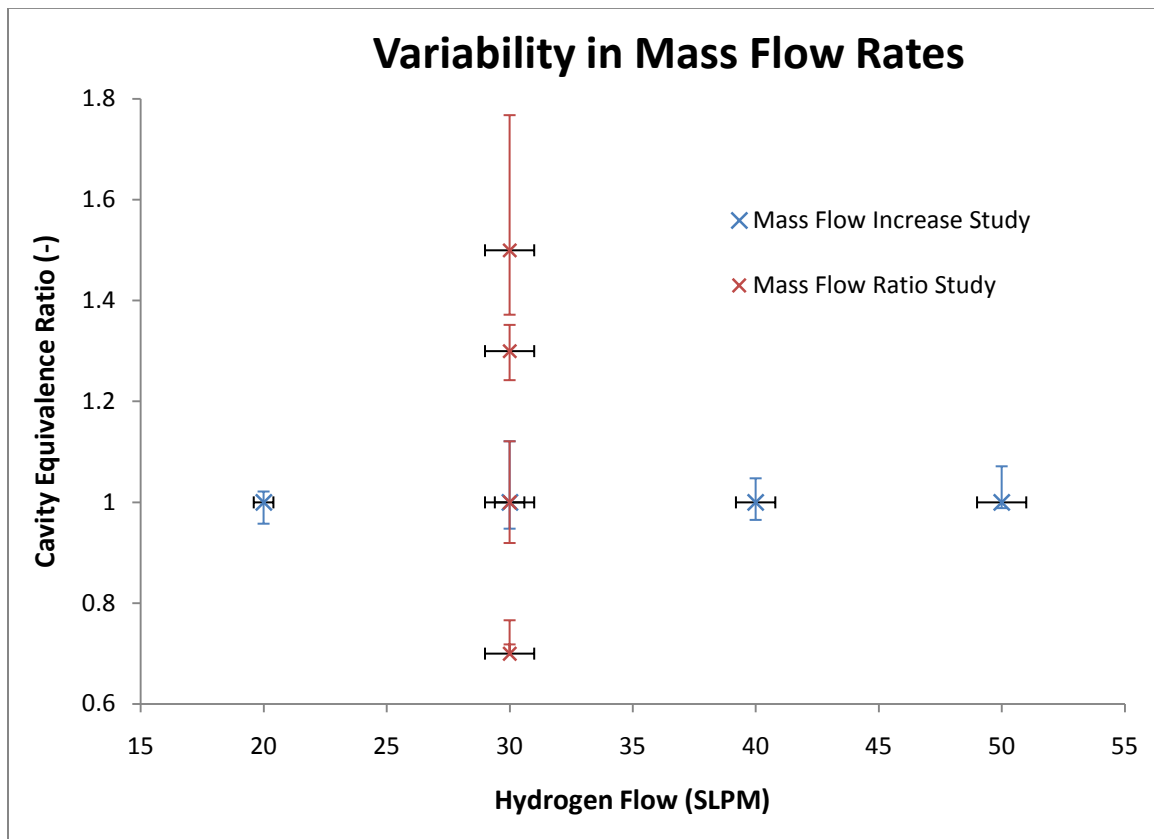


Figure 43. Results from air mass flow variability study

The vertical error bars display the resulting variability in the equivalence ratio for an error in the cavity mass flow rate. The horizontal error bars show a constant  $\pm$  one percent error in the hydrogen mass flow rate. The hydrogen mass flow controller proved to be the limiting factor in setting flow rates. In the mass flow ratio study, the hydrogen was set to 30 standard liters per minute (SLPM), and the equivalence ratio ( $\phi$ ) was increased by decreasing the cavity mass flow rate. For  $\phi=1.5$ , the cavity flow rate was set at 0.0613 kg/min. At this low flow rate, the system seemed to be near its lower limit of operability. This limit can be seen in the figure above, as the error bars for the  $\phi=1.5$  point are the largest, indicating a wide variability of mass flow rates.

This study did not reveal the actual uncertainty limits for a set confidence interval. However, it did allow for basic quantification of the results. When the flow conditions were set for an experimental run at an equivalence ratio of 1.0, the actual equivalence ratio was between 0.92 and 1.12, based on the observed variability of the mass flow rates. This range was calculated by taking the root-mean-square of the effective error in the equivalence ratio caused by the variability in air mass flow as well as the published uncertainty value for the mass flow controllers. These ranges are shown in the table below.

Table 6. Observed variability in equivalence ratio

Equivalence Ratio	Lower Bounds	Upper Bounds
0.7	0.68	0.77
1	0.92	1.12
1.3	1.24	1.35
1.5	1.37	1.77

The other primary variable was the ratio of cavity air to main air mass flow rate. The ratios under investigation were 0.05, 0.1, 0.15, and 0.2, which correspond to cavity air mass flow rates 5%, 10%, 15%, and 20% of the main air mass flow rate. As neither the main nor the cavity air mass flow rates were constant, there was a range of ratios at each set condition. This variability is shown in Fig. 44 below.

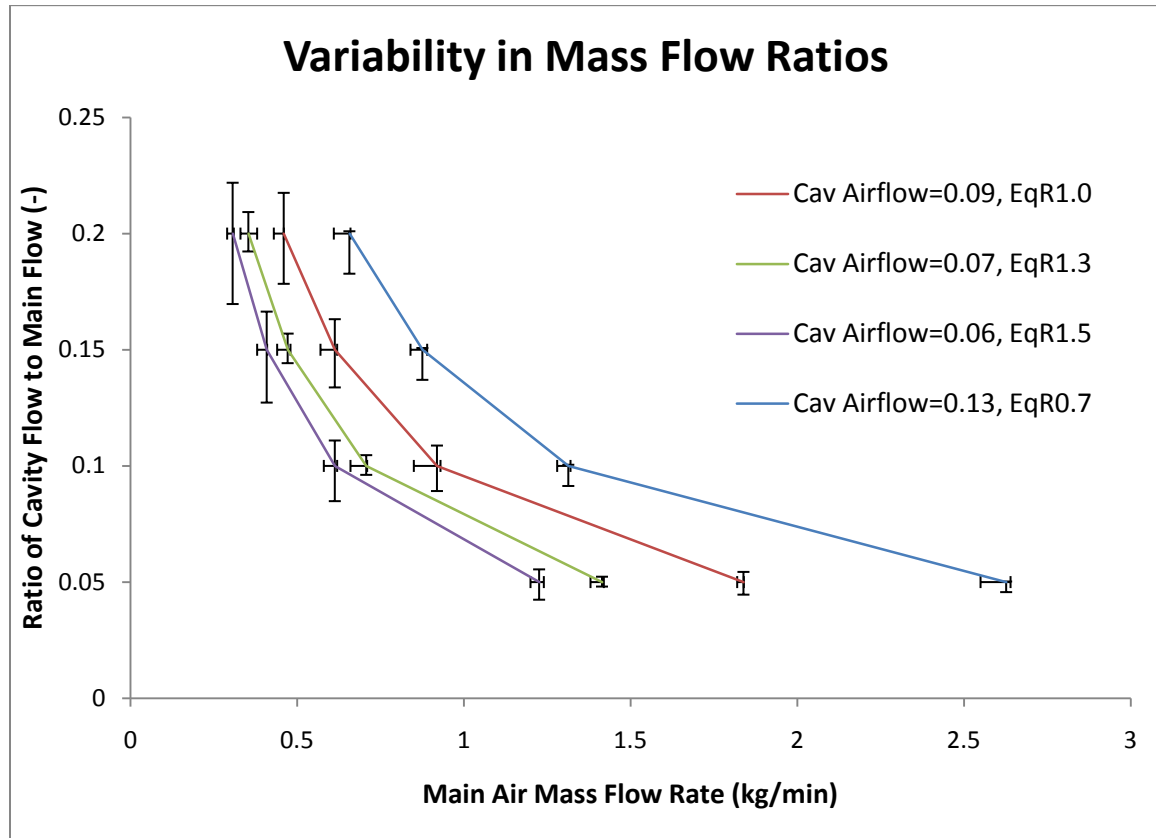


Figure 44. Variability in air mass flow rates

In this figure, the vertical error bars represent the variability in the ratio caused by error in the cavity flow rate. The horizontal error bars represent the variability in the ratio caused by error in the main air mass flow rate. The most significant conclusion that was drawn from this mass flow variability study was that the higher mass flow rates had less

variance. Therefore, results and conclusions drawn at the higher mass flow rates will have a higher “degree of goodness” with respect to those at lower flow rates.

### III.8.2 Statistical Accuracy

In addition to inaccuracies in experimental measurement, there is also a degree of inaccuracy from random sampling. PIV measurements are not continuous, but discretely sample the flow field recording only a portion of the tracer particle locations. The statistics of laser velocimetry depend on the velocity of the light scattering particles which are generally randomly distributed. This generally random distribution results in a random sampling of the velocity.<sup>40</sup> The measurement rate was 7.4 Hz for all testing. Depending on the case, either 50 or 75 measurements were taken. Even if each of these measurements were perfectly accurate, inherent error remains from sampling. This statistical error is calculated using the following formula:

$$\bar{u}_{error} = \pm \frac{Z\sqrt{\bar{u}^2}}{\sqrt{N}} \quad (18)^{42}$$

$$Percent \bar{u}_{error} = 200 * \frac{Z * \sigma_{rms}}{U\sqrt{N}} \quad (19)$$

In the above equation  $\bar{u}$  is the average measured velocity,  $\sqrt{\bar{u}^2}$  is equal to  $\sigma_{rms}$  (the standard deviation), N is the number of valid measurements, U is the mean velocity, and Z is the “standard score” value of 1.96 corresponding to a 95% confidence interval (CI). A 95% CI, the customary interval<sup>41</sup> for flow measurement, there is a 0.95 probability the true value is within the interval<sup>38</sup> for a given measurement.

Table 7. Statistical accuracy for straight configuration at equivalence ratio = 1.0

<b>Statistical Accuracy at 95% Confidence Interval</b>							
Eq. Ratio = 1.0		Distance to Cavity: 75% Vane Width					
Main Flow kg/min	Mean U (m/s)	Mean V (m/s)	StdevU (m/s)	StdevV (m/s)	Nsamp (-)	Uncertainty (m/s)	% U
0.46	-20.20	0.24	1.81	1.46	44.03	1.64	8.14
0.61	-24.50	0.16	2.53	1.99	41.05	2.54	10.36
0.61	-25.39	0.22	2.99	2.26	34.14	2.54	9.99
0.92	-34.70	0.44	3.29	2.95	43.80	2.65	7.64
0.92	-33.91	0.23	4.11	2.97	35.90	4.08	12.05
1.22	-43.67	1.10	4.26	3.76	46.48	3.29	7.53
1.53	-54.76	0.80	5.29	4.63	46.75	4.08	7.44
1.84	-62.72	-0.93	6.37	4.73	44.02	5.93	9.46

Within an averaged velocity vector map, certain regions had more vectors rejected through the data validation and filtering compared to others. Therefore, the mean quantities determined over regions with more valid vectors have a higher level of certainty than those quantities determined from regions with a low number of valid vectors. Regions with higher statistical uncertainty must be considered when observing vector maps and turbulence maps, as there is less confidence in the data taken from certain regions. For example, the figure below shows the mean velocity vectors plotted over a color-map of the percent statistical uncertainty.

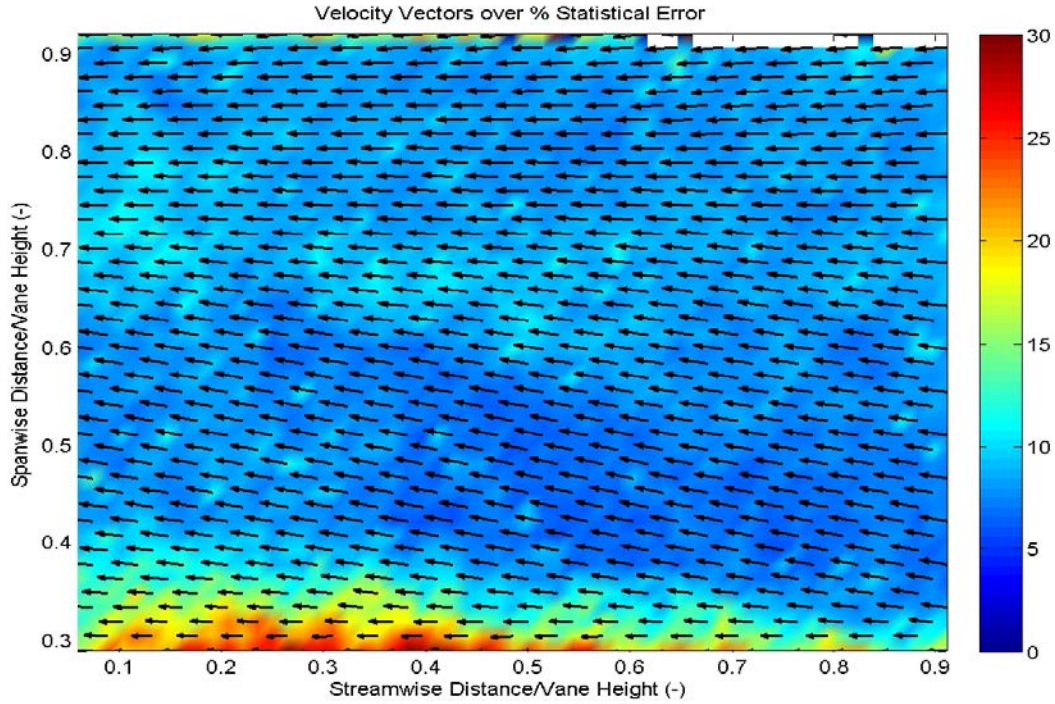


Figure 45. Velocity vectors superimposed on a color-map of the % statistical error for a 95% CI: straight cavity, 1.5 kg/min airflow,  $EqR. = 1.0$

The data consisted of 74 image pairs, the maximum capacity for the PIV data acquisition system. Very few of the vectors were rejected from the center region of the map. The regions with red coloring have a higher statistical error due to either a low number of samples or a high standard deviation. At the extreme top of the map the color drops off precipitously due to the edge of the window. Above the edge of this window seed particle reflections do not have line-of sight to the camera and are therefore not recorded. In the lower region of the map, near the radial vane cavity, there is also a region of higher uncertainty due to the combination of a large number of vectors being rejected from this region and a high standard deviation. This trend was observed in nearly all cases. Adversely, one of the main parameters to be measured, turbulence,



decreases data quality. The velocity fluctuation, caused by turbulence, increases the probability that loss-of-pairs will occur in an interrogation region. Furthermore, the random nature of turbulence decreases peak correlation heights, because the distance-scale over which the flow velocity is relatively constant decreases.

The geometry of the radial vane cavity (RVC) increases this effect.<sup>43</sup> This cavity is angled to promote mass transfer from the cavity vane to the main vane. The resulting out-of-plane velocity decreases the correlation due to loss-of-pairs.

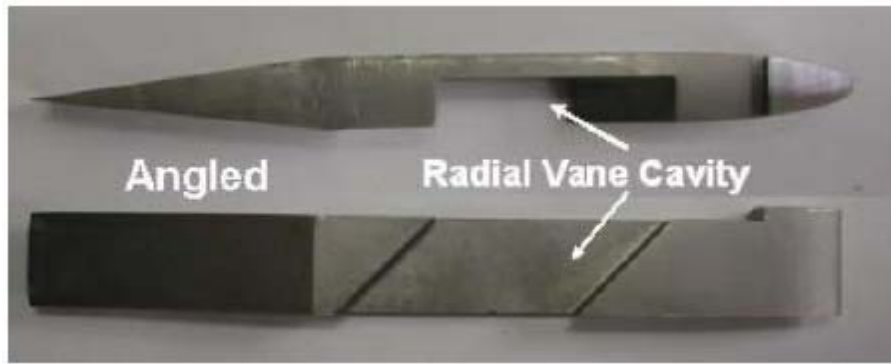


Figure 46. Radial vane cavity<sup>43</sup>

The bottom picture in the figure above, which shows a top view of the RVC, displays the angle of the cavity promoting mass transfer into the main vane.

The laser reflection from the walls of the main vane decreased the number of valid samples in some of the data. The camera was positioned to be perpendicular to the experimental plane, which was parallel to the main vane. In the experimental runs with the curved cavity vane configuration, the repositioning of the camera appeared to be at an angle slightly less than 90 degrees to the experimental plane. This slight change in angle

introduced a significant amount of laser reflection that overpowered the PIV signal. This overpowering of the signal can be observed in the figure below.

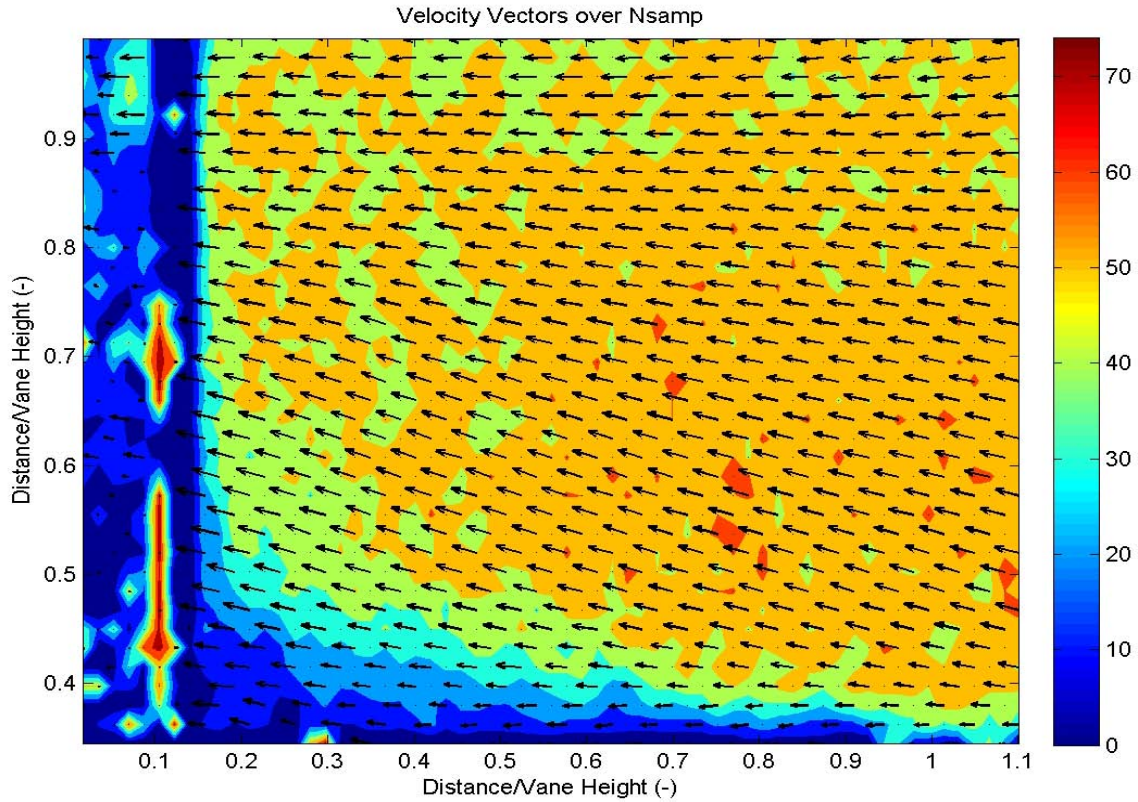


Figure 47. Velocity vectors superimposed on a color-map of the number of valid samples at each interrogation region: curved cavity, 1.2 kg/min airflow, EqR. = 1.0, position 1 (Near Cavity), mean velocity over experimental plane = 40.92 m/s

Most spurious vectors calculated in this region were successfully eliminated via data validation and filtering. However, vector statistics calculated over this region are likely to have a greater degree of uncertainty. This decrease in signal-to-noise ratio, caused by laser reflection off the main vane, occurred for the entire data set from the curved cavity

vane configuration. Therefore, conclusions drawn from the leftmost region in this set of data are less reliable.

The maximum number of image pairs possible during one data acquisition set was 74. Interestingly, many of the initial practice runs consisted of only 15 image pairs, but still appeared to produce valid results. The question then arises, “how many image pairs are required to attain valid data within a reasonable level of confidence?” A sensitivity study was performed by increasing the number of image pairs taken from 15 up to 74. Although the variance in measured velocity did change with the number of image pairs acquired, a steady trend was not observed. For purely random errors, one would expect the standard deviation of measured values to be inversely proportional to the sample size. Instead, the elapsed time over which data acquisition took place for 50 image pairs was significantly longer than the cyclic nature of the particle seeder. At the data acquisition frequency of 7.4Hz, the total elapsed time is 6.76 seconds. Some of the data sets taken with 20 or less image pairs showed low seed density over a significant portion of the data acquisition. For this reason, 50 image pairs were taken for most of the cases, while the maximum number, 74, was taken in select cases.

### *III.8.3 Measurement Repeatability*

One test case was repeated for comparison purposes. In this case the UCC was setup in the straight cavity vane configuration. The cavity equivalence ratio was 1.5 and a cavity to main airflow ratio was 0.15. Fifty image pairs were acquired for each case, except the first case in which 74 image pairs were acquired. Due to the unsteady nature of the flow inside the UCC, the results from these two runs were not expected to be

exactly identical. However, the observed differences provide a rough magnitude of the variability of the PIV data in general. The first parameters compared were the mean velocity vectors and the number of valid vectors after data validation and filtering. This is shown below.

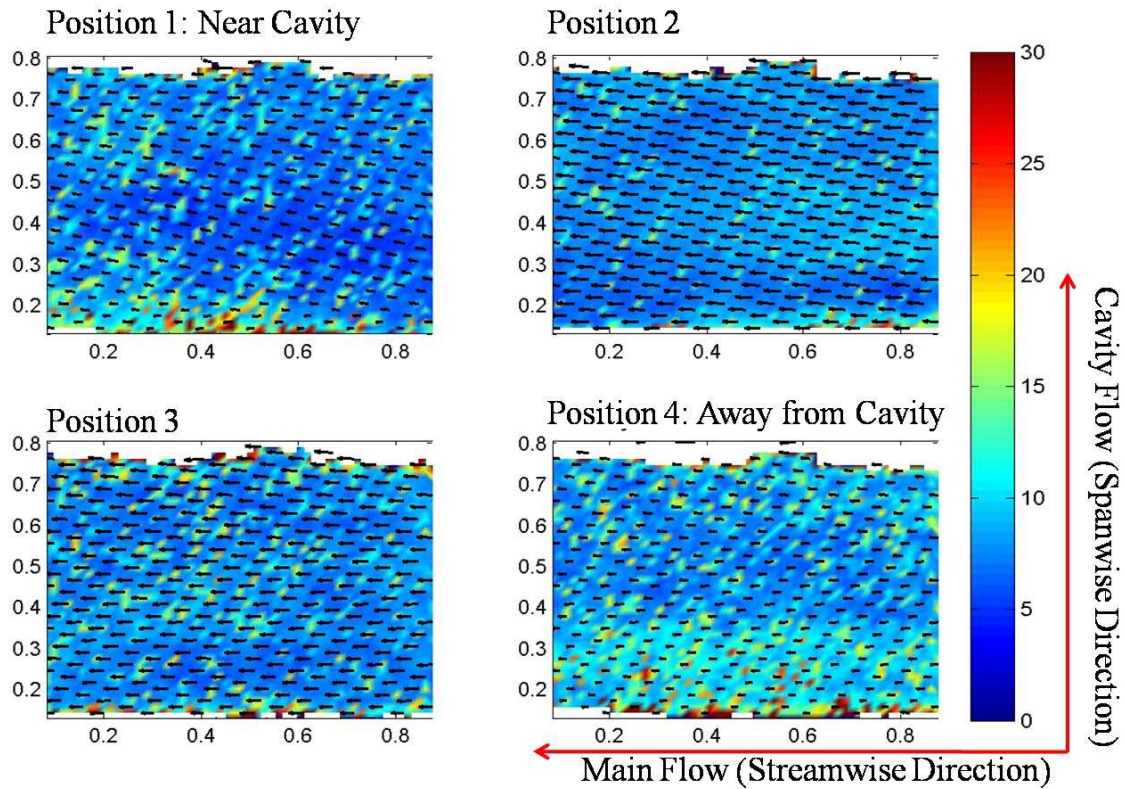


Figure 48. Mean velocity vectors superimposed over statistical error at 95% CI: straight cavity, equiv ratio: 1.5, ratio of mass flows: 0.15, case one



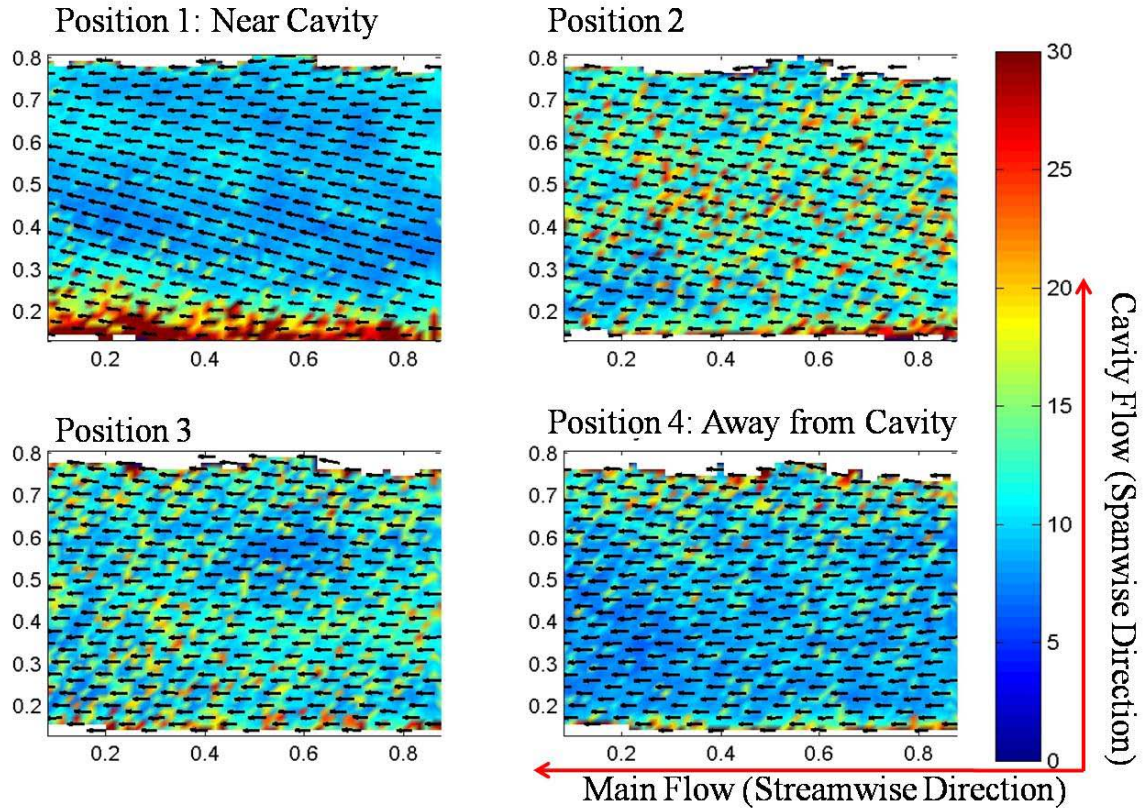


Figure 49. Mean velocity vectors superimposed over statistical error at 95% CI: straight cavity, equiv ratio: 1.5, ratio of mass flows: 0.15, case two

The subplots in the figures above are arranged according to their position from left to right. Position one is on the top left, whereas position four is on the bottom right. Comparing vector plots from their respective position in these two figures, such as the top right in Fig. 48 to the top right in Fig. 49, shows the mean measured velocity is similar but not the equal. Mean values are tabulated for each position from the two identical cases in Table 8 below.

Table 8. Mean values from a repeated testing condition

Repeat Test Average Values					
Straight Cavity Vane Config			Equivalence Ratio: 1.5		
MdotMain: 0.41 kg/min			MdotCav: 0.06 kg/min		
Position	Mean U_Vel	Mean V_Vel	Mean Stdv_U	Mean Stdv_V	Mean Nsamp
1	-16.78	1.87	2.32	1.78	63.93
1	-17.33	2.17	2.29	1.96	40.03
2	-17.61	0.98	1.79	1.65	39.88
2	-18.59	1.70	2.64	2.19	28.04
3	-18.28	0.12	1.98	1.48	34.00
3	-19.51	0.31	2.56	2.09	29.10
4	-18.10	-0.04	2.22	1.57	32.26
4	-20.66	-0.29	2.45	1.92	30.77

There are three significant findings of note in the table of mean values shown above: (1) variation of the average streamwise velocity, (2) variation of the average spanwise velocity, and (3) variation of the standard deviations compared to the number of valid samples.

- The mean streamwise velocity should be roughly equal for each position pair.  
The majority of the difference in velocity can be accounted for by the uncertainty of the measurement and variation in actual mass flow rates.
- The mean spanwise velocity is positive near the cavity vane (position one), but proximal to zero when away from the main vane (position 4). This trend will be discussed later in this chapter.
- The variation of standard deviation compared to the mean number of valid samples reveals no apparent relationship. This lack relationship suggests the variance caused in the flow velocity is primarily due to unsteady phenomenon, such as vortex shedding, rather than an inadequate sample size.

As described in the above paragraphs addressing uncertainty, there was a significant amount of variability in the measurements taken in this thesis. Both air mass flow rates continuously experienced fluctuations that effectively altered each of the three independent factors in this thesis: the bulk mass flow rate, the ratio of cavity to main mass flow rate, and the equivalence ratio in the cavity vane. This variability is considered when examining the trends and results seen in the rest of this chapter. The uncertainty limits were determined where practical. In addition, data from regions over which the number of valid samples was inadequate was not used to formulate trends and conclusions about the actual UCC behavior.

## **IV. Discussion and Results**

### **IV.1 Data Processing**

The results discussed in this chapter refer to data taken within the main flow channel of the UCC just above the RVC as shown in Fig. 30 from Chapter III.6.2. Plots of velocity, turbulence, and vorticity have left and right boundaries of the upstream edge and downstream edge of the cavity flow channel and upper and lower bounds of the window mount of the main flow channel. As discussed in Chapter III, 50 or 74 image pairs were taken at each experimental condition, the data was validated and filtered, and the time averaged statistics are presented in this chapter. Velocity maps over a single image pair were analyzed in addition to the averaged statistics. However, in regions of low turbulence the velocity patterns are relatively steady while the regions of high turbulence or vorticity reveal large velocity gradients as well as a higher rate of signal drop-out. As parameters such as turbulence intensity and vorticity are defined over multiple images, velocity maps generated from only a single image pair are not presented in this chapter. The following sections discuss how the data was processed to determine statistical quantities such as mean velocities, turbulence intensity, and vorticity.

#### *IV.1.1 Statistical Analysis*

As described in Chapter III, the final step in the PIV processing is to compute vector statistics on the set of vector maps. A single velocity vector is determined for each interrogation region from the cross-correlation algorithm. Through filtering and validation, some of the vectors in each map are rejected. The remaining vectors become



the input data for the vector statistics. A map of mean velocity vectors is shown in the figure below.

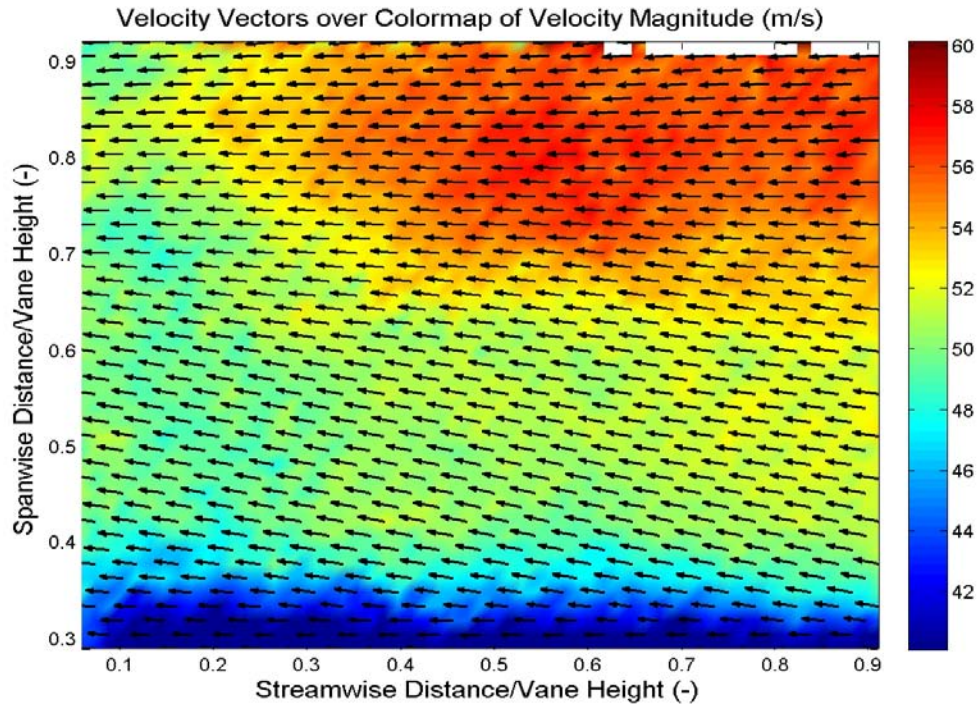


Figure 50. Sample mean velocity vector map at position closest to cavity vane

This vector map was obtained by averaging the cross-correlation results from 74 image pairs. The UCC was configured with the straight cavity vane and had 1.5kg/min and 0.15 kg/min of airflow through the main and cavity vanes respectively with a cavity air to hydrogen equivalence ratio of 1.0. The plot shows only every third vector for ease of viewing. The axes are non-dimensionalized by the height of the main vane, 30.5mm. The plot was generated using Matlab® R2007b. This general format for plotting results will be repeated throughout the rest of Chapter IV.

A single map of statistical parameters is determined by comparing vectors from the same interrogation region over all the velocity vector maps. The following statistical calculations were performed:

Mean velocity for u and v components:  $\mu_u = \frac{1}{N} \sum_{i=1}^N U \text{ or } V$  (20)<sup>26</sup>

Variance for u and v components:  $\sigma_u^2 = \frac{1}{N-1} \sum_{i=1}^N (u_i - \mu_u)^2$  (21)<sup>26</sup>

Covariance:  $Cov\{U|V\} = \frac{1}{N-1} \sum_{i=1}^N (u_i - \mu_u)(v_i - \mu_v)$  (22)<sup>26</sup>

Correlation Coefficient:  $\rho = Cov\{U|V\} / \sigma_u \sigma_v$  (23)<sup>26</sup>

In addition to measuring the velocity inside the UCC, one of the primary goals of this thesis is to quantify the turbulence intensity for different flow conditions. Turbulence intensity is of great concern, as the UCC is thought to rely on the turbulent transport mechanism for the quick mixing of air and fuel.

One common way to quantify the relative level of turbulence is the turbulence intensity parameter,<sup>44</sup> defined as:

$$T.I. = \frac{u'}{\bar{U}} \cong \sigma / \mu \quad (24)$$

In this definition,  $u'$  is the root-mean-square or the standard deviation of the velocity fluctuations at a location over a specific amount of time and number of samples.  $\bar{U}$  is the average of the velocity at that location over the same time and number of samples. In the above equation, there is a second equality showing this definition is approximately equal to the standard deviation over the mean. The results for turbulence intensity values presented in this thesis were calculated using this method. The standard deviation for one or both velocity components is divided by the mean velocity.

This method is not a direct measurement of turbulence, but of time-averaged turbulence. Over the set of velocity vector maps, the turbulent velocity map can be decomposed into the average velocity and the velocity fluctuation vector.<sup>45</sup>

$$\mathbf{U} = \bar{\mathbf{U}} + \mathbf{u} \quad (25)$$

The square of this velocity fluctuation vector is directly proportional to the turbulent kinetic energy and drives the turbulent transport mechanism. The average velocity,  $\bar{\mathbf{U}}$ , is measured, and the velocity fluctuation,  $\mathbf{u}$ , is estimated with the variance of the sampled data. The turbulence intensity statistic is an indirect way to quantify the velocity fluctuation vector.

#### *IV.1.2 Turbulence Intensity: Dynamic Studio Method*

Once the vector statistics have been calculated, several scalar values representing different flow properties over each interrogation region can then be plotted using the Dynamic Studio® software. Among these are: the number of valid samples, correlation coefficient, vorticity, variance, standard deviation, velocity components, and turbulence intensity. The method of calculating turbulence intensity is similar to the definition described above. Two turbulence intensities can be calculated, one for each component: Turbulence Intensity in the streamwise:  $TI_u = u'/\bar{U}$ ; and in the spanwise:  $TI_v = v'/\bar{V}$ . Analyzing the data with this method, the spanwise turbulence intensity was found to be lower near the cross-flow of the cavity vane. This result seemed peculiar as one would expect the turbulence intensity to be elevated near regions of high-shear and dissipate as the experimental plane moves away from the cross-flow. Fig. 51 below shows scalar maps of spanwise turbulence intensity generated from the mass flow ratio study. Each of

these subplots represents data taken in the experimental plane inside the main flow channel defined on the right and left by the upstream and downstream edges of the cavity flow channel, on the top by the top of the optical access window in the main channel, and on the bottom by the top edge of the RVC.

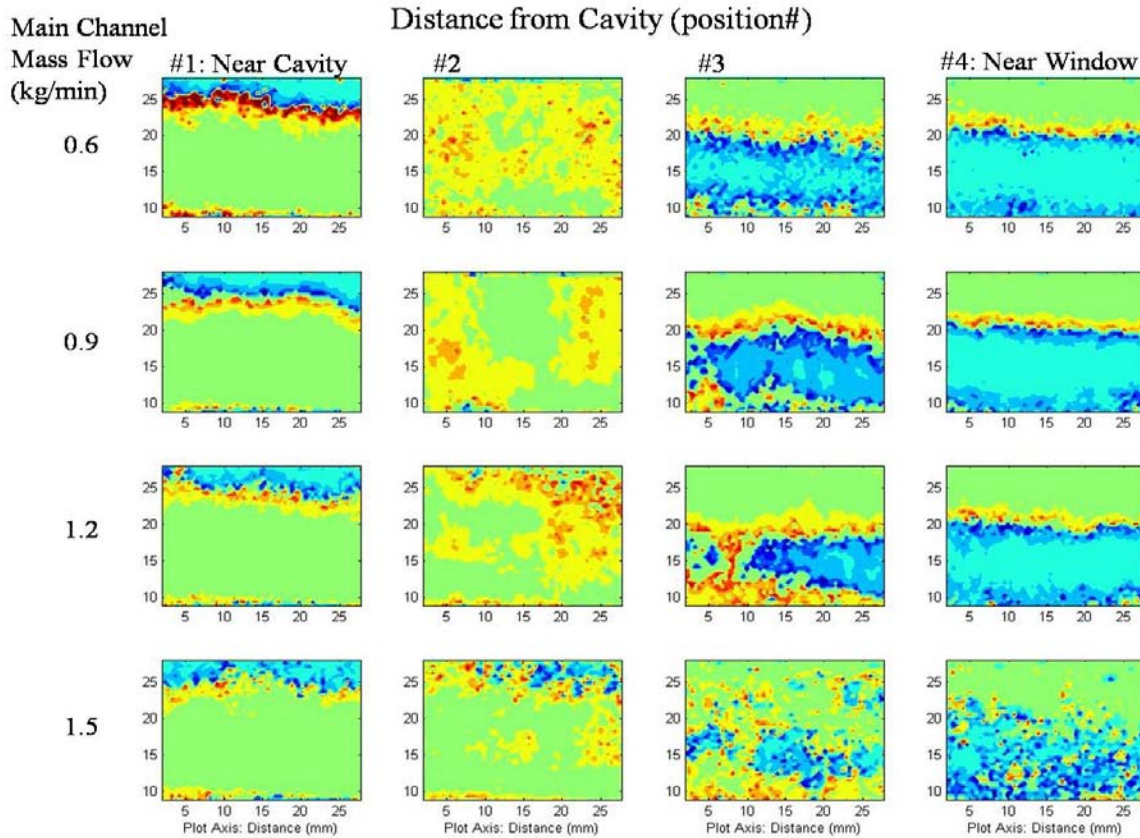


Figure 51. Spanwise turbulence intensity calculated by Dynamic Studio® PIV software

In Fig. 51 above, spanwise turbulence was calculated with the Dynamics Studio® algorithm for sixteen data sets – data from four experimental plane depths at four increasing airflow rates. The rows correspond to constant test configurations while the columns correspond to the location of the experimental plane. The spanwise turbulence intensity data represented in Fig. 51 shows the peculiar trend that the turbulence intensity

levels at all four mass flow rates would increase with distance away from the cross-flow of the cavity vane. This trend was observed in all data taken. Although this method of calculating turbulence intensity as the velocity component variation over the component average is technically correct, it is misleading when one of the velocity components is proximal to zero.

#### *IV.1.3 Turbulence Intensity: New Method*

Turbulence intensity was calculated as being highest at the experimental plane location away from the cross flow of the cavity vane and lowest near the cross flow. These preliminary results were unexpected, as this trend is directly opposed to basic principles of turbulence. Regions of high flow-shear create more, not less, turbulence. In fact, this trend turned out to be an artifact of how the data was being presented. As mentioned above, the turbulence intensity is normalized by the local mean velocity,  $\bar{U}$ . The Dynamic Studio® PIV software's calculation of this value uses the component velocity mean as the denominator, instead of the mean of the total velocity. The drawback with this method is when the flow is nearly parallel to one of the axes defining the coordinate system, the average velocity component in the perpendicular direction will be nearly zero. Therefore, any velocity fluctuations in that direction will be artificially magnified, as they will be divided by a number close to zero. The velocity vector map shown in Fig. 50 on page 119 is typical of those taken at the experimental plane closest to the cavity vane, position one, for all flow conditions. The velocity map shown below is from position three ( $\frac{3}{4}$  of the main channel depth away from the cross-flow of the cavity vane).

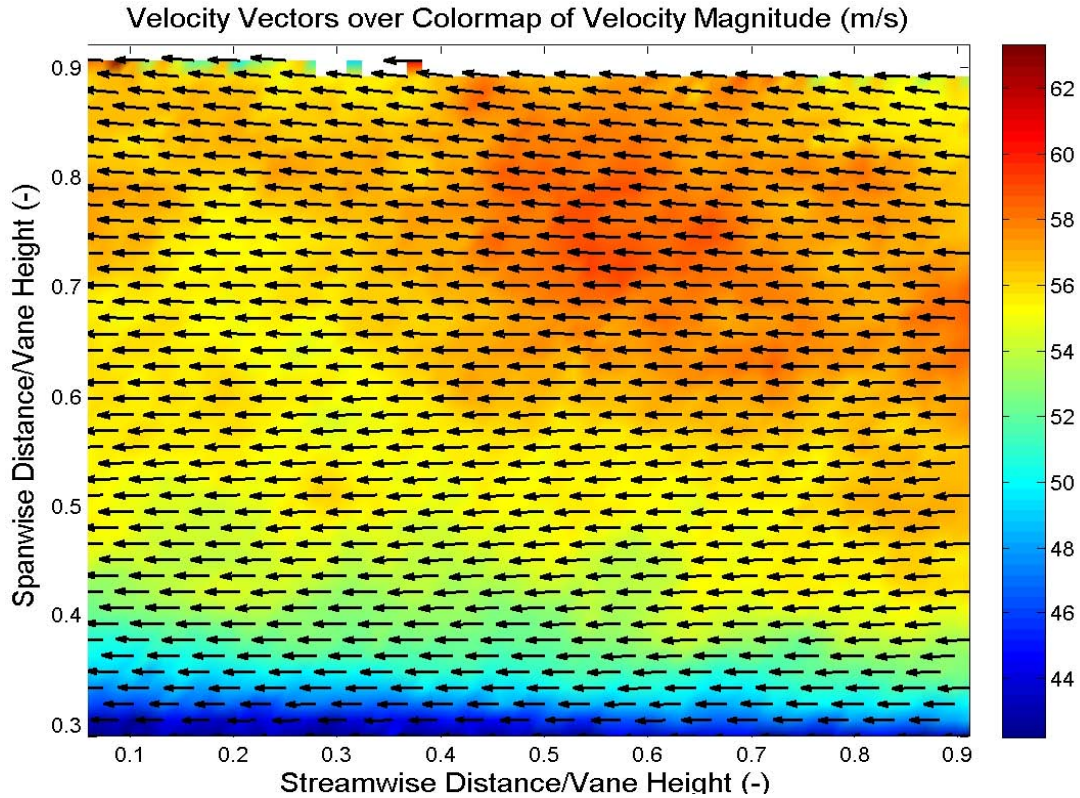


Figure 52. Mean velocity vector map at position three – away from cavity vane

This map is fairly typical for position three, in that the flow is almost entirely in the streamwise direction. The cavity vane channel is 14 mm in height at the point where it mixes with the main channel, which is 14 mm in width. There are essentially two flow paths of the same dimension flowing perpendicular to each other. This figure shows that at the third experimental plane, 75% of the vane width away from the cross-flow, the turbulence has dissipated and the main flow is relatively undisturbed. This trend is confirmed in the two velocity plots below.



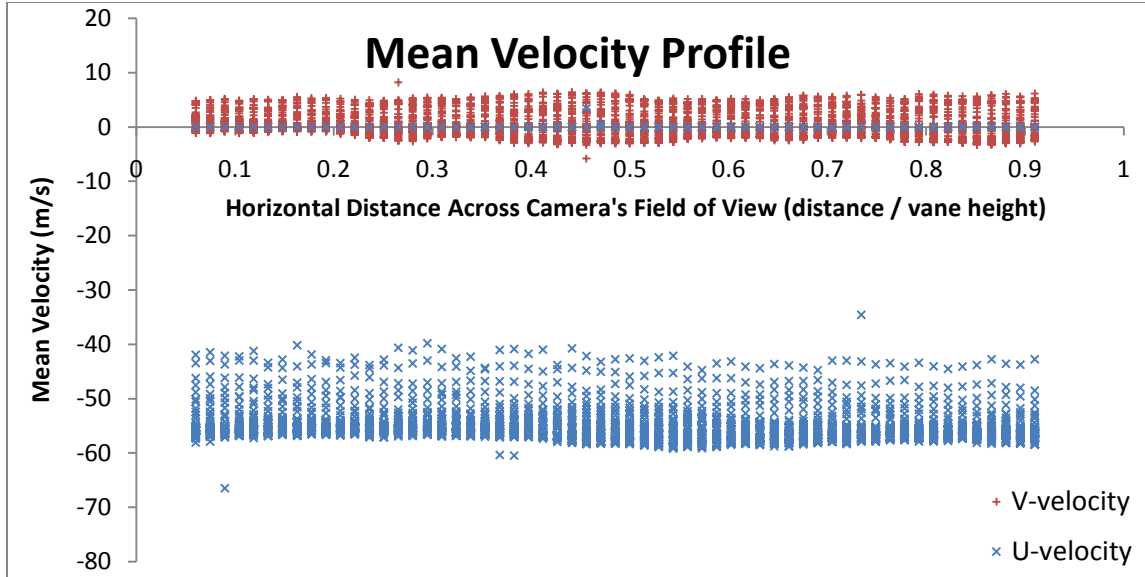


Figure 53. Mean velocity profile away from cavity vane

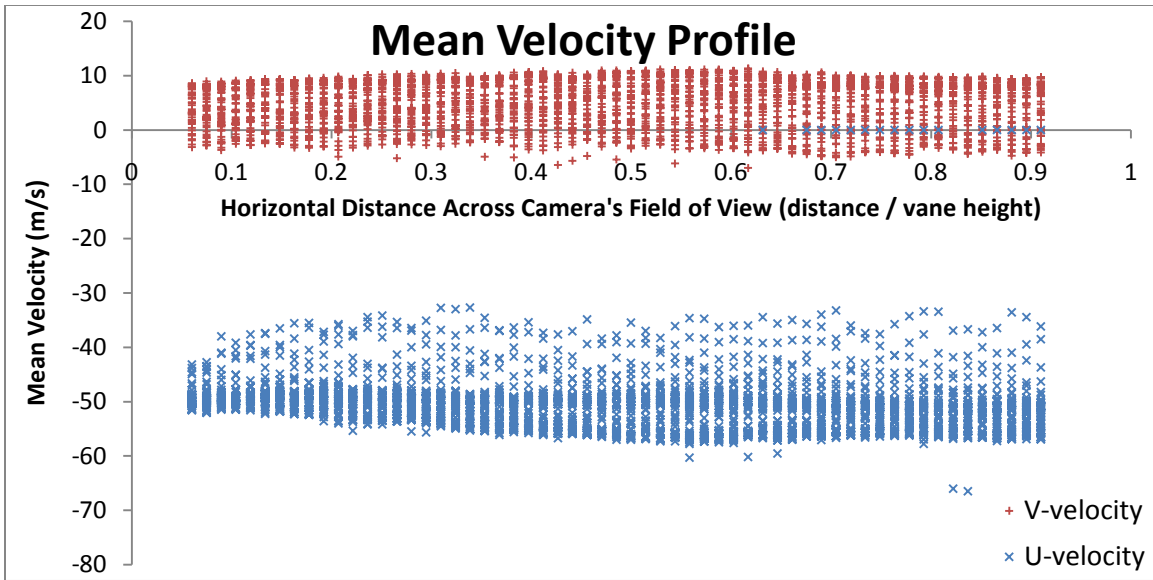


Figure 54. Mean velocity profile near cavity vane

This trend of nearly horizontal flow away from the cross-flow of the cavity vane indicates velocity fluctuations near the cavity are being divided by a larger number than those

occurring away from the cavity vane. A more representative method is required to accurately compare turbulence statistics.

Although it is necessary to separate turbulence by component variance, the same denominator must be used in order to accurately compare turbulence statistics independent of main flow direction. The root-mean-square of the mean velocity over all valid samples for each respective interrogation region was used to normalize turbulence intensity for the remainder of the data processing:

$$\text{Streamwise turbulence intensity:} \quad TI_u = \frac{\sigma_u}{\sqrt{\mu_u^2 + \mu_v^2}} \quad (26)$$

$$\text{Spanwise turbulence intensity:} \quad TI_v = \frac{\sigma_v}{\sqrt{\mu_u^2 + \mu_v^2}} \quad (27)$$

$$\text{RMS-direction turbulence intensity:} \quad TI_{rms} = \frac{\sqrt{\sigma_u^2 + \sigma_v^2}}{\sqrt{\mu_u^2 + \mu_v^2}} \quad (28)$$

In these definitions,  $\sigma$  is the local standard deviation and  $\mu$  is the local mean over all valid samples. These definitions for turbulence intensity are used throughout the rest of Chapter IV.

#### *IV.1.4 Validation of Data Export and Processing*

The data was further analyzed using Microsoft Excel® and Matlab®. Excel® was primarily used for validation and for generating scatter plots. In comparison, Matlab® is a more powerful graphical tool, capable of generating scalar maps, three-dimensional surfaces, and vector maps. Unlike Excel®, where the user highlights the data for each plot, Matlab® is more like a computing language. This makes data



processing much more efficient, but somewhat less intuitive. Therefore, it was then necessary to validate the Matlab® algorithm. This was accomplished by creating a program that read-in data and recreated the plots generated by the Dynamic Studio® software. One example of this is shown in the two figures below.

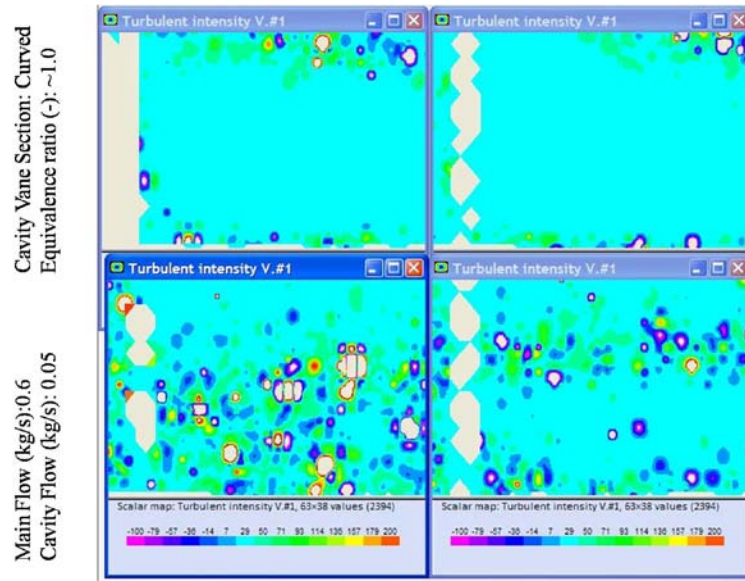


Figure 55. Spanwise turbulence intensity scalar map: Dynamic Studio®

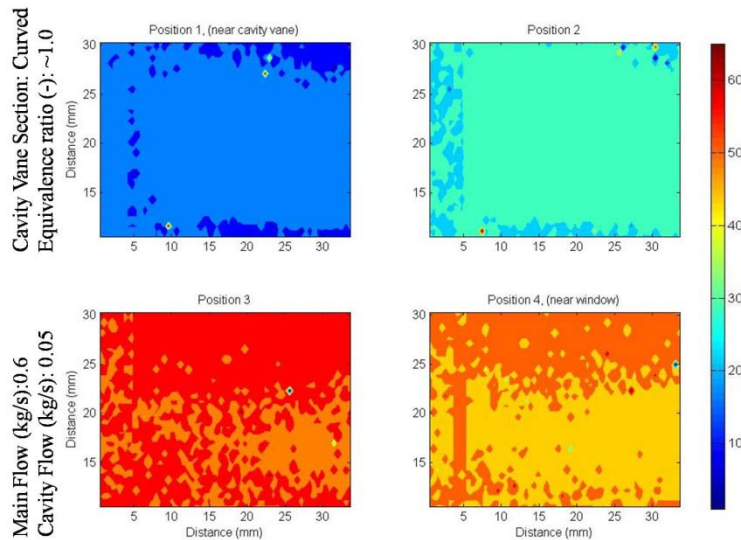


Figure 56. spanwise turbulence intensity scalar map: Matlab®

The new method was validated by producing plots of the same type. At this point, the data may be analyzed using the aforementioned definitions for turbulence intensity (equations 26-28) which normalize by the total flow velocity. With the new definitions for spanwise turbulence intensity ( $TI_v$ ), streamwise turbulence intensity ( $TI_u$ ), and RMS-turbulence intensity ( $TI_{rms}$ ), the following scalar plots were then generated with the same data used to create the vector maps and the scatter plots of velocity.

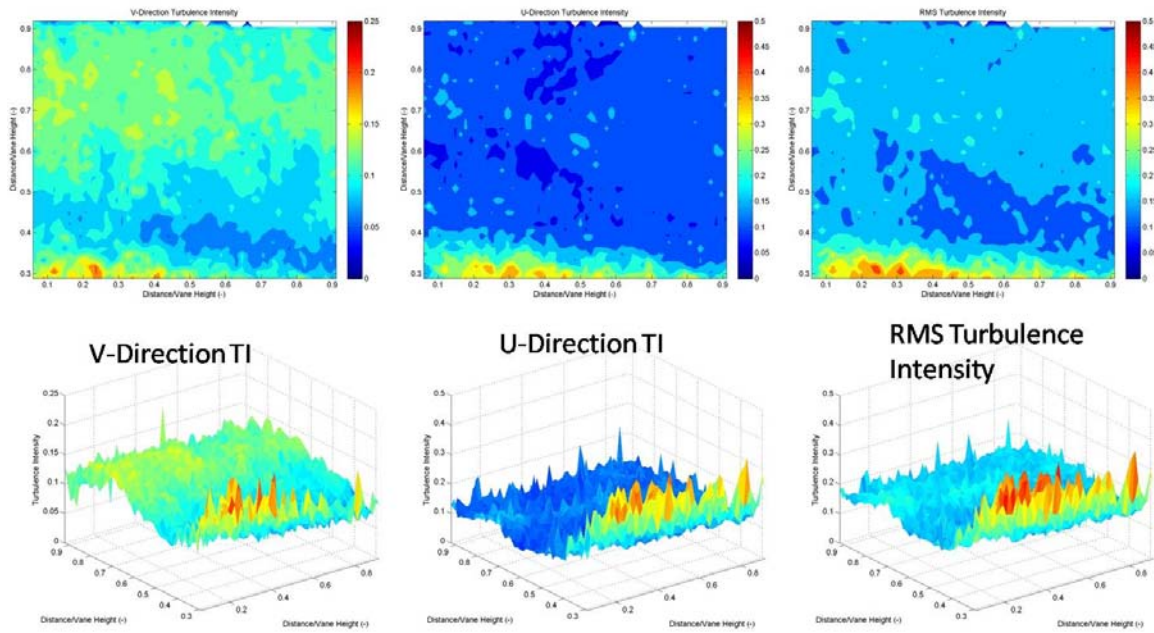


Figure 57. V, U, & RMS turbulence intensity scalar plots of data taken in the UCC flowing 1.5 & 0.15 kg/min in the main and cavity vanes at equivalence ratio = 1.0. x-axis & y-axis in main flow direction, z-axis & color represent turbulence intensity

The turbulence intensity plots generated with the new method appear to be more comparative. The turbulence intensity plots generated with Dynamic Studio® were displaying spanwise turbulence intensity ( $TI_v$ ) values averaging between -10 and 10.

This corresponds to a turbulent fluctuation vector magnitude that is 1000% of the magnitude of the mean flow velocity. In the figure above,  $TI_v$  is approximately 0.1 for much of the plot. A turbulent fluctuation vector magnitude that is 10% of the mean value is a more realistic value. Further, this method represents the turbulence intensities in a more intuitive form. For example, a turbulence intensity value of “10% fluctuation with respect to the total velocity” is more descriptive than “1000% of a number close to zero.”

#### *IV.1.5 Limits Used for Data Filtering*

The process of rejecting outliers can be fairly subjective. Before discussing observed trends it is therefore necessary to track exactly what data is represented in the plots. As discussed in Chapter III, a single velocity vector results from the cross-correlation process for every interrogation region. The velocity maps are then filtered to reject those outlying vectors. The boundaries between accepted data and outliers were set in terms of vector magnitude in each direction, as well as the relative strength of the correlation peak. Additional filtering was performed when the data was imported into Matlab®. The following categories of data were rejected as outliers:

- Any vector whose total magnitude was exactly zero (no data)
- Any  $TI_v$ ,  $TI_u$ , or  $TI_{rms}$  value that was exactly zero (no data)
- Any  $TI_v$  value above 0.25 for the straight cavity vane configuration
- Any  $TI_v$  value above 0.3 for the curved cavity vane configuration
- Any  $TI_v$  value above 0.5 for the straight cavity vane configuration
- Any  $TI_v$  value above 0.6 for the curved cavity vane configuration

These values were chosen after examining of the distribution of turbulence intensities in histogram plots to identify reasonable bounds for rejecting outliers.

#### IV.1.6 Vorticity

While turbulence is desirable for fast flame speeds and mixing of the cavity flow into the main channel, turbulent flow is, by definition, chaotic and unpredictable.

Vortices can exist in flow fields in a semi-steady state, allowing for more predictability while generating flow mixing. Cavities, and other blunt-bodies, cause rotation when the flow moving past is unable to turn quickly enough to stay “attached” to the surface.

Vorticity is the measure of the local rotation of the flow field, and is mathematically defined as the curl of the velocity field.

$$\text{curl}(V) = \nabla \times V = \left( \frac{\partial V_z}{\partial y} - \frac{\partial V_y}{\partial z} \right) \hat{i} + \left( \frac{\partial V_x}{\partial z} - \frac{\partial V_z}{\partial x} \right) \hat{j} + \left( \frac{\partial V_y}{\partial x} - \frac{\partial V_x}{\partial y} \right) \hat{k} \quad (29)^{26}$$

This calculation requires a three-dimensional flow field and yields the local flow rotation around each axis. With PIV, the velocity field is really a projection of the 3D velocity field onto the experimental plane. Without knowledge of the third velocity component,  $V_z$ , only the rotation about the z-axis (in x-y plane) can be calculated. For a 2-D velocity field the equation for vorticity reduces to:

$$\text{curl}(V) = \left( \frac{\partial V_y}{\partial x} - \frac{\partial V_x}{\partial y} \right) \hat{k} \quad (30)^{26}$$

PIV velocity fields are discrete, having one vector per interrogation region. Therefore, differencing is used in place of the above equation for a continuous field.

$$\text{Vorticity}(m, n) = \frac{V_y(m+1, n) - V_y(m-1, n)}{\Delta x} - \frac{V_x(m, n+1) - V_x(m, n-1)}{\Delta y} \quad (31)^{26}$$

$V(m,n)$  is the velocity vector field.  $\Delta x$  and  $\Delta y$  define the grid spacing. The orientation of the camera with respect to the UCC main channel is such that this equation defines positive vorticity for counterclockwise rotation.

## **IV.2 Observed Trends**

The following sections describe some of the trends observed in the analysis of the PIV data to include the flow direction, turbulence, and vorticity over the different regions.

### *IV.2.1 Mean Measured Velocity*

Main channel flow velocities were calculated, as described in Chapter III, by using the Equation of State for a perfect gas and the equation for steady one-dimensional mass flow. This information helped estimate the appropriate timing on the PIV-laser pulse delay. The actual mass flow in the main channel is measured upstream of the cavity vane, but not over the radial vane cavity, rendering this bulk calculation limited in nature. For this reason, averages of the PIV measurements were used to determine mean flow velocity for different conditions as shown in the figure below.

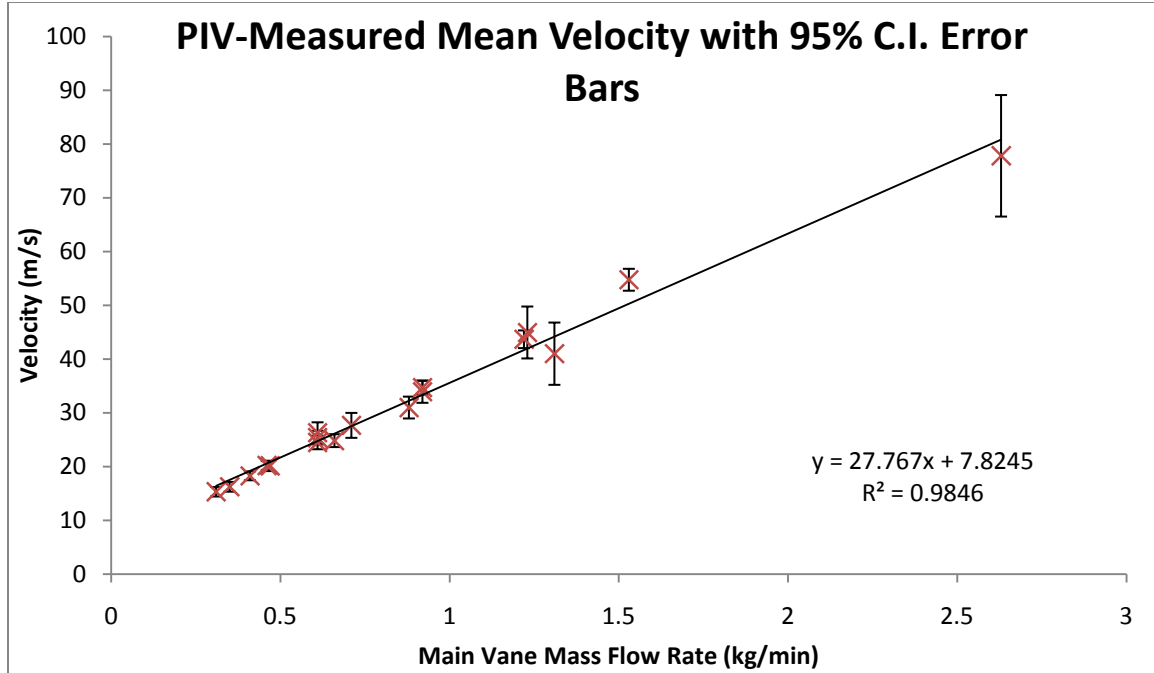


Figure 58. Mean velocity in the main vane for experimental plane three

In Fig. 58 above, the mean velocities calculated from the PIV measurements are plotted at the set value for main channel mass flow rate. The error bars show a 95% CI based on the number of valid samples and standard deviation at the corresponding conditions. A linear regression was used because, in theory, velocity is directly proportional to the mass flow rate according to the Equation of State and the equation for one dimensional, steady mass flow:

$$V = \dot{m}RT/pA \quad (32)$$

As the gas constant (R), temperature (T), pressure (p), and cross sectional area (A) are constant, velocity (V) should vary linearly with mass flow rate ( $\dot{m}$ ). The square of the correlation coefficient ( $R^2$ ), shown on the plot above, is 0.9846. As the correlation coefficient is close to the theoretical maximum of 1.0, there is a high degree of

correlation between mass flow and velocity. These velocities were generated from data taken from experimental plane three, which exists over a laser sheet 3 mm, thick positioned  $\frac{3}{4}$  of the vane width from the back wall and cavity channel. As will be discussed later in this chapter, the data from the third experimental plane is the steadiest from the four planes. In effect, the third experimental plane is far enough from the cross-flow of the cavity vane, yet not close enough to the optical window to be affected by boundary-layer effects.

The streamwise velocity is expected to be relatively constant throughout the depth of the UCC main vane. The depth within the main vane is expressed as the position number of the experimental plane, where position one is adjacent to the cavity flow and plane number four is adjacent to the optical window. While the values for velocity in Fig. 58 were taken at position three, Fig. 59 and Fig. 60 below show the decrease in measured streamwise velocity at the first experimental plane which was observed for all cases.

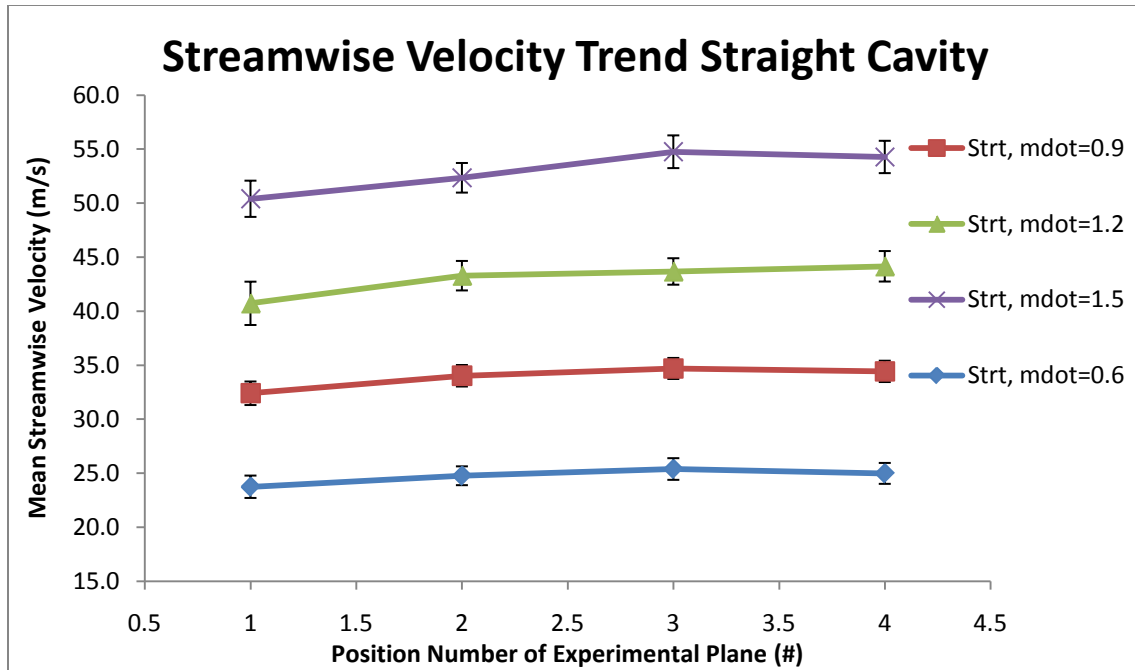


Figure 59. Mean streamwise (U) velocity at each experimental plane for the straight cavity configuration, error bars at 95% CI

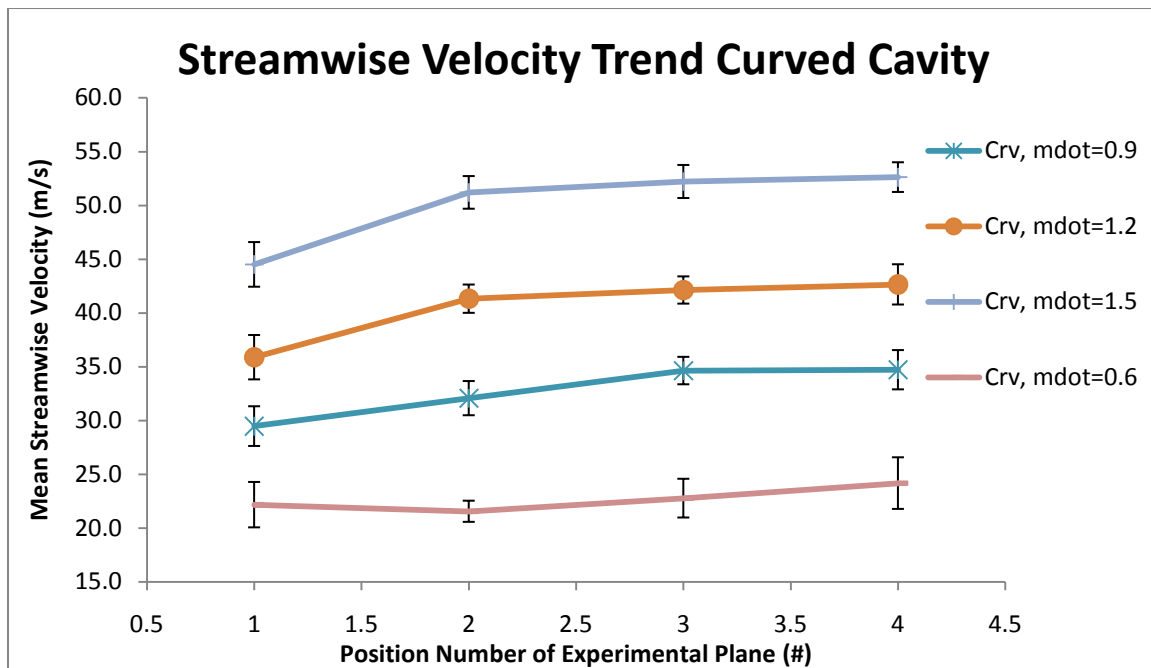


Figure 60. Mean streamwise (U) velocity at each experimental plane for the curved cavity configuration, error bars at 95% CI



The error bars display in Fig. 59 and Fig. 60 above are relatively small with an average total error of 6.65% for the straight and 10.2% for the curved configuration at a 95% CI. The relative percent error becomes ambiguous for the spanwise velocity as mean averages approach zero. Therefore, spanwise error is compared in terms of magnitude, not percent. For the velocity study, the mean spanwise velocity error for the straight configuration was  $\pm 1.08$  m/s and  $\pm 1.16$  m/s for the curved configuration, a 7.5% increase in statistical error at the 95% CI. Although the relative error is high, a strong dependence on distance from the cavity flow was observed in the spanwise velocity, as shown in Fig. 61 and Fig. Fig. 62 below.

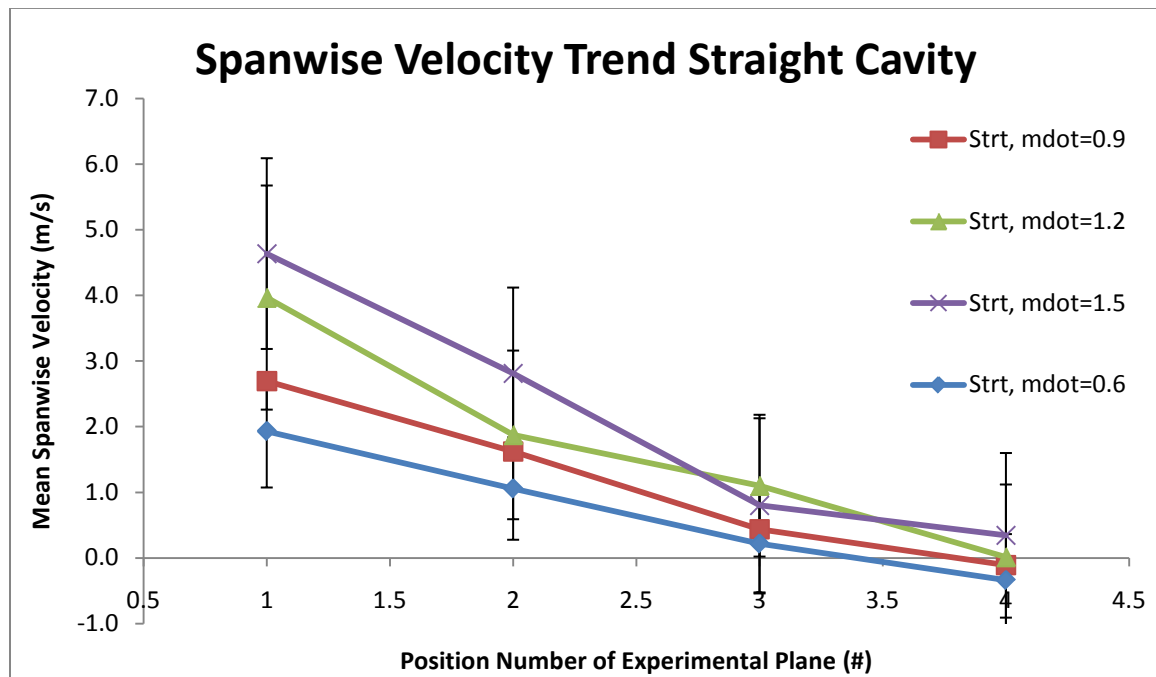


Figure 61. Mean spanwise ( $V$ ) velocity at each experimental plane for the straight cavity configuration, error bars at 95% CI

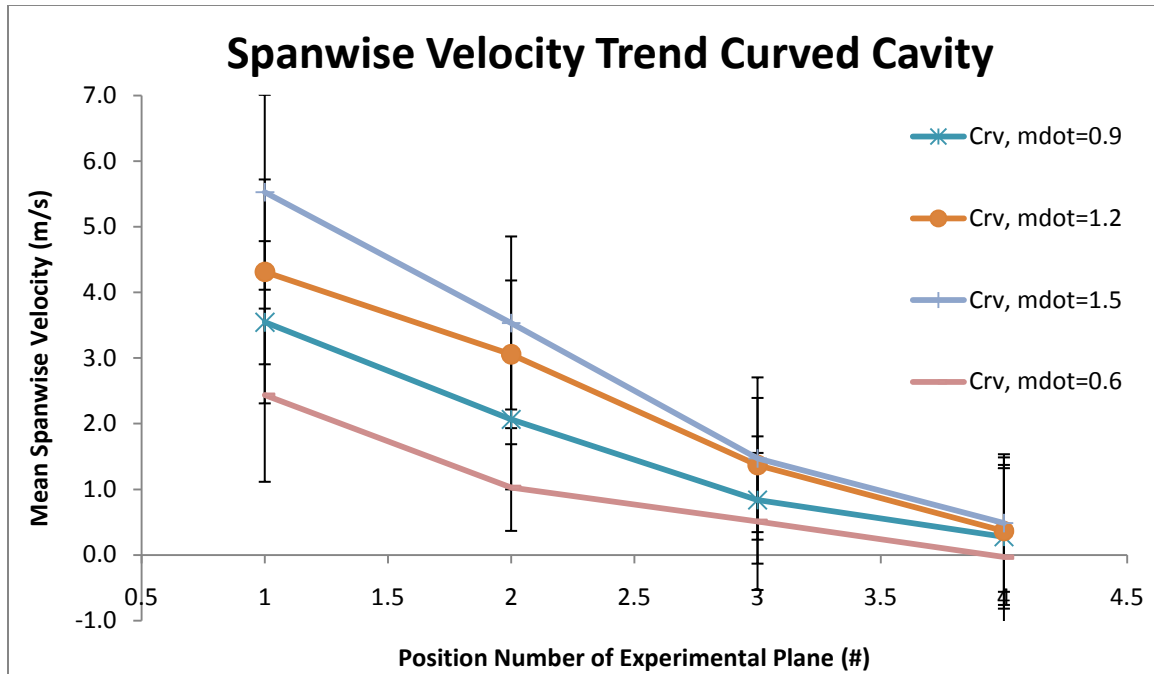


Figure 62. Mean spanwise ( $V$ ) velocity at each experimental plane for the straight cavity configuration, error bars at 95% CI

Momentum exchange exists in the flow near the cavity vane as the two flows mix together. This mixing results in the main vane flow gaining a component of velocity in the spanwise. Although the depth of the main vane was separated into only four planes, the above figure suggests the amount of velocity gained in the spanwise varies with the distance from the cavity flow in a nearly linear relationship. Although expected, this trend of decreasing streamwise velocity is indicative of an important parameter in the design of a full-scale UCC – strong radial variation in spanwise velocity.

#### IV.2.2 Vector Plots and Flow Direction

The matrix of velocity values resulting from the PIV process can be represented visually with vector maps. It is beneficial to view these vector maps superimposed on a

color plot of the number of valid samples to give an idea of the level of uncertainty at that point.

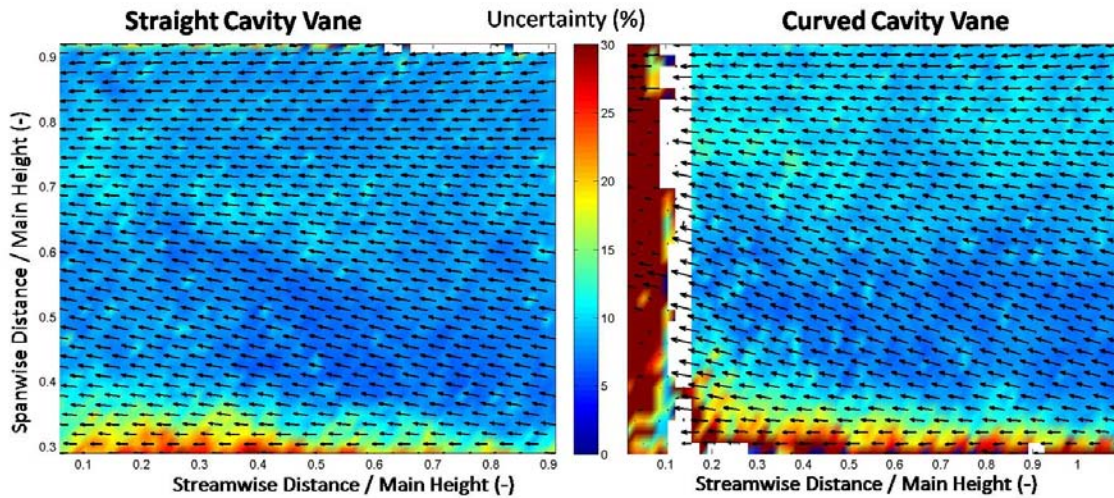


Figure 63. Vector map superimposed on color map of % statistical error at a 95% CI: curved config., main & cav. flows: 1.5 & 0.15kg/min, equivalence ratio: 1.0, position 1

The vector map in the figure above illustrates the flow direction and uncertainty based on the local number of valid samples and standard deviation. The dark red hue over the leftmost region shows a statistical error of greater than 30%. Therefore, data from this region is considered invalid. For example, it would be incorrect to assume there is a sharp decrease in spanwise velocity in the leftmost region of this vector map, even though the vectors precipitously decrease in magnitude there.

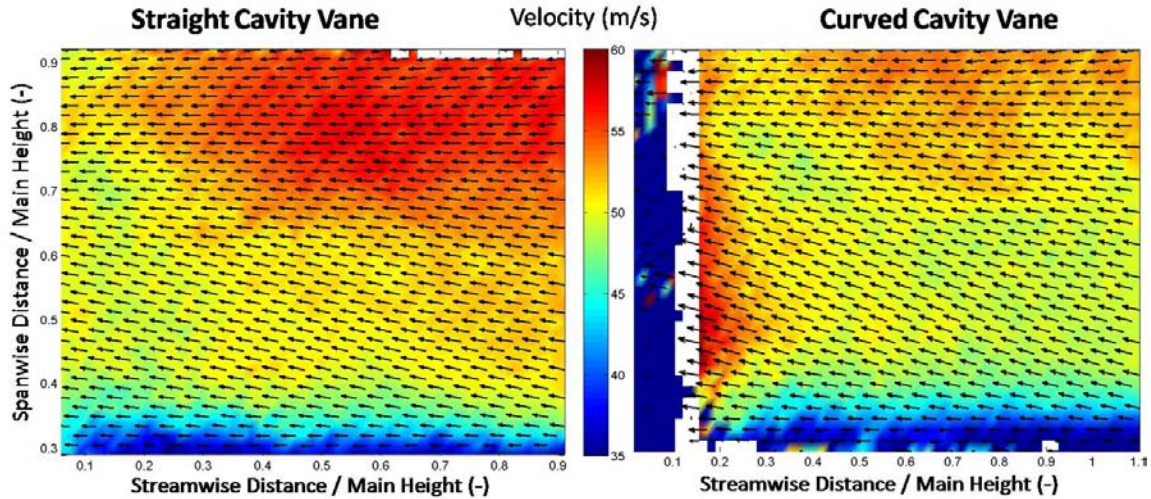


Figure 64. Vector map over color map of velocity for straight vane (left) & curved vane (right): main & cav. mass flows: 1.5 & 0.15kg/min, equiv ratio: 1.0, position 1

In the lower half of the left graph in Fig. 64 the vectors have a noticeable spanwise component in the direction of the cavity flow. In the right graph, representing curved vane data, the vertical component is much higher. The bulk velocity of the flow in the main channel upstream of the radial vane cavity is on average only in the streamwise, as the flow passage is entirely enclosed. Therefore, the spanwise velocity component is likely to have been caused by the cross flow of the cavity channel. As this data was taken at experimental plane position one, which is adjacent to the cavity-cross flow over its entire region, the spanwise component is expected to be positive in the direction of the cross-flow over the entire region. However, it is observed in Fig. 64, as well as for all test conditions in position one that the top half of the vector plots show mean velocity in the streamwise direction only. This decrease in spanwise velocity component near the top of the main vane is likely to be due to the physical wall

constituting the top of the main channel blocking the flow. The wall creates the obvious boundary condition that the velocity cannot go through the wall. Therefore spanwise turbulence is expected in the top region of the main channel due to the wall causing the spanwise flow to change direction.

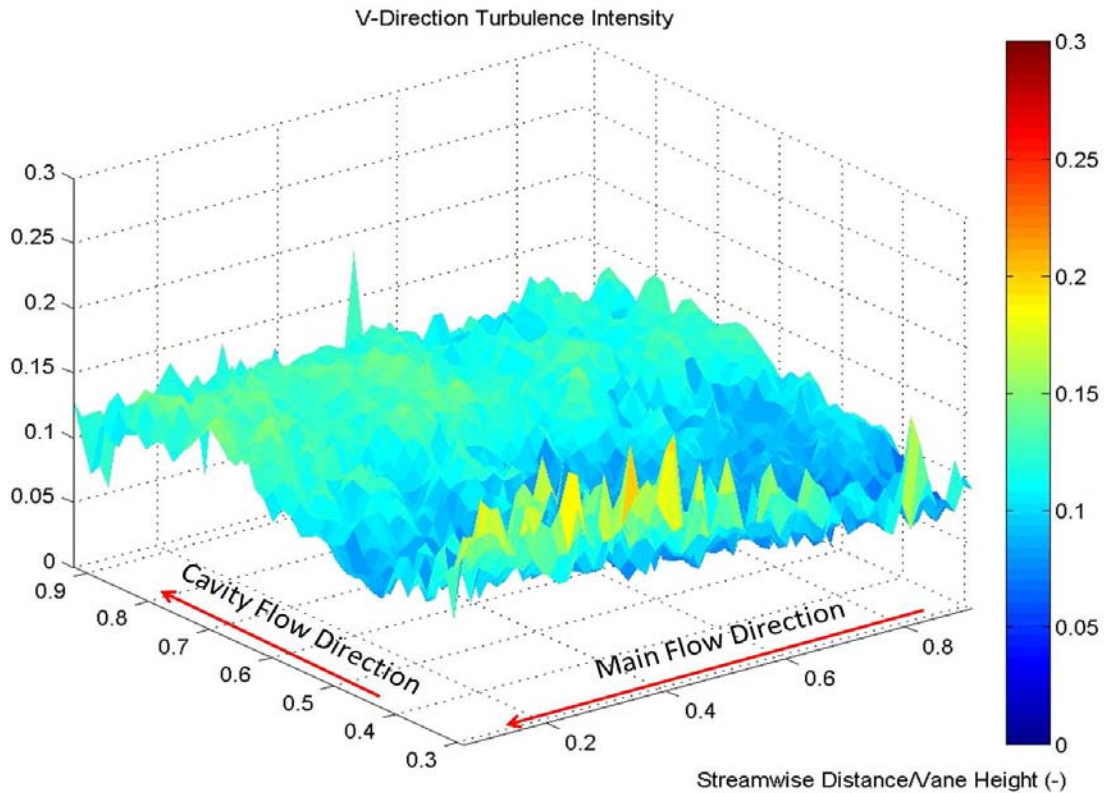


Figure 65. Spanwise turbulence intensity, straight vane config., main & cav. mass flows: 1.5 & 0.15kg/min, equiv ratio: 1.0, position 1

As seen in the spanwise turbulence intensity surface plot above, there are higher values in the uppermost regions of the main channel. The spanwise turbulence in the bottom of the main vane is likely caused by vortex shedding off the radial vane cavity. Examining the area above the RVC (the bottom of the plots) in Fig. 64 and Fig. 65, there is a spanwise



velocity component as well as a highly turbulent region. These two observations suggest there is a significant amount of momentum exchange between flows in the two channels in the bottom half, but the mixing is steadier than in the upper half of the main vane.

#### IV.2.3 Vorticity over the Radial Vane Cavity

The Radial Vane Cavity (RVC) uses a cavity slanted at an angle from the cavity channel in toward the main channel to promote mixing. As the main flow moves over the RVC from right to left, flow rotation is expected in the counterclockwise direction. This expectation was affirmed as positive vorticity (counterclockwise flow rotation) was observed above the RVC in all conditions.

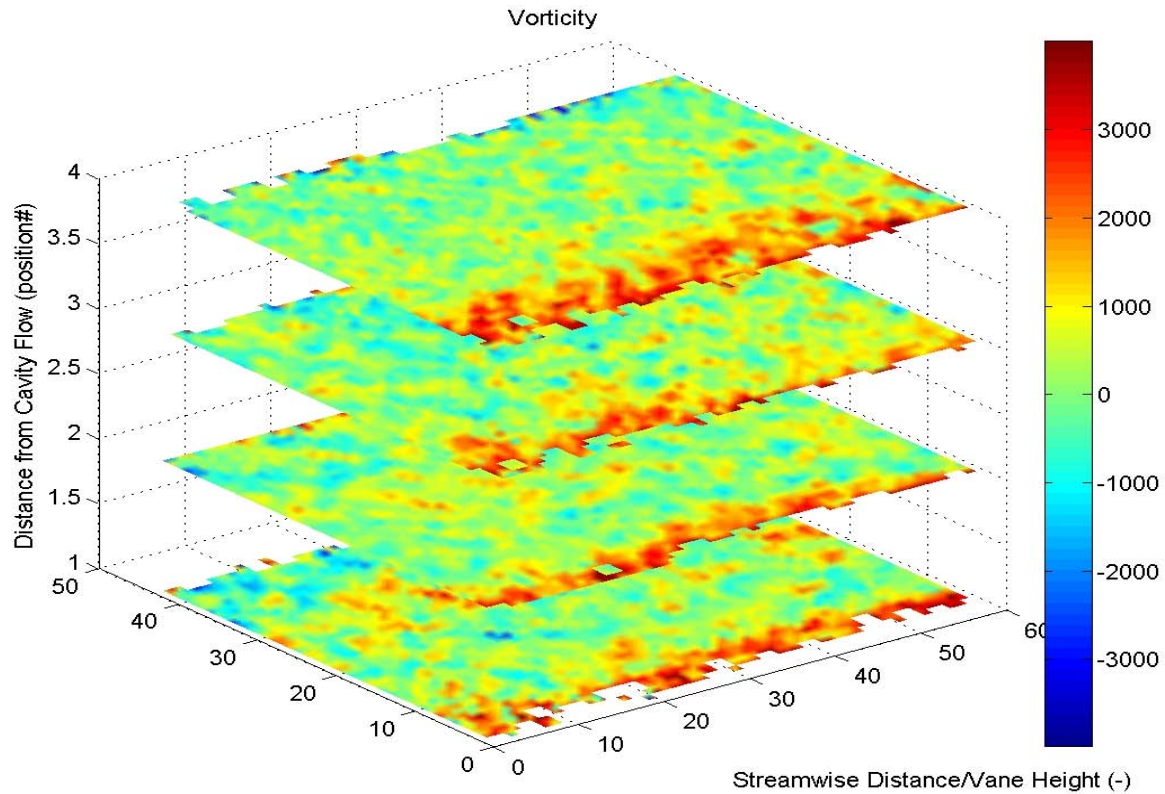


Figure 66. Vorticity progression through within the main channel: straight cavity vane, equivalence ratio : 1.0, main & cavity mass flows: 0.9, 0.09 kg/min

Vorticity levels fluctuate around zero over most of the experimental plane area at all depths within the main channel. As with turbulence, greater fluctuation in vorticity exists near the cavity flow. However the fluctuations remain centered about zero suggesting the flow rotation in the majority of the main channel is due to random turbulence. The only region exhibiting a net vorticity is above the RVC. As cavities are known to create vorticity, rotation in the flow just above the RVC was expected. Another trend observed was that vorticity increased with velocity. As previously discussed, vorticity is calculated by the difference in partial derivatives of the velocity components with respect to their perpendicular directions. Unlike turbulence intensity, vorticity is not non-dimensional as the derivative of velocity with respect to distance yields units of  $\text{seconds}^{-1}$ . This explains why vorticity magnitudes increased with velocity.

Vorticity sharply increased over the RVC as expected, but also increased with distance from the cavity vane as shown below in the histograms of vorticity in Fig. 67.

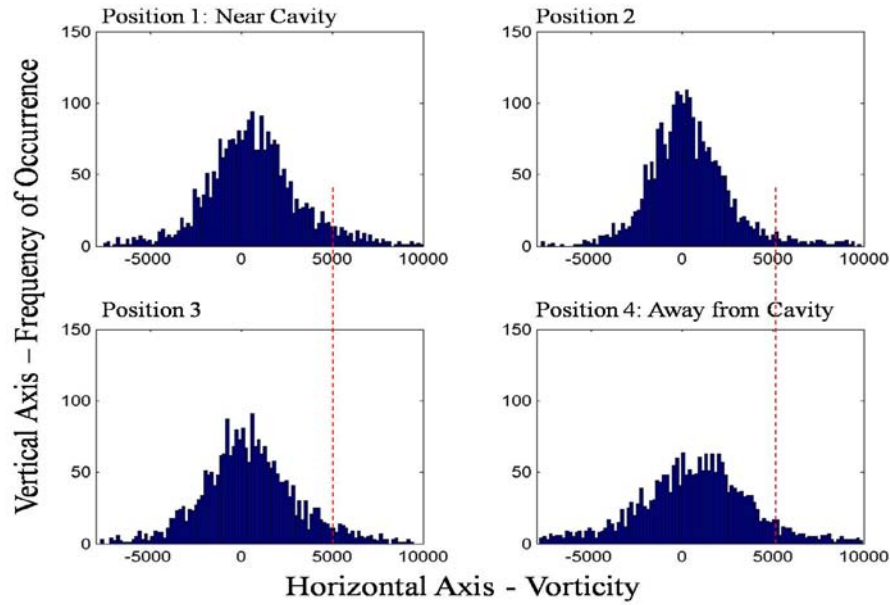


Figure 67. Histograms of vorticity, straight cavity, equivalence ratio: 1.0, main & cavity  
mass flows: 1.5 & 0.15 kg/min

Fig. 67 shows only the total number of interrogation regions whose vorticity values were calculated in each range irrespective of location. However, these histograms clearly show the shape of the distributions. The distributions all appear Gaussian in shape, but only the middle positions (two and three) are centered at zero. The experimental plane locations adjacent to the cavity vane and at the full main channel depth away from the cavity vane (positions one and four) have distributions centered about a positive value. Further, the vorticity values are more widely distributed in position four signifying more regions of higher absolute vorticity.



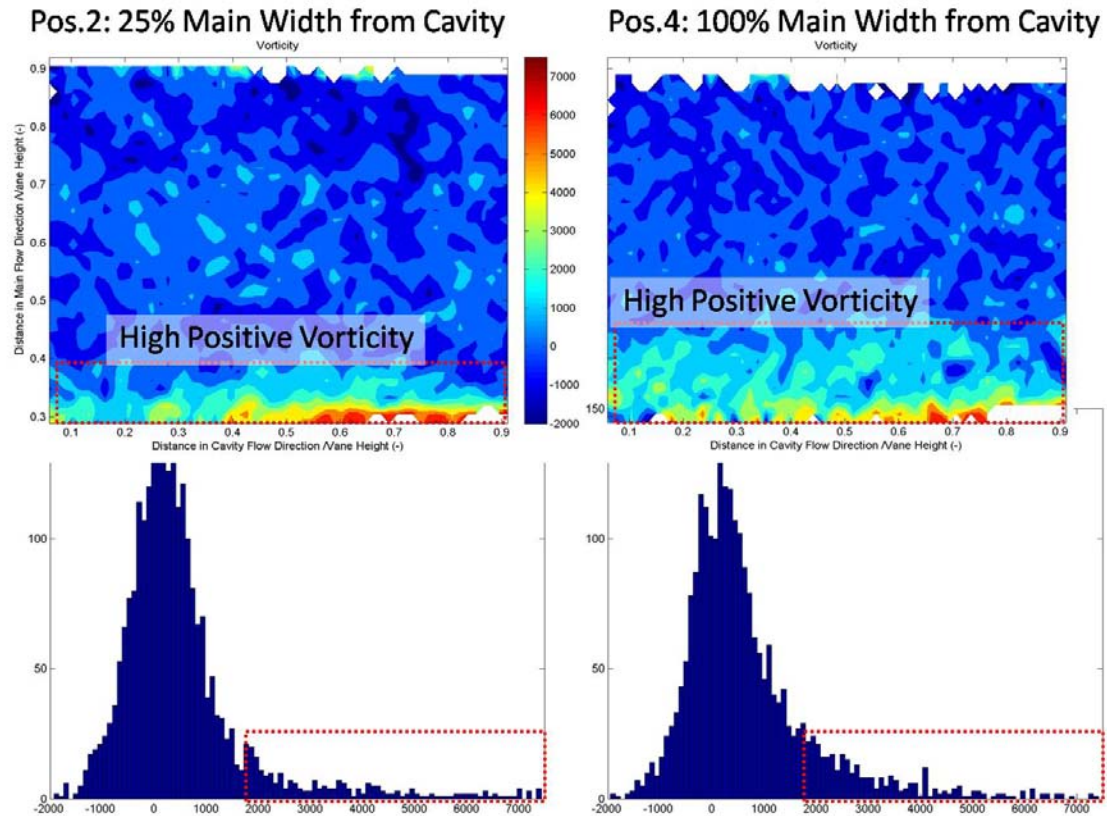


Figure 68. Increase in region of high vorticity shown away from cavity vane: vorticity colormaps & histograms for experimental plane positions 2 & 4

The region exhibiting high positive vorticity, counterclockwise rotation in the flow, was larger away from the cavity vane. This can be explained by the shape of the RVC which is not directly perpendicular to the streamwise velocity, but angled into the flow. The observed increase in vorticity with distance from the cavity suggests that the RVC is effectively building up increasing flow rotation with the angled cavity.

#### IV.2.4 Turbulence Intensity Levels

One of the most evident trends in turbulence intensity is the overall level of turbulence is highest across position one (closest to the cavity vane). It then tapers off to an overall minimum at position three before rising in position four (farthest from the cavity vane). This trend is expected as this location is where the cross-flow in the cavity vane meets the flow in the main vane. Any time two flows are introduced at different velocities, a viscous shear layer forms where momentum exchange can take place. This flow field is precisely what occurs at the interface between the cavity and main flows. The following subplot of histograms illustrates this trend.

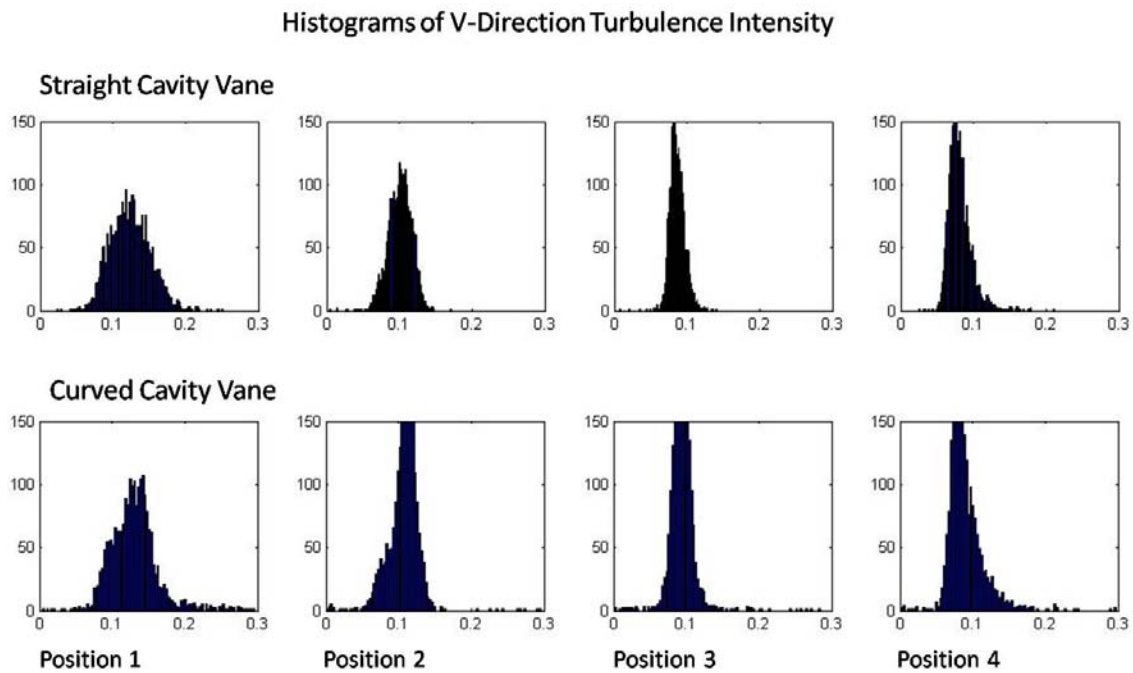


Figure 69. Spanwise turbulence intensity, mass flows of 1.2 & 0.12, eq. ratio 1.0

Fig. 69 above shows histograms of turbulence intensity values. These values are irrespective of their spatial location, but show only the frequency of occurrence for a

given value. For example, the plot in the first column, top row shows at nearly every location over the turbulence map had values between five and twenty percent. The values of turbulence intensity were fairly distributed. The histogram in the third column, top row shows nearly all of the turbulence intensity values were just below ten percent. This narrow distribution shows there is little variability in the value of turbulence intensity at this location and testing condition. The histograms for turbulence intensity in both the straight and curved cavity vane configurations show a wider distribution at position one. The center value in the histograms for position one is also at a higher turbulence intensity value. In position three, the distributions are the narrowest, with turbulence intensity just below ten percent. As expected for random turbulence, the distributions are fairly symmetric in shape.

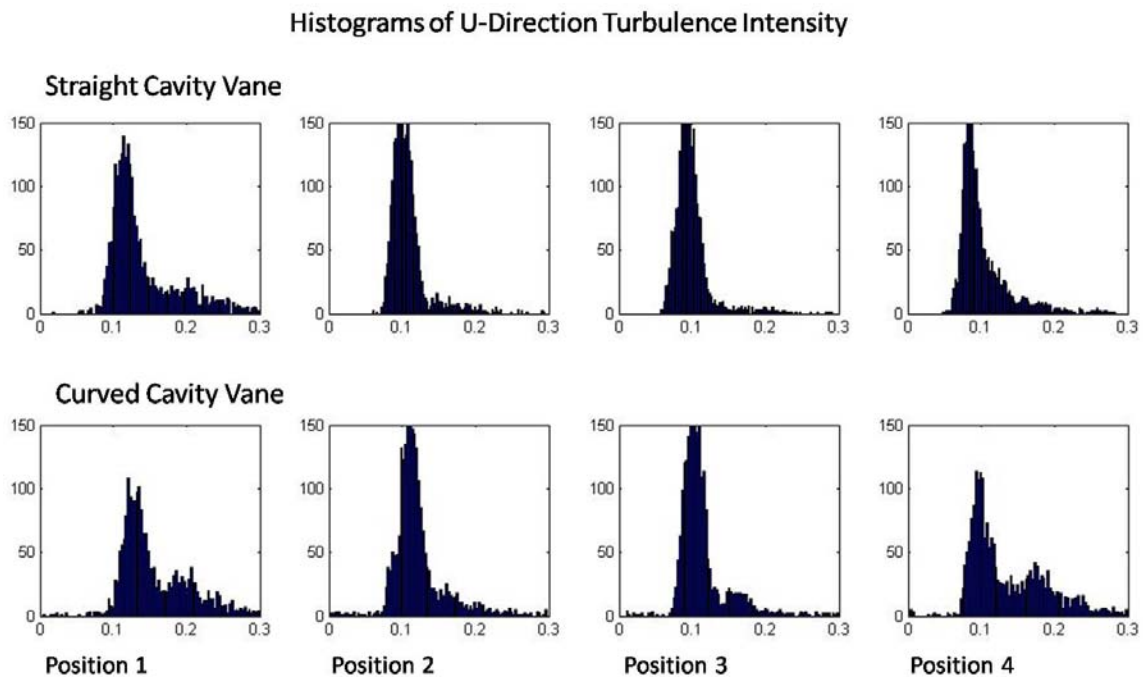


Figure 70. Streamwise turbulence intensity, mass flows of 1.2 & 0.12, equiv. ratio 1.0

The streamwise turbulence distributions reveal similar trends seen in those of the spanwise direction. Position one shows the highest overall turbulence levels with wider distributions, whereas position three shows the narrowest distribution.

Overall RMS averages for turbulence intensity were measured at 14.6% for the straight cavity and 21.3% for the curved cavity. Fig. 71 shows average RMS turbulence intensity values over the four experimental planes. Experimental plane one is near the cavity vane and plane four is the full depth of the main channel (14mm) away from the cavity vane.

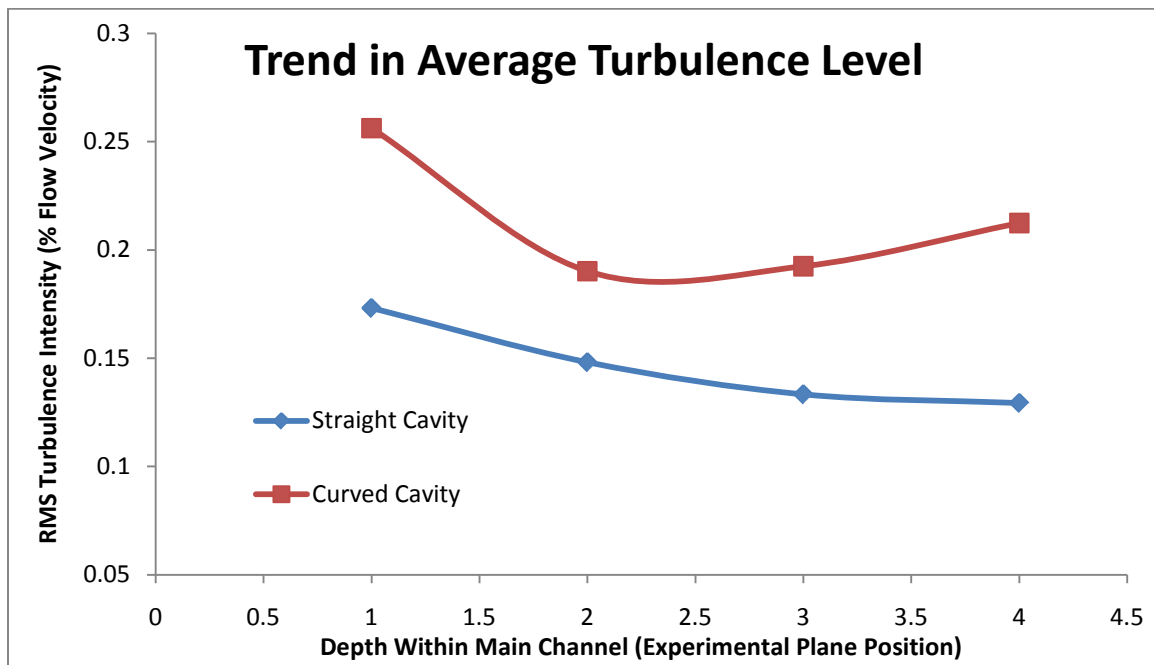


Figure 71. RMS average turbulence intensity over the depth of the main channel

#### IV.2.5 Boundary Layer Induced Turbulence

One significant difference observed in all histograms of streamwise turbulence intensity is their distributions are not symmetrical, as was observed in the spanwise direction. Primary peaks around ten percent turbulence intensity are observed. There is

also a significant right skew to the distribution. In addition to the rightward skew, several conditions show a second peak at higher turbulence intensities (farther right on the histogram). At all measured conditions, this phenomenon appears to be the most pronounced in position one and four. Positions one and four are immediately adjacent to the front and back wall of the UCC main vane, whereas positions two and three are closer to the center. This same trend has been established to occur in fully developed flow through a pipe, where the sheering in the boundary layer near the walls creates turbulence. This turbulence exists primarily in the direction of the main flow velocity. Although the main channel of the UCC test rig is rectangular in cross section, not round, the same phenomenon seems to occur. While the boundary layer effect would explain the rightward skew of the distribution of streamwise turbulence intensity, it does not explain why turbulence intensity in the spanwise is at a minimum in position three. In fact, it is contrary to the observed trend in that a boundary layer primarily formed in the flow direction, the streamwise, would tend to damp out flow perturbations in the spanwise. A minimum in streamwise turbulence intensity is expected at position three as it is not directly adjacent to the cavity vane cross flow, and not close enough to the inner wall to be in the most severe boundary layer region. However, this rational does not explain why spanwise turbulence is also at a minimum in position three. The complexity of this flow field cannot simply be explained by these turbulent trends alone.

#### *IV.2.6 Location of Turbulence Peaks within an Experimental Plane*

There were regions showing higher and lower turbulence intensity values specific to the experimental plane. For example, both spanwise and streamwise turbulence

intensities peaked at the bottom of the experimental plane in position one. The fact that turbulence intensity peaked just above the radial vane cavity suggests that its contribution to flow mixing is significant compared to the contribution resulting from the cavity vane. This trend is shown in Fig. 72 below for streamwise turbulence intensity.

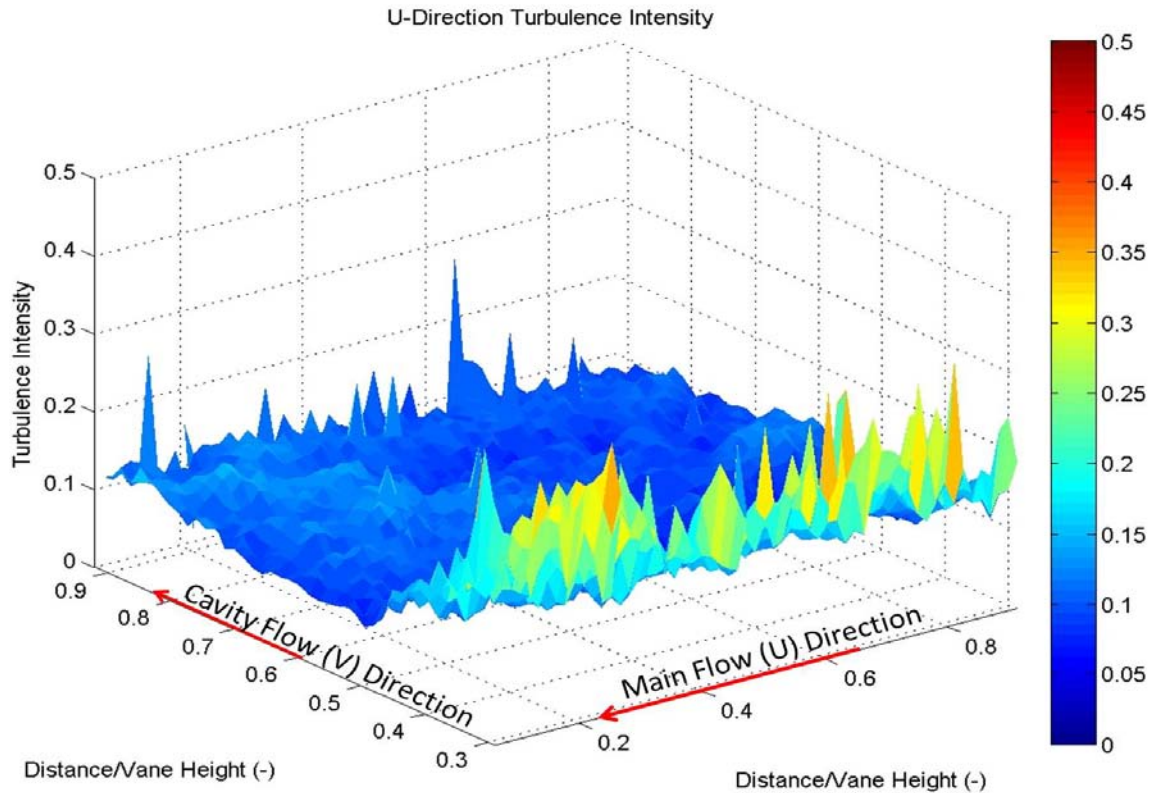


Figure 72. Streamwise turbulence intensity, equiv ratio = 1.0, straight cavity vane config, main & cavity airflows: 0.9 & 0.09 kg/min

As shown in the figure above, the turbulence intensity values are highest near the bottom. There is little increase in turbulence as one examines from the bottom toward the top. This trend is in contrast to the plot of spanwise turbulence intensity. The values are high

over the radial vane cavity as with the streamwise. However, the overall value increases as one examines from the bottom to the top of the surface plot of spanwise turbulence intensity values in Fig. 73 below.

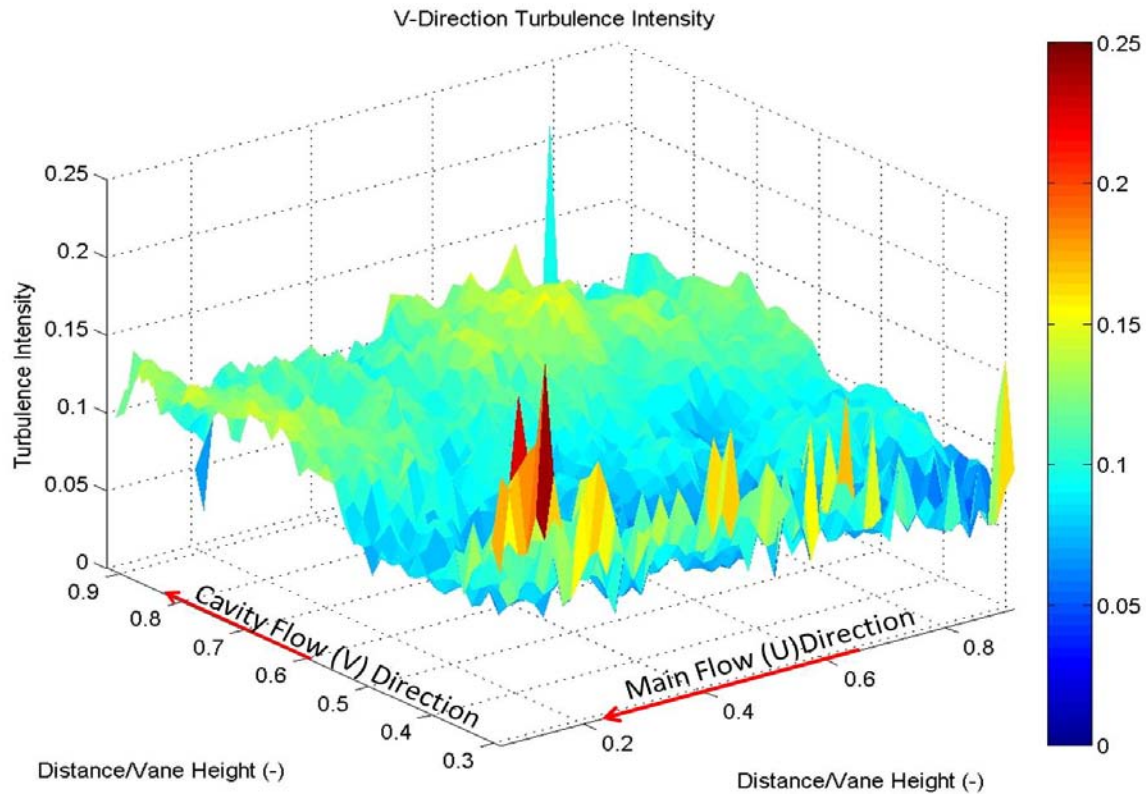


Figure 73. Spanwise turbulence intensity, equiv ratio = 1.0, straight cavity vane config,  
main & cavity airflows: 0.9 & 0.09 kg/min

The height of this surface plot, which corresponds to spanwise turbulence intensity, clearly increases with distance from the bottom of the main vane. Unlike in the streamwise direction, spanwise turbulence intensity is influenced more by the cross flow of the cavity vane than it is by the radial vane cavity. As seen in the figure above, turbulence intensity peaks just above the radial vane cavity, but then drops off with



height above the bottom of the main vane. It then ramps up by a factor of approximately two in the top half of the main vane. This trend was observed for all equivalence ratios and ratios of cavity to main air mass flow, but is only seen in the first experimental plane position. The turbulence intensity subplots in Fig. 74 below show this trend.

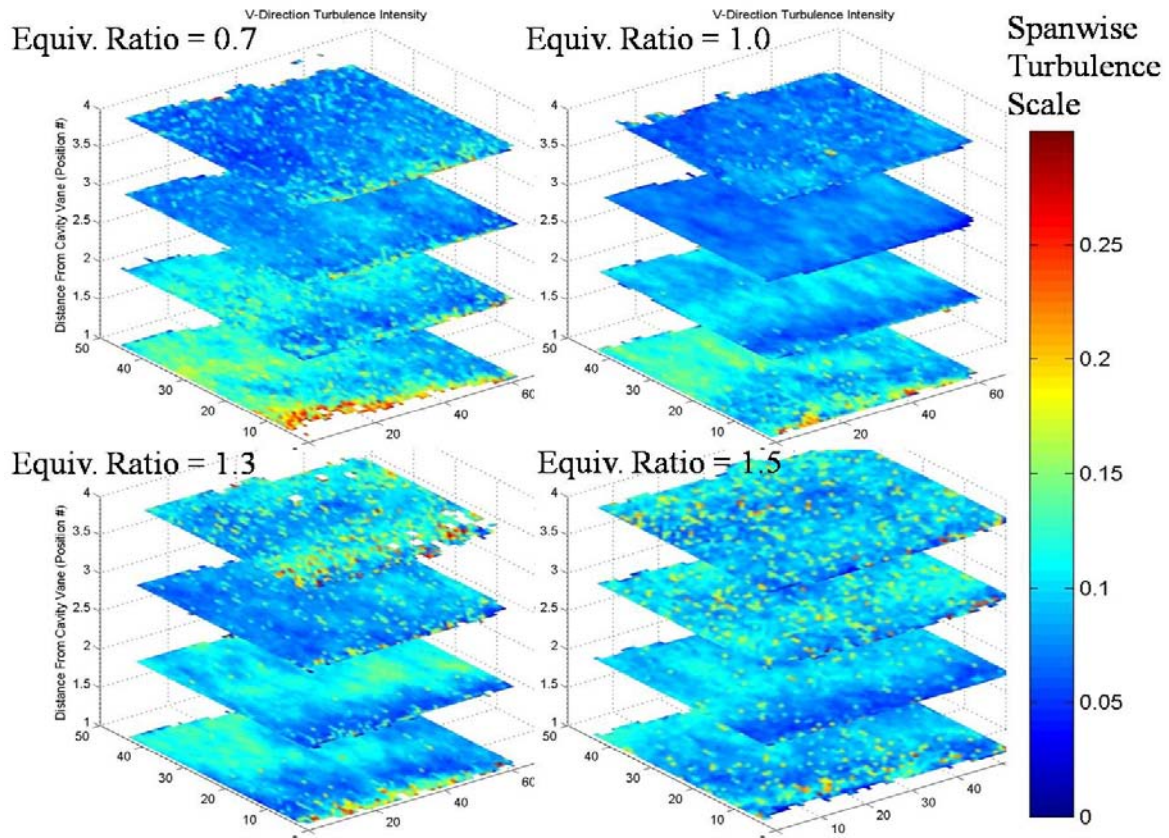


Figure 74. Spanwise turbulence intensity throughout main channel depth: cavity to main mass flow ratio: 0.2, equivalence ratios of 0.7, 1.0, 1.3, & 1.5

Although PIV measurements were taken at four discrete planes within the UCC main vane, the thickness of these planes stacked together would nearly fill the vane depth of 14 mm. Therefore, the slice view shown in the two plots above can be visually interpolated to imply trends. For example, when comparing position two to position one in these slice



plots, the region of higher turbulence, occurring over nearly the entire upper half of position one, shifts down and slightly to the right as shown by the dotted red ovals in Fig. 75 below.

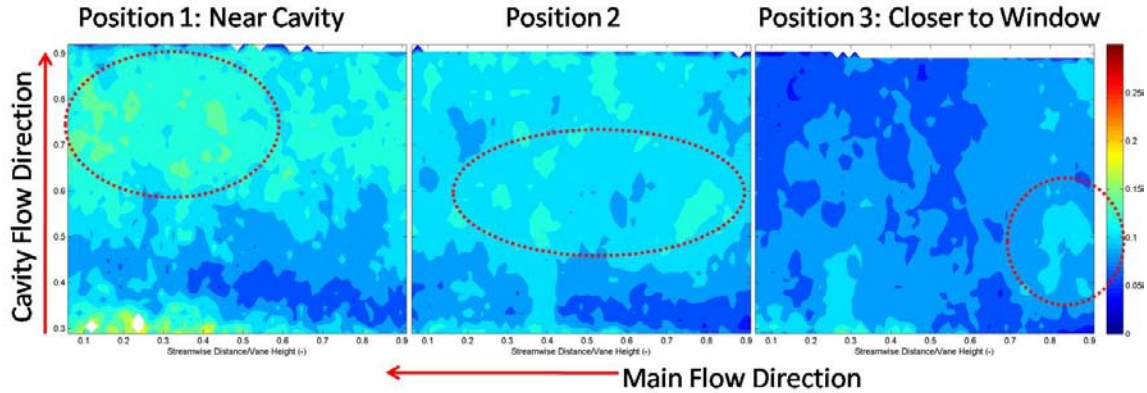


Figure 75. Spanwise turbulence intensity progression with distance from cavity, main & cavity mass flows: 1.5 & 0.15 kg/min, straight cavity channel

The downward shift of spanwise turbulence intensity with distance from the cavity channel was observed in both the straight cavity vane and the curved cavity vane configurations. The above figure shows the region of peak spanwise turbulence intensity occurs successively toward the bottom of the main vane and in the upstream direction. At the full vane depth away from the cavity channel, position four, the spanwise turbulence becomes relatively isotropic except over the RVC which still exhibits a sharp increase in turbulence. This trend demonstrates the spanwise turbulence caused from the cross-flow of the cavity channel penetrates into approximately half the thickness of the main vane for all equivalence ratios except at the richest condition. At an equivalence ratio of  $\phi = 1.5$ , the spanwise turbulence intensity was observed to penetrate farther into the depth of the main channel. The bottom right subplot in Fig. 74, corresponding to

$\phi=1.5$ , shows this trend while the other three subplots, corresponding to the lower equivalence ratios, show spanwise turbulence intensity dropping off after half the main channel thickness ( after the second experimental plane). This is a significant finding in that spanwise turbulence dissipation beyond half the main channel thickness implies the combustion products from the cavity vane may not be properly mixing except just over the RVC at leaner operating conditions. Demonstrating this effect is not based on flow velocity, the main channel mass flow was increased; these results are shown below.

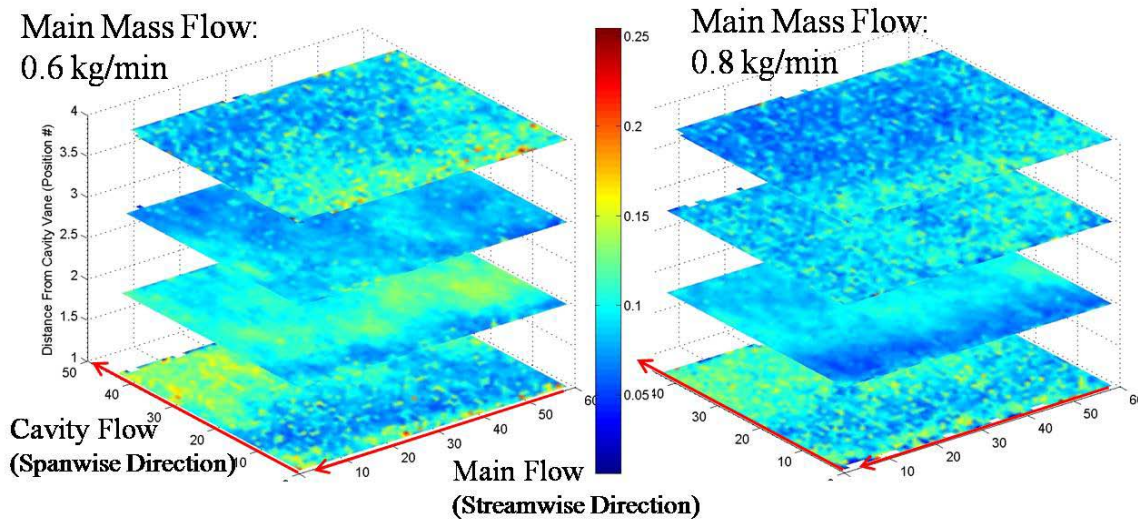


Figure 76. Spanwise turbulence intensity throughout main channel depth: straight cavity vane, equiv. ratio: 1.5, main mass flow: 0.6 kg/min (left) & 0.8 kg/min (right)

Fig. 74 and Fig. Fig. 76 demonstrate the increased spanwise turbulence penetration into the main channel depth for main mass flow rates of 0.31, 0.61, and 0.82 kg/min at a cavity to main mass flow ratio of 0.2 and an equivalence ratio of 1.5.

#### IV.2.7 Mean Turbulence Intensity Dependence on Mass Flow Rate

Turbulence intensity is a measure of relative, average turbulence. The standard deviation, used to measure relative velocity fluctuation over time, is normalized by the root-mean-square (RMS) of the mean velocity at each location. The turbulence intensity should remain relatively constant when the velocity is increased as long as the other parameters are scaled to match. As described in Chapter III, a mass flow increase study was performed with the UCC in both the straight cavity vane and curved cavity vane configurations. In this study, the ratio of mass flows was held constant at 0.1 and the equivalence ratio was held constant at 1.0. Table 9 below shows the mean values of the data taken with the straight cavity vane configuration.

Table 9. Mean values from the mass flow increase study, straight config.

<b>Mean Parameters for UCC in Straight Cavity Vane Configuration</b>								
Equivalence Ratio = 1.0			Cavity to Main Air Mass Flow Ratio = 0.10					
Main m_dot (kg/s)	Position of Exp. Plane	Mean U_Vel (m/s)	Mean V_Vel (m/s)	Mean Stdv_U (m/s)	Mean Stdv_V (m/s)	Mean Nsamp (No.)	Mean TI_u (-)	Mean TI_v (-)
0.6	1	-23.75	1.93	3.19	2.64	36.37	0.14	0.11
0.6	2	-24.76	1.06	2.78	2.49	39.16	0.11	0.10
0.6	3	-25.39	0.22	2.99	2.26	34.14	0.12	0.09
0.6	4	-24.98	-0.34	2.90	2.10	34.46	0.12	0.09
0.9	1	-32.40	2.69	3.74	3.37	45.24	0.12	0.10
0.9	2	-34.02	1.62	3.49	3.36	47.14	0.10	0.10
0.9	3	-34.70	0.44	3.29	2.95	43.80	0.10	0.09
0.9	4	-34.43	-0.11	3.27	2.65	42.28	0.10	0.08
1.2	1	-40.73	3.97	5.97	5.08	34.01	0.15	0.12
1.2	2	-43.28	1.87	4.64	4.37	44.44	0.11	0.10
1.2	3	-43.67	1.10	4.26	3.76	46.48	0.10	0.09
1.2	4	-44.15	0.01	4.50	3.53	39.04	0.11	0.08
1.5	1	-50.40	4.64	6.61	5.73	59.62	0.13	0.11
1.5	2	-52.35	2.81	5.79	5.52	68.46	0.11	0.10
1.5	3	-54.76	0.80	5.29	4.63	46.75	0.10	0.09
1.5	4	-54.27	0.34	5.08	4.26	44.27	0.10	0.08

Several of the trends previously described can be seen in these tabulated mean values, such as higher spanwise turbulence intensity in position one. When comparing the turbulence intensity values from the four different cases, which correspond to increasing mass flow rates, the variation is small enough to consider well within the measurement-uncertainty of this thesis.

Identical conditions were run in the mass flow rate increase study with the curved cavity vane configuration. These values are shown in Table 10 below. In the curved cavity vane configuration the mean streamwise (u) velocities are similar except for in position one, which shows a lower average value due to the increased mixing of the cross-flow. This increased mixing is more pronounced with the curved cavity.

Table 10. Mean values from the mass flow increase study, curved config.

<b>Mean Parameters for UCC in Curved Cavity Vane Configuration</b>								
Equivalence Ratio = 1.0				Cavity to Main Air Mass Flow Ratio = 0.10				
Main m_dot (kg/s)	Position of Exp. Plane	Mean U_Vel (m/s)	Mean V_Vel (m/s)	Mean Stdv_U (m/s)	Mean Stdv_V (m/s)	Mean Nsamp (No.)	Mean TI_u (-)	Mean TI_v (-)
0.6	1	-22.17	2.43	6.12	3.83	32.34	0.29	0.17
0.6	2	-21.56	1.03	3.75	2.52	55.96	0.26	0.18
0.6	3	-22.78	0.51	5.90	3.42	41.20	0.28	0.17
0.6	4	-24.18	-0.03	7.05	3.98	33.18	0.31	0.17
0.9	1	-29.47	3.55	6.21	4.16	43.47	0.30	0.20
0.9	2	-32.07	2.07	5.86	3.93	52.18	0.19	0.14
0.9	3	-34.64	0.84	4.76	3.61	53.36	0.14	0.11
0.9	4	-34.72	0.28	6.14	3.69	43.54	0.19	0.12
1.2	1	-35.88	4.31	6.98	4.77	44.05	0.28	0.16
1.2	2	-41.32	3.06	5.28	4.51	61.77	0.14	0.12
1.2	3	-42.13	1.37	4.91	3.97	57.92	0.14	0.11
1.2	4	-42.65	0.36	6.35	3.82	44.33	0.19	0.13
1.5	1	-44.51	5.53	7.86	5.63	55.16	0.31	0.16
1.5	2	-51.20	3.54	6.36	5.52	67.40	0.13	0.12
1.5	3	-52.22	1.47	6.04	4.86	59.39	0.14	0.10
1.5	4	-52.62	0.49	5.64	4.29	64.23	0.14	0.11

Similarly, the spanwise (v) velocities are all higher for the curved data in position one and two. These trends are expected. What was not expected was a turbulence intensity dependence on the mass flow rate. Further, a decrease in turbulence intensity with increasing mass flow was observed. When the values for each set of runs are averaged and plotted for comparison, the straight section data shows little variation with increasing mass flow. However, the curved cavity vane section data shows a decrease in the mean turbulence intensity with increasing mass flow as shown in the figure below.

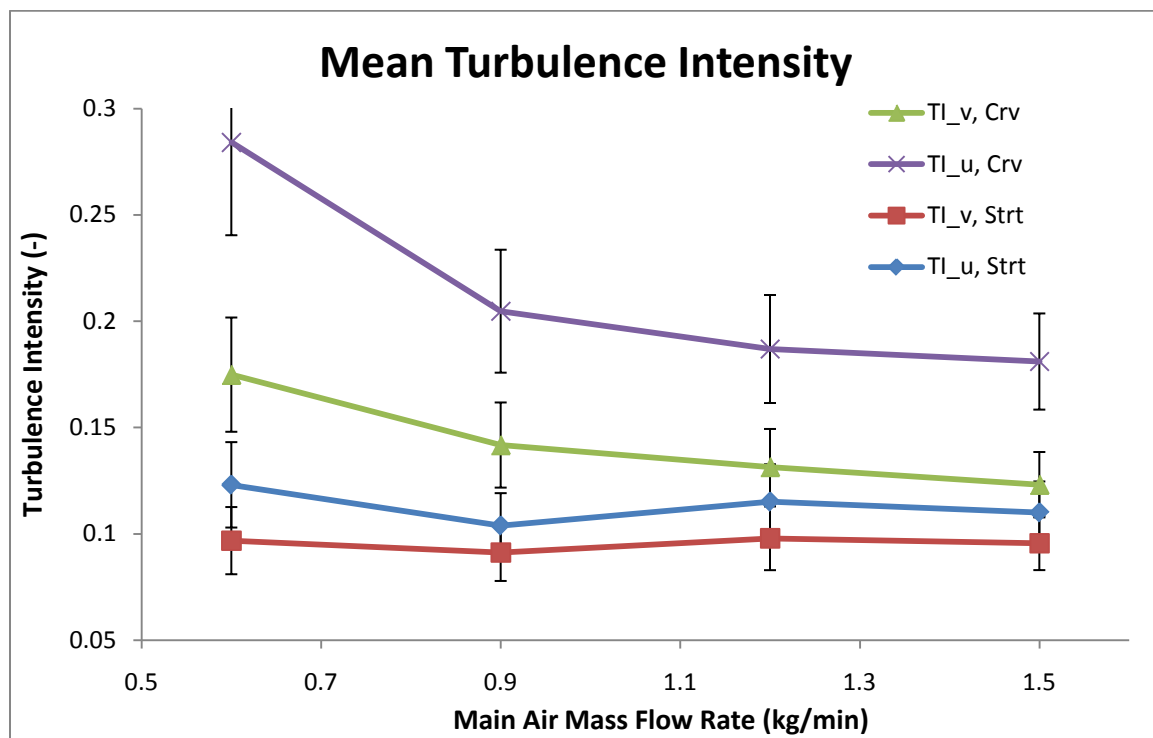


Figure 77. Mean turbulence intensity dependence on mass flow rate with 95% CI

This trend is most pronounced in the streamwise (u-direction) turbulence intensity, but can also be seen in the spanwise (v-direction) data as well.

#### *IV.2.8 Possible Error in PIV Measurement*

The trend of turbulence intensity decrease with mass flow rate would become less evident without the data point from the 0.6 kg/min mass flow rate condition. As discussed in the Uncertainty Analysis section of this chapter, the mass flow was less steady at the lower flow rates. The variability in the main mass flow rate is not likely to cause a significant increase in turbulence. However, a quick drop in the cavity mass flow rate would create a proportional increase in the cavity equivalence ratio. If the fluctuations in cavity air flow were to result in a significant portion of the fuel entering the main flow as it began to burn, the main flow would experience a decrease in density from the heat addition. This heat addition would result in fluctuations of velocity through the main channel.

Another possibility for the measured increase in turbulence is some of the PIV data was unreliable. When comparing the calculated turbulence values some of the data appeared to have smoother contours than others, suggesting higher and lower noise levels in the measurements. Consider Fig. 78 and Fig. 79 below that show spanwise turbulence intensity for positions one and three of the straight cavity vane configuration at 0.6 and 1.5 kg/min mass flow rates.



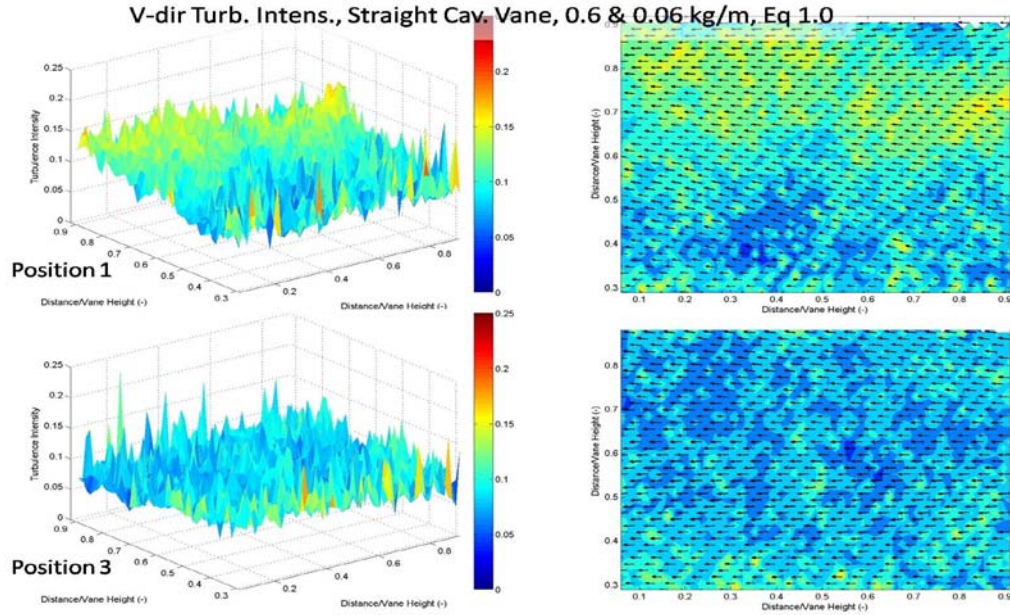


Figure 78. Surface & contour plots of spanwise turbulence intensity: straight cavity vane config., 0.6 & 0.06 kg/min main and cavity mass flow rates, equiv. ratio = 1.0

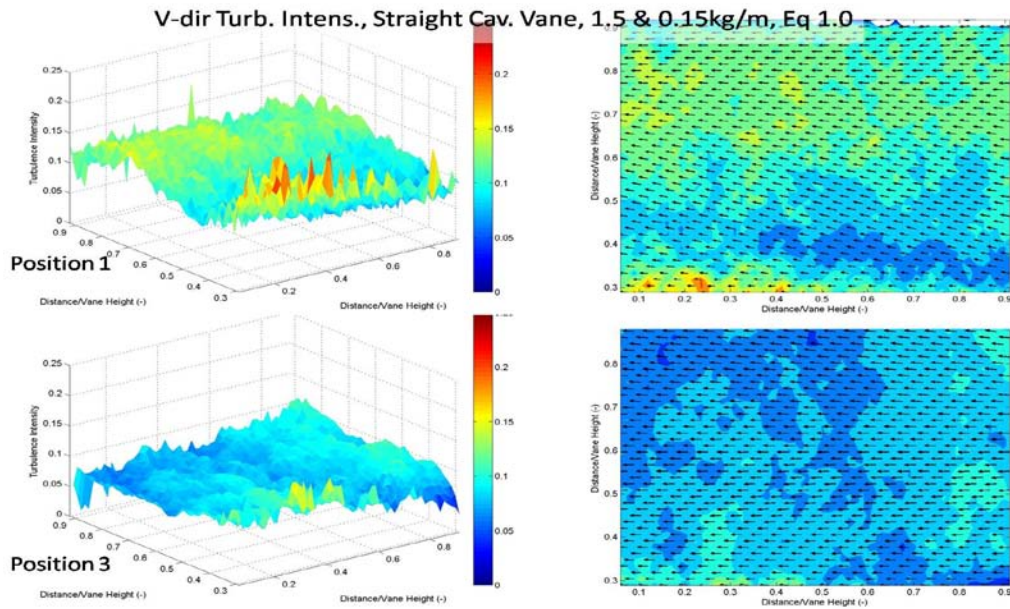


Figure 79. Surface & contour plots of spanwise turbulence intensity: straight cavity vane config., 1.5 & 0.15 kg/min main and cavity mass flow rates, equiv. ratio = 1.0

These figures present overall turbulence intensity values following the same trends previously discussed. They also show another observed trend that data taken at the lower flow rates, even at the same flow ratios and equivalence ratio, seemed to have a higher level of noise. This trend of data appearing “noisier” at the lower mass flow rates was significantly more pronounced in the curved cavity vane configuration. Fig. 80 and Fig. 81 below show data taken in the curved configuration at the same conditions as the previous two figures, which were from the straight configuration.

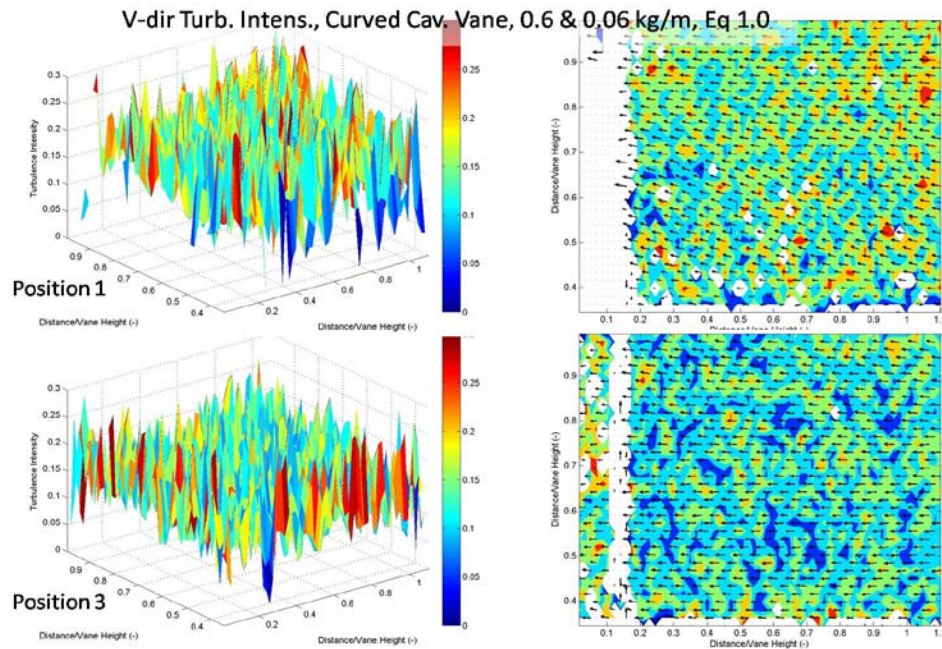


Figure 80. Surface & contour plots of spanwise turbulence intensity: curved cavity vane config., 0.6 & 0.06 kg/min main and cavity mass flow rates, equiv. ratio = 1.0



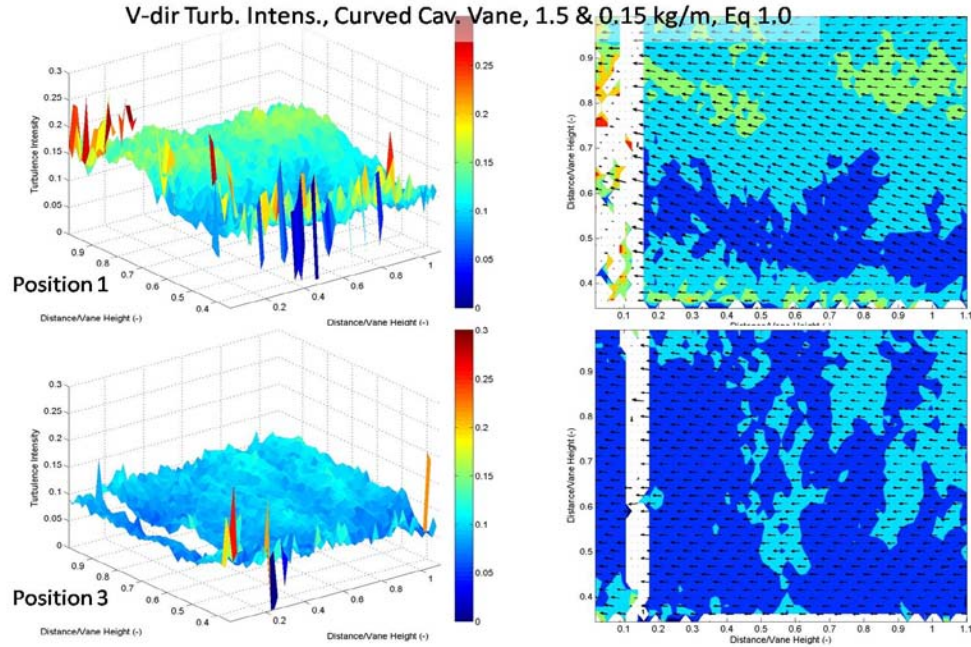


Figure 81. Surface & contour plots of spanwise turbulence intensity: curved cavity vane config., 1.5 & 0.15 kg/min main and cavity mass flow rates, equiv. ratio = 1.0

Contributors to this result could be of obfuscation of the optical window, low seed density, or out-of-plane velocity. Due to their small size, two  $\mu\text{m}$  mean diameter, the silicon carbide seed particles would coat the quartz window over time. This coating decreases the transparency of the window resulting in a drop of signal-to-noise ratio. However, if the windows were coated, the data from positions two through four, which was taken after the data from position one, would have experienced the same problem. Low seeding density was a common issue that presented intermittently throughout experimentation. Even after the modification performed on the particle seeder, discussed in Chapter III, the seed density was still observed to be cyclic and uneven in time. Out-of-plane velocity is another possible source of error in PIV measurements.

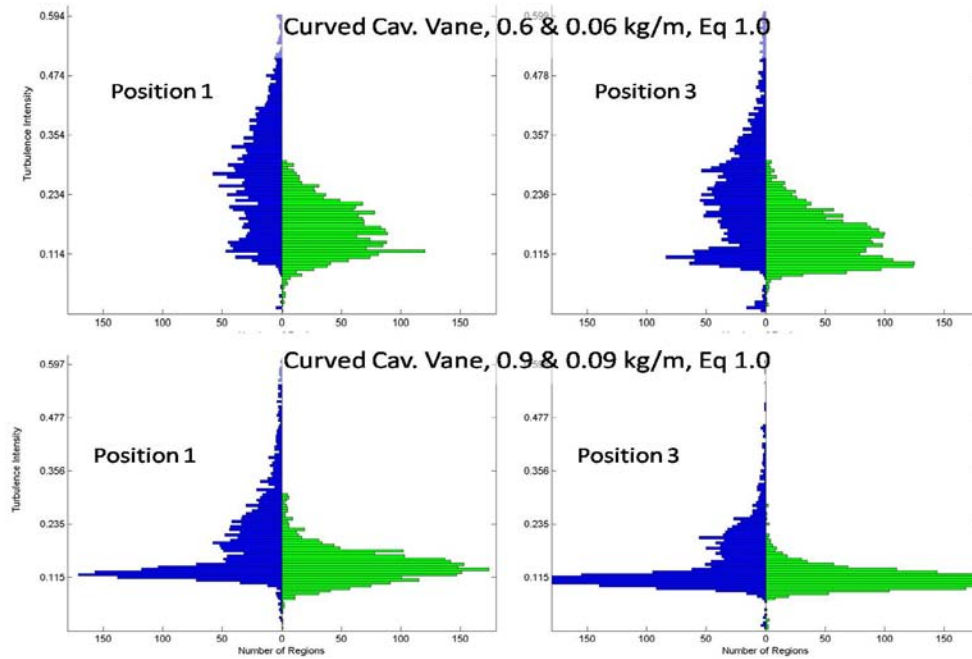


Figure 82. Histograms of turbulence intensity: streamwise TI on left, spanwise TI on right, ratio of mass flow rates = 0.1, equivalence ratio = 1.0

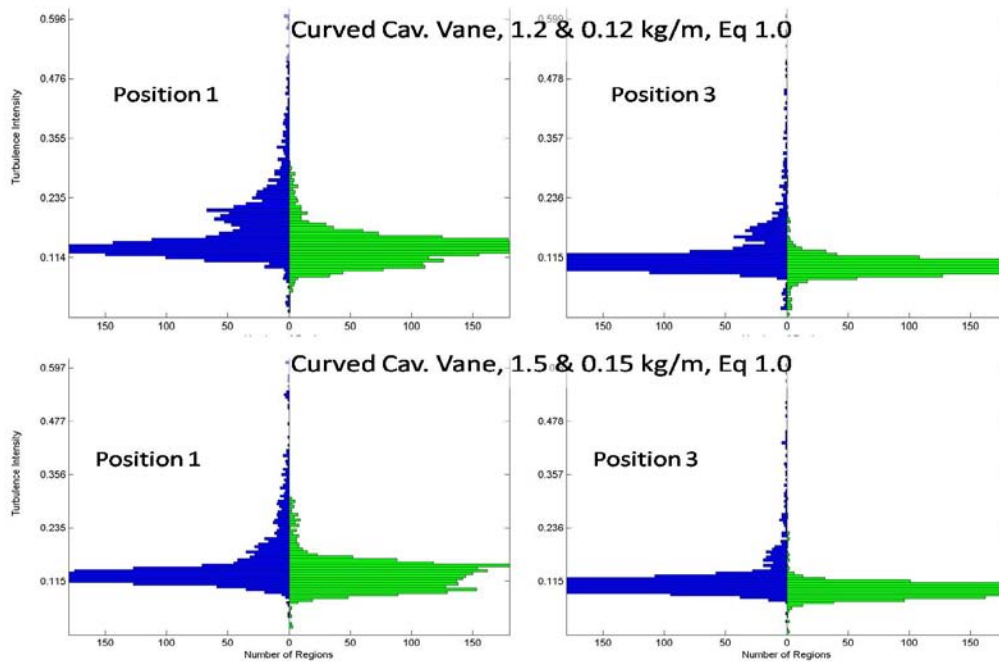


Figure 83. Histograms of turbulence intensity: streamwise TI on left, spanwise TI on right, ratio of mass flow rates = 0.1, equivalence ratio = 1.0

The histograms of turbulence intensities taken at successively higher mass flow rates shown in Fig. 82 and Fig. 83 exhibit narrowing of the turbulence distributions in both spanwise (shown on left column of plots) and streamwise (shown on right column of plots). Out of plane velocity is the likely cause of this phenomenon, the effect of which appears to decrease with increasing flow velocity.

As discussed in Chapter II, out-of-plane velocity causes error in the PIV measurement which manifests as a loss-of-pairs in the cross-correlation. This loss becomes a problem when there is a significant velocity component in the third dimension, defined as normal to the x-axis and y-axis, resulting in particles moving through, instead of parallel to the experimental plane. This potential error is significantly stronger in the data from the curved configuration, suggesting there is more out-of-plane velocity in the curved configuration data. This conclusion is not surprising as the flow path in the curved cavity vane physically turns into the main channel rather than flowing past it in a perpendicular plane.

### **IV.3 Summary of Observed Trends**

The following trends were observed:

- Higher spanwise velocity component near the cavity vane
- Higher overall turbulence intensity near the cavity vane
- The higher turbulence intensity from the cavity vane penetrates into approximately half the depth of the main vane and dissipates thereafter for all

cases except at the highest equivalence ratio of  $\phi=1.5$  where the turbulence penetrates through the full depth of the main channel.

- Peak spanwise turbulence occurs in the top of the main channel near the cavity vane and migrates downward with distance from the cavity vane.
- The Radial Vane Cavity appears to generate significant vorticity that increases with velocity and with distance from the cavity vane.
- Boundary layer effects for streamwise turbulence are significant along the wall farthest from the cavity vane but insignificant near the cavity.
- Possible boundary layer effects in appear to increase spanwise turbulence
- Turbulence intensity is relatively independent of the mass flow rate for the straight cavity configuration, but decreases with mass flow in the curved configuration
- Possible out of plane velocity is significant with low mass flows in the curved cavity vane creating high deviations in PIV measurements

## **V. Conclusions and Recommendations**

### **V.1 Satisfaction of the Research Objectives**

The overarching goal of the UCC research effort at AFIT is to obtain a physical understanding of combustion reaction with body force effects so the Ultra Compact Combustor is developed as a practical combustor. To obtain that goal, three specific research objectives are identified: (1) investigate the effect of the body forces independent of the velocity effect; (2) investigate whether trapped vortex combustion can be sustained effectively in the UCC; and (3) investigate the interaction between the main cavity, the vane cavity, and the main flow. This thesis was designed primarily to satisfy objective one, but did address objectives two and three.

In order to understand body forces, two factors must be determined: (1) the velocity and (2) the path. The PIV measurements taken in this thesis address both these factors. 2-D velocity profiles were measured throughout the width of the main vane over the RVC at several main flows, cavity flows, and equivalence ratios. Average velocities were shown to decrease and become more chaotic over the RVC and become more steady through the width of the main channel. In addition to the magnitude, the direction of these measurements also addressed this first research objective. Variation in the main flow direction was observed to be somewhat predictable by the proximity to the cavity vane as well as the RVC.

The second objective of sustaining trapped vortex combustion in the UCC was demonstrated as the equivalence ratio and mass flow rates were throttled up and down over a hundred times without a single instance of flame extinction. Turbulence

intensities remained relatively constant with increasing velocity suggesting operability over a wide range of velocities. As the RVC had a fixed geometry in this thesis, the third objective was not fully explored. However, the high positive vorticity measured over the RVC shows it is effectively creating flow rotation. Further, peak turbulence intensities measured above the RVC in the plane closest to the cavity were approximately twice the average for the plane suggesting significant turbulent mixing.

## **V.2 Physical Interpretation of Observed Trends**

Some of the observed trends from Chapter IV appear to be directly explainable, while the underlying cause of others remains yet undetermined. The following sections will attempt to elucidate the potential mechanics behind some of the trends previously discussed.

### *V.2.1 Variance in Velocity*

Cavity flow appears to be mixing into the main channel effectively according to the plots of spanwise velocity component, which Fig. 61 and Fig. 62 on page 136 show fairly linear increase in spanwise velocity as the experimental plane was moved closer to the cavity vane. As the main channel flows only in the streamwise direction, mixing of the flows will result in a net spanwise velocity proportional to the degree of mixing. Due to this spanwise velocity imparted onto the main flow by the cavity vane, mixing of the two flows is occurring. Although vorticity was observed to be a strong function of velocity, the turbulent fluctuation in terms of percent of the total velocity was relatively unaffected by velocity. This lack of velocity dependence on turbulence suggest a wide

range of operability with a relatively constant and predictable level of turbulence and flow mixing.

#### *V.2.2 Variance in Turbulence Intensity*

Examining the relative turbulence intensity in the main channel as a function of distance from the cavity is another way of measuring flow mixing. The Radial Vane Cavity (RVC) generates strong variation in velocity at all depths within the main channel. However, turbulence intensities, especially in the spanwise direction, over the entire plane drop off after approximately half the width of the main channel away from the cavity vane. This decrease in overall turbulence suggests that other than just above the RVC, cavity flow is not mixing into the full depth of the main channel. Large gradients in streamwise velocity were observed directly over the RVC. Streamwise turbulence intensities increased roughly three-fold over the distance of approximately one tenth of the main vane height. The RVC is clearly generating turbulent mixing, but may need to be increased in height to affect more of the main flow.

#### *V.2.3 Variance in Vorticity*

Overall vorticity levels exhibited a zero-mean value for the majority of the experimental plane area except just over the RVC. This region showed strong positive vorticity that increased with velocity and with distance from the cavity flow. As the depth of the cavity in the RVC is constant, the sweep is the probable cause of this increasing vorticity. However, the orientation of the RVC suggests it generates flow rotation mainly in the plane parallel to the main channel and cavity vane. Flow rotation

only in this plane would do little to promote mass transfer. Currently, only the angle of the RVC appears to be beneficial in mixing the cavity and main flows.

### **V.3 PIV in the UCC**

Whole field velocity measurements in the main channel of the AFIT sectional UCC rig have now been performed in the plane parallel to the main and cavity channels. The curved cavity vane was shown to mix the cavity flow into the main channel more than the straight cavity vane, as expected. The RVC was shown to generate turbulence and vorticity which is likely to increase mixing. The PIV measurements in this thesis were taken directly over the RVC in the main channel, but did not extend downstream. As such, the flow field downstream of the RVC remains unmeasured. Over the RVC, regions of high and low turbulence remain distinct. PIV measurements taken downstream of the RVC by at least the length of the main cavity would show how quickly the turbulence and mixing occurs. Further, integrating the velocity measurements over the full depth of the main channel will allow direct calculation of the mass flow downstream of the RVC to determine how much of the cavity flow entered into the main channel.

Due to the 2-D nature of PIV and the experimental setup used in this thesis, the velocity component in the third dimension remains unmeasured. This third dimension is paramount to understanding the flow interactions as it is the direction cavity flow must travel in order to mix into the main channel. Rotating the laser sheet by ninety degrees and moving the camera to stay perpendicular to the laser sheet would allow PIV



measurements in this third dimension. Quantifying this velocity component perpendicular to the cavity vane would also have a synergistic effect on reducing the error of PIV measurements as the out of plane velocity component would already be determined as the spanwise velocity measured in this thesis. Further, the measured spanwise velocity would quantify the out of plane velocity component for all data taken in this thesis.

#### **V.4 Future work**

Flow ratios and equivalence ratios were chosen in this thesis based on previous research performed, mainly by Hankins and Lakusta. The optimal case identified in this thesis ( $\phi=1.5$ , cavity airflow 20% of main) was at the limit of the test matrix in terms of equivalence ratio and cavity to main airflow ratio. Further investigation should be performed to investigate if the trend of increased spanwise turbulence intensity and spanwise velocity penetration into the main channel width continues with increasing equivalence ratio.

If further PIV measurements are to be taken a few key modifications should be made to the experimental setup.

- The camera should be angled at slightly more than ninety degrees to the laser sheet. This will decrease the amount of scattered light from the cavity vane reaching the camera and decrease the noise floor from that region
- The second camera should be used to take simultaneous PIV measurements downstream of the RVC. The PIV system includes a second camera for use with

stereoscopic PIV. This second camera could be used to increase the overall field of view without moving the camera back and decreasing resolution.

- The MatLab® link should be installed that is available with the Dynamic Studio v.3.3 ®. The PIV software, Dynamic Studio ® stores all data in a proprietary format not readable outside the program. Data files must be exported one-by-one, a tedious process. The MatLab ® link should make this process much more efficient.

The sectional AFIT UCC model may be creating flow patterns not representative of an axi-symmetric UCC. Both the curved and straight cavity vanes have optical-access windows mounted flush with the outer surfaces. As the walls of the model are much thicker than the quartz windows, there are two large cavities behind the windows, each more than a quarter inch in depth. These large cavities are almost certainly the cause of the dual-vortex flame shape Lakusta and Hankins observed in the cavity exhaust. As these cavities are significantly larger than the main combustion cavities within the cavity vane, the current design may not be accurately representing the UCC concept.

As previously discussed, the Radial Vane Cavity appears to be generating significant turbulence and vorticity, but may need to be modified to more effectively draw in the cavity vane exhaust. The RVC should either be tapered to be larger at the bottom, or canted into the direction of the circumferential cavity flow. With an angled RVC, a component of the generated vorticity would be in the direction of the cavity flow. This vorticity would further increase mass transfer and should help increase stability.

## Appendix A

### Data Processing with MatLab®

Matlab® is a powerful data processing and graphing tool with extensive online help available. The following code was used to read in comma delimited data files, calculate flow parameters, then graph and save the generated plots. The entire data processing portion of the code is included below. Only one of the plotting types used in this thesis is included in this code for brevity.

```
%%%%%%%%%%%%%%%%%%%%%%%%%%%%%%%%%%%%%%%%%%%%%%%%%%%%%%%%%%%%%%%%%%%%%%%%
% Levi Thomas
% Roctober 2009
%
% Program written to process particle image velocimetry data from *.csv
% files and calculate and plot vector maps, turbulence intensity, and
% uncertainty. It is specific to data files produced from the Dantec
% PIV software in the number of header lines it ignores and how it
% numbers the independent axis such as x and y values.
%
%%%%%%%%%%%%%%%%%%%%%%%%%%%%%%%%%%%%%%%%%%%%%%%%%%%%%%%%%%%%%%%%%%%%%%%%

clear all
close all
clc

Interactive = input('Choose (1)Interactive; (2) Default Values: ');

if Interactive == 1
    % Ask user for input parameters
    SvPlt = input('Save Plots? (1) Yes; (2) No: ');
    nRowsPlot = input('Enter number of rows to plot: ');
    nColsPlot = input('Enter number of columns to plot: ');
    Tmin_v = input('Cutoff for Min V-dir Turbulence: ');
    Tmax_v = input('Cutoff for Max V-dir Turbulence: ');
    Tmin = input('Cutoff for Min U-dir Turbulence: ');
    Tmax = input('Cutoff for Max U-dir Turbulence: ');

else
    % Hard Code input parameters
    SvPlt = 1;
    nRowsPlot = 2;
    nColsPlot = 2;
    Tmin_v = 0;
    Tmax_v = 0.3;
    Tmin = 0;
    Tmax = 0.5;
```

```

end

Z = 1.96;          % this is the "standard score" for a 95% Conf. Interv.
ErrorMin = 0;      % These are percent cutoff values for plotting
ErrorMax = 30;

VaneH = 30.5;      %Vane Height (this is the dist I am using to
Normalize

%outlier = input('Display outliers as (value): ');
outlier = NaN;

%thead = input('Enter number of lines of header to discard: ');
thead=9;

Ncase=0;           %count will be the counting variable that  = nRowsPlot
+ nColsPlot

% this says only record U and V values when k is a multiple of VecFilt

if (nRowsPlot ==1) && (nColsPlot ==1)
    VecFilt = 3;
else
    VecFilt = 7;
end

for i = 1:nRowsPlot
    for j = 1:nColsPlot
        clear data;
        Ncase = Ncase+1;
        disp(sprintf('Select data to be plotted in row #: %g and col#:
%g', i, j));

        [FileName,PathName] = uigetfile('*.csv','Select Comma Separated
File');
        cd(PathName);

        data = csvread(FileName,nhead,0);          %read in all data
starting with position (nhead,0)
        xcount(:,Ncase) = data(:,1);
        ycount(:,Ncase) = data(:,2);
        x_mm_vec(:,Ncase) = data(:,5);
        y_mm_vec(:,Ncase) = data(:,6);
        %these form the ind. axis for the vector plots

        % not recording all values bc vec plot is too busy looking
        %U_vel(:,Ncase) = data(:,9);
        %V_vel(:,Ncase) = data(:,10);

        xAx_count = 1;
        for k = 1:length(xcount(:,Ncase))
            %In this loop, k is the row of the data from the .csv file

```

```

        Nsamp(ycount(k,Ncase)+1,xcount(k,Ncase)+1,Ncase) =
data(k,15);      %populate the n-sampels matrix
        Corr(ycount(k,Ncase)+1,xcount(k,Ncase)+1,Ncase) =
data(k,14);      %populate the n-sampels matrix

        %The vector plots are way too "busy" looking so we only
plot
        %them when k is a multiple of VecFilt
        if mod(k,VecFilt) ==0;
            U_vel(k,Ncase) = data(k,9);
            V_vel(k,Ncase) = data(k,10);
        else
            U_vel(k,Ncase) = outlier;
            V_vel(k,Ncase) = outlier;
        end

        % store the turb values unless it has already been flagged
        % Dynamic Studio puts an '8' in the status column for fail
        if data(k,17) ~= 8;
            Var_u = data(k,11);
            Var_v = data(k,12);
            Var_rms = (Var_u^2 + Var_v^2)^(1/2);
            %Intermediate var to store stdev(V) value
            U_rms = ((data(k,9))^2 + (data(k,10))^2)^(1/2);
            %Intermediate var to store rms(u,v) value
            %this is what I am normalizing the turbulence by to
            %get Turb. Intens.
            TIu = Var_u/U_rms;
            TIv = Var_v/U_rms;
            TIrms = Var_rms/U_rms;

            Turb_mat_u(ycount(k,Ncase)+1,xcount(k,Ncase)+1, Ncase)
= TIu;
            Turb_mat_v(ycount(k,Ncase)+1,xcount(k,Ncase)+1, Ncase)
= TIv;
            Turb_mat_rms(ycount(k,Ncase)+1,xcount(k,Ncase)+1,
Ncase) = TIrms;
            %populate turbulence matrix in level = Ncase)
            Turb_line_u(k,Ncase) = TIu;
            Turb_line_v(k,Ncase) = TIv;
            Turb_line_rms(k,Ncase) = TIrms;
            %vector of turb values. same as Turb_mat, but some
            %plots (histogram plot) req this format instead of a
Mat.

            N_temp =
Nsamp(ycount(k,Ncase)+1,xcount(k,Ncase)+1,Ncase); %temp var to hold N
value
            ErrorMat(ycount(k,Ncase)+1,xcount(k,Ncase)+1, Ncase) =
200*Z*TIrms/((N_temp)^0.5);
            % This is the equation of statistical accuracy. It
assumes
            % data has a gaussian distribution. It is actually the

```

```

        % standard deviation on the numerator. Then
        % divide by the RMS of U to get it into %. This is the
        % same as having the RMS TI in the numerator. The 200
is
        % because it is +/- and in terms of percent.
    else
        Turb_mat_u(ycount(k,Ncase)+1,xcount(k,Ncase)+1, Ncase)
= outlier;
        Turb_mat_v(ycount(k,Ncase)+1,xcount(k,Ncase)+1, Ncase)
= outlier;
        Turb_mat_rms(ycount(k,Ncase)+1,xcount(k,Ncase)+1,
Ncase) = outlier;
        Turb_line_u(k,Ncase) = outlier;
        Turb_line_v(k,Ncase) = outlier;
        Turb_line_rms(k,Ncase) = outlier;
        ErrorMat(ycount(k,Ncase)+1,xcount(k,Ncase)+1, Ncase) =
outlier;
    end

    % Filter out data outside bounds or at '0'
    if Turb_mat_u(ycount(k,Ncase)+1,xcount(k,Ncase)+1,
Ncase)<Tmin
        Turb_mat_u(ycount(k,Ncase)+1,xcount(k,Ncase)+1, Ncase) =
outlier;
    elseif Turb_mat_u(ycount(k,Ncase)+1,xcount(k,Ncase)+1,
Ncase)>Tmax
        Turb_mat_u(ycount(k,Ncase)+1,xcount(k,Ncase)+1, Ncase) =
outlier;
    elseif Turb_mat_u(ycount(k,Ncase)+1,xcount(k,Ncase)+1,
Ncase)==0
        Turb_mat_u(ycount(k,Ncase)+1,xcount(k,Ncase)+1, Ncase) =
outlier;
    end
    if Turb_mat_v(ycount(k,Ncase)+1,xcount(k,Ncase)+1,
Ncase)<Tmin_v
        Turb_mat_v(ycount(k,Ncase)+1,xcount(k,Ncase)+1, Ncase) =
outlier;
    elseif Turb_mat_v(ycount(k,Ncase)+1,xcount(k,Ncase)+1,
Ncase)>Tmax_v
        Turb_mat_v(ycount(k,Ncase)+1,xcount(k,Ncase)+1, Ncase) =
outlier;
    elseif Turb_mat_v(ycount(k,Ncase)+1,xcount(k,Ncase)+1,
Ncase)==0
        Turb_mat_v(ycount(k,Ncase)+1,xcount(k,Ncase)+1, Ncase) =
outlier;
    end
    if Turb_mat_rms(ycount(k,Ncase)+1,xcount(k,Ncase)+1,
Ncase)<Tmin
        Turb_mat_rms(ycount(k,Ncase)+1,xcount(k,Ncase)+1, Ncase)
= outlier;
    elseif Turb_mat_rms(ycount(k,Ncase)+1,xcount(k,Ncase)+1,
Ncase)>Tmax
        Turb_mat_rms(ycount(k,Ncase)+1,xcount(k,Ncase)+1, Ncase)
= outlier;

```

```

elseif Turb_mat_rms(ycount(k,Ncase)+1,xcount(k,Ncase)+1,
Ncase)==0
    Turb_mat_rms(ycount(k,Ncase)+1,xcount(k,Ncase)+1, Ncase)
= outlier;
end

% Filter out data outside bounds or at '0'
if (Turb_line_u(k,Ncase)<Tmin)
    Turb_line_u(k,Ncase) = outlier;
elseif (Turb_line_u(k,Ncase)>Tmax)
    Turb_line_u(k,Ncase) = outlier;
elseif (Turb_line_u(k,Ncase)==0)
    Turb_line_u(k,Ncase) = outlier;
end
if (Turb_line_v(k,Ncase)<Tmin_v)
    Turb_line_v(k,Ncase) = outlier;
elseif (Turb_line_v(k,Ncase)>Tmax_v)
    Turb_line_v(k,Ncase) = outlier;
elseif (Turb_line_v(k,Ncase)==0)
    Turb_line_v(k,Ncase) = outlier;
end
if (Turb_line_rms(k,Ncase)<Tmin)
    Turb_line_rms(k,Ncase) = outlier;
elseif (Turb_line_rms(k,Ncase)>Tmax)
    Turb_line_rms(k,Ncase) = outlier;
elseif (Turb_line_rms(k,Ncase)==0)
    Turb_line_rms(k,Ncase) = outlier;
end

if k == 1 % assign values for first row of CSV file
    x_pix(k,Ncase) = data(k,3);
    y_pix(k,Ncase) = data(k,4);
    x_mm(k,Ncase) = data(k,5);
    y_mm(k,Ncase) = data(k,6);
else % all other rows after r1

    % assign X values only if the y-col starts over.
    if ycount(k,Ncase)-ycount(k-1,Ncase)<= -2
        xAx_count = xAx_count + 1;
        x_pix(xAx_count,Ncase) = data(k,3);
        x_mm(xAx_count,Ncase) = data(k,5);
    end

    % assign Y values as the first set of ascending numbers
    if (ycount(k, Ncase)-ycount(k-1, Ncase)== 1) && (k <=
max(ycount(:,Ncase))+1)
        y_pix(k, Ncase) = data(k,4);
        y_mm(k, Ncase) = data(k,6);
    end
end %ends loop that assigns indep axis values

end % end the k (rows) loop

%non-dimensionalize the independent indexes/ axes

```

```

        x_nd(:,Ncase) = x_mm(:,Ncase)/VaneH;
        y_nd(:,Ncase)= y_mm(:,Ncase)/VaneH;
        x_nd_vec(:,Ncase) = x_mm_vec(:,Ncase)/VaneH;
        y_nd_vec(:,Ncase) = y_mm_vec(:,Ncase)/VaneH;

    end                %end of nRowsPlot loop
end                    %end of nColsPlot loop
% data should now all be stored in the appropriate vectors/ matrices

%%%%%%%%%%%%%%%%%%%%%%%%%%%%%%%%%%%%%%%%%%%%%%%%%%%%%%%%%%%%%%%%%%%%%%%% Plot Time:%%%%%%%%%%%%%%%%%%%%%%%%%%%%%%%%%%%%%%%%%%%%%%%%%%%%%%%%%%%%%%%%%%%%%%%%

%set main plot dimensions
PlotX = 10;
PlotY = 40;
PlotdX = 1200;
PlotdY = 850;
PlotTIvMin = 0;
PlotTIvMax = Tmax_v*1.2;
PlotTIuMin = 0;
PlotTIuMax = Tmax*1.2;

%This plots the vector field over a color map of RMS turbulence
intensity
Ncase = 0;
myplot15=figure;
set(myplot15,'Position', [PlotX, PlotY, PlotdX, PlotdY])
for i = 1:nRowsPlot
    for j = 1:nColsPlot
        Ncase = Ncase+1;
        subplot(nRowsPlot,nColsPlot,Ncase),
        pcolor(x_nd(:,Ncase),y_nd(:,Ncase),Turb_mat_rms(:, :,Ncase))
        caxis([Tmin,Tmax]);
        shading interp
        axis([min(x_nd(:,Ncase)) max(x_nd(:,Ncase)) min(y_nd(:,Ncase))
max(y_nd(:,Ncase))])
        hold on

        quiver(x_nd_vec(:,Ncase),y_nd_vec(:,Ncase),U_vel(:,Ncase),V_vel(:,Ncase)
),scale,'LineWidth', lw,'color', 'black')
        hold off
    end
end
title('Velocity Vectors over TI_rms')
if (nRowsPlot ==1) && (nColsPlot ==1)
    ylabel('Spanwise Distance/Vane Height (-)')
    xlabel('Streamwise Distance/Vane Height (-)')
    colorbar;
end
if SvPlt == 1
    fn = 'C:\Users\Levi\Documents\MATLAB\Plots\VecTIrms.jpg';
    print(myplot15, '-djpeg100',fn);
end

```



## Appendix B

### Processed Data for Mass Flow Rate Increase Study

Curved cavity vane configuration

Cavity mass flow: 10% of main

Cavity equivalence ratio: 1.0

Main $\dot{m}$ (kg/s)	Position of Exp. Plane	Mean U_Vel (m/s)	Mean V_Vel (m/s)	+/- Error (m/s)	Percent Error (%)	Mean Stdv_U (m/s)	Mean Stdv_V (m/s)	Mean Nsamp (No.)	Mean TI_u (-)	Mean TI_v (-)
0.6	1	-22.173	2.434	2.490	22.322	6.125	3.829	32.338	0.289	0.175
0.6	2	-21.558	1.027	1.185	10.981	3.755	2.521	55.955	0.262	0.179
0.6	3	-22.778	0.511	2.082	18.272	5.897	3.420	41.201	0.278	0.174
0.6	4	-24.177	-0.033	2.755	22.793	7.049	3.984	33.178	0.307	0.172
0.9	1	-29.474	3.546	2.221	14.964	6.208	4.158	43.472	0.296	0.203
0.9	2	-32.075	2.066	1.915	11.913	5.858	3.933	52.176	0.195	0.136
0.9	3	-34.639	0.837	1.603	9.252	4.756	3.615	53.358	0.140	0.111
0.9	4	-34.718	0.277	2.129	12.261	6.144	3.688	43.540	0.188	0.117
1.2	1	-35.882	4.314	2.497	13.820	6.983	4.769	44.049	0.285	0.162
1.2	2	-41.322	3.058	1.731	8.357	5.276	4.513	61.772	0.138	0.125
1.2	3	-42.129	1.370	1.627	7.720	4.914	3.971	57.922	0.135	0.113
1.2	4	-42.651	0.362	2.182	10.233	6.354	3.819	44.332	0.190	0.126
1.5	1	-44.509	5.527	2.552	11.379	7.864	5.627	55.158	0.311	0.161
1.5	2	-51.203	3.535	2.010	7.834	6.356	5.523	67.400	0.133	0.119
1.5	3	-52.217	1.469	1.973	7.552	6.042	4.862	59.388	0.137	0.103
1.5	4	-52.625	0.486	1.733	6.586	5.642	4.286	64.229	0.143	0.110

**Straight cavity vane configuration**  
**Cavity mass flow: 10% of main**  
**Cavity equivalence ratio: 1.0**

Main m_dot (kg/s)	Position of Exp. Plane	Mean U_Vel (m/s)	Mean V_Vel (m/s)	+/- Error (m/s)	Percent Error (%)	Mean Stdv_U (m/s)	Mean Stdv_V (m/s)	Mean Nsamp (No.)	Mean TI_u (-)	Mean TI_v (-)
0.6	1	-23.746	1.931	1.345	11.295	3.187	2.642	36.367	0.136	0.112
0.6	2	-24.764	1.056	1.169	9.436	2.782	2.490	39.157	0.114	0.100
0.6	3	-25.389	0.217	1.258	9.907	2.990	2.262	34.143	0.119	0.090
0.6	4	-24.983	-0.339	1.196	9.570	2.899	2.102	34.464	0.124	0.086
0.9	1	-32.401	2.695	1.467	9.026	3.740	3.371	45.235	0.117	0.103
0.9	2	-34.021	1.622	1.383	8.118	3.488	3.360	47.143	0.103	0.099
0.9	3	-34.697	0.438	1.308	7.536	3.288	2.946	43.799	0.097	0.085
0.9	4	-34.427	-0.108	1.269	7.373	3.274	2.648	42.282	0.099	0.078
1.2	1	-40.725	3.967	2.634	12.873	5.966	5.082	34.013	0.148	0.124
1.2	2	-43.284	1.874	1.875	8.655	4.643	4.372	44.442	0.108	0.101
1.2	3	-43.674	1.100	1.633	7.478	4.261	3.759	46.479	0.099	0.086
1.2	4	-44.153	0.012	1.793	8.123	4.498	3.527	39.035	0.105	0.081
1.5	1	-50.402	4.637	2.219	8.768	6.606	5.726	59.624	0.134	0.113
1.5	2	-52.345	2.812	1.894	7.227	5.786	5.519	68.456	0.111	0.105
1.5	3	-54.756	0.800	2.014	7.356	5.286	4.630	46.752	0.098	0.085
1.5	4	-54.273	0.344	1.953	7.195	5.079	4.258	44.265	0.097	0.080

**Straight cavity vane configuration**  
**Cavity mass flow: 10% of main**  
**Cavity equivalence ratio: 1.5**

0.6	1	-23.326	2.455	1.086	9.264	3.139	2.568	53.534	0.137	0.109
0.6	2	-24.284	1.467	0.851	6.999	2.536	2.506	67.378	0.105	0.103
0.6	3	-24.724	0.561	0.774	6.263	2.416	2.031	63.809	0.099	0.082
0.6	4	-24.559	0.047	1.156	9.412	3.223	2.296	45.032	0.139	0.095
0.8	1	-28.727	3.397	1.809	12.511	4.564	3.479	38.641	0.161	0.120
0.8	2	-30.361	1.905	1.038	6.827	3.126	2.996	66.787	0.104	0.098
0.8	3	-30.669	0.751	1.761	11.481	4.497	3.117	37.081	0.149	0.102
0.8	4	-30.515	0.449	1.574	10.312	4.204	2.769	39.310	0.147	0.092

## Processed Data for Mass Flow Ratio Study

Straight cavity vane configuration

Cavity mass flow 0.131 kg/min; Equivalence ratio: 0.7

Position of Exp. Plane	Cavity to Main Ratio	Main $\dot{m}$ (kg/s)	Mean U_Vel (m/s)	Mean V_Vel (m/s)	+/- Error (m/s)	Percent Error (%)	Mean Stdv_U (m/s)	Mean Stdv_V (m/s)	Mean Nsamp (No.)	Mean TI_u (-)	Mean TI_v (-)
1	0.05	2.627	43.016	1.154	5.848	27.181	11.483	5.148	17.787	0.320	0.146
2	0.05	2.627	74.928	2.774	8.856	23.622	14.749	8.656	14.326	0.251	0.135
3	0.05	2.627	77.819	0.810	8.223	21.132	14.189	7.781	14.879	0.251	0.137
4	0.05	2.627	75.014	1.958	10.244	27.302	16.629	7.528	12.199	0.293	0.135
1	0.1	1.313	38.593	3.605	3.466	17.885	7.984	5.497	30.043	0.230	0.150
2	0.1	1.313	39.332	3.637	3.474	17.592	8.161	5.409	30.504	0.235	0.150
3	0.1	1.313	40.966	1.794	4.979	24.286	9.993	5.507	20.172	0.287	0.151
4	0.1	1.313	43.562	0.321	4.477	20.552	9.165	5.127	21.142	0.235	0.131
1	0.15	0.876	27.277	2.932	2.386	17.394	5.016	3.771	26.577	0.208	0.148
2	0.15	0.876	29.369	1.819	2.273	15.451	4.369	3.341	22.485	0.156	0.116
3	0.15	0.876	30.986	0.084	1.843	11.896	3.906	2.959	27.161	0.138	0.107
4	0.15	0.876	30.728	0.470	1.532	9.970	3.513	2.496	30.398	0.131	0.092
1	0.2	0.657	21.421	2.717	1.516	14.042	3.698	2.783	35.807	0.194	0.137
2	0.2	0.657	23.505	1.863	1.356	11.502	3.239	2.447	34.433	0.143	0.106
3	0.2	0.657	24.825	0.321	1.126	9.067	2.776	2.148	37.355	0.120	0.090
4	0.2	0.657	24.835	0.369	1.251	10.074	2.916	2.099	31.687	0.132	0.094

# Straight cavity vane configuration

Cavity mass flow 0.092 kg/min; Equivalence ratio: 1.0

Position of Exp. Plane	Cavity to Main Ratio	Main $\dot{m}$ (kg/s)	Mean U_Vel (m/s)	Mean V_Vel (m/s)	+/- Error (m/s)	Percent Error (%)	Mean Stdv_U (m/s)	Mean Stdv_V (m/s)	Mean Nsamp (No.)	Mean TI_u (-)	Mean TI_v (-)
1	0.05	1.839	57.655	4.652	2.756	9.530	6.999	6.251	44.535	0.153	0.114
2	0.05	1.839	59.610	1.504	2.526	8.471	6.495	5.606	44.333	0.147	0.102
3	0.05	1.839	62.721	0.933	2.345	7.476	6.373	4.730	44.018	0.136	0.085
4	0.05	1.839	57.747	1.763	2.494	8.634	6.860	4.489	41.503	0.174	0.090
1	0.1	0.919	31.457	2.717	1.851	11.725	4.474	3.565	36.693	0.168	0.119
2	0.1	0.919	33.390	1.153	1.638	9.807	4.039	3.378	39.685	0.150	0.105
3	0.1	0.919	33.907	0.232	1.659	9.787	4.109	2.975	35.905	0.154	0.101
4	0.1	0.919	32.043	0.623	2.749	17.153	6.062	3.486	24.864	0.232	0.123
1	0.15	0.613	22.383	2.931	1.542	13.666	3.445	2.523	29.440	0.179	0.169
2	0.15	0.613	24.602	0.777	1.131	9.194	2.886	2.336	41.357	0.151	0.104
3	0.15	0.613	24.495	0.160	0.985	8.043	2.531	1.990	41.053	0.143	0.091
4	0.15	0.613	23.011	0.335	1.115	9.690	2.714	1.772	32.470	0.282	0.180
1	0.2	0.460	18.167	2.433	1.034	11.287	2.689	2.039	40.894	0.195	0.118
2	0.2	0.460	20.134	1.242	0.820	8.127	2.099	1.825	44.234	0.123	0.096
3	0.2	0.460	20.203	0.243	0.689	6.820	1.815	1.465	44.026	0.113	0.079
4	0.2	0.460	18.926	0.168	0.881	9.315	2.162	1.468	33.779	0.199	0.124

# Straight cavity vane configuration

Cavity mass flow 0.071 kg/min; Equivalence ratio: 1.3

Position of Exp. Plane	Cavity to Main Ratio	Main $\dot{m}$ (kg/s)	Mean $U_{Vel}$ (m/s)	Mean $V_{Vel}$ (m/s)	+/- Error (m/s)	Percent Error (%)	Mean $Stdv\_U$ (m/s)	Mean $Stdv\_V$ (m/s)	Mean $N_{samp}$ (No.)	Mean $TI\_u$ (-)	Mean $TI\_v$ (-)
1	0.05	1.414	44.781	3.371	2.783	12.394	6.465	4.945	32.862	0.179	0.112
2	0.05	1.414	47.280	0.844	2.577	10.899	6.055	4.669	33.821	0.176	0.106
3	0.05	1.414	48.422	0.367	2.535	10.471	6.091	4.023	31.850	0.196	0.095
4	0.05	1.414	43.816	1.042	3.447	15.728	8.009	3.918	25.705	0.252	0.101
1	0.1	0.707	25.782	2.592	1.794	13.848	4.238	3.205	33.696	0.173	0.124
2	0.1	0.707	26.422	1.138	2.330	17.618	5.235	3.425	27.700	0.235	0.131
3	0.1	0.707	27.670	0.000	2.007	14.503	4.673	3.074	29.856	0.203	0.117
4	0.1	0.707	26.819	0.214	3.047	22.719	6.101	3.793	21.364	0.240	0.143
1	0.15	0.471	18.591	2.487	1.493	15.924	3.404	2.315	29.196	0.205	0.125
2	0.15	0.471	19.745	0.991	1.054	10.663	2.649	1.989	37.953	0.183	0.109
3	0.15	0.471	20.130	0.295	0.767	7.621	2.012	1.588	42.895	0.135	0.086
4	0.15	0.471	18.935	0.159	1.558	16.459	3.557	2.030	26.534	0.229	0.115
1	0.2	0.354	15.045	1.964	0.733	9.663	1.951	1.553	44.469	0.155	0.104
2	0.2	0.354	15.833	0.705	0.687	8.665	1.688	1.567	43.232	0.130	0.103
3	0.2	0.354	16.239	0.253	0.729	8.977	1.896	1.397	40.085	0.156	0.091
4	0.2	0.354	14.876	0.058	1.200	16.139	2.926	1.699	30.521	0.236	0.122

# Straight cavity vane configuration

Cavity mass flow 0.061 kg/min; Equivalence ratio: 1.5

Position of Exp. Plane	Cavity to Main Ratio	Main $\dot{m}$ (kg/s)	Mean $U_{Vel}$ (m/s)	Mean $V_{Vel}$ (m/s)	+/- Error (m/s)	Percent Error (%)	Mean Stdv $_U$ (m/s)	Mean Stdv $_V$ (m/s)	Mean Nsamp (No.)	Mean $TI_u$ (-)	Mean $TI_v$ (-)
1	0.05	1.226	40.545	3.970	3.556	17.460	7.764	5.611	27.870	0.209	0.143
2	0.05	1.226	41.404	2.322	5.313	25.622	9.870	5.723	17.718	0.278	0.169
3	0.05	1.226	44.952	0.071	4.578	20.368	8.539	5.337	18.587	0.199	0.127
4	0.05	1.226	45.221	1.052	5.148	22.760	9.460	5.199	16.893	0.224	0.132
1	0.1	0.613	23.738	2.549	1.648	13.807	3.296	2.765	26.173	0.140	0.115
2	0.1	0.613	24.920	2.110	2.297	18.367	3.310	2.925	14.215	0.133	0.116
3	0.1	0.613	26.287	0.540	1.943	14.779	3.076	2.701	17.056	0.118	0.103
4	0.1	0.613	25.284	0.301	4.232	33.475	8.468	5.100	20.957	0.366	0.235
1	0.15	0.409	16.778	1.868	0.716	8.483	2.318	1.777	63.929	0.137	0.105
2	0.15	0.409	17.608	0.975	0.756	8.573	1.792	1.650	39.878	0.102	0.093
3	0.15	0.409	18.282	0.124	0.831	9.094	1.983	1.477	33.997	0.108	0.081
4	0.15	0.409	18.105	0.041	0.938	10.363	2.219	1.570	32.261	0.123	0.087
1	0.2	0.306	15.492	2.243	0.788	10.066	1.873	1.463	34.951	0.119	0.093
2	0.2	0.306	15.692	1.289	0.648	8.234	1.537	1.378	38.966	0.098	0.087
3	0.2	0.306	15.316	0.062	0.883	11.527	2.005	1.581	32.137	0.131	0.103
4	0.2	0.306	15.400	0.193	0.880	11.432	1.944	1.494	29.797	0.126	0.097

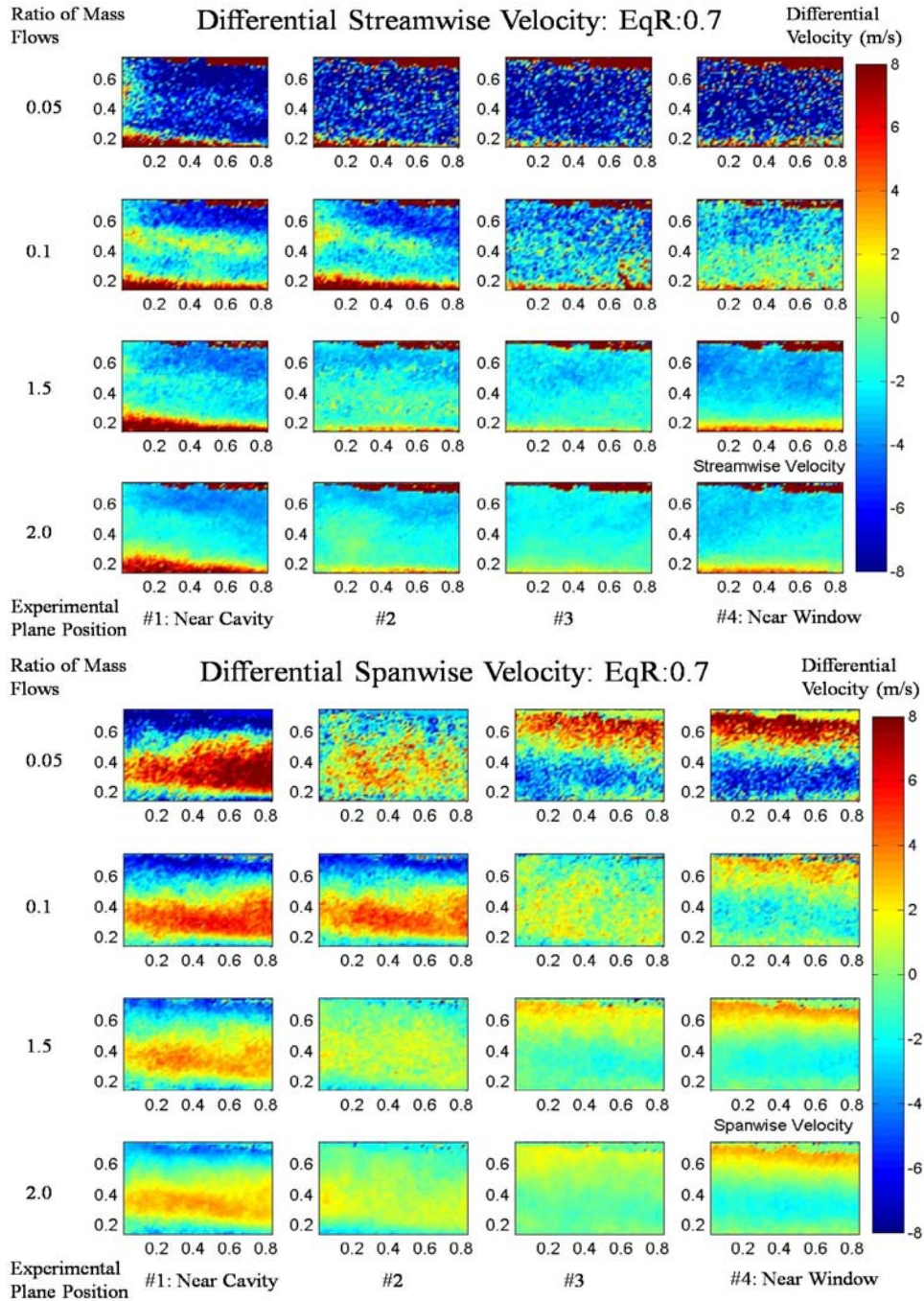
## Appendix C

### Differential Velocity Maps

**Straight cavity vane configuration**

**Cavity mass flow 0.131 kg/min; Equivalence ratio: 0.7**

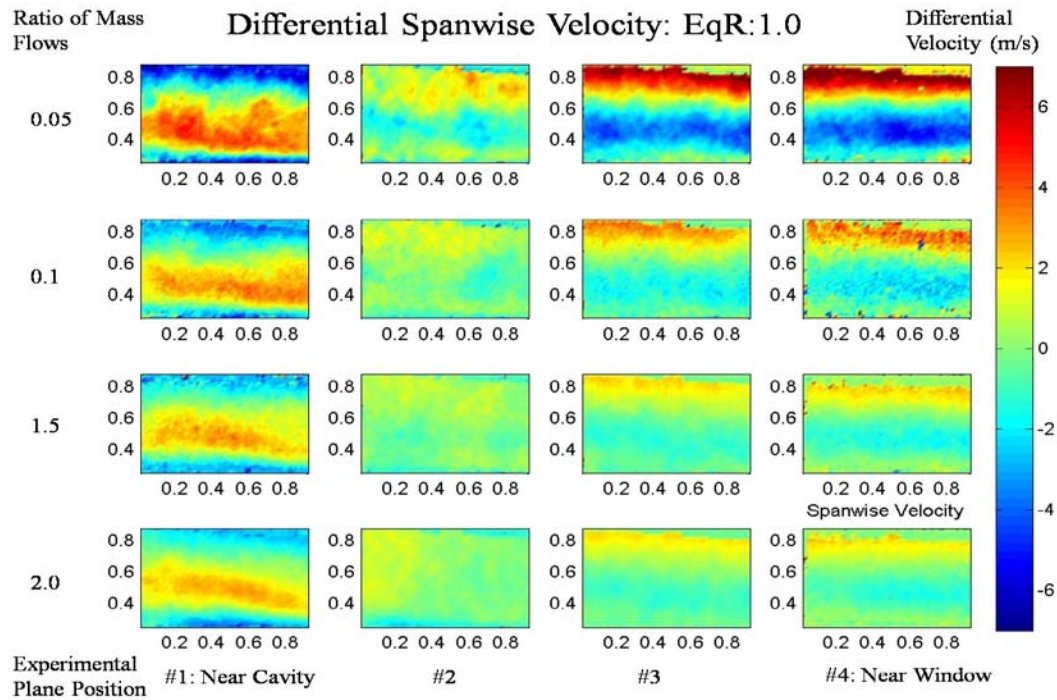
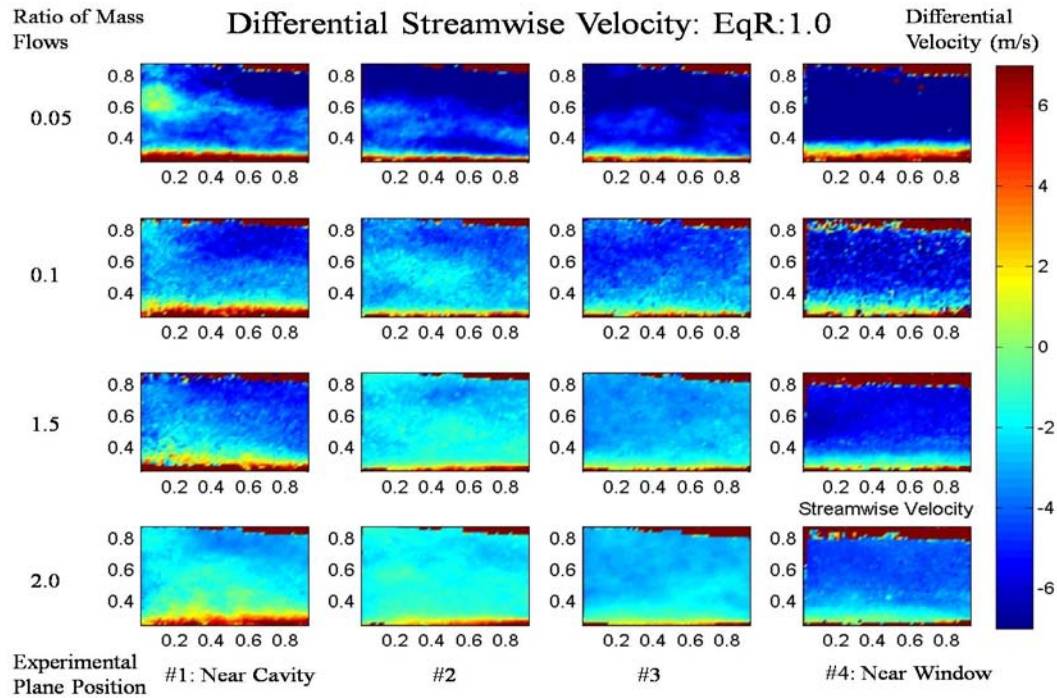
Respective average velocity subtracted from every point showing only the difference





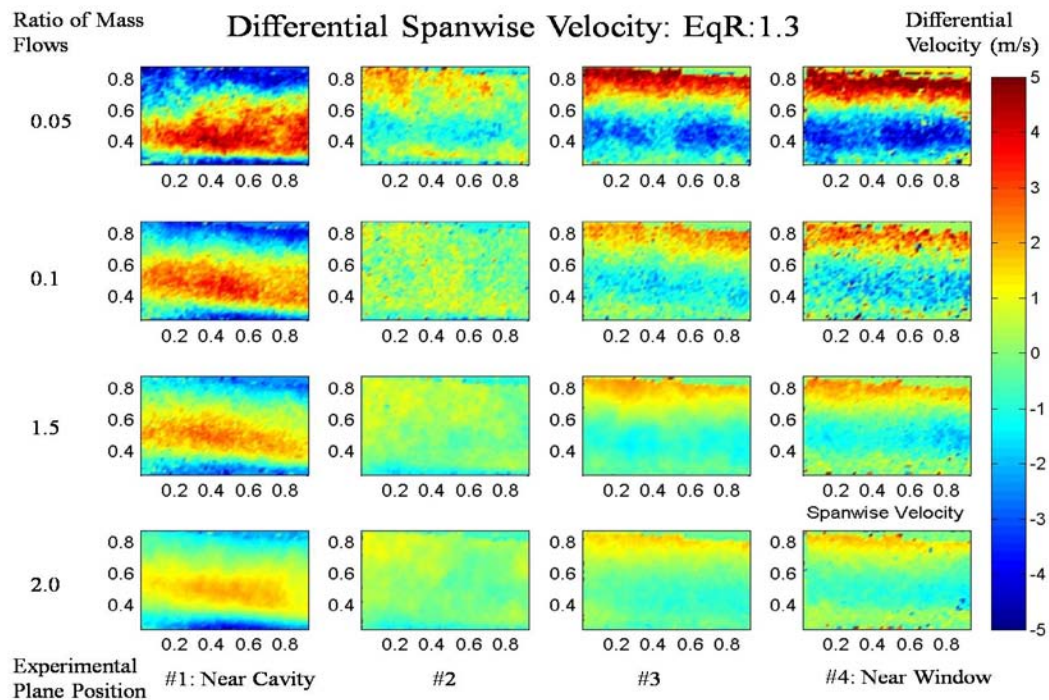
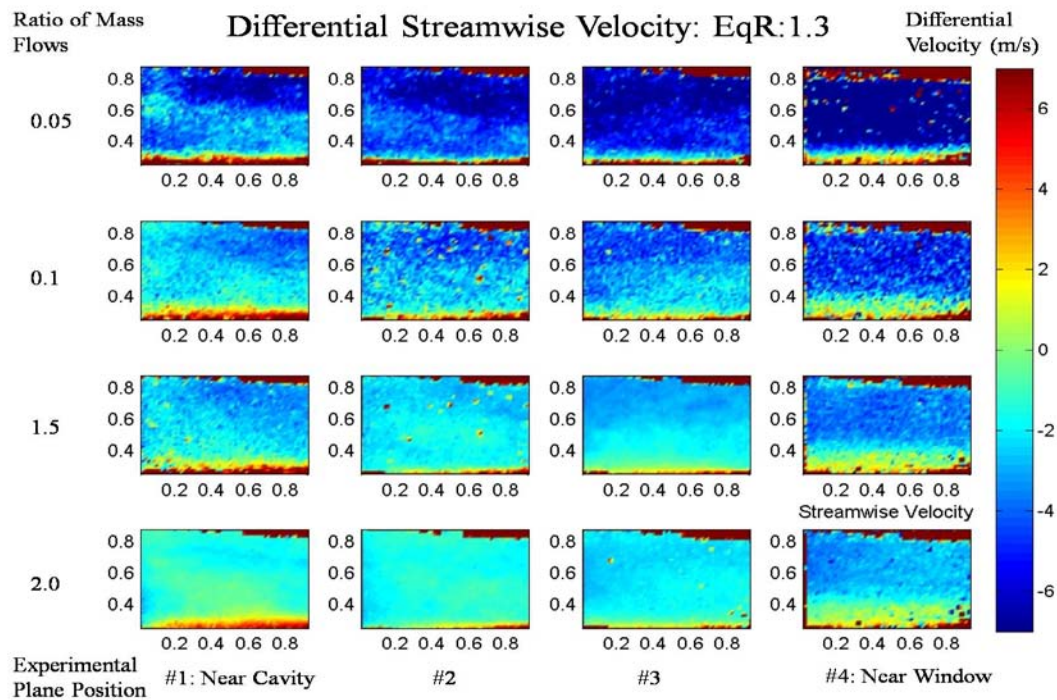
## Straight cavity vane configuration

Cavity mass flow 0.092 kg/min; Equivalence ratio: 1.0



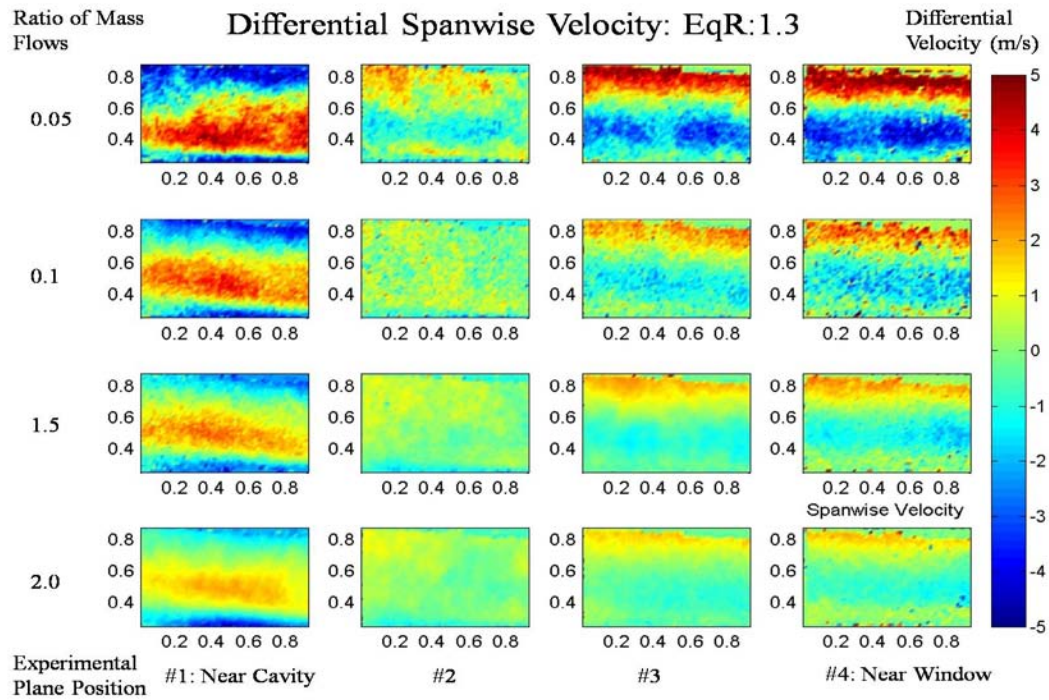
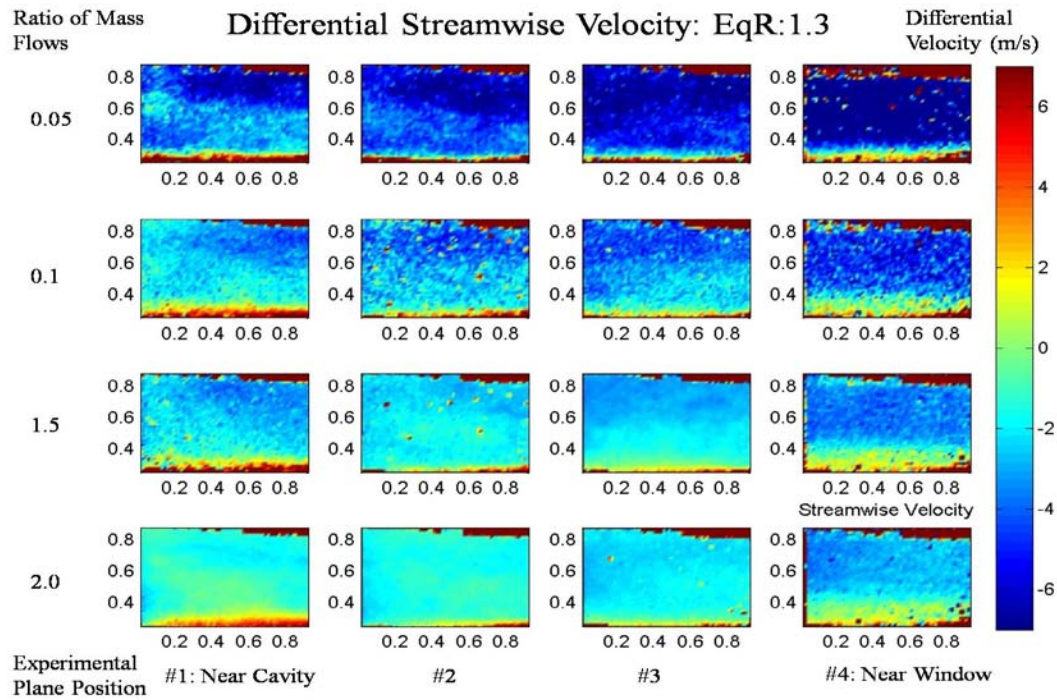


**Cavity mass flow 0.071 kg/min; Equivalence ratio: 1.3**



## Straight cavity vane configuration

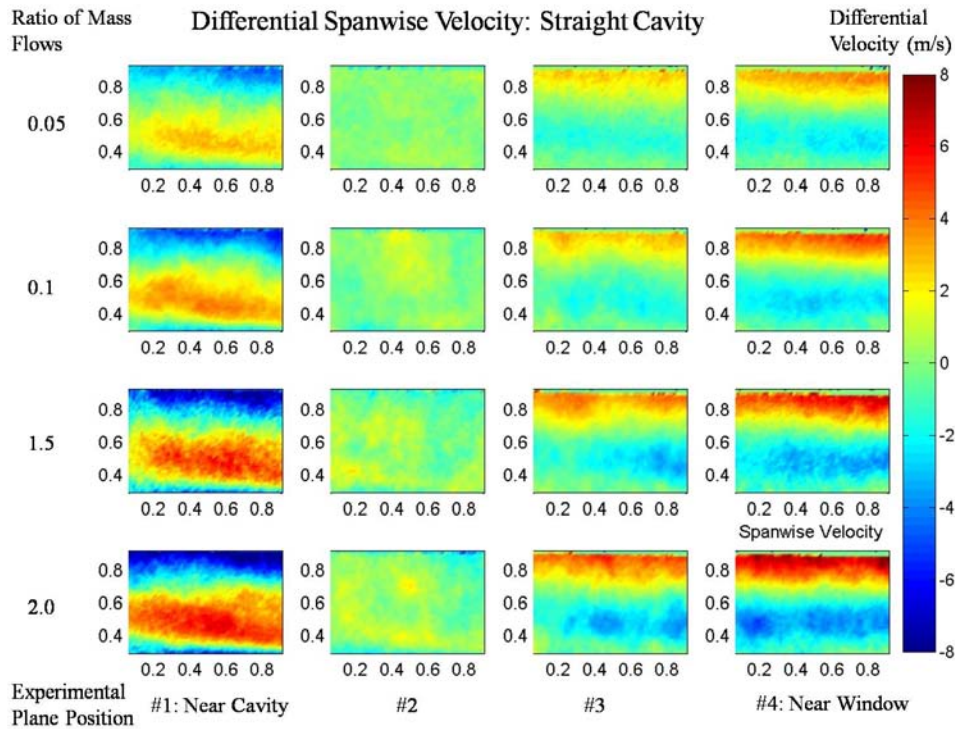
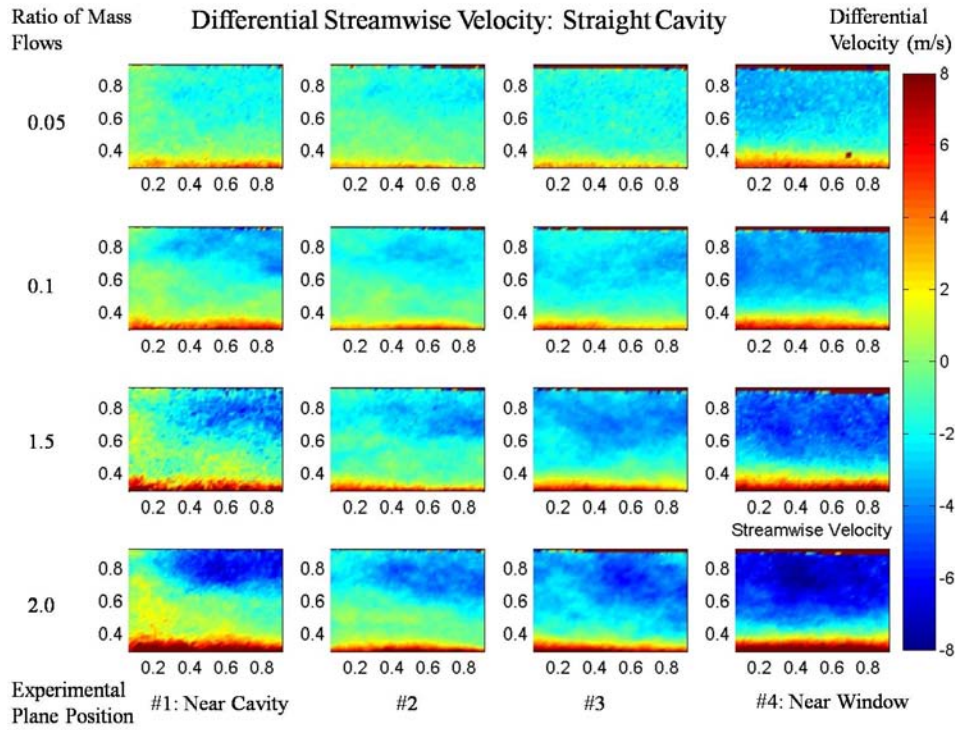
Cavity mass flow 0.061 kg/min; Equivalence ratio: 1.5





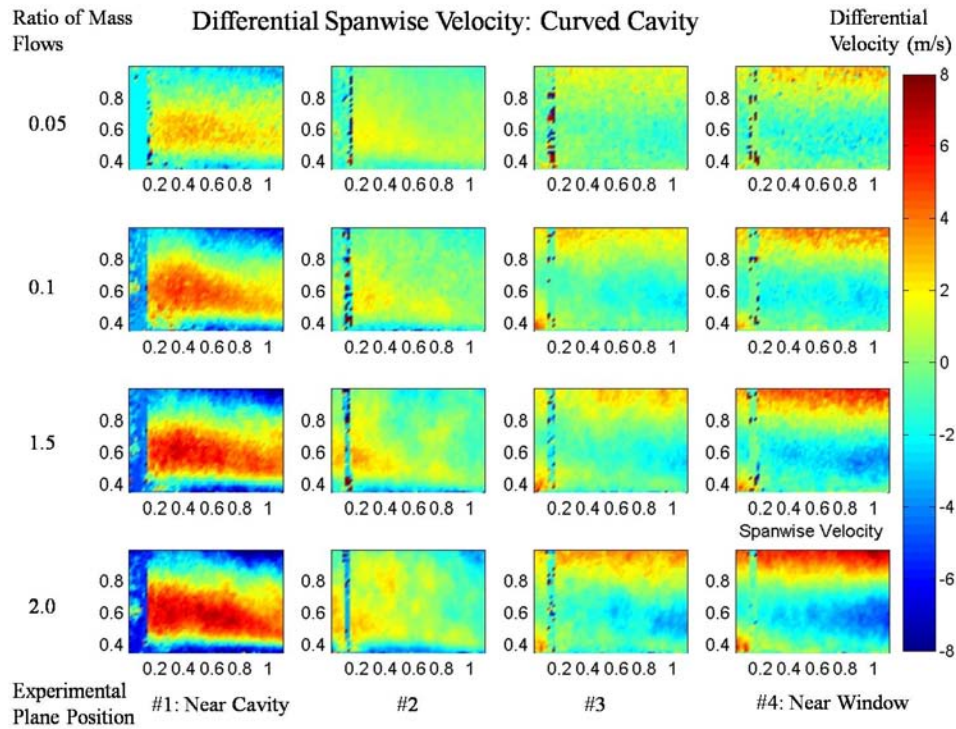
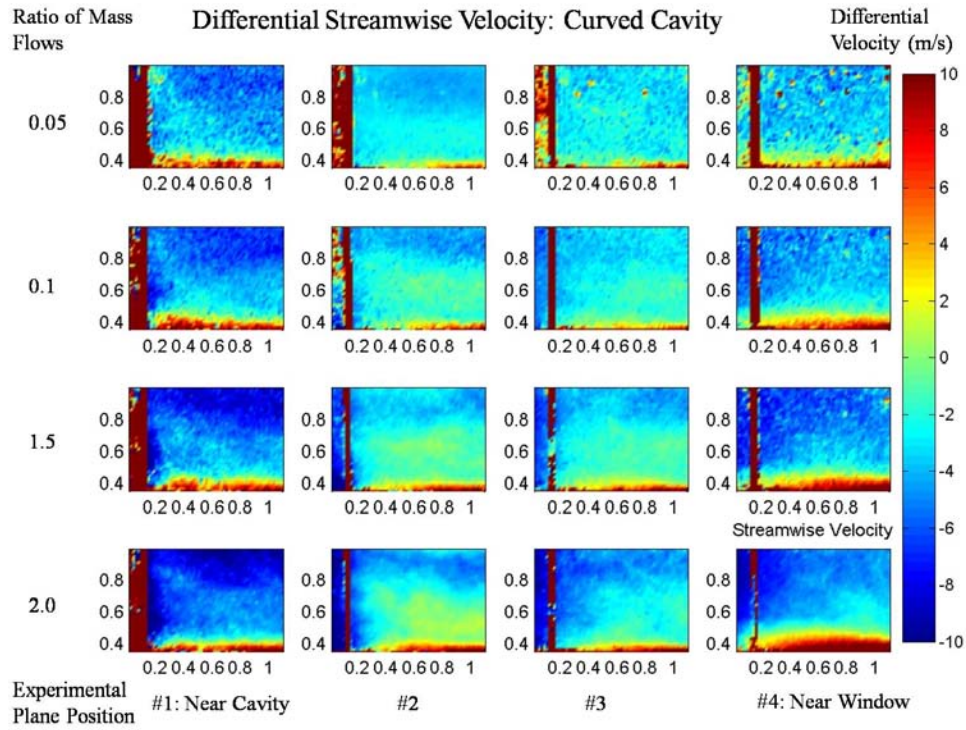
## Straight cavity vane configuration

Cavity to Main mass flow ratio = 0.10; Equivalence ratio: 1.0



## Curved cavity vane configuration

Cavity to Main mass flow ratio = 0.10; Equivalence ratio: 1.0



## Bibliography (In Order of Appearance)

1. Energy Information Administration. "Oil: Crude and Petroleum Products: Data & Statistics" 14 July 2009. [<http://www.eia.doe.gov/basics/quickoil.html>. Accessed 16 August 2009]
2. Mattingly, J. D., Heiser, W. H., & Pratt, D. T., *Aircraft Engine Design*(2<sup>nd</sup> ed.) American Institute of Aeronautics and Astronautics, Inc., 2002.
3. Sirignano, W.A., and Liu, F., "Performance Increases for Gas-Turbine Engines Through Combustion Inside the Turbine," *Journal of Propulsion and Power*, **15**:1 pp.111-118 (1999).
4. Mattingly, J. D., *Elements of Gas Turbine Propulsion*. McGraw-Hill, Inc., 1996.
5. Lakusta, P. J., *Laser-Induced Fluorescence and Performance Analysis of the Ultra-Compact Combustor*. MS thesis, AFIT/GAE/ENY/08-J03. Graduate School of Engineering and Management, Air Force Institute of Technology (AU), Wright-Patterson AFB OH, June 2008.
6. Greenwood, R. T., *Numerical Analysis and Optimization of the Ultra Compact Combustor*. MS thesis, AFIT/GAE/ENY/05-M10. Graduate School of Engineering and Management, Air Force Institute of Technology (AU), Wright-Patterson AFB OH, March 2005.
7. Greenwood, R. T., Anthenien, R. A. "Computational Analysis of the Ultra Compact Combustor" 43<sup>rd</sup> AIAA Aerospace Sciences Meeting and Exhibit. Reno, Nevada, 2005
8. Saravanamuttoo, H., Rogers, G., & Cohen, H., *Gas Turbine Theory* (5<sup>th</sup> ed.), London: Prentice Hall, 2001.
9. Brandt, S. A., Stiles, R. J., Bertin, J. J., Whitford, R., *Introduction to Aeronautics: A Design Perspective*. American Institute of Aeronautics and Astronautics, Inc. 1997
10. Anisko, J. "AIAA Conference Paper" 44<sup>th</sup> AIAA Aerospace Sciences Meeting and Exhibit. Reno, Nevada, 2006
11. Lefebvre, A. H., *Gas Turbine Combustion*. New York: McGraw-Hill, Inc. 1983.

12. Turns, S. R., *An Introduction to Combustion* (2<sup>nd</sup> Ed.). New York: McGraw-Hill, Inc., 1996.
13. Quaale, R. J., *Experimental Results for a High Swirl, Ultra Compact Combustor for Gas Turbine Engines*. MS thesis, AFIT/GAE/ENY/03-5. Graduate School of Engineering and Management, Air Force Institute of Technology (AU), Wright-Patterson AFB OH, March 2003.
14. Anthenien, R. A., Zelina, J., "Experimental Results on the Turbulent Combustion Regimes within a Small-Scale Atmospheric Pressure High-g Combustor." Spring Technical Meeting of the Central States Section: Combustion institute, May 2006.
15. Anisko, J., *Numerical Investigation of Cavity-Vane Interactions Within the Ultra Compact Combustor*. MS thesis, AFIT/GAE/ENY/06-M01. Graduate School of Engineering and Management, Air Force Institute of Technology (AU), Wright-Patterson AFB OH, March 2006.
16. Koether, S. J., *Validation of the AFIT Small Scale Combustion Facility and OH Laser-Induced Fluorescence of an Atmospheric Laminar Premixed Flame*. MS thesis, AFIT/GAE/ENY/07-S03. Graduate School of Engineering and Management, Air Force Institute of Technology (AU), Wright-Patterson AFB OH, September 2007.
17. Moenter, D. S., *Design and Numerical Simulation of Two Dimensional Ultra Compact Combustor Model Sections for Experimental Observation of Cavity-Vane Interactions*. MS thesis, AFIT/GAE/ENY/06-S07. Graduate School of Engineering and Management, Air Force Institute of Technology (AU), Wright-Patterson AFB OH, September 2006.
18. Dittman, E. R., *Design, Build and Validation of Small Scale Combustion Chamber Testing Facility*. MS thesis, AFIT/GAE/ENY/06-M06. Graduate School of Engineering and Management, Air Force Institute of Technology (AU), Wright-Patterson AFB OH, March 2006.
19. Anderson, W. S., *Design, Construction, and Validation of the AFIT Small Scale Combustion Facility and Sectional Model of the Ultra-compact Combustor*. MS thesis, AFIT/GAE/ENY/07-M01. Graduate School of Engineering and Management, Air Force Institute of Technology (AU), Wright-Patterson AFB OH, March 2007.
20. Koether S. J., *Validation of the AFIT Small Scale Combustion Facility and OH Laser-Induced Fluorescence of an Atmospheric Laminar Premixed Flame*. MS thesis, AFIT/GAE/ENY/08-M14. Graduate School of Engineering and Management, Air Force Institute of Technology (AU), Wright-Patterson AFB OH, March 2008.

21. Hankins, T. B., *Laser Diagnostic System Validation and Ultra-Compact Combustor Characterization*. MS thesis, AFIT/GAE/ENY/08-M14. Graduate School of Engineering and Management, Air Force Institute of Technology (AU), Wright-Patterson AFB OH, March 2008.
22. Dantec Dynamics, *2D PIV Reference Manual* (2<sup>nd</sup> ed.) DK-2740 Skovlunde, Denmark, October 2006.
23. TSI, Inc., *Laser Diagnostics: Seed Particle Specifications product information sheet*, [[http://www.mie.uth.gr/ekp\\_yliko/SeedParticles\\_2980461.pdf](http://www.mie.uth.gr/ekp_yliko/SeedParticles_2980461.pdf). Accessed March 2009.]
24. Capitani, G. C., Di Pierro, S., & Tempesta, G., "The 6H-SiC Structure Model: Further Refinement from SCXRD Data from a Terrestrial Moissanite," *American Mineralogist*, Feb. 2007, v.92; p.403-407.
25. Mercer, C., *Optical Metrology for Fluids, Combustion and Solids*. National Aeronautics and Space Administration Glenn Research Center. Kluwer Academic Publishers, 2003
26. Dantec Dynamics, *FlowManager Software and Introduction to PIV Instrumentation: software user's guide* (6<sup>th</sup> ed.), September 2002
27. Paschotta, R. "Encyclopedia of Laser Physics and Technology," 22 May 2009. [<http://www.rp-photonics.com/encyclopedia.html>. Accessed 20 September 2009.]
28. Dantec Dynamics, *DC Image Acquisition System user's guide* (5<sup>th</sup> ed.), November 2005
29. Dantec Dynamics, *Specification on 9080C0411 Camera Filter, 532 nm*, 23 June 2009.
30. Pust, O., *PIV: Direct Cross-Correlation compared with FFT-based Cross-Correlation*, Dept. Fluid Mechanics, Mechanical Engineering, University of the Federal Armed Forces, D-22039 Hamburg.
31. Rekab, K., & Shaikh, M., *Statistical Design of Experiments with Engineering Applications*, Florida: CRC Press, Taylor & Francis Group, 2005.
32. Newport Corp., *ESP300 Motion Controller/Driver User's Manual*. Irvine California 2002 [<http://phubner.eng.ua.edu/Files/ESP300.pdf>. Accessed 6 July 2009.]

33. Unifrax Corp. *Fiberfrax High temperature Insulation: product information sheet*,  
[<http://www.fiberfrax.com>. Accessed 20 September 2009.]
34. Scitec *PS-10 Remote Operation Power Seeder Operating Manual*, Derby DE1 2BU, UK
35. Nikon Corp., *AF Micro-Nikkor 60mm f/2.8 D instruction manual*, Tokyo, Japan, January 2007.
36. Dantec Dynamics, *80X70 Light-Sheet Series installation & user's guide* (2<sup>nd</sup> ed.), July 2002.
37. New Wave Research, *Solo PIV: Nd:YAG Laser System Operator's manual*, Fremont, California, April 2006.
38. Coleman H. W., & Steele W. G. *Experimentation and Uncertainty Analysis for Engineers* (2<sup>nd</sup> Ed.). Wiley & Sons, Inc., 1999.
39. MKS Instruments. *Alta Type 1480A Mass Flow Controller: product data sheet*,  
[[www.mksinst.com](http://www.mksinst.com). Accessed 29 October 2009.]
40. Lading, L., Wigley, G., & Buchhave, P. *Optical Diagnostics for Flow Processes*. New York: Plenum Press 1994.
41. Baker, R. C., *Flow Measurement Handbook*, Cambridge University Press, 2000.
42. Boutier, A., "Accuracy of Laser Velocimetry," von Karman Institute for Fluid Dynamics, Onera France, Lecture Series 199105.
43. Zelina, J., Sturgess, G. J., & Shouse, D. T. *The Behavior of an Ultra-Compact Combustor (UCC) Based on Centrifugally-Enhanced Turbulent Burning Rates*. 2004.
44. TSI Inc., *Turbulence Intensity Measurements: Application Note AF-141*, August 2008  
[[http://www.tsi.com/uploadedFiles/Product\\_Information/Literature/Application\\_Notes/AF-141%20Turbulence%20Intensity.pdf](http://www.tsi.com/uploadedFiles/Product_Information/Literature/Application_Notes/AF-141%20Turbulence%20Intensity.pdf). Accessed 28 October 2009.]
45. Bernard, P. S., & Wallace, J. M., *Turbulent Flow: Analysis, Measurement and Prediction*. Wiley & Sons, Inc., 2002.



## **VI. Vita**

First Lieutenant Levi M. Thomas graduated from Amador Valley High School in Pleasanton, California in 2001. He received an ROTC scholarship and attended the University of California, Davis from September 2001 until June 2002. In June 2002 he left Davis for Basic Cadet Training at the United States Air Force Academy (USAFA). In May 2006 he earned a Bachelor of Science in Aeronautical Engineering from USAFA, and was commissioned as a Second Lieutenant. He was married to Erika VanWyck Pope on 2 June 2006.

His first assignment was to the National Air and Space Intelligence Center (NASIC), Wright-Patterson AFB where he worked as a foreign air-to-air missile analyst from August 2006 until July 2009. In August 2009 he had a permanent change of assignment to the combustion branch (RZTC) of the Air Force Research Laboratory's Propulsion Division where he currently works in their detonation research facility under the direction of Dr. Fred Schauer. In January 2006, he entered the Graduate School of Engineering and Management, Air Force Institute of Technology as a part time student. He was awarded a fellowship under the Dayton Area Graduate Studies Institute in April 2007 that funded tuition costs. Upon graduation he will remain assigned to the combustion branch at the Air Force Research Laboratory. Most importantly, he is scheduled to become a father in December 2009.

REPORT DOCUMENTATION PAGE				Form Approved OMB No. 074-0188	
<p>The public reporting burden for this collection of information is estimated to average 1 hour per response, including the time for reviewing instructions, searching existing data sources, gathering and maintaining the data needed, and completing and reviewing the collection of information. Send comments regarding this burden estimate or any other aspect of the collection of information, including suggestions for reducing this burden to Department of Defense, Washington Headquarters Services, Directorate for Information Operations and Reports (0704-0188), 1215 Jefferson Davis Highway, Suite 1204, Arlington, VA 22202-4302. Respondents should be aware that notwithstanding any other provision of law, no person shall be subject to a penalty for failing to comply with a collection of information if it does not display a currently valid OMB control number.</p> <p><b>PLEASE DO NOT RETURN YOUR FORM TO THE ABOVE ADDRESS.</b></p>					
1. REPORT DATE (DD-MM-YYYY) 07-12-2009		2. REPORT TYPE Master's Thesis		3. DATES COVERED (From - To) June 2007 - December 2009	
4. TITLE AND SUBTITLE  Flow Measurements Using Particle Image Velocimetry in the Ultra Compact Combustor				5a. CONTRACT NUMBER	
				5b. GRANT NUMBER	
				5c. PROGRAM ELEMENT NUMBER	
6. AUTHOR(S)  Thomas, Levi M., First Lieutenant, USAF				5d. PROJECT NUMBER	
				5e. TASK NUMBER	
				5f. WORK UNIT NUMBER	
7. PERFORMING ORGANIZATION NAMES(S) AND ADDRESS(S) Air Force Institute of Technology Graduate School of Engineering and Management (AFIT/EN) 2950 Hobson Way, Building 640 WPAFB OH 45433-8865				8. PERFORMING ORGANIZATION REPORT NUMBER  AFIT/GAE/ENY/09-D04	
9. SPONSORING/MONITORING AGENCY NAME(S) AND ADDRESS(ES) Air Force Office of Scientific Research Dr. Julian Tishkoff 4015 Wilson Boulevard, Room 713 Arlington, VA 22203-1954				10. SPONSOR/MONITOR'S ACRONYM(S) AFOSR	
				11. SPONSOR/MONITOR'S REPORT NUMBER(S)	
12. DISTRIBUTION/AVAILABILITY STATEMENT  APPROVED FOR PUBLIC RELEASE; DISTRIBUTION UNLIMITED.					
13. SUPPLEMENTARY NOTES					
14. ABSTRACT Velocity measurements were performed using the Particle Image Velocimetry (PIV) technique on the Ultra Compact Combustor (UCC) test rig at the Air Force Institute of Technology (AFIT). Velocity patterns and time-averaged turbulence statistics were calculated for data taken with the UCC burning hydrogen fuel in the straight cavity vane and curved cavity vane configurations. The equivalence was varied from 0.7 to 1.5, while the ratio of cavity air to main air was varied from 5% to 20%. Spanwise turbulence intensity penetrated into less than 50% of the main channel for all conditions except the richest (equivalence ratio of 1.5). A study was performed with the curved and straight sections increasing flow rates while holding other factors constant to determine velocity dependence. Relative turbulence intensities were independent of overall flow velocity in the straight configuration, while a negative correlation was observed in the curved configuration. Overall turbulence intensity levels were measured at 15% and 21% for the straight and curved configurations respective. The RVC generated significant flow rotation. Peak vorticity was observed farthest from the cavity vane suggesting the angle of the RVC is effective in generating increasing flow rotation with streamwise velocity.					
15. SUBJECT TERMS Combustion, Combustors, Laser Diagnostics, Ultra-Compact Combustor, Particle Image Velocimetry					
16. SECURITY CLASSIFICATION OF:			17. LIMITATION OF ABSTRACT	18. NUMBER OF PAGES	19a. NAME OF RESPONSIBLE PERSON
a. REPORT	b. ABSTRACT	c. THIS PAGE			Richard Branam, Lt Col, USAF
U	U	U	UU	210	19b. TELEPHONE NUMBER (Include area code) (937) 255-6565, ext 7485 (emailname@afit.edu)

Standard Form 298 (Rev. 8-98)  
Prescribed by ANSI Std. Z39-18